

NASA  
Technical  
Paper  
2116

May 1983

NASA  
TP  
2116  
c.1



TECH LIBRARY KAFB, NM

# Effect of Empennage Location on Twin-Engine Afterbody/Nozzle Aerodynam. Characteristics at Mach Numbers From 0.6 to 1.2

Laurence D. Leavitt

LOAN COPY: RETURN TO  
AMM TECHNICAL LIBRARY  
KIRTLAND AFB, N.M.

NASA

25

25th Anniversary  
1958-1983



0067859

**NASA  
Technical  
Paper  
2116**

1983

**Effect of Empennage  
Location on Twin-Engine  
Afterbody/Nozzle Aerodynamic  
Characteristics at Mach  
Numbers From 0.6 to 1.2**

Laurence D. Leavitt  
*Langley Research Center*  
*Hampton, Virginia*



National Aeronautics  
and Space Administration

Scientific and Technical  
Information Branch

Use of trade names or names of manufacturers in this report does not constitute an official endorsement of such products or manufacturers, either expressed or implied, by the National Aeronautics and Space Administration.

## SUMMARY

An investigation has been conducted in the Langley 16-Foot Transonic Tunnel to determine the effects of several empennage and afterbody parameters on the aft-end aerodynamic characteristics of a twin-engine fighter-type configuration. Model variables were as follows: horizontal tail axial location and incidence, vertical tail axial location and configuration (twin- versus single-tail arrangements), tail booms, and nozzle power setting. Tests were conducted over a Mach number range from 0.6 to 1.2 and over an angle-of-attack range from  $-2^\circ$  to  $10^\circ$ . Jet total-pressure ratio was varied from jet off to approximately 10.0.

Results of this investigation indicate that tail interference effects were present throughout the range of Mach number tested and provided a significant percentage of total aft-end drag in the transonic speed range. Few general statements could be made concerning the effects of empennage location variables on aft-end lift and drag, as these effects were generally dependent on Mach number, angle of attack, and configuration variables such as nozzle power setting, tail booms, and vertical tail configuration (single versus twin vertical tails).

## INTRODUCTION

Much attention has been given in recent years to the proper integration of the propulsion system into the airframes of highly maneuverable fighter-type configurations. This is especially true for multimission aircraft, which must be capable of operating over a broad range of Mach number, altitude, and angle of attack. These multimission aircraft typically require a variable-geometry nozzle to provide high nozzle internal (thrust) performance over the range of operating Mach numbers and engine pressure ratios. In addition to internal performance, nozzle geometry is also important because it affects the aft-end shape, the ratio of nozzle exit area to maximum airplane cross-sectional area, and local boattail angles, which in turn affect the drag performance of the airframe-nozzle installation. Many studies have been conducted that show large drag penalties can result from the installation of isolated nozzles into a realistic aft end, and that these penalties are generally more significant for the cruise (or closed-down) nozzle configuration than for the afterburning nozzle configuration. (See refs. 1 to 14.) In addition, significant adverse interactions originating from empennage surfaces, base areas, actuator fairings, and tail booms have been found to occur and are reported in references 15 to 19. These interactions can alter the afterbody pressure distributions and cause flow separation on both single- and twin-engine installations. The twin-engine installations are further complicated by the complexity of the flow field, especially in the region between the engines.

As a result of the complex interactions associated with afterbody/nozzle integration and their possible large impact on aircraft lift and drag characteristics, an investigation to determine the effects of empennage location on twin-engine afterbody/nozzle lift and drag has been conducted in the Langley 16-Foot Transonic Wind Tunnel. Model geometric variables were as follows: horizontal tail axial location and incidence, vertical tail axial location and configuration (twin- versus single-tail arrangements), tail boom presence, and nozzle power setting (dry power versus afterburning power). The objectives of this investigation were to provide a

parametric data base on the effects of empennage location on twin-engine aft-end drag, individual aft-end component drag, and tail interference drag increments.

#### SYMBOLS AND ABBREVIATIONS

All forces and moments are referenced to the stability axis system. The moment reference center was located 4.45 cm above the model centerline at fuselage station 104.24.

A	cross-sectional area of model fuselage, $\text{cm}^2$
$A_{an}$	maximum cross-sectional area of internal nozzle at the nozzle exit, $42.6 \text{ cm}^2$ for dry power nozzles and $120.8 \text{ cm}^2$ for A/B nozzles (see fig. 2(b))
$A_{fus}$	maximum cross-sectional area of model fuselage, $317.0 \text{ cm}^2$
$A_{max}$	maximum cross-sectional area of model wing-fuselage combination, $475.1 \text{ cm}^2$
$A_o$	total internal area of outer nozzle exit opening, $49.0 \text{ cm}^2$ for dry power nozzles and $135.9 \text{ cm}^2$ for A/B nozzles (see fig. 2(b))
$A_{seal}$	cross-sectional area enclosed by metric-break seal, $297.2 \text{ cm}^2$
$C_D$	total aft-end drag coefficient, $D/q_\infty S$
$C_{D,a}$	afterbody drag coefficient, $D_a/q_\infty S$
$C_{D,n}$	nozzle drag coefficient, $D_n/q_\infty S$
$C_{D,tails}$	tail drag coefficient, $D_{tails}/q_\infty S$
$\Delta C_{D,ia}$	increment in afterbody-empennage interference-drag coefficient (see eq. (6))
$\Delta C_{D,in}$	increment in nozzle-empennage interference-drag coefficient (see eq. (5))
$\Delta C_{D,it}$	increment in total aft-end empennage interference-drag coefficient (see eq. (4))
$C_L$	total aft-end lift coefficient, $L/q_\infty S$
$C_m$	total aft-end pitching-moment coefficient, $m/q_\infty S\bar{c}$
$C_p$	pressure coefficient, $(p - p_\infty)/q_\infty$

$c$	chord length, cm
$\bar{c}$	support-system-wing mean geometric chord, 44.4 cm
$D$	aft-end drag, N
$D_a$	afterbody drag, N
$D_{bal}$	total aft-end drag measured by balance, N
$D_n$	nozzle drag, N
$D_{tails}$	tail drag, N
$d_{max}$	maximum diameter at nozzle connect location, 9.86 cm
$d_{th}$	nozzle throat diameter, cm
$L$	total aft-end lift, N
$\iota$	model length from nose to nozzle exit, 174.74 cm for dry power nozzle and 174.96 cm for A/B nozzle
$M$	Mach number
$m$	total afterbody pitching moment referenced to $\bar{c}/4$ in support-system-wing chord plane, N-m
$N_{Re}$	Reynolds number
$p$	local static pressure, Pa
$p_{an}$	local pressure at nozzle annular clearance gap, Pa (see fig. 2(b))
$p_{es}$	local static pressure external to metric-break seal, Pa (see fig. 2(b))
$p_{in}$	local internal static pressure, Pa (see fig. 2(b))
$p_{t,j}$	jet total pressure, Pa
$p_{t,\infty}$	free-stream total pressure, Pa
$p_\infty$	free-stream static pressure, Pa
$q_\infty$	free-stream dynamic pressure, Pa
$r$	radius, cm
$r_{max}$	maximum radius at nozzle connect station, $d_{max}/2$
$S$	support-system-wing reference area, $4286 \text{ cm}^2$
$T$	temperature, K

$T_{t,\infty}$	free-stream total temperature, K
$t$	airfoil thickness, cm
$x$	axial distance from model nose, cm
$\alpha$	afterbody angle of attack, deg
$\alpha_{nom}$	nominal angle of attack, deg
$\delta_h$	horizontal tail incidence angle (positive with leading edge up), deg
$\phi$	meridian angle about nozzle axis (see fig. 2(e))
$\Lambda_{le}$	sweep angle at leading edge, deg

**Abbreviations:**

A/B	afterburning
BL	buttock line
FS	fuselage station
LH	left hand
RH	right hand
Sta.	tunnel station
WL	water line

#### APPARATUS AND PROCEDURE

##### Test Facility

The investigation was conducted in the Langley 16-Foot Transonic Tunnel. The facility, shown schematically in figure 1, is a continuous-flow, single-return, atmospheric wind tunnel with a slotted octagonal throat and test section and continuous air exchange. The tunnel has a variable-speed range from  $M = 0.2$  to  $M = 1.3$ . A complete description of this facility and its calibration is presented in reference 20.

##### Model and Support-System Description

Details of the twin-engine tail interference afterbody model and wing-tip-mounted support system used in this investigation are presented in figure 2, and photographs of the model and support system installed in the Langley 16-Foot Transonic Tunnel are shown in figure 3.

The wing-tip-mounted model support system shown in figure 2(a) consisted of three major portions: the twin support booms, the forebody (nose), and the wing and centerbody. These pieces made up the nonmetric portion (that portion not mounted on

force balance) of the twin-engine tail interference model. The centerbody fuselage was essentially rectangular in cross section, with a constant width and height of 25.40 cm and 12.70 cm. The four corners were rounded by a radius of 2.54 cm. The maximum cross-sectional area of the centerbody (fuselage) was  $317.04 \text{ cm}^2$ . The support-system forebody was typical of a powered-model forebody in that the inlets were faired. The "wings" of the support system were mounted above the model centerline in a "high-wing" position, which is typical of many current fighter designs. The support-system wing had a leading-edge sweep of 45°, a taper ratio of 0.5, an aspect ratio of 2.4, and a cranked trailing edge. The airfoil was symmetrical, and the thickness ratios near the wing-fuselage junction at BL 12.70 were realistic ( $t/c = 0.067$ ). From BL 27.94 to the support booms, however, wing thickness ratio increased from 0.077 to 0.10. This increase provided structural support for the model and permitted the transfer of compressed air from the booms to the model propulsion system.

The wing-tip support system was designed to provide a minimum level of support interference, yet provide a more realistic aircraft flow field for the afterbody than would be produced by a blade-mounted support system. Although no support-interference tests have been conducted, support-interference results on a similar wing-tip support system (ref. 21) indicate that relatively low levels of interference exist compared with other propulsion support systems. The results presented in reference 21 also indicate that the lift and drag increments between various empennage parameters investigated should be essentially unaffected by support interference.

The twin-engine afterbody shown in figure 2(b) was attached to the support-system wing and centerbody by mounting on a six-component strain-gage balance. The combined forces and moments for the afterbody shell, empennage surfaces and tail booms (when present), and outer nozzles were measured by the balance and are referred to as total aft-end forces and moments in this paper. The model propulsion system (thrust) forces and moments were not measured by the balance. The propulsion system was grounded to the model support system, and clearance was provided between the metric and nonmetric portions of the model. The afterbody lines were chosen to be typical of current closely spaced twin-engine fighter designs and to fair the afterbody smoothly from the constant cross section of the centerbody down to the nozzles. In addition, the afterbody was required to house the afterbody balance, model propulsion simulation system, and related instrumentation.

Sketches of the axisymmetric nozzles tested are shown in figures 2(c) and 2(d). The two nozzle configurations represent dry (or cruise) and maximum afterburning power settings of a convergent-divergent nozzle design with fully variable throat-area and expansion-ratio control. The nozzles were sized consistent with advanced mixed-flow turbine-engine cycles (ref. 22). As shown in the sketches, the nozzles consisted of an inner- and an outer-nozzle model part. The inner nozzle attached to the model propulsion system, and the outer nozzle attached directly to the afterbody. The inner and outer nozzles were separated by a nominal 0.19-cm gap to prevent fouling (or grounding) between the metric aft end and the nonmetric internal propulsion system. Figure 2(e) is a sketch of the orientation of the nozzle pressure instrumentation.

As stated previously, the primary objective of this investigation was to determine the effects of empennage surface location on the total aft-end aerodynamic characteristics. The basic afterbody (booms off) had provisions for mounting the twin vertical tails and the horizontal tails in three axial locations. (See fig. 2(f).) Note that the leading edge of the root chords for the horizontal and vertical tails could be located at FS 127.00, FS 136.68, and FS 145.57. Addition of the tail booms

moved the empennage surfaces outboard. (See fig. 2(g).) The booms also had provisions for mounting the twin vertical tails at three axial locations. The forward and mid locations on the booms (FS 136.68 and FS 145.57) were the same as the mid and aft locations on the basic afterbody. Placement of the horizontal tails on the booms was limited to two axial positions (FS 145.57 and FS 155.50). The single vertical tail, which was located on the model centerline, also had the capability of being mounted in two axial locations. (See fig. 2(h).)

Sketches of the vertical and horizontal tail surfaces and tail booms are shown in figures 2(i) to 2(l). These tail surfaces and booms were sized to be representative (as were the afterbody and nozzles) of current twin-engine fighter-aircraft designs. As indicated in each of the tail sketches, individual root fairings (fitters) contoured the tails to the afterbody at each tail location.

Normal cross-sectional area distributions for various configurations are presented in figure 4. The area distributions are provided for the various individual components. For example, the distribution for twin vertical tail location is shown in figure 4(a), and the distribution for horizontal tail location is shown in figure 4(b). To determine the area distribution of a complete configuration (e.g., forward twin vertical tails and aft horizontal tails), area increments at their respective  $x/l$  locations for the individual components must be added to the basic wing-fuselage area distribution.

#### Instrumentation

External aerodynamic forces and moments on the model aft end (including empennage surfaces and outer nozzles) were measured with a six-component strain-gage balance. Forces and moments on the propulsion simulation system were not measured.

Eight external-seal static-pressure orifices  $p_{es}$  were located in the area of the metric-break gap between the centerbody and afterbody. (See fig. 2(b).) Also, two internal-pressure orifices  $p_{in}$  located in the annular gap between the inner and outer nozzles were used to measure internal pressures in the model. These pressures, along with corresponding areas, were used to correct the balance measurements.

Each internal nozzle was instrumented with two total-pressure-probe rakes located  $180^\circ$  apart and staggered to prevent appreciable flow blockage. Each rake contained two total-pressure probes. (See figs. 2(c) and 2(d).) An additional probe was located in each nozzle and contained a thermocouple for the measurement of total temperature.

Each outer nozzle had three rows of external pressure orifices (with five pressure orifices in each row) for the measurement of external pressure distribution on the nozzles. Tables showing the 30 orifice locations on each pair of nozzles are included in figures 2(c) and 2(d). These static-pressure measurements were used in a pressure-area integration over the nozzle surface to obtain nozzle pressure drag.

#### Tests

Data were obtained in the Langley 16-Foot Transonic Tunnel at Mach numbers from 0.6 to 1.2. Angle of attack was varied from  $-2^\circ$  to  $10^\circ$ , and the nozzle pressure ratio (ratio of jet total pressure to free-stream static pressure) ranged from 1.0 (jet off) to approximately 10.0. Typical variations of free-stream tunnel parameters

with Mach number observed during this investigation are shown in figure 5. No testing was conducted between Mach numbers of 0.95 and 1.15 because of potential blockage and shock reflection problems. All configurations were tested with fixed boundary-layer transition strips on the model nose and wings and on the afterbody empennage surfaces. A 0.254-cm-wide strip of No. 120 carborundum grit was located 5.08 cm from the nose of the forebody and along the wing span at 5 percent of the root chord and 10 percent of the tip chord. Transition strips, 0.254 cm wide, of No. 120 silicon carbide grit were located 1.27 cm from the leading edge of the vertical and horizontal tails. The procedure used for selecting grit size and location is described in reference 23.

#### Data Acquisition and Procedure

Data for both model and wind-tunnel test instrumentation were recorded on magnetic tape. At each test point, 50 samples of data were recorded over a 5-second period. The samples were averaged, and the averaged values were used for all computations.

Total aft-end drag was measured directly from the six-component strain-gage balance, but was corrected for various pressure-area terms. Total aft-end drag was computed from the following equation:

$$D = D_{bal} - \sum (p_{es} - p_{\infty})(A_{fus} - A_{seal}) - \sum (p_{in} - p_{\infty})(A_{seal} - A_o) \\ - \sum (p_{an} - p_{\infty})(A_o - A_{an}) \quad (1)$$

The first two pressure-area terms correct for forces felt on the balance term  $D_{bal}$ . The last term in equation (1) is an external-base pressure drag that is not actually felt by the balance but has been changed to aft-end drag throughout this report. This was done to partially account for the additional nozzle boattail drag that would have been measured had no clearance between internal and external nozzle parts been required.

Nozzle drag  $D_n$  was obtained by adding nozzle pressure drag to a computed nozzle skin-friction drag. Nozzle pressure drag was determined by integration of nozzle pressure distributions over the nozzle surface area. Nozzle skin-friction drag was computed using the method of Frankl and Voishel for compressible, turbulent flow on a flat plate. (See ref. 24.)

Vertical and horizontal tail drag was defined as the sum of form drag and skin-friction drag ( $M < 0.9$ ) or wave drag and skin-friction drag ( $M > 1.0$ ). Skin-friction drag and wave drag were computed using the methods of references 24 and 25. The subsonic form factors for the tails were obtained from empirical data correlations of unpublished NASA data and were calculated as follows:

$$\text{Form factor} = 1 + 1.44(t/c) + 2(t/c)^2 \quad (2)$$

The individual root fairings required for each tail location were also included in the skin-friction and wave-drag calculations. Using previously determined drag components, afterbody drag  $D_a$  was obtained from the following equation:

$$D_a = D - D_n - D_{\text{tails}} \quad (3)$$

The tail interference terms used in this report are consistent with those used in reference 15. The total tail interference increment on the aft end was determined as follows:

$$\Delta C_{D,it} = (C_D)_{\text{tails on}} - (C_D)_{\text{tails off}} - C_{D,\text{tails}} \quad (4)$$

where  $(C_D)_{\text{tails on}}$  is the measured total aft-end drag for a given configuration;  $(C_D)_{\text{tails off}}$  is the measured aft-end drag for the same basic configuration with the tails removed; and  $C_{D,\text{tails}}$  is the computed value of tail drag. The empennage interference effects on the nozzles alone were found from the following equation:

$$\Delta C_{D,in} = (C_{D,n})_{\text{tails on}} - (C_{D,n})_{\text{tails off}} \quad (5)$$

where the nozzle drags are integrated pressure distributions over the nozzle surface. This empennage interference increment, then, is the result of changes in nozzle pressure distribution resulting from adding empennage surfaces to an afterbody-nozzle-boom configuration. The empennage interference increment on the afterbody component was then defined in the following equation as the difference between the empennage interference increments on the total aft end and the nozzles:

$$\Delta C_{D,ia} = \Delta C_{D,it} - \Delta C_{D,in} \quad (6)$$

Any interference effects of one tail surface on another or of the afterbody/nozzle on the tails are included in this afterbody interference increment. In an effort to avoid errors associated with computation of lift-induced drag on the horizontal tail surfaces, afterbody, and nozzles, these interference terms were computed only at an angle of attack of  $0^\circ$ .

## RESULTS AND DISCUSSION

### Basic Data

The basic data obtained during this investigation are presented in figures 6 to 27 and are indexed in table I. The two types of data figures, lift coefficient versus angle of attack, drag coefficient, and pitching-moment coefficient (figs. 6 to 16) and drag coefficient versus jet total-pressure ratio (figs. 17 to 27) are presented to provide the complete parametric data base. The total aft-end aerodynamic characteristics in figures 6 to 16 are presented at a jet-off ( $p_{t,j}/p_\infty = 1.0$ ) condition only, because examination of the entire data set showed that only drag coefficient varied significantly with jet total-pressure ratio. The effects of jet total-pressure ratio on lift and pitching-moment characteristics were negligible in most cases. However, the total aft-end lift-coefficient data of figures 6 to 16 indicate nonlinear trends with increasing angle of attack, particularly at  $M = 0.9$ , when compared with lift-coefficient data trends obtained from nonpropulsion, completely metric, aerodynamic models. This result is typical for partially metric,

afterbody propulsion model data (e.g., see ref. 26) and is the result of changing wing downwash characteristics on the afterbody and empennage in the transonic speed range.

The total aft-end drag coefficient as a function of jet total-pressure ratio is presented in figures 17 to 27. Several general statements can be made about these data. Examination of the dry power nozzle data in figures 17 to 22 shows that for  $M < 0.95$ , jet-off total aft-end drag coefficients were higher in all cases than the jet-on data. This was usually the case for the supersonic data as well. The variation of aft-end drag coefficient with jet total-pressure ratio is characterized by a significant reduction in drag as the jet is initially turned on. As jet total-pressure ratio continued increasing to approximately 3.0, total aft-end drag generally increased. Above  $P_{t,j}/P_\infty \approx 3.0$ , the drag generally decreased with increasing jet total-pressure ratio. When the jet is not in operation, a large base region behind the nozzles results. The nozzle boattail is being aspirated as the external flow expands into this base region. This expansion lowers the nozzle boattail pressures and results in a drag force on the nozzle. At the initial operation of the jet, this base region is filled by the jet plume, and the extreme expansion flow field is eliminated. After initial operation of the jet, further increases in jet total-pressure ratio cause the external flow field to become entrained by the jet flow. This entrainment decreases boattail pressures and, in turn, increases drag. Eventually, a point is reached at which the plume begins to enlarge (usually near the design nozzle pressure ratio). This causes the external flow on the nozzles to decelerate (and in turn increase pressures) and results in a drag reduction.

The A/B power nozzle data (figs. 23 to 27) exhibit some of the same trends with increasing nozzle pressure ratio as the dry power nozzle data. For example, initial jet operation was accompanied by a decrease in aft-end drag. However, as jet total pressure was increased, the aft-end drag increased for some configurations to levels higher than the jet-off drag. Aft-end drag values peaked between  $P_{t,j}/P_\infty = 3.0$  and  $P_{t,j}/P_\infty = 4.0$  (because the A/B power nozzle design jet total-pressure ratio was higher than that for the dry power nozzle) and again tended to fall off as jet total-pressure ratio was increased. Overall reductions in drag due to jet operation were considerably less for the afterburning nozzle than for the dry power nozzle cases, probably because of smaller axial projected area on the A/B power nozzles.

#### Nozzle Pressure Distributions

The effects of jet total-pressure ratio on external nozzle pressure distribution at six radial angles and several Mach numbers are shown in figures 28 to 31. The dry power nozzle with tails-off and tails-on pressure distributions are presented in figures 28 and 29, respectively, and the A/B nozzle with tails-off and tails-on pressure distributions are presented in figures 30 and 31, respectively.

#### Dry Power Nozzles

As shown in figures 28 and 29, jet operation increased nozzle boattail pressures both subsonically and supersonically for all dry power nozzle cases. Generally, as jet total-pressure ratio increased, the nozzle boattail pressure also increased, especially for jet total-pressure ratios above design pressure ratio. It can also be seen that the jet interference effects fed forward over the entire nozzle surface at subsonic speeds. However, at supersonic speeds, jet interference effects generally did not spread forward of  $x/l = 0.963$  (see figs. 28(c) and 29(c)). The only

exception was for the  $\phi = 90^\circ$  (see fig. 2(e) for  $\phi$  locations) row, where effects caused by operation of the jet were measured over the entire length of the nozzle boattail. This  $\phi = 90^\circ$  row of pressure orifices lie in an area directly behind the engine interfairing between the nozzles. The data seem to indicate that this region is dominated by subsonic flow (probably the result of flow separation upstream of the nozzles in the interfairing region).

Another characteristic of the dry power nozzle pressure distribution is that the nozzle pressure coefficient generally tends to increase over the entire nozzle boattail region. This increase is the result of recompression of the afterbody external flow field on the nozzles after it has expanded over the model afterbody and nozzle shoulder. For the subsonic cases, pressure recovery is extensive enough to result in positive pressure coefficients (or pressure above ambient) on a large portion of the nozzle surface. Positive pressure coefficients on the aft-facing nozzle boattail result in negative drags (or thrust) on the nozzles, which are of course very favorable. At  $M = 1.2$ , pressure recovery still occurs but is not complete enough to give significant positive pressure coefficients on the nozzle boattail. These characteristics at supersonic speeds are typical of other twin-engine data and show evidence of shock movement with varying jet total-pressure ratio.

Comparisons of the nozzle pressure distributions for the dry power nozzles, tails off versus tails on, can be made by comparing figures 28 and 29. Addition of empennage surfaces tended to reduce pressures on the nozzle boattail, primarily at supersonic speeds. However, some localized effects were found at subsonic speeds in the region directly behind the aft-located horizontal tails ( $\phi = 270^\circ$ ). The data for  $M = 1.2$  show that the addition of tail surfaces produces interference effects on the entire nozzle. The data at  $\phi = 270^\circ$  show that, at subsonic speeds, the largest tail interference effects occur in the nozzle pressure distribution directly behind the aft-located horizontal tail. Pressure distribution data not presented indicate that as the vertical tails are moved aft and in close proximity to the nozzle, the interference effects on the nozzle become more significant.

#### Afterburning Nozzles

The effects of jet total-pressure ratio on nozzle pressure distributions for the A/B nozzles are presented in figures 30 and 31 for tails off and tails on, respectively. In general, the effects of jet total-pressure ratio on nozzle boattail pressures remained consistent with those previously noted for the dry power nozzle cases.

The nozzle boattail pressure coefficients decreased from positive values on the forward portion of the nozzle to negative values near the nozzle exit. It is believed that the high-pressure region on the forward portion of the nozzle was caused by a recompression region located at the juncture between the circular arc and conical sections of the nozzle at  $x/l = 0.94$ . The decreasing pressure coefficients were a result of the expansion of the flow field toward free-stream static pressure down the nozzle boattail. As discussed previously, the flow may in many cases be further accelerated as a result of jet entrainment.

Jet interference effects (variation of local static pressure with varying jet total-pressure ratio) fed forward over the entire A/B nozzle boattail at subsonic speeds. This was similar to the dry power nozzle case. At supersonic speeds, these effects appeared primarily at  $x/l = 0.986$  and occasionally as far forward as  $x/l = 0.974$ .

Addition of empennage surfaces had little or no effect on nozzle pressure distributions at subsonic speeds, with the exception of the region directly behind the aft-located horizontal tails ( $\phi = 270^\circ$ ). In this region, the addition of tails increased nozzle boattail pressures near the nozzle exit plane.

At  $M = 1.2$ , the addition of tails tended to reduce nozzle boattail pressures in nozzle regions which were in line with or in close proximity to the tail surfaces ( $\phi = 270^\circ$  and  $\phi = 315^\circ$ ). This reduction in boattail pressures due to tail surfaces occurred for other tail locations as well. Tail surfaces tended to increase nozzle boattail pressures on the forward portion of the nozzle for  $\phi = 90^\circ$  (engine inter-fairing region) at  $M = 1.2$ .

#### Angle of Attack

The effects of angle of attack on dry power nozzle pressure distributions are presented in figures 32 and 33 for tails-off and tails-on conditions, respectively. As shown in both figures at Mach numbers of 0.6 and 0.9, there was very little effect of angle of attack on nozzle boattail pressures except at the most forward pressure orifice location. In a similar study for which pressures were measured (ref. 18), the primary effects of angle of attack were found on the forebody and afterbody forward of the nozzles. The exception again occurred at supersonic speeds, at which nozzle boattail pressures became a strong function of model angle of attack for  $\alpha > 4^\circ$ . The pressure coefficient data for the tails-off case shown in figure 32(c) show that nozzle boattail pressure coefficient generally decreased as angle of attack increased. The addition of tail surfaces further complicates the afterbody flow field, as illustrated by nozzle pressure coefficients in figures 33(e) and 33(f). These figures show that nozzle pressure coefficients were highly dependent on angle of attack.

#### DATA COMPARISONS

In an effort to simplify the data analysis, data have been cross-plotted at selected jet total-pressure ratios. Figure 34 presents the typical turbofan-engine pressure-ratio schedule with Mach number used for this analysis. Although the figure comparisons are based on this particular schedule of  $p_{t,j}/p_\infty$  as a function of Mach number, the results would also be generally valid for other schedules. However, the relative differences between comparisons may vary.

Data comparisons are presented in figures 35 to 73. Table II is an index to these comparison figures. Three types of figures were used for these comparisons. In the first type, total aft-end drag and lift are plotted as functions of Mach number for two values of afterbody angle of attack,  $0.1^\circ$  and  $8.1^\circ$ , and are presented for all configuration comparisons. In the second type, plots of individual aft-end drag-coefficient components ( $C_{D,n}$ ,  $C_{D,tails}$ , and  $C_{D,a}$ ) and tail interference drag-coefficient increments ( $\Delta C_{D,it}$ ,  $\Delta C_{D,in}$ , and  $\Delta C_{D,ia}$ ) versus Mach number are provided for many of the comparisons. These component drags and interference increments are presented only at an afterbody angle of attack of  $0.1^\circ$ . Figures of the third type are drag summary plots, in which drag values for a given general afterbody configuration (such as dry power nozzles with tail booms off) are summarized.

## Vertical Tail Location

### Twin Vertical Tail Axial Location

The effects of twin vertical tail axial location on total aft-end lift and drag coefficients, individual component drag coefficients, and tail interference drag coefficients are presented in figures 35 to 47. Discussion of the data is broken down into four general afterbody configurations: dry power nozzles with tail booms off (figs. 35 to 38); dry power nozzles with tail booms on (figs. 39 to 41); A/B nozzles with tail booms off (figs. 42 to 44); and A/B nozzles with tail booms on (figs. 45 to 47).

Dry power nozzles with tail booms off.- The effects of vertical tail location on aft-end lift and drag at various horizontal tail locations for the dry power nozzle, booms-off configuration are shown in figures 35 to 37, and data summarizing the total aft-end drag characteristics are presented in figure 38. Examination of figures 35(a), 36(a), 37(a), and 38 indicates that both lift and drag characteristics were a function of Mach number, angle of attack, and horizontal tail location; however, some trends can be noted. At  $\alpha = 0.1^\circ$ , the aft location of the vertical tails generally resulted in higher drag and lower lift throughout the Mach number range tested. Closer examination of the supersonic data ( $M > 1.15$ ) indicates that the empennage arrangements with the lowest drag were all staggered-tail (horizontal and vertical tails at different axial locations) configurations.

Total aft-end drag data at  $\alpha = 8.1^\circ$  were obtained only at  $M = 0.6$  and  $0.9$ . The only general trend was for the  $M = 0.9$  data. At this Mach number, the aft vertical tail location provides significant reductions in drag over the forward and mid locations. This is a reversal of the trends found at  $\alpha = 0.1^\circ$ , and it illustrates the complexity of the Mach number and angle-of-attack relationship on total aft-end drag.

Examination of the individual aft-end component drag values and tail interference drag increments provides insight into the actual mechanisms involved with various empennage arrangements. (See figs. 35(b), 36(b), and 37(b).) Variation in computed tail drag  $C_{D,tails}$  with changes in vertical tail location is almost insignificant. Tail-drag variations would result only from the small differences in the tail root fairings as discussed in the section "Data Acquisition and Procedure." Values of nozzle drag  $C_{D,n}$  for the three vertical tail locations vary significantly. In general, moving the vertical tails closer to the nozzles increased nozzle drag over the entire Mach number range tested. The afterbody drag  $C_{D,a}$  (obtained by removing nozzle drag and tail drag from the total aft-end drag  $C_D$ ) is seen to be relatively unaffected by vertical tail locations for  $M < 0.8$ , but becomes increasingly more sensitive to tail location as Mach number is increased. In most cases the afterbody drag-coefficient component actually decreased (and in some cases remained unchanged) as vertical tails were moved aft.

The tail interference drag-coefficient increments on the total aft end  $\Delta C_{D,it}$ , the nozzles  $\Delta C_{D,in}$ , and the afterbody  $\Delta C_{D,ia}$  are on the right-hand side of figures 35(b), 36(b), and 37(b). Values less than zero represent favorable interference and values greater than zero represent unfavorable interference. Examination of the tail interference drag increment on the total aft end shows that, in almost all cases, the tail interference was unfavorable. These unfavorable effects increased with increasing subsonic Mach number and decreased with increasing supersonic Mach number. For  $M < 0.95$ , tail interference on the total aft end increased as the twin vertical tails were moved aft. The tail interference increment at supersonic speeds

was lowest for the mid vertical tail location and generally highest for the aft vertical tail location. Examination of these interference data again indicate lower interference effects for the staggered-tail configurations at the supersonic Mach numbers except for the mid horizontal tail, mid vertical tail configuration. It is important to compare the aft-end interference increment with the total aft-end drag. For example, compare the total aft-end interference increment  $\Delta C_{D,it}$  with the total aft-end drag coefficient  $C_D$  for the aft horizontal tail, aft vertical tail arrangement of figure 37. First, consider  $M = 0.6$ . The tail interference drag-coefficient increment on the total aft end is 0.0008 (fig. 37(b)), and the total aft-end drag coefficient is 0.0081 (fig. 37(a)). Nearly 10 percent of the total aft-end drag is the result of tail interference effects. At  $M = 0.9$  and  $M = 1.2$ , tail interference accounts for approximately 38 percent and 5 percent, respectively, of the total aft-end drag. Tail interference effects are significant throughout the Mach number range, but they are extremely large in the high subsonic-transonic speed range.

The tail interference drag increments on the nozzles  $\Delta C_{D,in}$  indicate similar trends as discussed for nozzle drag coefficient. For all Mach numbers tested, the unfavorable interference effects originating from the vertical tails increased as the vertical tails were moved aft. This is probably the result of local flow separation directly behind the tail surfaces and increased local velocities elsewhere on the nozzles.

The tail interference drag-coefficient increment on the afterbody  $\Delta C_{D,ia}$  was highly dependent on configuration and Mach number. However, tail interference increments on the afterbody were generally unfavorable (and increasingly more unfavorable with increasing Mach number) in the subsonic-transonic Mach number range. At supersonic speeds, the interference effects on the afterbody were generally favorable.

Dry power nozzles with tail booms on.- The effects of twin vertical tail axial location on aft-end drag and lift characteristics for the dry power nozzle, booms-on configurations are shown in figures 39 and 40, and data summarizing the total aft-end drag characteristics are presented in figure 41. As previously shown for the booms-off configurations, the total aft-end lift decreased as vertical tails were moved from the forward location to the mid or aft location. However, the drag data presented in figure 41 varied somewhat from the booms-off characteristics shown in figure 38. For  $\alpha = 0.1^\circ$ , the  $M = 0.6$  data indicate no effect on drag due to vertical tail location. This was not the case, however, at  $M = 0.9$ , where aft-end drag trends resulting from vertical tail placement varied with horizontal tail location. The drag-coefficient data at  $M = 1.2$  clearly indicate that aft movement of the vertical tails resulted in significant increases in drag. At  $\alpha = 8.1^\circ$  and  $M < 0.9$ , relocation of the vertical tails from forward to mid or aft locations resulted in substantial drag reductions.

Examination of the aft-end component drag coefficients and tail interference drag-coefficient increments (figs. 39(b) and 40(b)) at  $\alpha = 0.1^\circ$  shows that the nozzle drag coefficients increased throughout the Mach number range by aft movement of the twin vertical tails, as was the case with the booms-off data of figures 35 to 38. For  $M < 0.9$ , the variations in tail interference increment on the total aft end were small for the different vertical tail locations tested. The tail interference increment was substantially lower for the forward-located position at  $M > 1.15$ . The tail interference drag increment on the nozzles  $\Delta C_{D,in}$  was increased by aft movement of the vertical tails for all Mach numbers tested.

A/B nozzles, tail booms off.- The effects of twin vertical tail axial location on aft-end characteristics for the A/B nozzle, booms-off configurations are shown in figures 42 and 43, and data summarizing the total aft-end drag characteristics are presented in figure 44. The data shown in figures 42(a) and 43(a) indicate that lift-coefficient trends were a function of horizontal tail location and vertical tail location. The summary of the drag data presented in figure 44 indicates that for subsonic Mach numbers the aft vertical tail location provided the lowest total aft-end drag. At supersonic speeds, the opposite was true. Forward vertical tail location resulted in the lowest total aft-end drag.

The effects of vertical tail location on the individual aft-end drag-coefficient components were generally very small for A/B nozzle configurations at subsonic-transonic Mach numbers. At  $M < 0.9$ , tail interference increments on the total aft end  $\Delta C_{D,it}$  were usually the same or more favorable for the aft vertical tail placement when compared with the forward vertical tail placement. Since the interference effects on the nozzle were almost nonexistent (as a result of the reduced boattailing associated with the A/B nozzles), the interference increments on the afterbody  $\Delta C_{D,ia}$  were almost identical to those for the total aft-end  $\Delta C_{D,it}$ . The tail interference drag increment on the total aft end  $\Delta C_{D,it}$  is generally larger for the dry power nozzles than for the A/B nozzles.

A/B nozzles with tail booms on.- The effects of twin vertical tail axial location on aft-end characteristics for the A/B nozzle, booms-on configurations are shown in figures 45 and 46, and data summarizing the total aft-end drag characteristics are presented in figure 47. The lift-coefficient data in figures 45(a) and 46(c) indicate decreased values of  $C_L$  as the vertical tails are moved from forward to mid or aft locations. The total aft-end drag data presented in figure 47 show that the drag trends are dependent upon Mach number, angle of attack, and horizontal tail location. At  $\alpha = 8.1^\circ$  drag trends did indicate that relocation of the vertical tails from forward to mid or aft locations was beneficial.

The effects of twin vertical tail location on the aft-end drag-coefficient components and tail interference drag increments (figs. 45(b) and 46(b)) were similar to the A/B nozzle, booms-off data of figures 42(b) and 43(b). The only exceptions were at supersonic Mach numbers on the total aft-end tail interference increment  $\Delta C_{D,it}$  and on the afterbody tail interference increment  $\Delta C_{D,ia}$ , where trends were reversed.

The effects of various axial locations of the vertical tail on total aft-end drag were considered in this investigation; however, vertical tail alignment could also have a significant effect on the results.

#### Twin Vertical Tail Lateral Location

The effects of twin vertical tail lateral location on the aft-end aerodynamic characteristics are presented in figure 48. Only one comparison was made, and limited data were obtained. The horizontal tails were mounted on the tail booms in the aft location (see fig. 2(g)). The lateral tail location comparison was made by mounting the twin vertical tails on the fuselage (body) at BL -10.16 (see fig. 2(f)) and then moving the twin vertical tails outboard onto the tail booms. Vertical tail axial location was fixed at FS 136.68. Only limited data were obtained at  $M = 0.6$  and  $M = 0.9$  with the vertical tail mounted on the body. As with the total aft-end lift and drag, individual aft-end component drag coefficients and tail interference

drag-coefficient increments, there was little or no effect resulting from twin vertical tail lateral location.

#### Single Vertical Tail Axial Location

The effects of single vertical tail axial location on total aft-end lift and drag, individual aft-end component drag coefficients, and tail interference drag-coefficient increments are shown in figures 49 to 52. Data are presented for two dry power nozzle, booms-off configurations (figs. 49 to 51) and for one A/B nozzle, booms-off configuration (fig. 52). These were the only configurations tested with the single vertical tail with which comparisons could be made.

Dry power nozzles with tail booms off.- The effects of single vertical tail location on aft-end characteristics in the presence of dry power nozzles (figs. 49 to 51) were generally similar to the results obtained with the twin vertical tail arrangement. Total aft-end lift (figs. 49(a) and 50(a)) was reduced when the single vertical tail was moved from the forward location to the aft location. The summary of drag results shown in figure 51 indicates that the effect of vertical tail axial location is a function of Mach number and angle of attack.

Examination of the individual aft-end component drag coefficients (figs. 49(b) and 50(b)) indicates that nozzle drag  $C_{D,n}$  significantly increased at all Mach numbers with aft placement of the single vertical tail. The contribution of the afterbody alone to total drag was in turn somewhat larger for the single vertical forward placement.

The tail interference increments on the total aft-end drag trends were also dependent upon Mach number. Aft location of the single vertical tail is unfavorable for  $M < 0.9$  and favorable for  $M > 1.15$ , when compared with the forward tail location.

A/B nozzles with tail booms off.- Single vertical tail location in the presence of the A/B nozzles is shown in figure 52 to have very little effect on the afterbody aerodynamic characteristics, except at supersonic speeds. For  $M > 1.15$ , the aft-end total lift and drag coefficients increased as the single vertical tail was moved aft. These trends are opposite of those observed on the dry power nozzle configurations. The tail interference drag-coefficient increments on the total aft-end  $\Delta C_{D,it}$  showed definite adverse interference effects as the single vertical tail was moved aft. Except at  $M = 1.2$ , both vertical tail locations provided favorable interference effects on the total aft end.

#### Horizontal Tail Location

The effects of horizontal tail location on total aft-end lift and drag coefficients are presented in figures 53 to 63. Individual aft-end component drag coefficients and tail interference drag-coefficient increments are provided only for the dry power nozzle cases (figs. 53 to 55 and 57), because the effects of horizontal tail location in the presence of the A/B nozzle were relatively small.

Horizontal tail location generally had only small effects on lift or drag coefficients at  $M < 0.9$ , especially for  $\alpha = 0.1^\circ$ . Trends were more configuration-dependent at  $M > 1.15$ . Summary figures of the effects of horizontal tail location on aft-end drag in the presence of dry power nozzles (figs. 56 and 63) indicate that

the aft horizontal tail location produced the largest aft-end drag. The exception to this was for the tail-booms-on case (fig. 57), for which forward horizontal tail placement increased drag. For configurations with A/B nozzles (figs. 58 to 60), drag coefficients at supersonic speeds indicate that staggering the empennage surfaces is best for low drag.

The only general statements that can be made about the individual aft-end drag-coefficient components and tail interference drag-coefficient increments (figs. 53(b), 54(b), and 55(b)) are that aft location of the horizontal tails provided higher levels of nozzle drag and that the tail interference drag-coefficient increment on the total aft end was almost always unfavorable.

#### Effects of Horizontal Tail Incidence

The effects of horizontal tail incidence on total aft-end drag and lift are presented in figure 64 for the tail-booms-off, dry power nozzle configuration with empennage surfaces located forward and aft. As expected, lift is decreased and drag is increased by negative (leading edge down) horizontal tail deflections at  $\alpha = 0.1^\circ$ . At  $\alpha = 8.1^\circ$ , although lift is still decreased, negative horizontal tail deflections (up to  $-10^\circ$ ) reduce drag.

Some interesting lift-drag relationships can be seen in figure 64(b). As expected, at  $\alpha = 0.1^\circ$  and  $M = 0.6$  it is apparent that the lift increment due to horizontal tail deflection from  $0^\circ$  to  $-5^\circ$  is approximately equal to the lift increment resulting from  $-5^\circ$  to  $-10^\circ$  deflection. The drag coefficients corresponding to these deflections (top left-hand part of fig. 64(b)) exhibit the trends expected of lift-induced drag, in that they vary in proportion to the square of the lift coefficient. The drag-coefficient penalty at  $M = 0.6$  for  $\delta_h = 5^\circ$  is approximately 0.0025. For  $\delta_h = 10^\circ$ , the lift is doubled and the drag-coefficient increment is approximately 0.0100, or four times the drag increment associated with the first  $5^\circ$  of deflection. At  $M = 0.9$ , a tail incidence of  $-10^\circ$  is not as effective in producing lift as a  $-5^\circ$  deflection. This is shown by a reduction in the lift increment produced. Local separation on the horizontal tails may be the explanation for this. The drag data may also give some credibility to this explanation, in that the drag increment between tail settings with  $\delta_h = 5^\circ$  and  $\delta_h = -10^\circ$  is well over the lift-induced drag increment. This excess indicates a problem, such as local flow separation, on the tail surface.

Examination of the  $\alpha = 8.1^\circ$  data in figure 64(b) offers further insight into the flow properties around the model aft end. As seen from the lift data, the lift-coefficient values decrease with increasing Mach number. The magnitude of these decreases is much larger than at the  $\alpha = 0.1^\circ$  condition. The severity of the decrease in lift coefficient with increasing Mach number may be the result of a downwash field created by the support-system wings when at lifting conditions. As Mach number increases, the strength of this downwash field is increased and results in higher negative local angles of attack at the horizontal tail. This might also explain the larger tail-deflection lift increments associated with the forward horizontal tail configuration shown in figure 64(a). The assumption is that the downwash field is stronger (higher negative local angle of attack) as you move closer to the wing trailing edge.

### Effects of Vertical Tail Configuration

The effects of vertical tail configuration (single versus twin) on total aft-end drag and lift coefficients, aft-end drag-coefficient components, and tail interference drag-coefficient increments for various Mach numbers and model angles of attack are presented in figures 65 to 71. Data are provided for several empennage location arrangements, for tail booms off and on, and for dry power and A/B nozzle power settings. The data for aft-end component drag coefficients and tail interference drag-coefficient increments are shown only for the booms-off, dry power nozzle cases at two empennage location arrangements: both horizontal and vertical tails forward (fig. 65(b)) and both horizontal and vertical tails aft (fig. 68(b)). These two cases provided sufficient insight into the mechanisms involved in the planform comparisons.

In all cases at  $M < 0.95$ , the total aft-end lift and drag were lower for the single vertical tail configuration. At  $M > 1.15$  for  $\alpha = 0.1^\circ$ , the total aft-end lift and drag increments resulting from vertical tail configuration differences are directly related to vertical tail location. (See figs. 65 to 71.) With the vertical tails in the forward location on the afterbody, the total aft-end drag (and generally aft-end lift also) was lower for the twin-tail arrangement. The exact opposite was true when the vertical tails were located in the aft position. The twin vertical tails in the aft position apparently increase the acceleration of flow over the afterbody and nozzles in the region between the tails. As a result, the pressures on the top of the afterbody are reduced, which results in increased drag and lift compared with the single vertical tail.

As stated previously, the effects of vertical tail configuration on aft-end component drag coefficients and tail interference drag-coefficient increments are presented for only two empennage arrangements: both horizontal and vertical tails forward (fig. 65(b)) and both horizontal and vertical tails aft (fig. 68(b)). As expected, the tail interference drag increment on the total aft-end  $\Delta C_{D,it}$  indicates that at  $M < 0.9$  the twin vertical tail configurations produced a larger unfavorable effect than did the single vertical tail arrangement. These adverse interferences became more significant as the vertical tail or tails were moved aft.

### Effects of Nozzle Power Setting

The effects of nozzle power setting on aft-end lift and drag coefficients are presented in figure 72. Data are presented for tails-off cases and a variety of empennage and empennage-boom arrangements. Probably the only general comment concerning nozzle power setting that can be made is that, in all cases tested at  $M > 1.0$ , the aft-end drag of A/B nozzle configurations was significantly lower than for the dry power nozzle configurations. This result was expected and is a direct result of reduced closure (aft projected area) with the A/B nozzles. Most other effects of nozzle power setting on aft-end lift and drag are configuration-dependent.

The effects of nozzle power setting on aft-end characteristics with tails off are presented in figures 72(a) and 72(b). The lift characteristics remain essentially unaffected by nozzle power setting at both angles of attack presented. Afterbody drag at supersonic speeds was significantly less for A/B nozzle configurations; however, at subsonic-transonic speeds dry power nozzles resulted in the lowest drag levels. As discussed in the section "Nozzle Pressure Distributions," at subsonic-transonic speeds the dry power nozzles have a favorable pressure (higher than free stream) over a large portion of the aft-facing nozzle area. This favorable

pressure results in a thrust force on the nozzle boattail. Although the A/B nozzle may also have favorable pressure distributions, the aft-facing area of the A/B nozzles is too small to provide a significant boattail thrust force.

With the addition of empennage surfaces, it can be seen in figures 72(c) to 72(k) that nozzle power setting effects on aft-end lift and drag characteristics became configuration-dependent. For all empennage arrangements tested, subsonic drag coefficients were lower for the dry power nozzles than for the A/B nozzle configurations, except for those configurations (with tail booms off) in which the vertical tail or tails were placed aft (figs. 72(d), 72(f), and 72(h)). This result was expected, since adverse tail interference effects from vertical tail surfaces in near proximity to the nozzles have a larger adverse impact on dry power nozzles (with larger aft-facing areas) than on the A/B nozzles.

#### Effects of Tail Booms

The effects of tail booms (and mounting tails on these booms) on aft-end lift and drag characteristics are shown in figure 73. Data are presented for both dry power and A/B nozzle power settings with tails off (figs. 73(a) and 73(c)) and with empennage surfaces (figs. 73(b) and 73(d)). For the tails-on configurations, the axial location of the vertical and horizontal tails (booms off and booms on) is held constant.

Examination of the aft-end drag data shows that in all cases, over the entire Mach number and angle-of-attack range shown, addition of tail booms increased aft-end drag. The increases in drag were more pronounced at supersonic speeds and at the higher angles of attack. Drag increases resulting from tail booms were generally larger for the dry power nozzle configurations than for the A/B nozzle configurations, probably because of increased nozzle boattail area and tail-boom interference effects on the nozzle.

The aft-end lift data show that the addition of tail booms generally has little or no effect on lift at  $\alpha = 0.1^\circ$ . However, lift was increased at  $\alpha = 8.1^\circ$  with the addition of tail booms. The tail booms increase the aft-end lifting surface area.

#### CONCLUSIONS

An investigation has been conducted in the Langley 16-Foot Transonic Tunnel to determine the effects of several empennage and afterbody parameters on the aft-end aerodynamic characteristics of a twin-engine fighter-type configuration. Model variables were as follows: horizontal tail axial location and incidence, vertical tail axial location and configuration (twin- versus single-tail arrangements), tail booms, and nozzle power setting. Tests were conducted over a Mach number range from 0.6 to 1.2 and over an angle-of-attack range from  $-2^\circ$  to  $10^\circ$ . Jet total-pressure ratio was varied from jet off to approximately 10.0. The results of this investigation indicate the following:

1. Tail interference effects were present throughout the range of Mach numbers tested and provided a significant percentage of total aft-end drag in the transonic speed range.

2. Adverse tail interference effects on the complete aft end were larger on dry power configurations than on afterburning nozzle configurations.

3. Tail interference effects on the nozzles alone were generally adverse, and the magnitude of these effects usually increased as empennage surfaces were moved closer to the nozzles.

4. The effects of vertical tail location on aft-end lift and drag characteristics were generally more pronounced than the effects of horizontal tail location, but were usually dependent on Mach number, angle of attack, and configuration. For example, at low angle of attack, aft location of the twin vertical tails generally resulted in the highest aft-end drag for the afterbody configurations with dry power nozzles and tail booms off. However, at high angles of attack (approximately 8°), aft placement of the vertical tail or tails generally provided the lowest aft-end drag for all configurations tested.

5. Addition of tail booms increased total aft-end drag. Aft-end lift was also increased by addition of tail booms at angles of attack greater than zero.

Langley Research Center  
National Aeronautics and Space Administration  
Hampton, VA 23665  
December 28, 1982

## REFERENCES

1. Berrier, Bobby L.: Effect of Nozzle Lateral Spacing on Afterbody Drag and Performance of Twin-Jet Afterbody Models With Cone Plug Nozzles at Mach Numbers up to 2.20. NASA TM X-2632, 1972.
2. Sams, H.: F-15 Propulsion System Design and Development. AIAA Paper No. 75-1042, Aug. 1975.
3. Martens, Richard E.: F-15 Nozzle/Afterbody Integration. AIAA Paper No. 74-1100, Oct. 1974.
4. Brazier, Michael E.; and Ball, William H.: Accounting of Aerodynamic Forces on Airframe/Propulsion Systems. Airframe/Propulsion Interference, AGARD-CP-150, Mar. 1975, pp. 22-1 - 22-15.
5. Bergman, Dave: Unique Characteristics of Exhaust-Plume Interference. J. Aircr., vol. 10, no. 8, Aug. 1973, pp. 508-511.
6. Reubush, David E.; and Mercer, Charles E.: Effects of Nozzle Interfairing Modifications on Longitudinal Aerodynamic Characteristics of a Twin-Jet, Variable-Wing-Sweep Fighter Model. NASA TN D-7817, 1975.
7. Richey, G. K.; Surber, L. E.; and Laughrey, J. A.: Airframe/Propulsion System Flow Field Interference and the Effect on Air Intake and Exhaust Nozzle Performance. Airframe/Propulsion Interference, AGARD-CP-150, Mar. 1975, pp. 23-1 - 23-31.
8. Glasgow, E. R.; and Santman, D. M.: Aft-End Design Criteria and Performance Prediction Methods Applicable to Air Superiority Fighters Having Twin Buried Engines and Dual Nozzles. AIAA Paper No. 72-1111, Nov.-Dec. 1972.
9. Bergman, Dave: Implementing the Design of Airplane Engine Exhaust Systems. AIAA Paper No. 72-1112, Nov.-Dec. 1972.
10. Glasgow, E. R.: Integrated Airframe-Nozzle Performance for Designing Twin-Engine Fighters. AIAA Paper No. 73-1303, Nov. 1973.
11. Herrick, Paul W.: Predicting Propulsion Related Drag of Jet Aftbodies. [Preprint] 751088, Soc. Automot. Eng., Nov. 1975.
12. Pendergraft, Odis C., Jr.: Fuselage and Nozzle Pressure Distributions on a 1/12-Scale F-15 Propulsion Model at Transonic Speeds. NASA TP-1521, 1979.
13. Lee, Edwin E., Jr.; and Runckel, Jack F.: Performance of Closely Spaced Twin-Jet Afterbodies With Different Inboard-Outboard Fairing and Nozzle Shapes. NASA TM X-2329, 1971.
14. Pendergraft, Odis C., Jr.; and Schmeer, James W.: Effect of Nozzle Lateral Spacing on Afterbody Drag and Performance of Twin-Jet Afterbody Models With Convergent-Divergent Nozzles at Mach Numbers up to 2.2. NASA TM X-2601, 1972.
15. Berrier, Bobby L.: Effect of Nonlifting Empennage Surfaces on Single-Engine Afterbody/Nozzle Drag at Mach Numbers From 0.5 to 2.2. NASA TN D-8326, 1977.

16. Maiden, Donald L.; and Berrier, Bobby L.: Effect of Airframe Modifications on Longitudinal Aerodynamic Characteristics of a Fixed-Wing, Twin-Jet Fighter Airplane Model. NASA TM X-2523, 1972.
17. Castells, O. T.; et al.: Twin Jet Exhaust System Interaction Test - Volumes I and II. R72AEG235, General Electric Co., 1972.
18. Exhaust System Interaction Program. Volumes I-XVII. D162-10467-11 (Contract no. F33615-70-C-1450), Boeing Co., Apr. 1973.
19. Swavely, C. E.; and Soileau, J. F.: Aircraft Aftbody/Propulsion System Integration for Low Drag. AIAA Paper No. 72-1101, Nov.-Dec. 1972.
20. Corson, Blake W., Jr.; Runckel, Jack F.; and Igoe, William B.: Calibration of the Langley 16-Foot Transonic Tunnel With Test Section Air Removal. NASA TR R-423, 1974.
21. Price, Earl A., Jr.: An Investigation of F-16 Nozzle-Afterbody Forces at Transonic Mach Numbers With Emphasis on Support System Interference. AEDC-TR-79-56, AFAPL-TR-79-2099, U.S. Air Force, Dec. 1979. (Available from DTIC as AD A078 693.)
22. Stevens, H. L.: F-15/Nonaxisymmetric Nozzle System Integration Study Support Program. NASA CR-135252, 1978.
23. Braslow, Albert L.; Hicks, Raymond M.; and Harris, Roy V., Jr.: Use of Grit-Type Boundary-Layer-Transition Trips on Wind-Tunnel Models. NASA TN D-3579, 1966.
24. Shapiro, Ascher H.: The Dynamics and Thermodynamics of Compressible Fluid Flow. Vol. II. Ronald Press Co., c.1954.
25. Harris, Roy V., Jr.: An Analysis and Correlation of Aircraft Wave Drag. NASA TM X-947, 1964.
26. Capone, Francis J.; and Berrier, Bobby L.: Investigation of Axisymmetric and Nonaxisymmetric Nozzles Installed on a 0.10-Scale F-18 Prototype Airplane Model. NASA TP-1638, 1980.

TABLE I.- INDEX TO BASIC DATA

Horizontal tail location	Vertical tail location	Vertical tail planform	Booms	Nozzle type	$\delta_h$ , deg	Figure	Jet-off aerodynamic characteristics	Jet effects on drag
Off Fwd	Off Fwd	Off	Off	Dry	Off	6		17
	Fwd	Twin			0	7(a)		18(a)
	Fwd				-10	7(b)		18(b)
	Mid				0	7(c)		18(c)
	Aft				0	7(d)		18(d)
	Aft				-10	7(e)		18(e)
	Fwd				0	7(f)		18(f)
	Mid					7(g)		18(g)
	Mid					7(h)		18(h)
	Aft					7(i)		18(i)
	Fwd				-10	7(j)		18(j)
	Mid				0	7(k)		18(k)
	Aft				0	7(l)		18(l)
	Aft				-5	7(m)		18(m)
	Aft				-10	7(n)		18(n)
Fwd	Fwd	Single			0	8(a)		19(a)
Fwd	Aft					8(b)		19(b)
Aft	Fwd					8(c)		19(c)
Aft	Aft					8(d)		19(d)
Off	Off	Off	On	Off		9		20
Fwd	Fwd	Twin				10(a)		21(a)
Fwd	Mid					10(b)		21(b)
Aft	Fwd					10(c)		21(c)
Aft	Aft					10(d)		21(d)
Aft	Mid on body					10(e)		21(e)
Fwd	Aft	Single				11		22
Off	Off	Off	Off	A/B	Off	12		23
Fwd	Fwd	Twin				13(a)		24(a)
Fwd	Aft					13(b)		24(b)
Aft	Fwd					13(c)		24(c)
	Aft					13(d)		24(d)
	Fwd					14(a)		25(a)
	Aft					14(b)		25(b)
Off	Off	Single	On	Off		15		26
Fwd	Fwd	Off				16(a)		27(a)
Fwd	Mid					16(b)		27(b)
Aft	Fwd					16(c)		27(c)
Aft	Aft					16(d)		27(d)

TABLE II.- INDEX TO CONFIGURATION COMPARISONS

Comparison	Horizontal tail location	Vertical tail and location	Tail booms	Nozzle type	Figure	
					Comparison	Drag summary
Twin vertical tail location	Fwd		Off	Dry	35	38
	Mid		Off	Dry	36	
	Aft		Off	Dry	37	
	Fwd		On	Dry	39	41
	Aft		On	Dry	40	
	Fwd		Off	A/B	42	44
	Aft		Off	A/B	43	
	Fwd		On	A/B	45	47
	Aft		On	A/B	46	
	Aft		On	Dry	48	
Single vertical tail location	Fwd		Off	Dry	49	51
	Aft		Off	Dry	50	
	Aft		Off	A/B	52	
		Twin/fwd Twin/mid Twin/aft	Off	Dry	53	56
			Off	Dry	54	
			Off	Dry	55	
		Twin/fwd Twin/fwd Twin/aft	On	Dry	57	
			Off	A/B	58	
			Off	A/B	59	
		Twin/fwd Single/fwd Single/aft	On	A/B	60	
			Off	Dry	61	63
			Off	Dry	62	
Horizontal tail incidence	Fwd	Twin/fwd Twin/aft	Off	Dry	64(a)	
	Aft		Off	Dry	64(b)	
	Fwd	Fwd Aft Fwd Aft	Off	Dry	65	
	Fwd		Off	Dry	66	
	Aft		Off	Dry	67	
	Aft		Off	Dry	68	
	Aft	Aft	On	Dry	69	
	Aft		Off	A/B	70	
	Aft	Aft	Off	A/B	71	
Nozzle power setting	Off	Off	Off		72(a)	
	Off		Off		72(b)	
	Fwd	Twin/fwd Twin/aft Twin/fwd Twin/aft Single/fwd Single/aft	Off		72(c)	
	Fwd		Off		72(d)	
	Aft		Off		72(e)	
	Aft		Off		72(f)	
	Aft		Off		72(g)	
	Aft		Off		72(h)	
	Fwd	Twin/fwd Twin/fwd Twin/aft	On		72(i)	
	Fwd		On		72(j)	
	Aft		On		72(k)	
Tail boom presence	Off	Off Twin/FS 136.68		Dry	73(a)	
	FS 145.57			Dry	73(b)	
	Off	Off Twin/FS 145.57		A/B	73(c)	
	FS 145.57			A/B	73(d)	

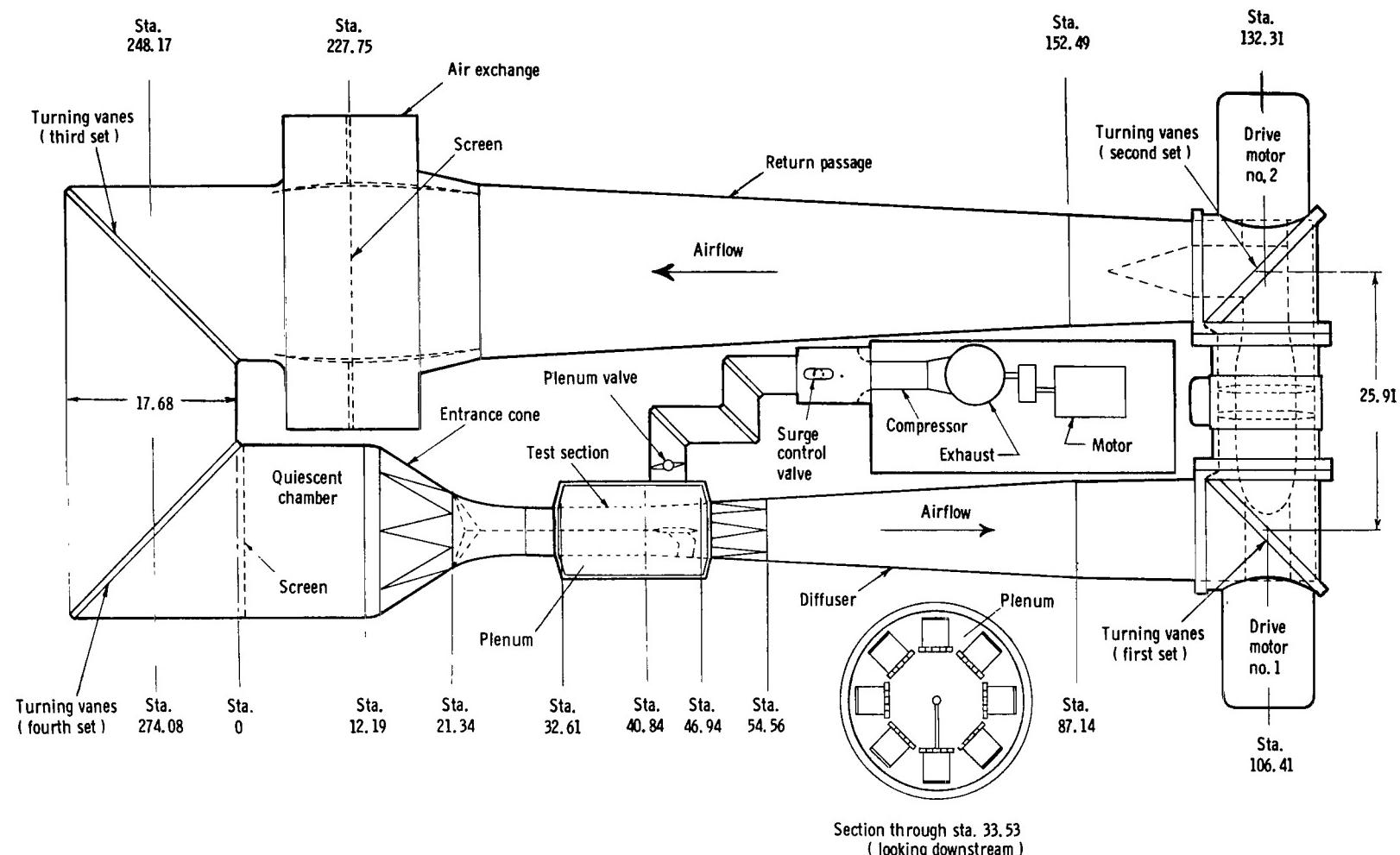
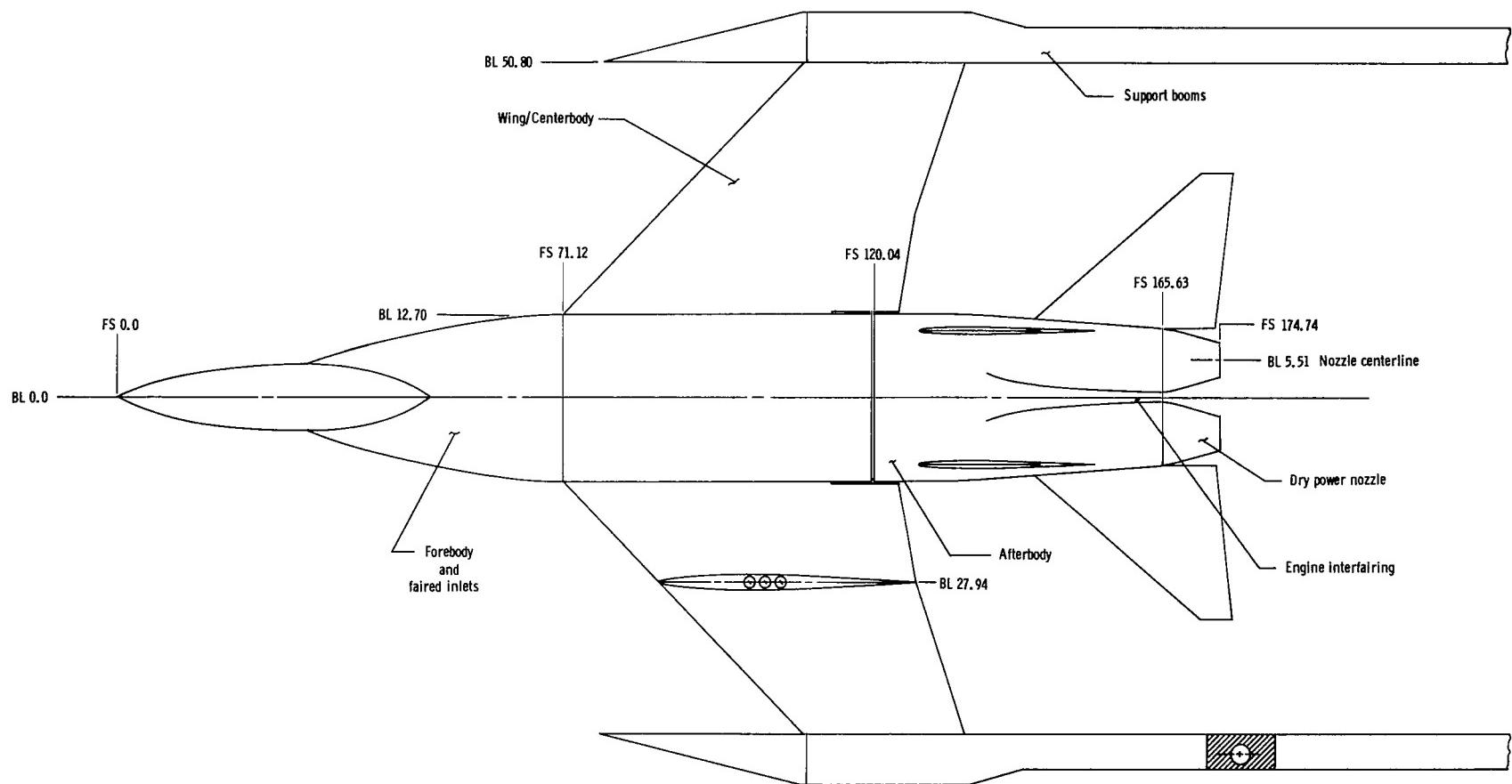
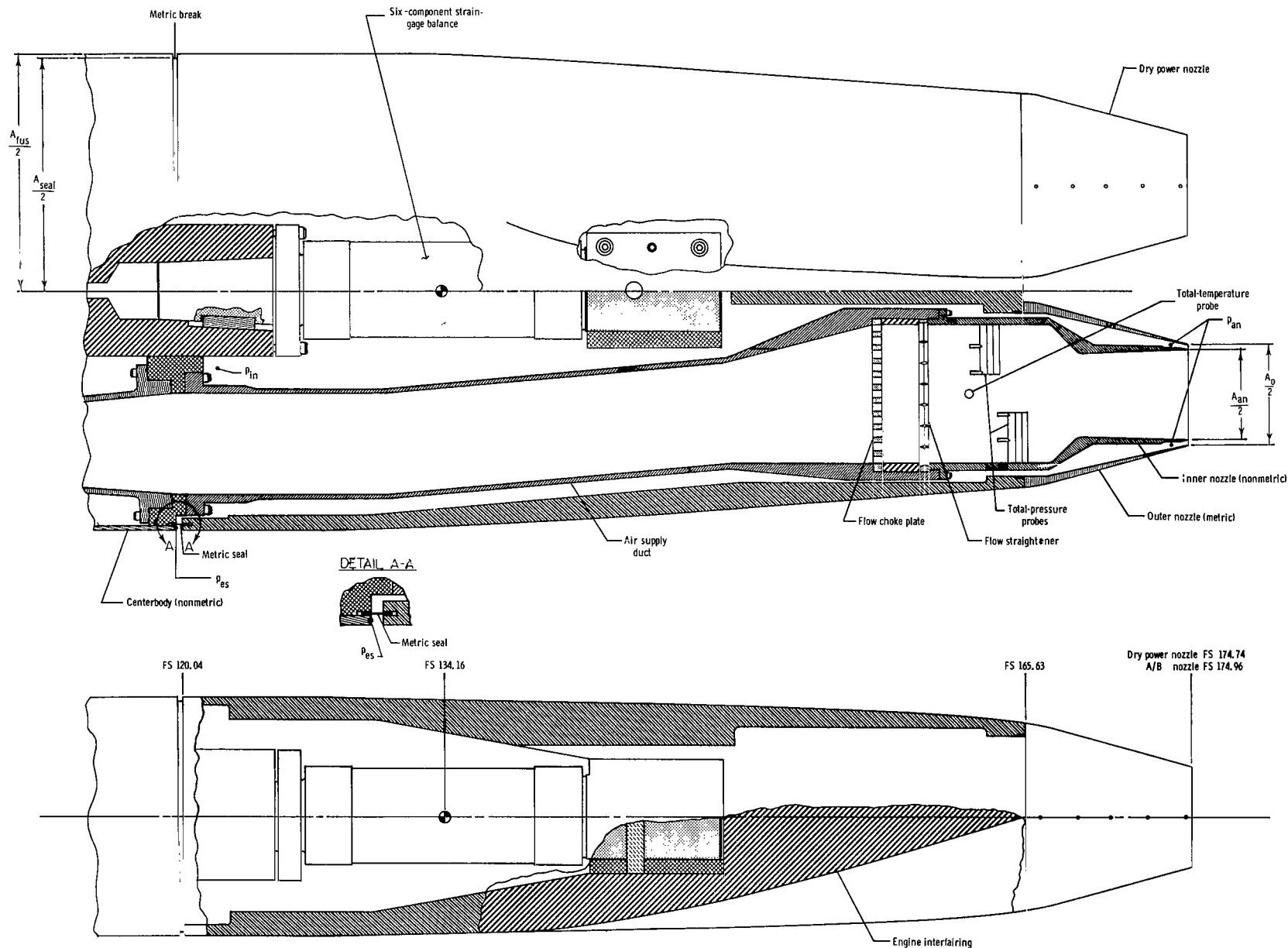


Figure 1.- Arrangement of Langley 16-Foot Transonic Tunnel. Dimensions are in meters.



(a) Twin tail interference model and wing-tip support system.

Figure 2.- Model sketches. (All dimensions are in cm unless otherwise noted.)



(b) Afterbody.

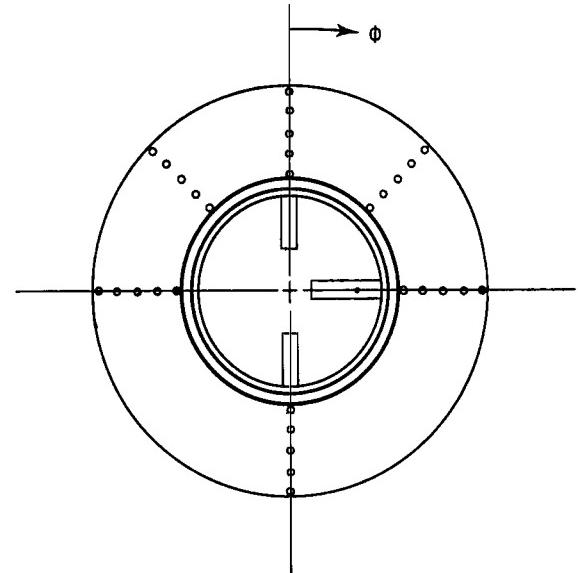
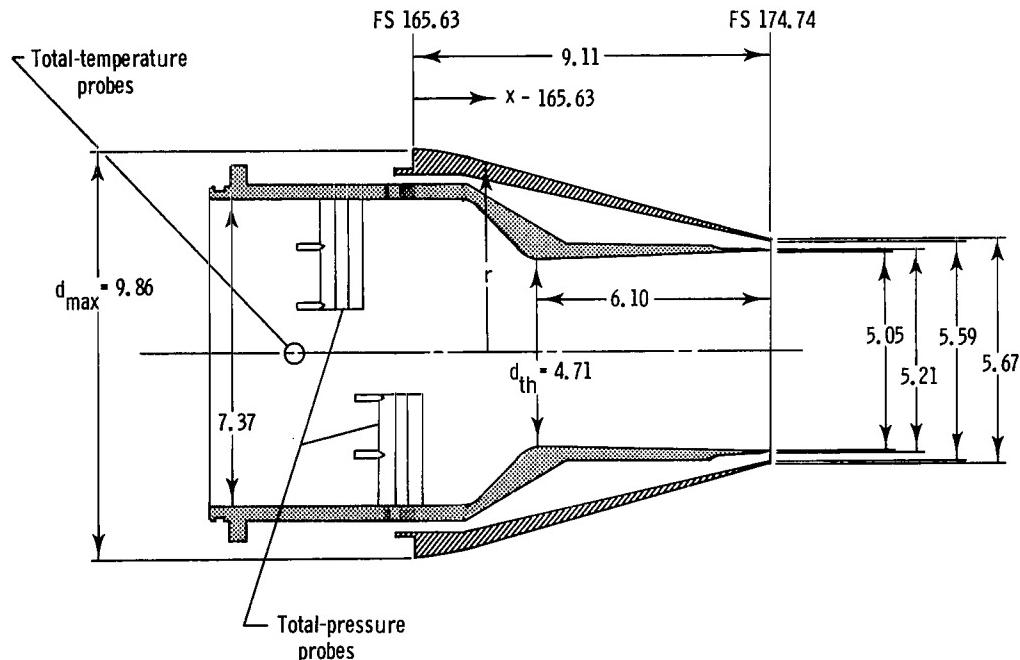
Figure 2.- Continued.

Nozzle External Geometry

$x/l$	$r/r_{\max}$
.948	1.000
.949	.996
.951	.991
.952	.984
.954	.975
.955	.963
1.000	.575

External Nozzle Static-Pressure Orifice Locations

$\phi$ , deg		$x/l$		Nozzle
0	.	.951	.	RH
45		.963	.	LH
90		.974	.	RH
180		.986	.	RH
270	Y	.997	Y	LH
315	Y		Y	LH



NOTE: All orifices are shown on the left-hand nozzle for simplicity.

(c) Dry power nozzle.

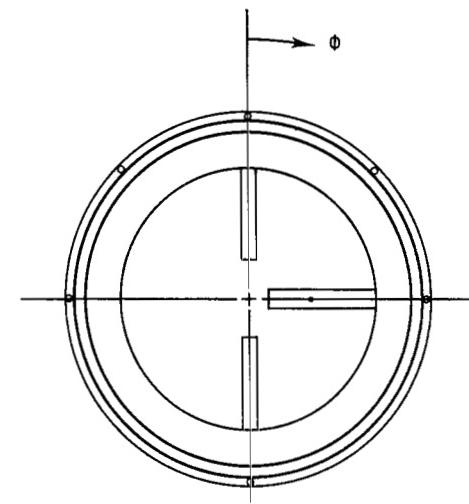
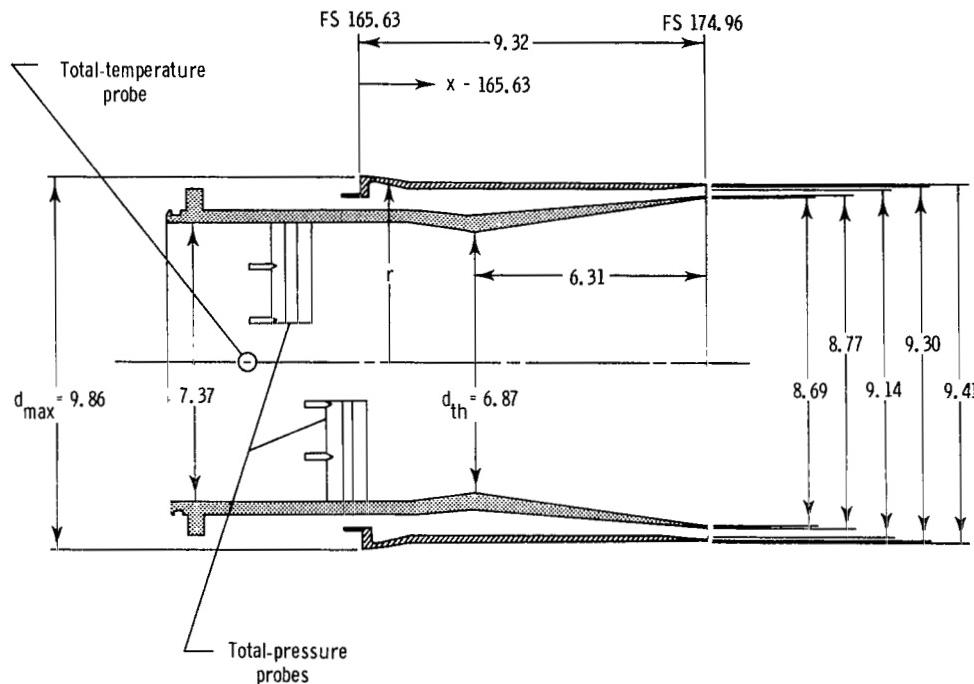
Figure 2.- Continued.

Nozzle External Geometry

$x/l$	$r/r_{\max}$
.947	1.000
.948	.996
.950	.991
.951	.984
.952	.975
.954	.963
1.000	.954

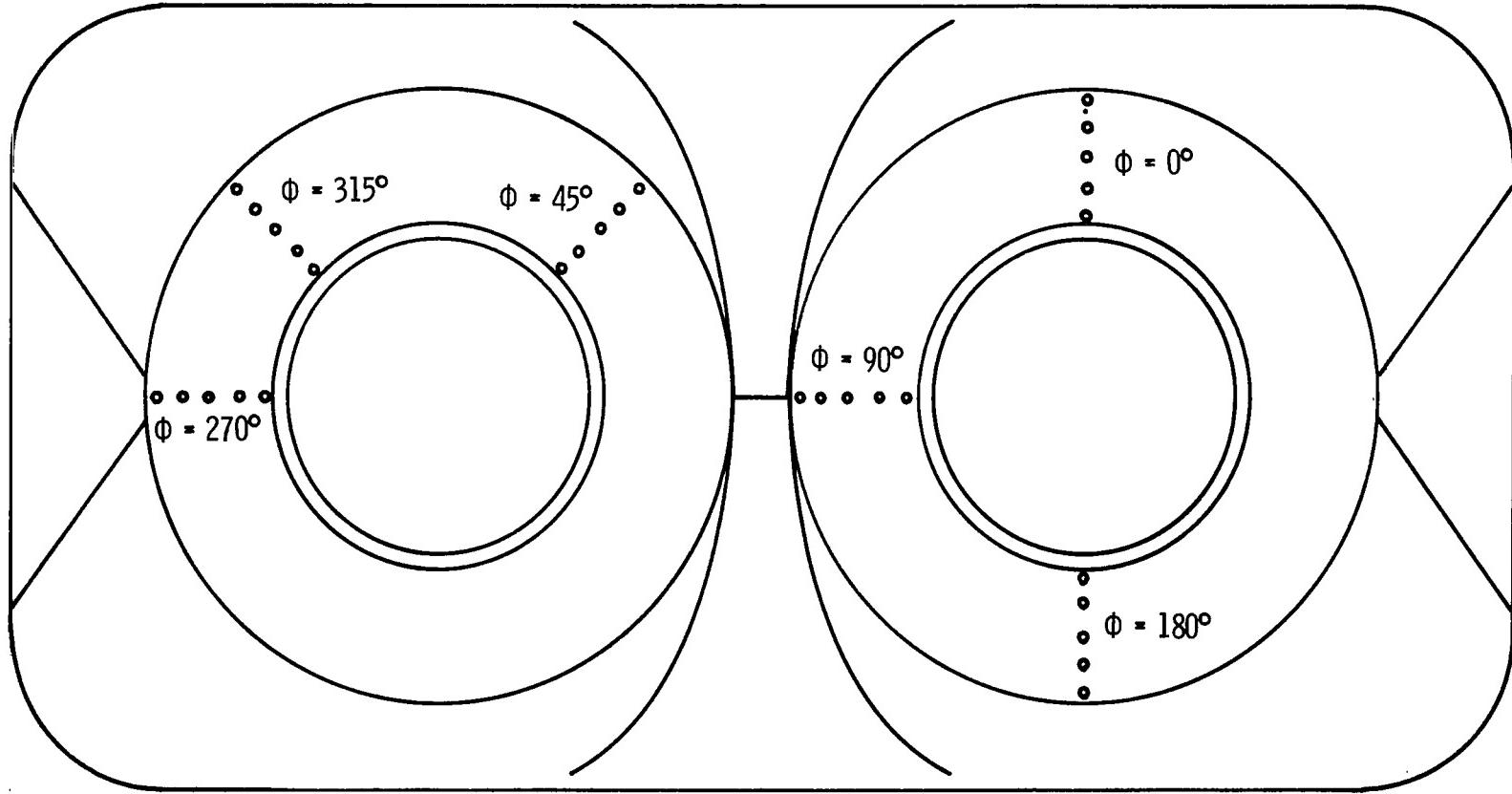
External Nozzle Static-Pressure Orifice Locations

$\phi$ , deg	$x/l$					Nozzle
	.951	.963	.974	.986	.997	
0	✓					RH
45		✓				LH
90			✓			RH
180				✓		RH
270					✓	LH
315					✓	LH



(d) Afterburning nozzle.

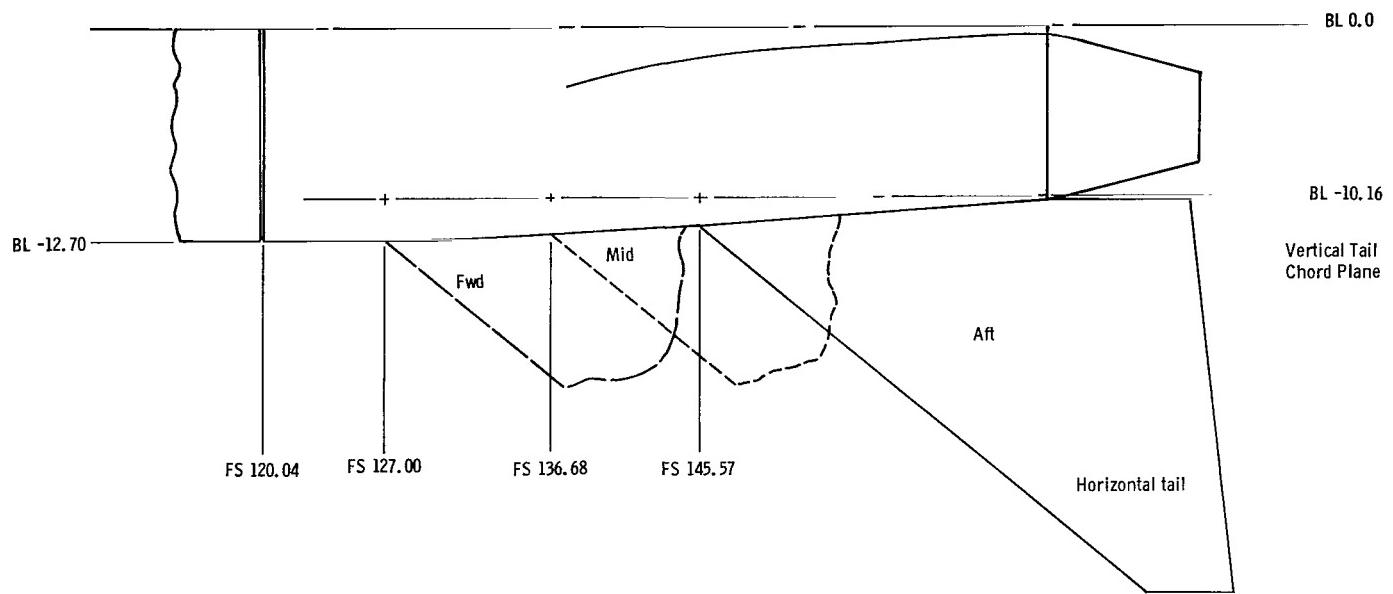
Figure 2.- Continued.



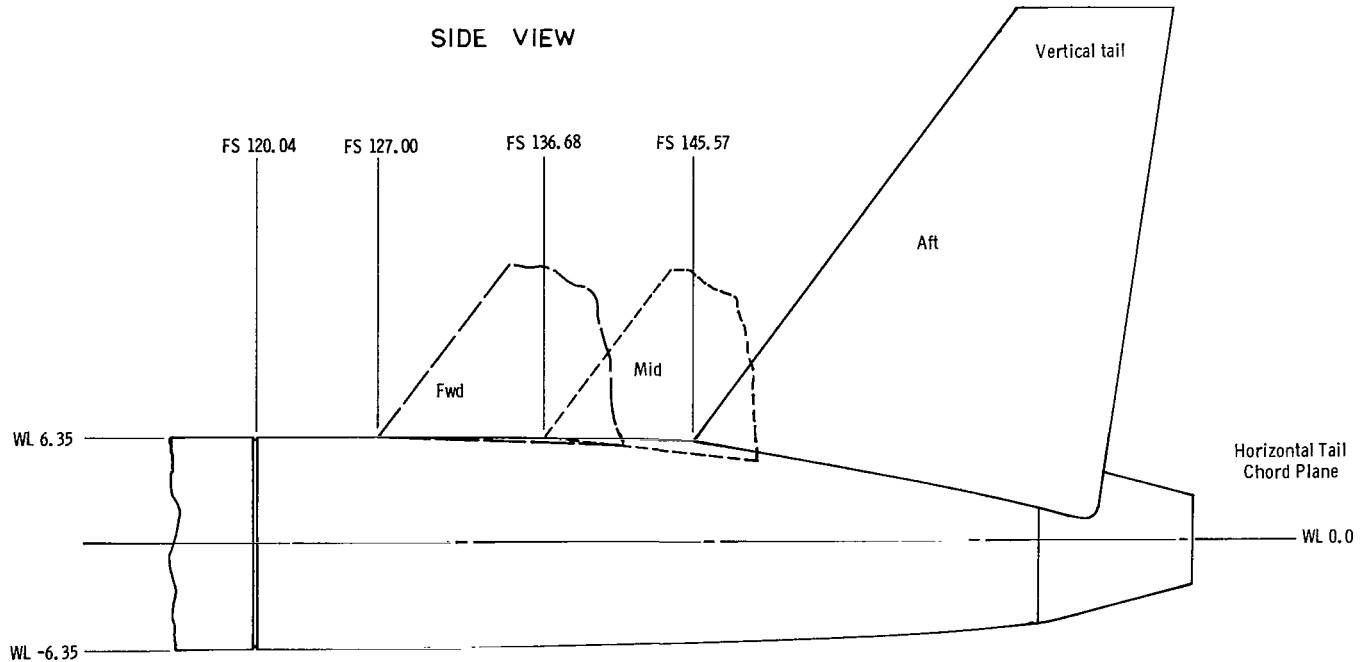
(e) Nozzle external static-pressure instrumentation orientation.

Figure 2.- Continued.

TOP VIEW

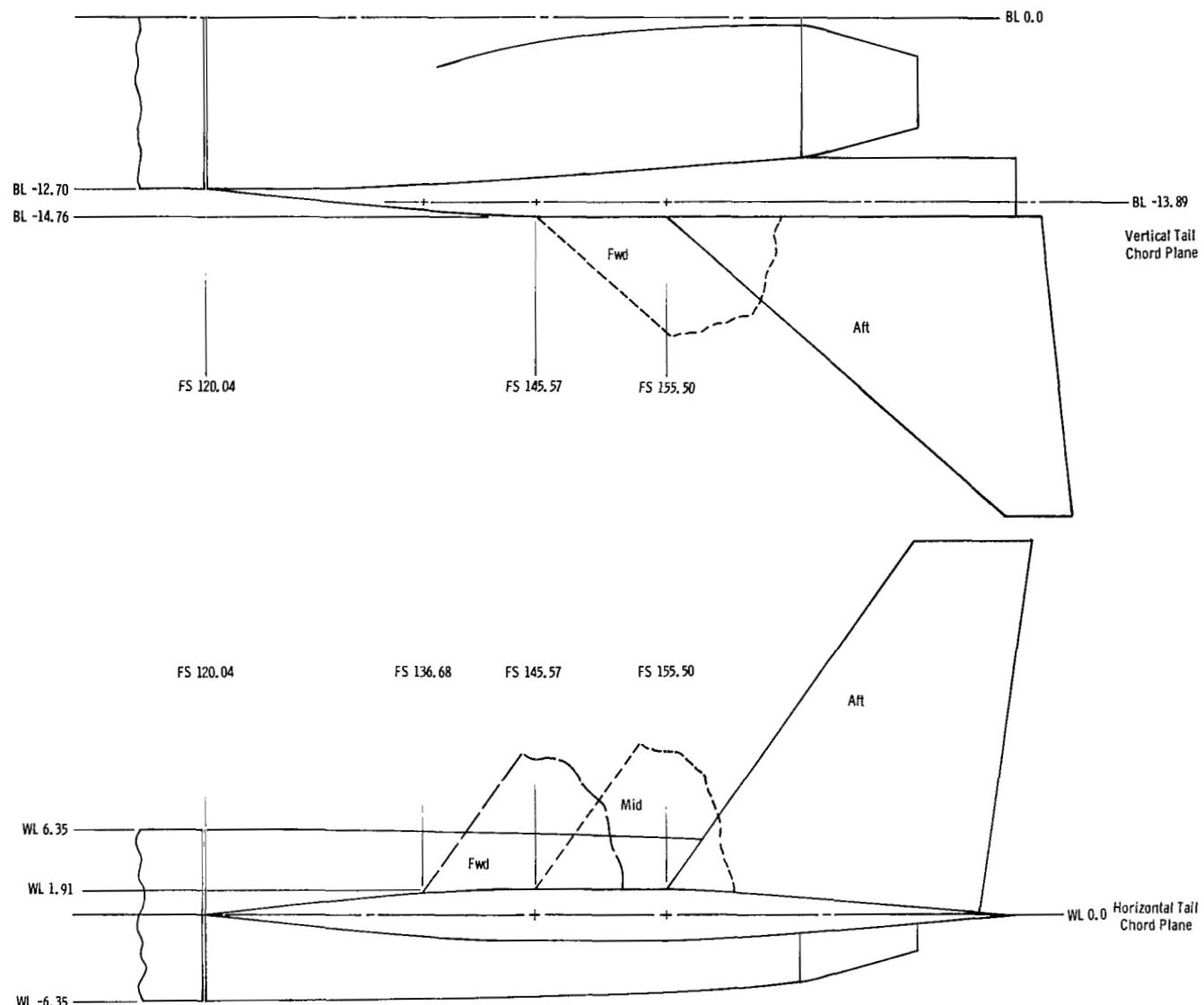


SIDE VIEW



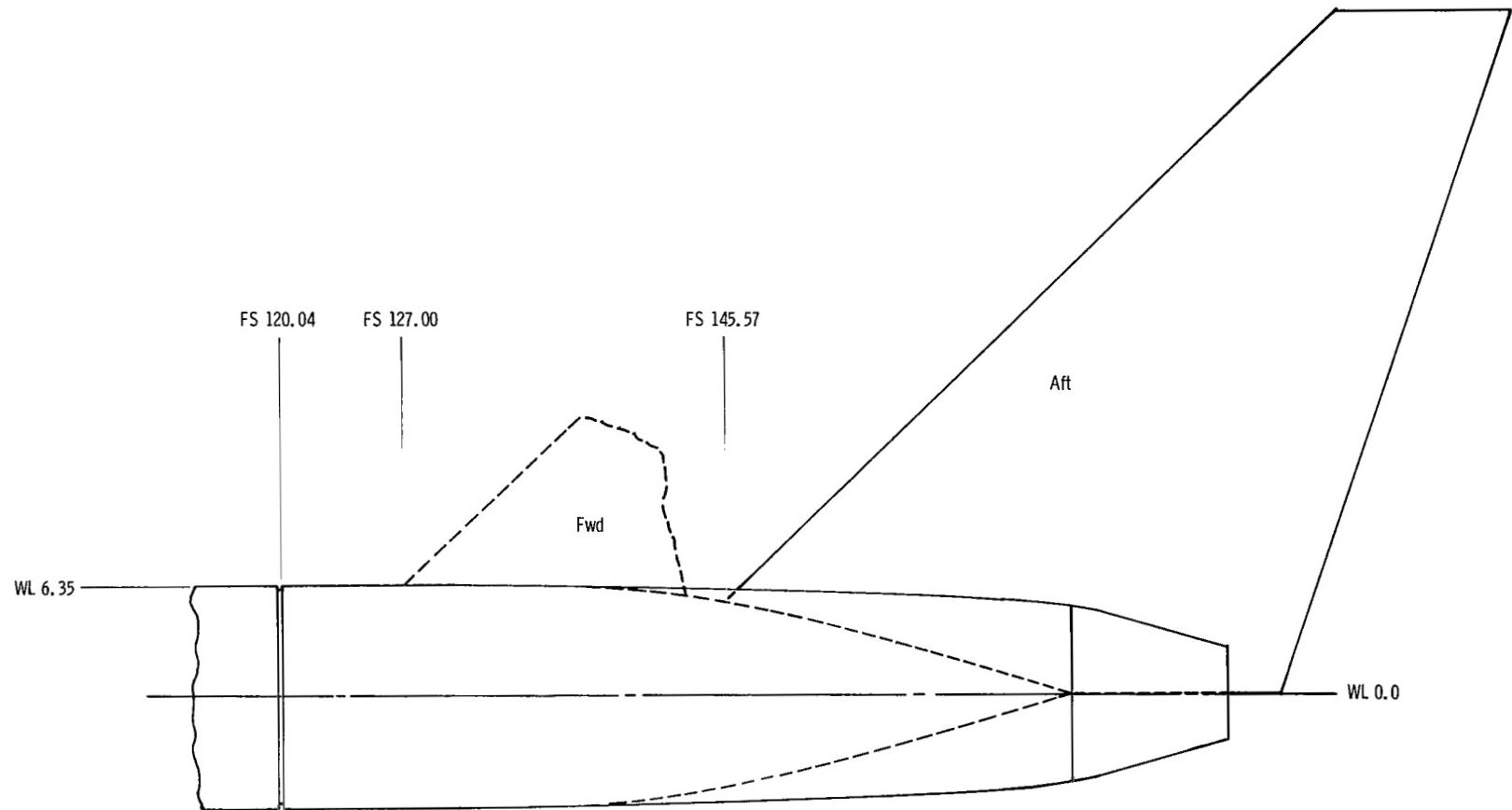
(f) Empennage locations on basic afterbody.

Figure 2.- Continued.



(g) Empennage locations on afterbody with booms.

Figure 2.- Continued.



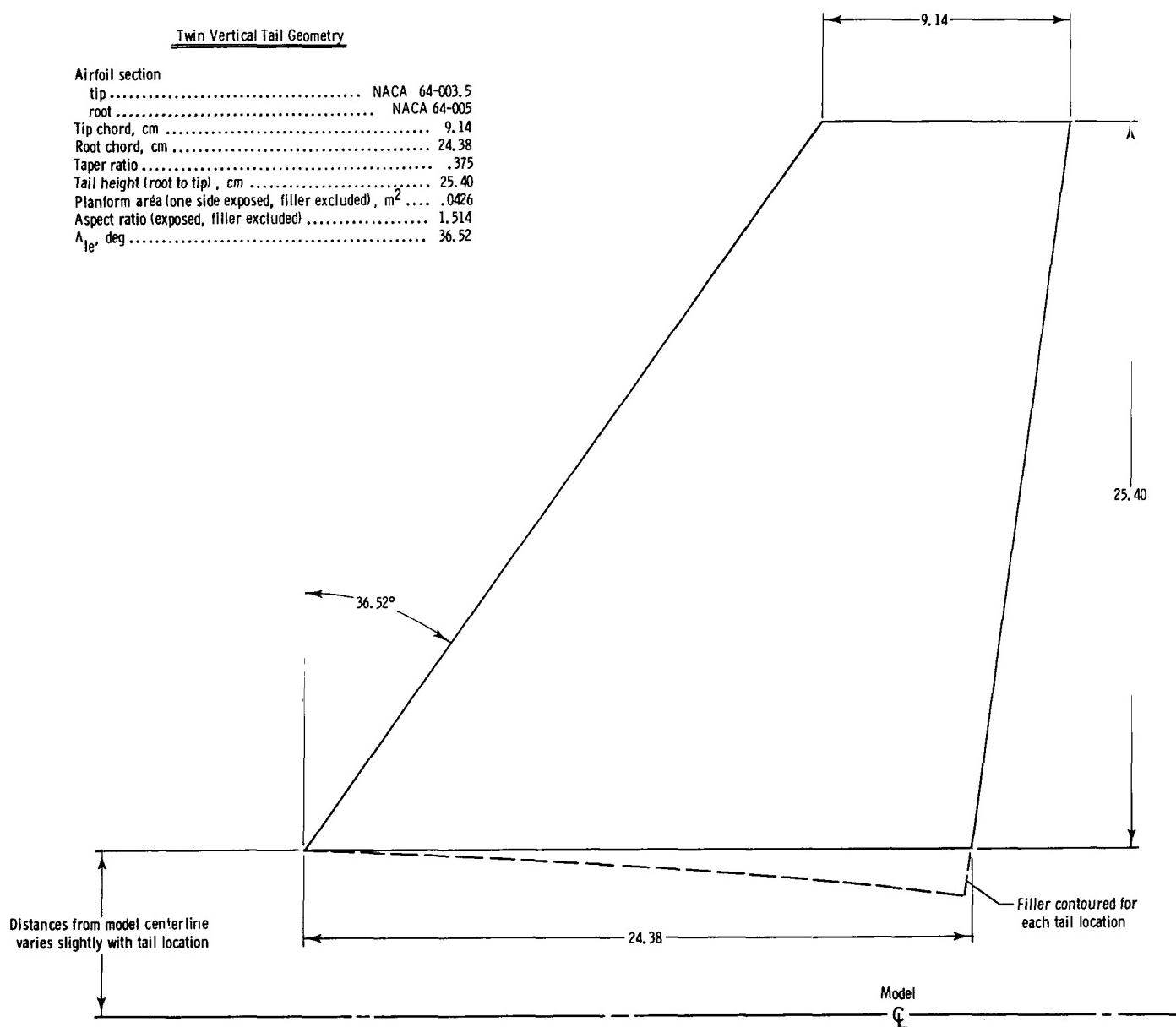
(h) Locations of single vertical tail.

Figure 2.- Continued.

Twin Vertical Tail Geometry

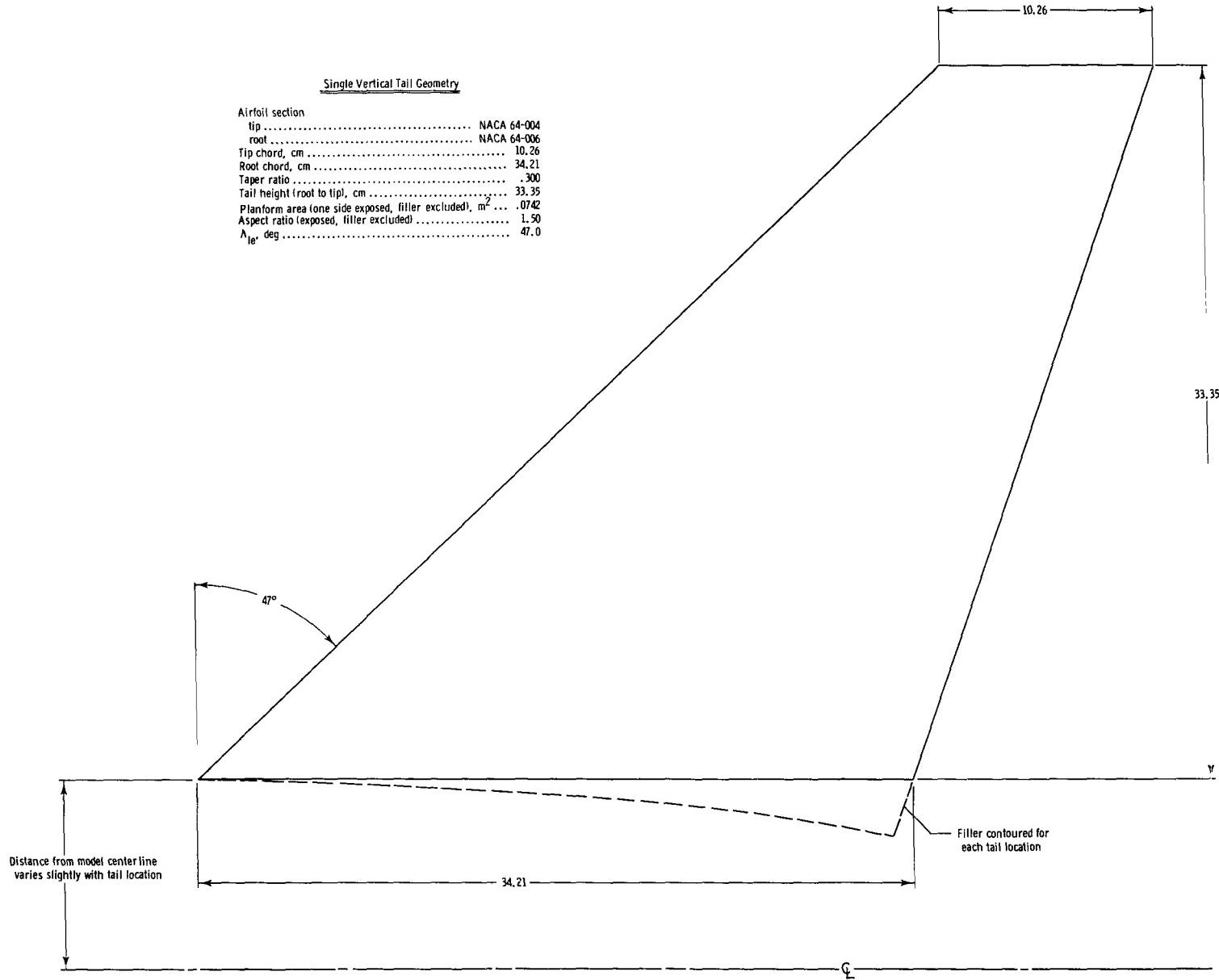
Airfoil section

tip .....	NACA 64-003.5
root .....	NACA 64-005
Tip chord, cm .....	9.14
Root chord, cm .....	24.38
Taper ratio .....	.375
Tail height (root to tip), cm .....	25.40
Planform area (one side exposed, filler excluded), m <sup>2</sup> .....	.0426
Aspect ratio (exposed, filler excluded) .....	1.514
$\Lambda_{le}$ , deg .....	36.52



(i) Twin vertical tail.

Figure 2.- Continued.



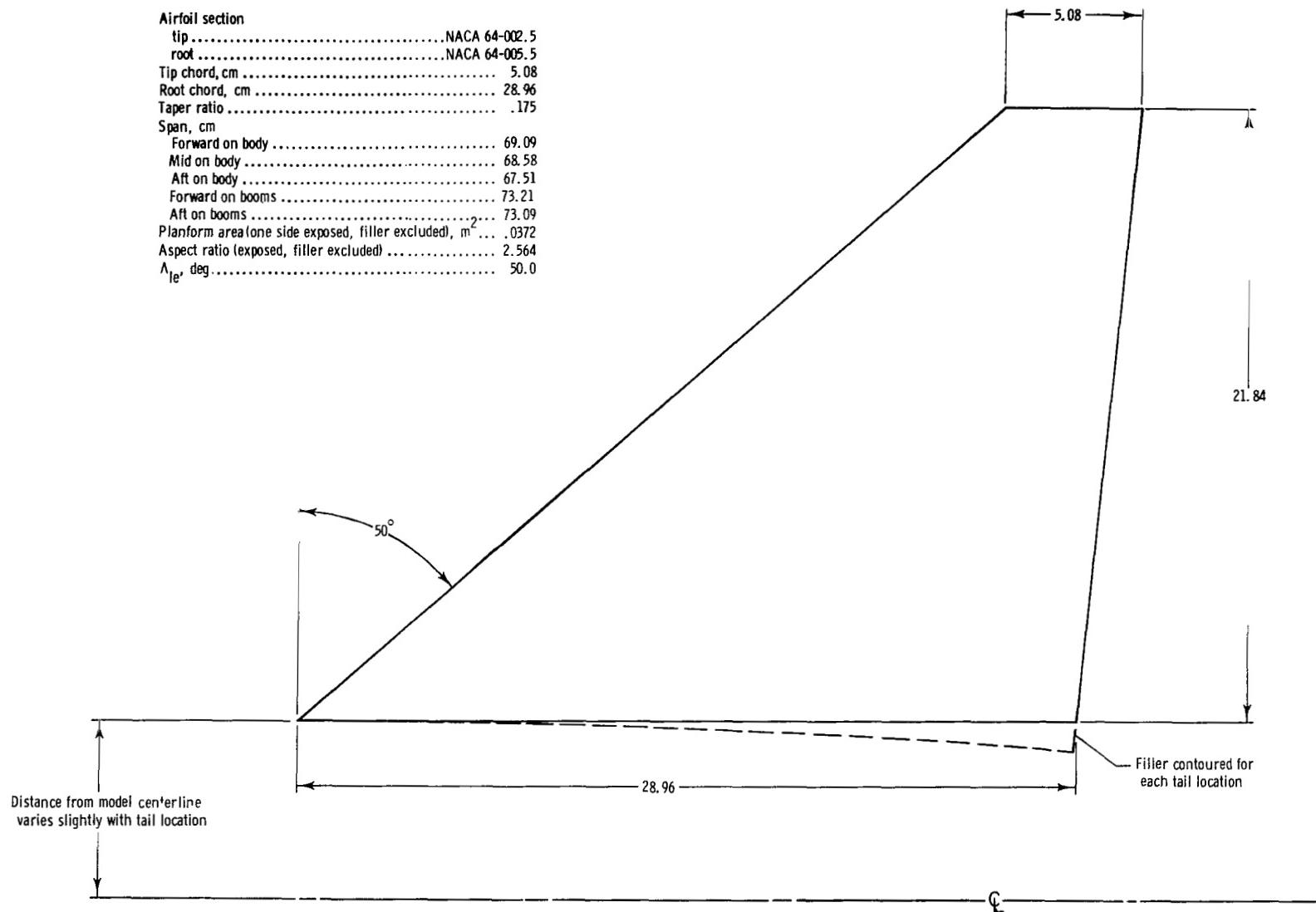
(j) Single vertical tail.

Figure 2.- Continued.

### Horizontal Tail Geometry

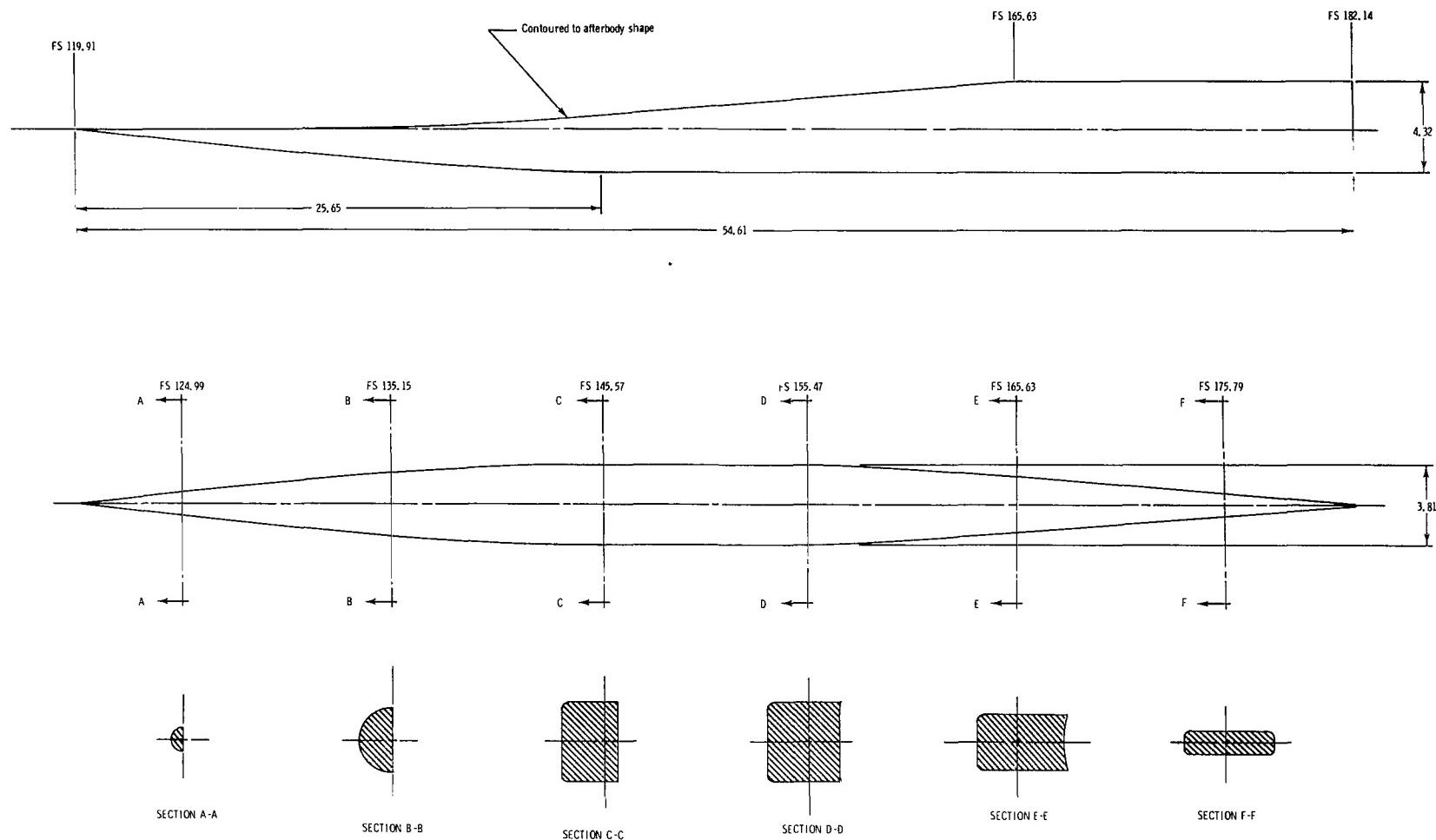
#### Airfoil section

tip .....	NACA 64-002.5
root .....	NACA 64-005.5
Tip chord, cm .....	5.08
Root chord, cm .....	28.96
Taper ratio .....	.175
Span, cm .....	
Forward on body .....	69.09
Mid on body .....	68.58
Aft on body .....	67.51
Forward on booms .....	73.21
Aft on booms .....	73.09
Planform area (one side exposed, filler excluded), m <sup>2</sup> .....	.0372
Aspect ratio (exposed, filler excluded) .....	2.564
$\Lambda_{le}$ , deg .....	50.0



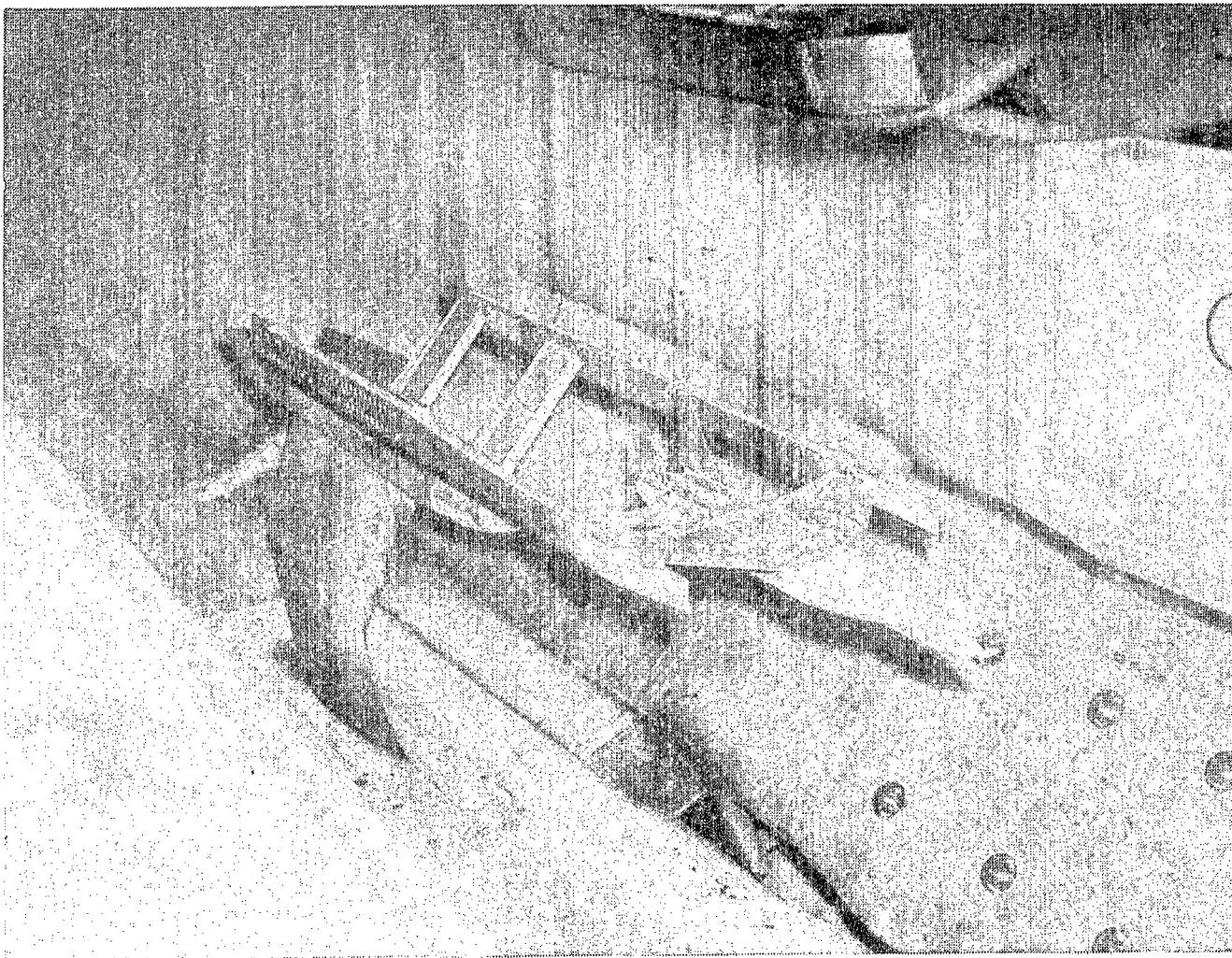
(k) Horizontal tail.

Figure 2.- Continued.



(1) Tail booms.

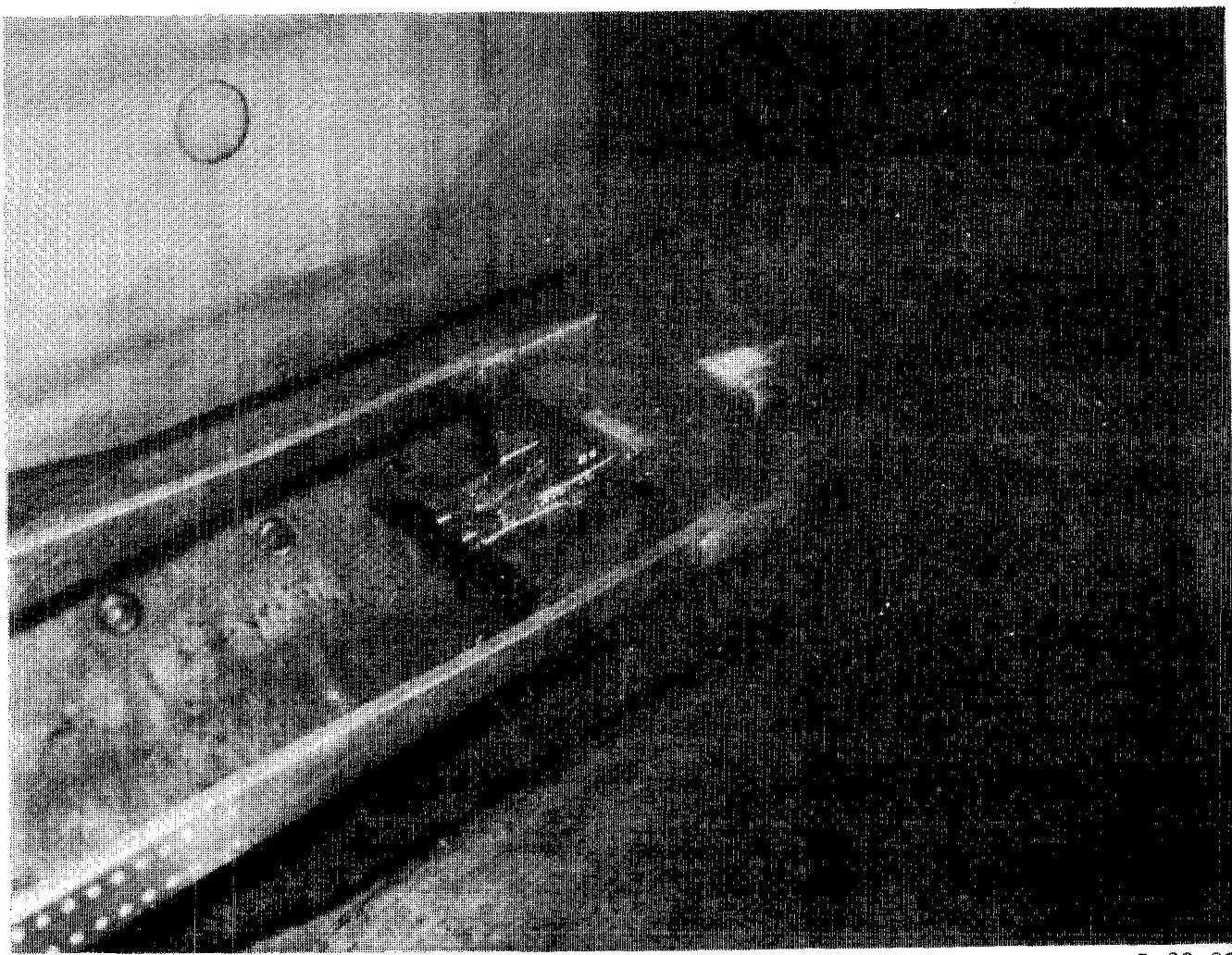
Figure 2.- Concluded.



L-83-01

(a) Model and wing-tip support system.

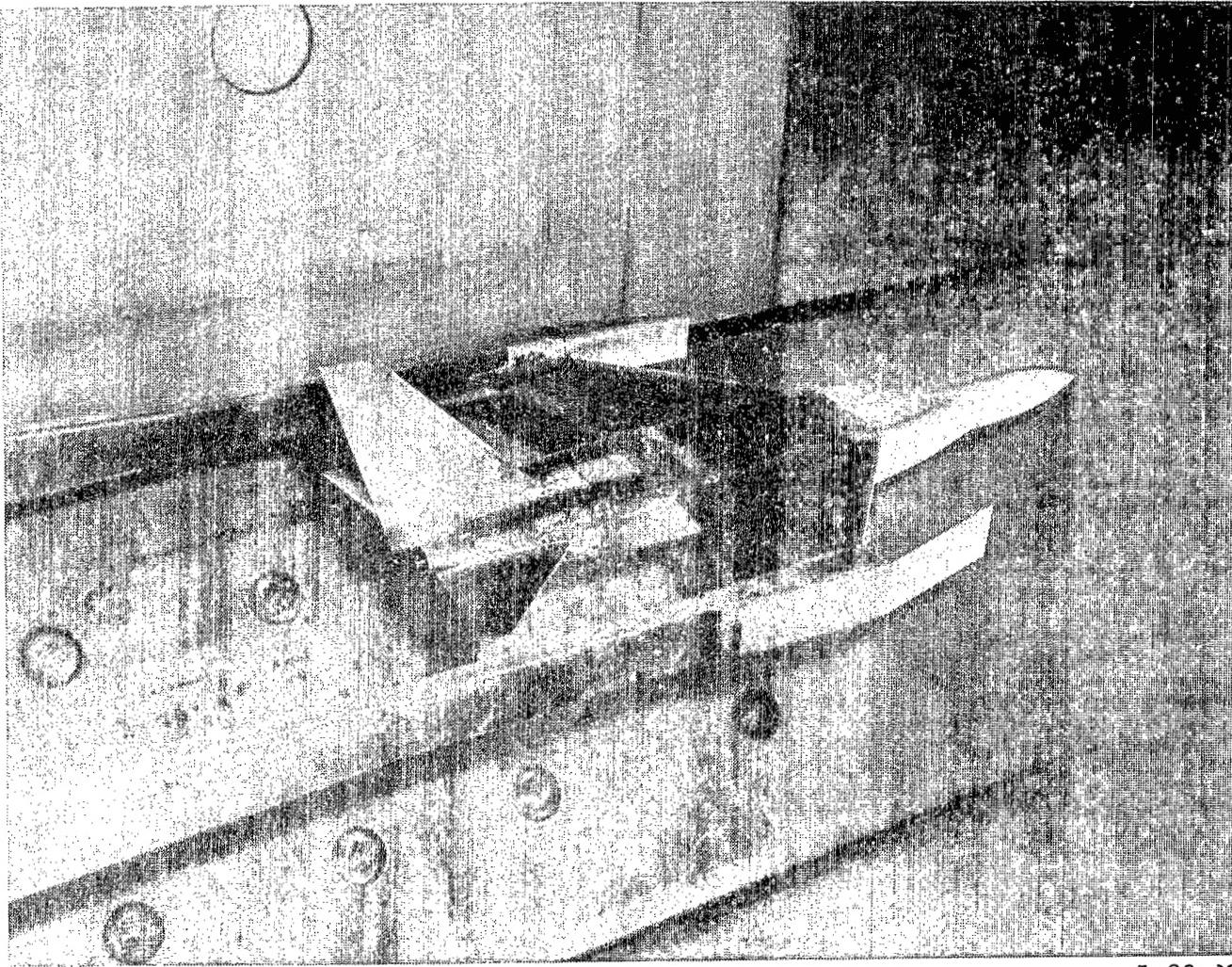
Figure 3.- Photographs of twin-engine tail interference model installed in  
Langley 16-Foot Transonic Tunnel.



L-83-02

(b) Twin vertical tail configuration.

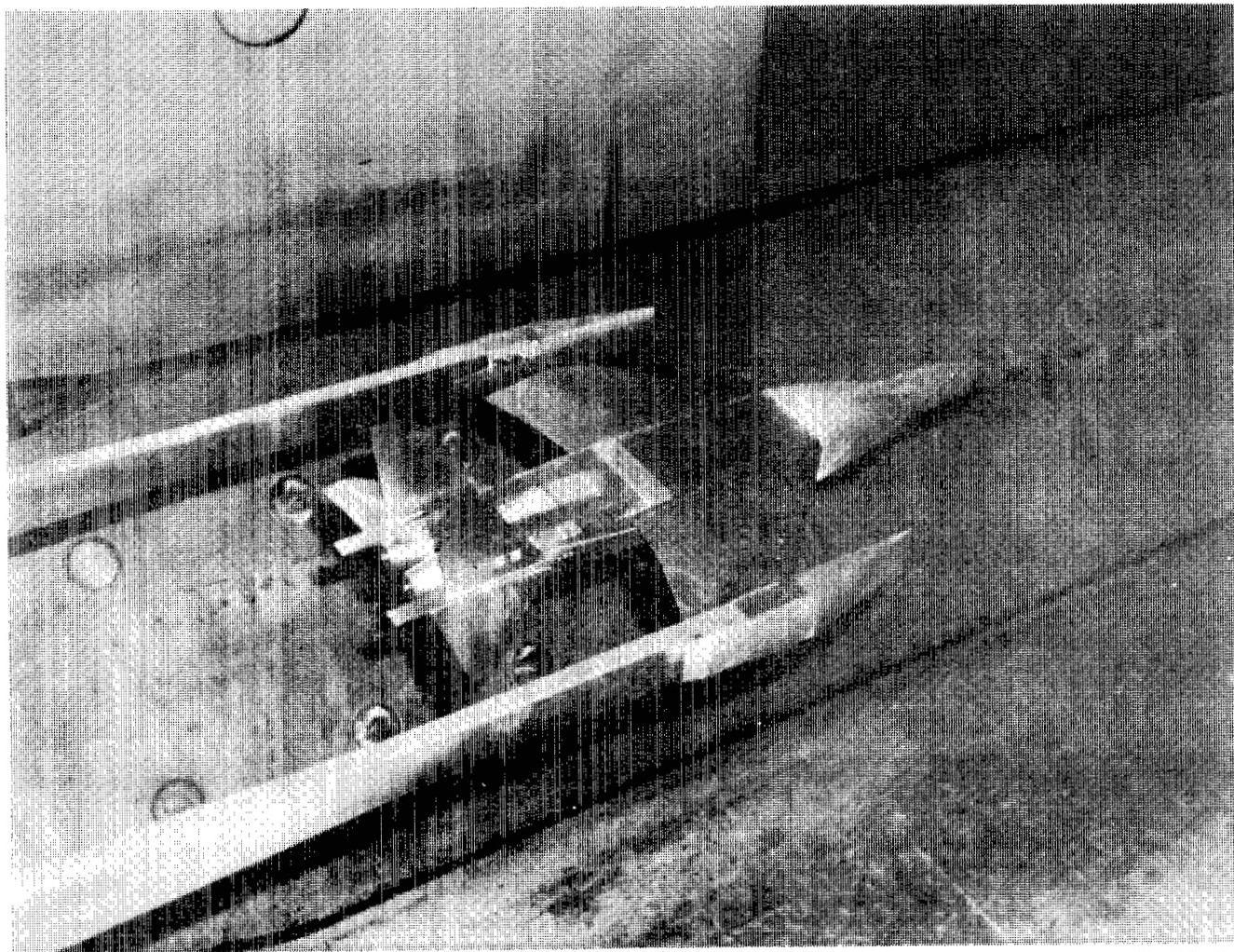
Figure 3.- Continued.



L-83-03

(c) Single vertical tail configuration.

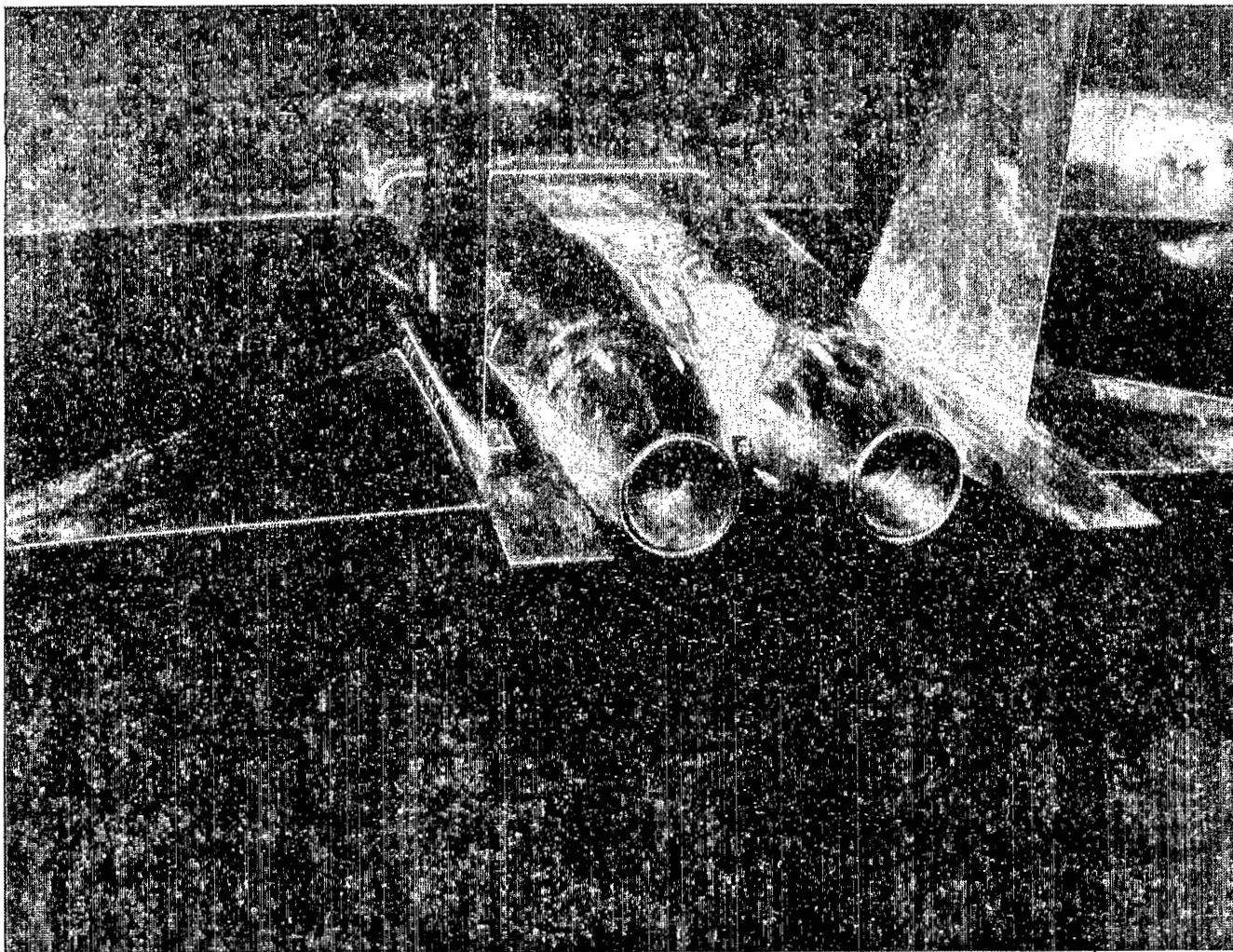
Figure 3.- Continued.



I-83-04

(d) Twin vertical tail configuration with tail booms.

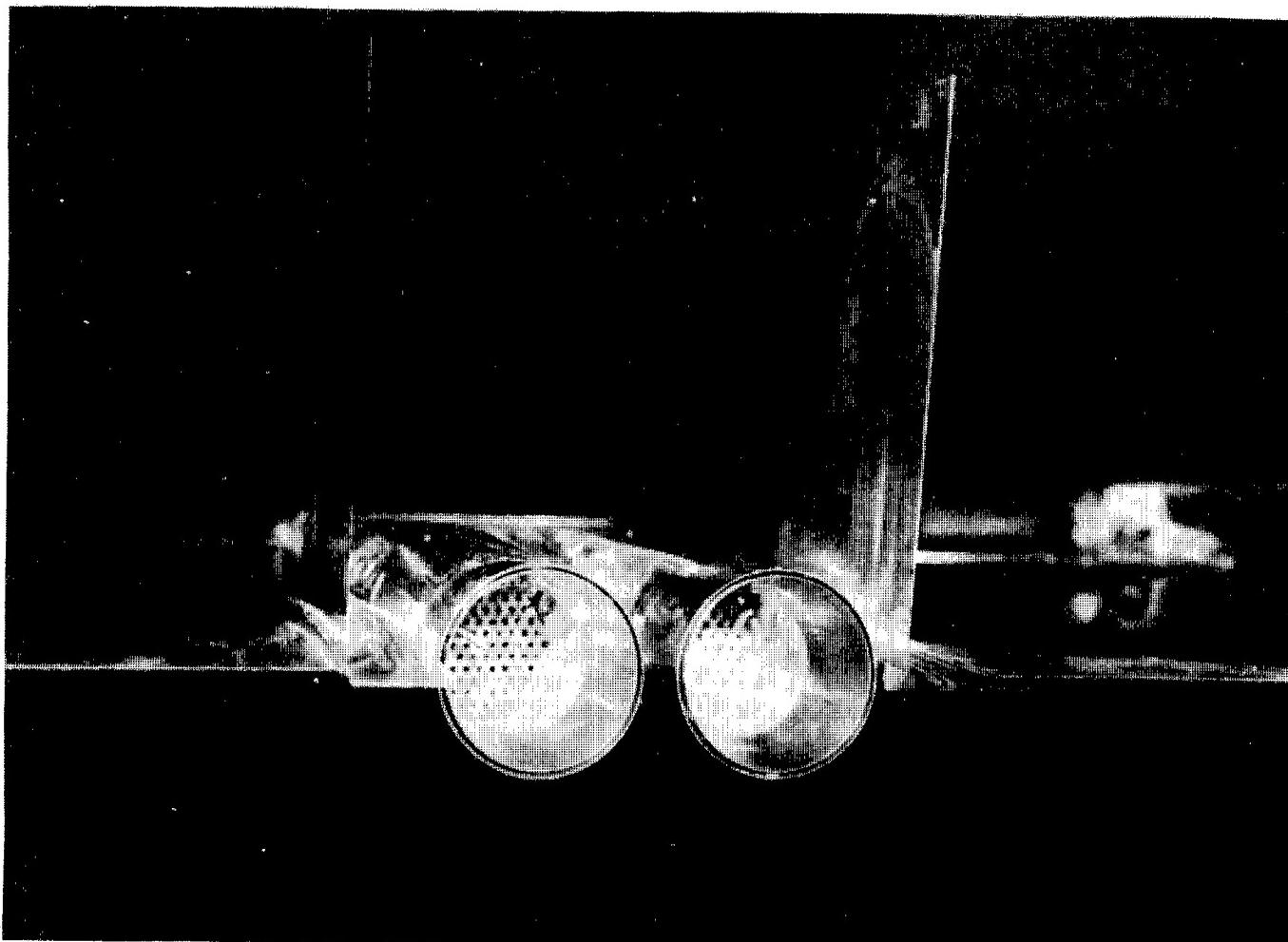
Figure 3.- Continued.



L-83-05

(e) Dry power nozzles.

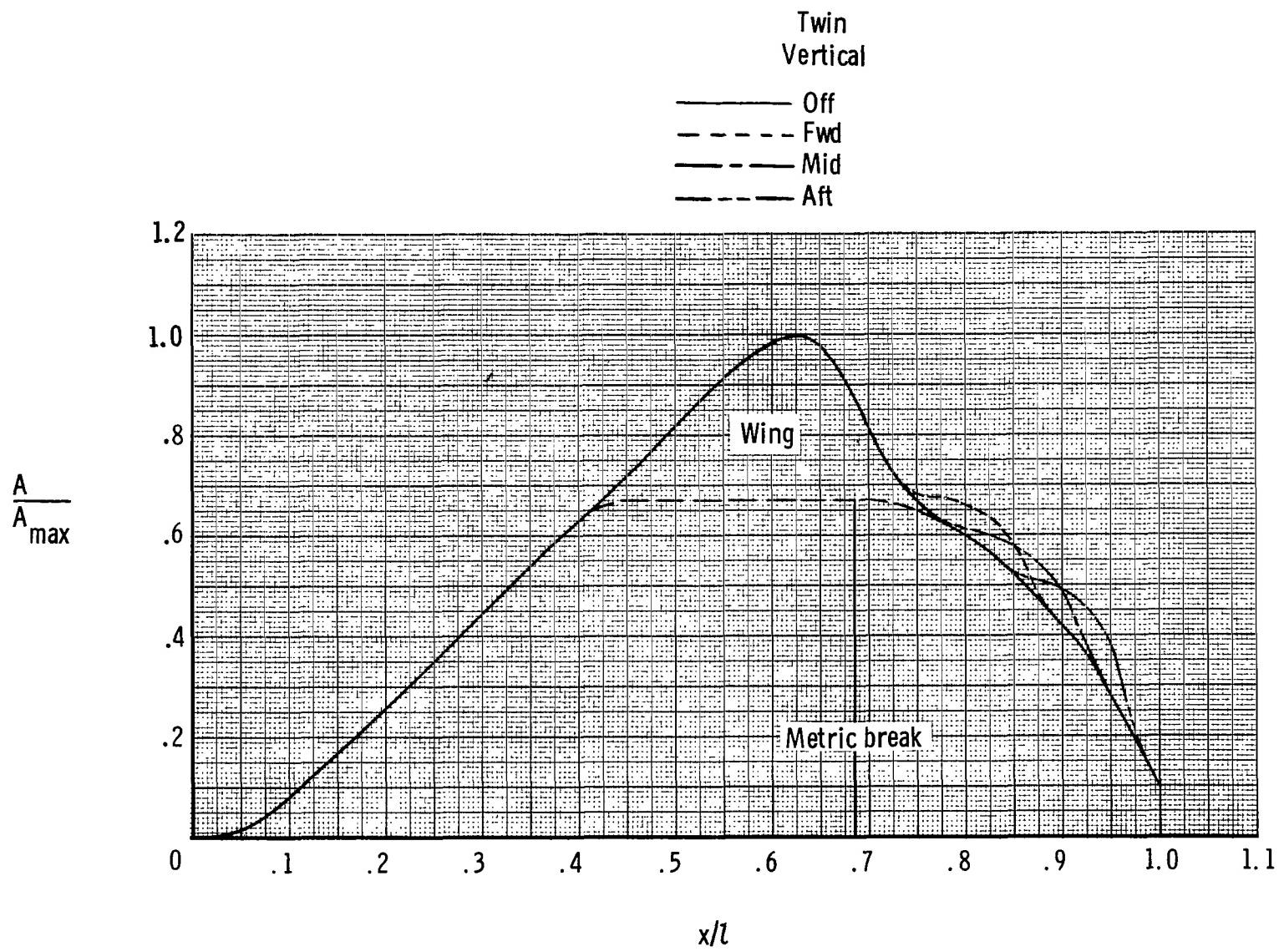
Figure 3.- Continued.



L-83-06

(f) A/B nozzles.

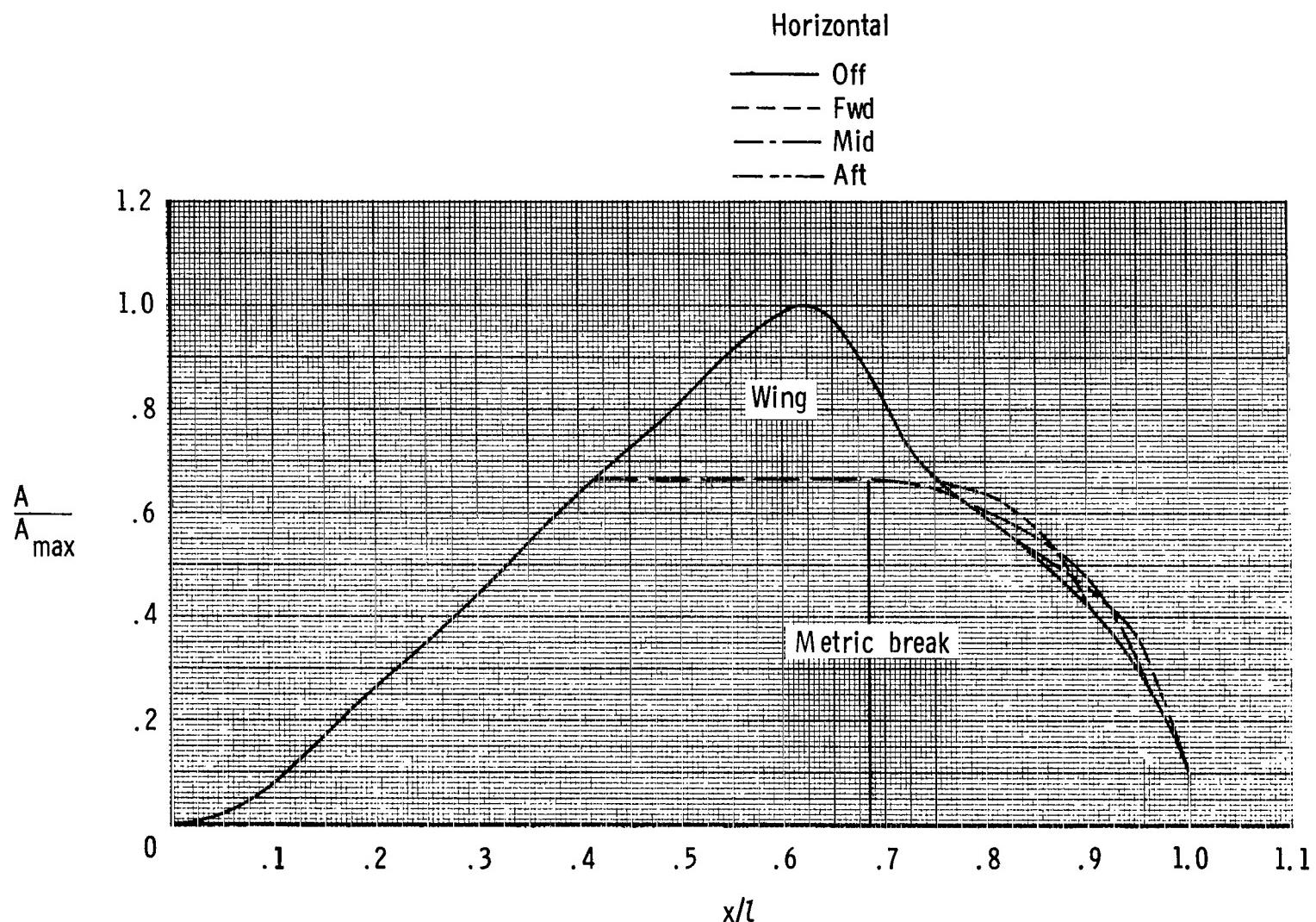
Figure 3.- Concluded.



(a) Booms off; dry power nozzle; twin vertical tail.

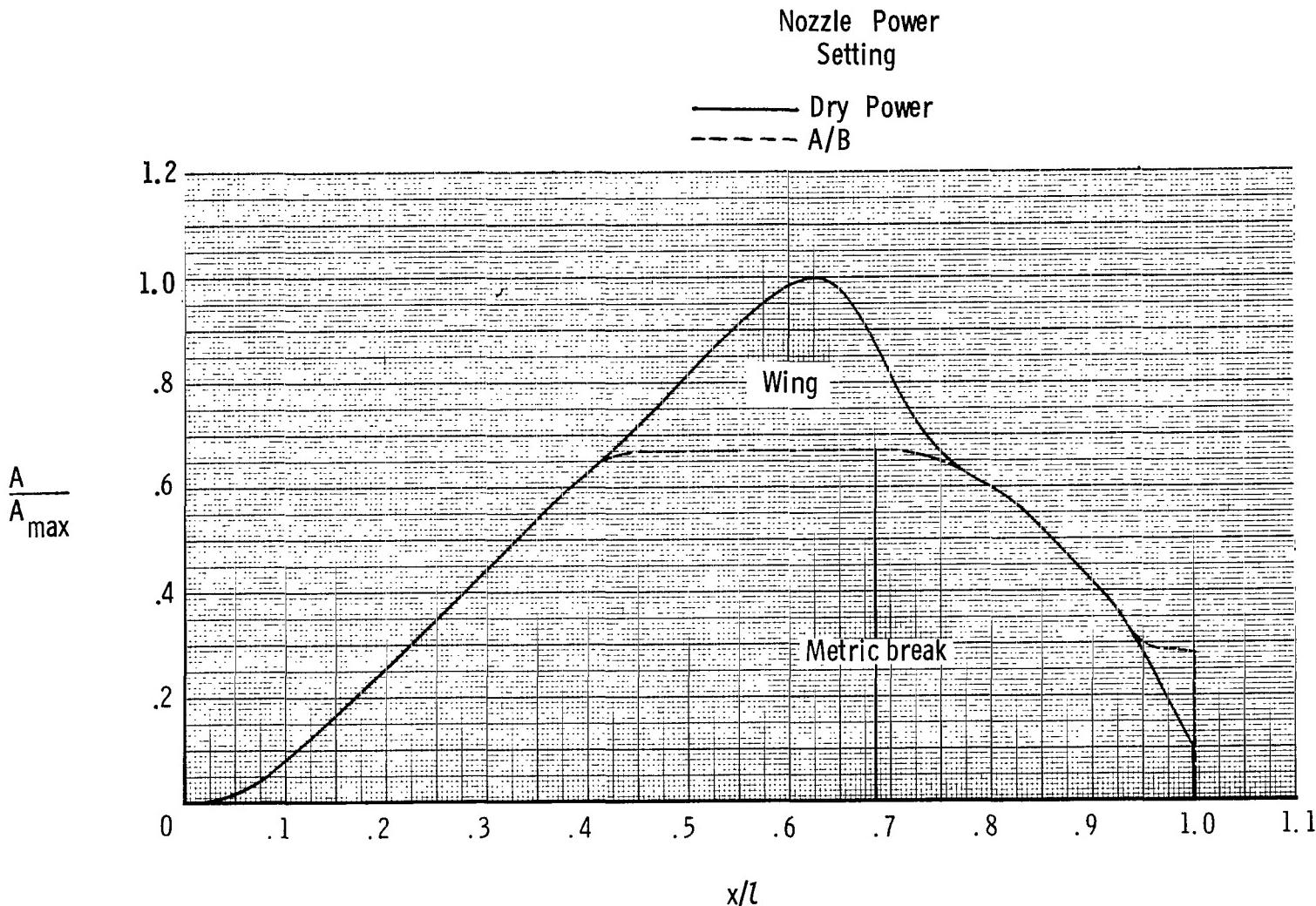
Figure 4.- Normal area distributions for various model configurations.

$$A_{\max} = 475.45 \text{ cm}^2; l = 174.74 \text{ cm.}$$



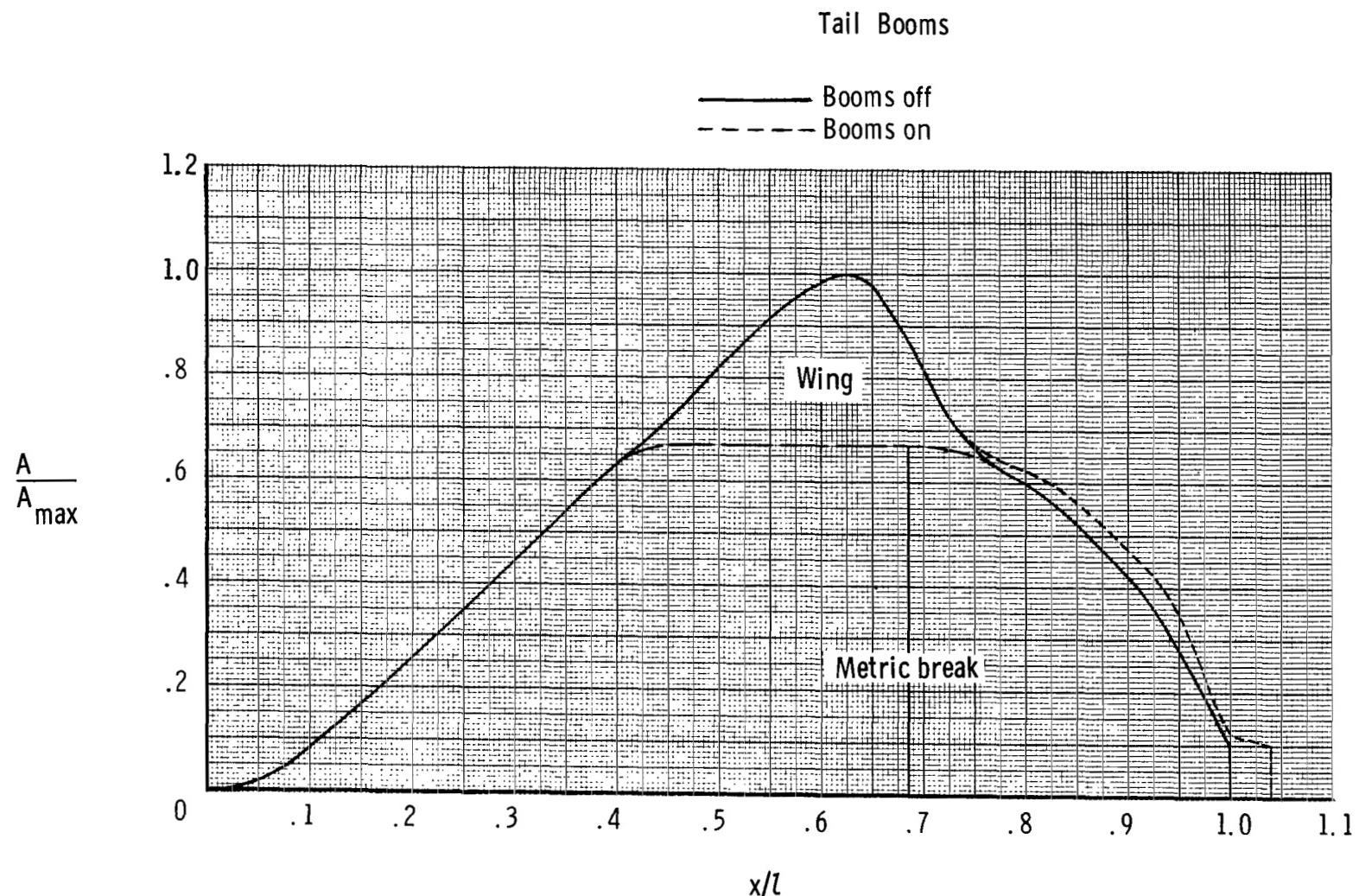
(b) Booms off; dry power nozzle; horizontal tail.

Figure 4.- Continued.



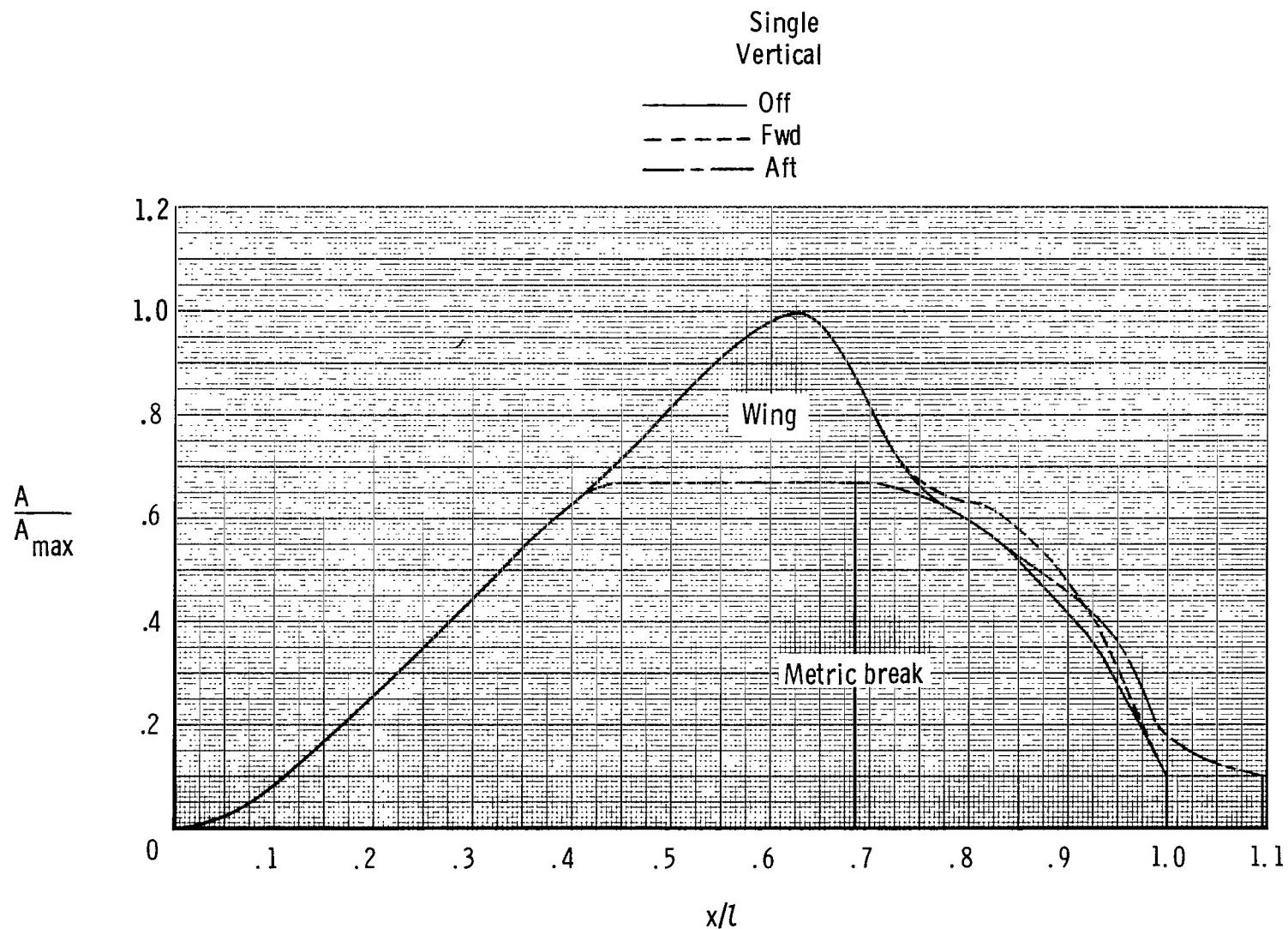
(c) Tails off; booms off.

Figure 4.- Continued.



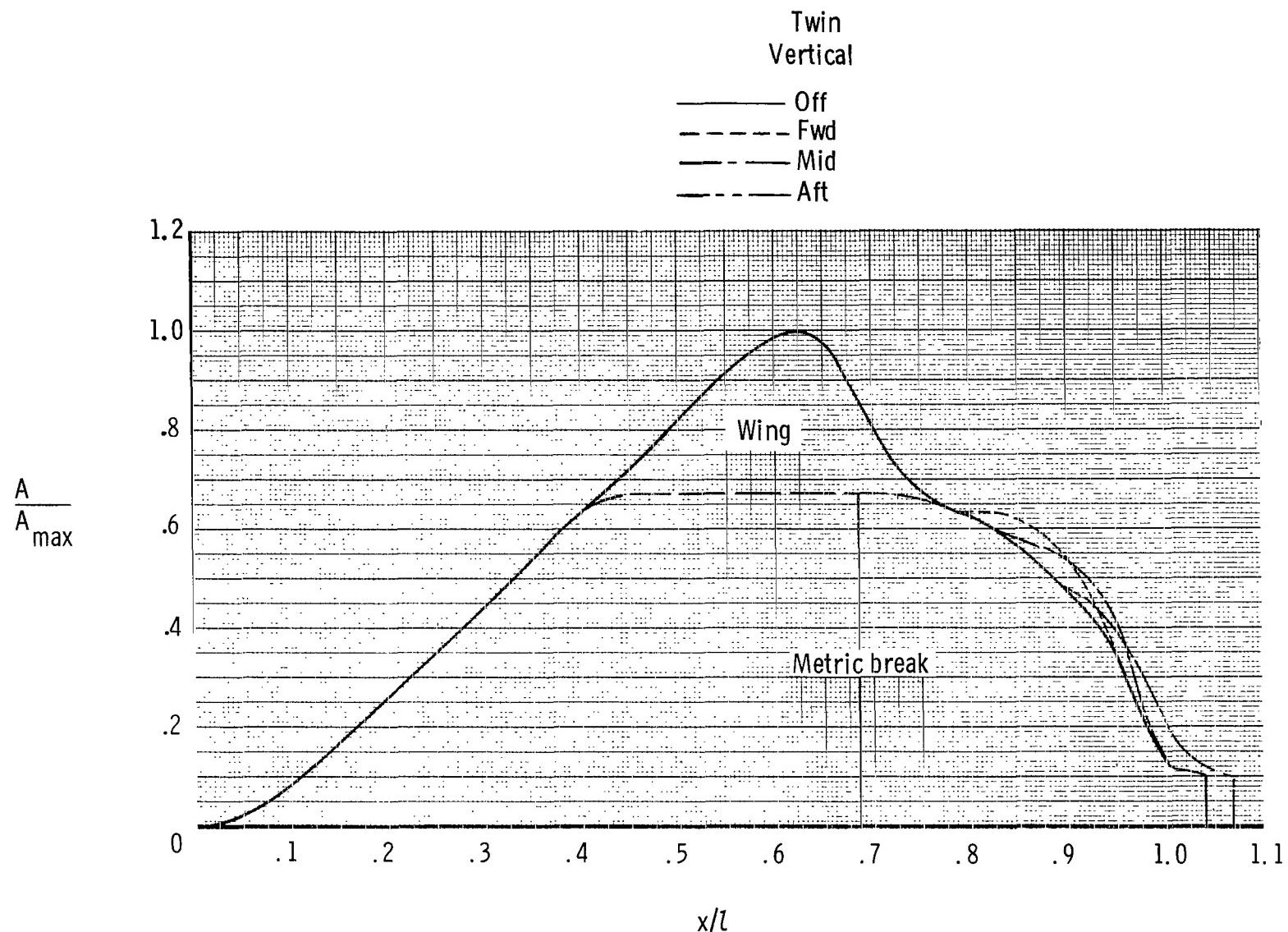
(d) Tails off; dry power nozzle.

Figure 4.- Continued.



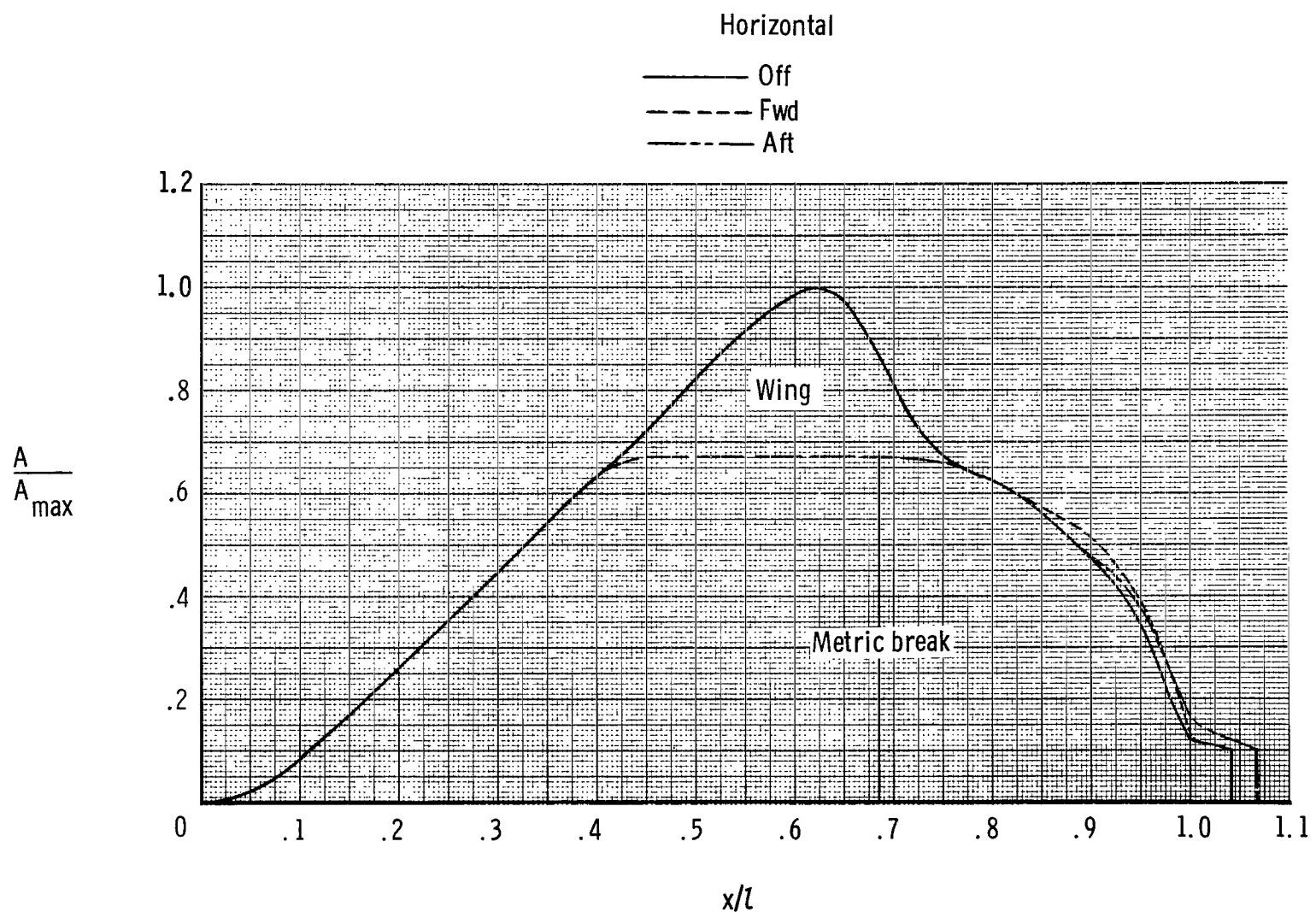
(e) Booms off; dry power nozzle; single vertical tail.

Figure 4.- Continued.



(f) Booms on; dry power nozzle; twin vertical tail.

Figure 4.- Continued.



(g) Booms on; dry power nozzle; horizontal tail.

Figure 4.- Concluded.

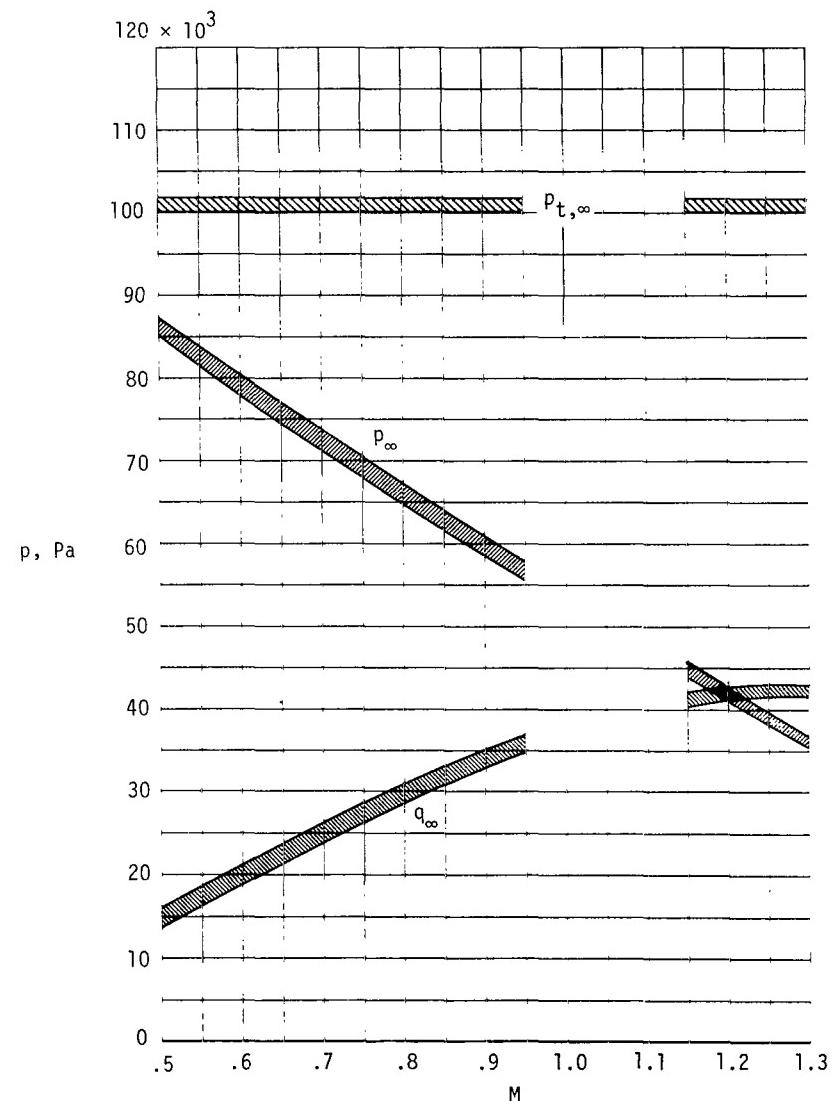
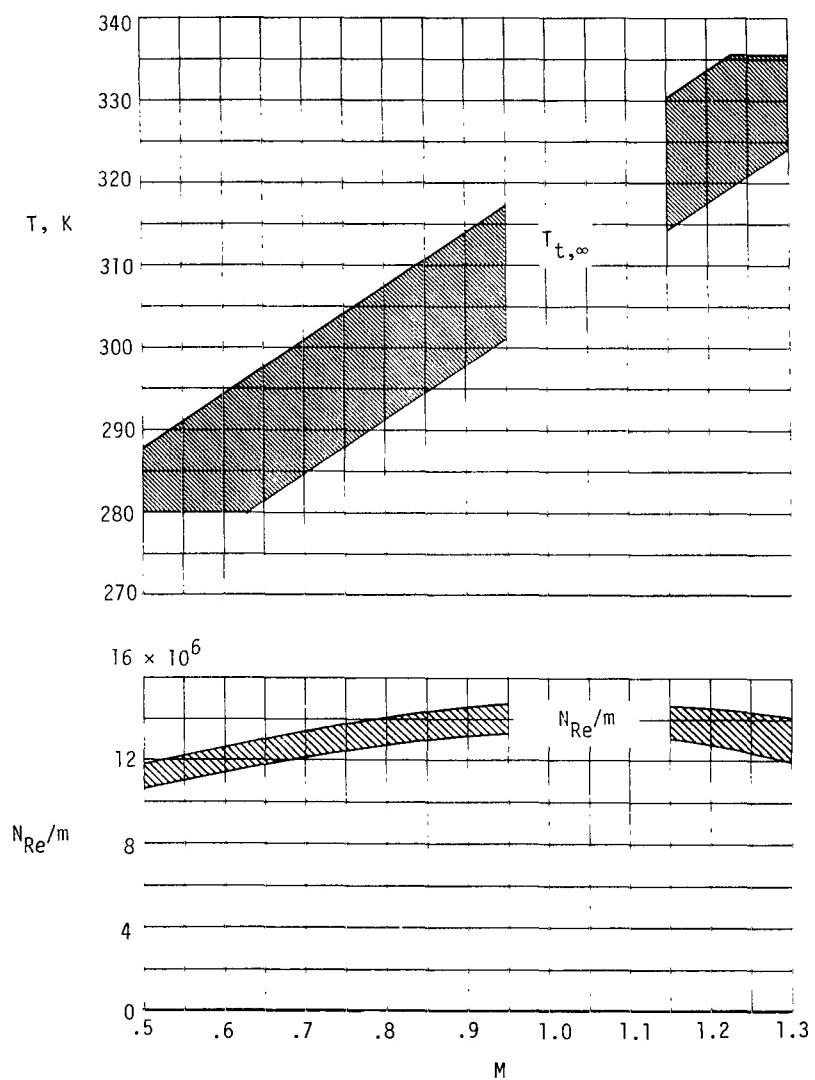


Figure 5.- Typical tunnel free-stream parameter variations with Mach number.

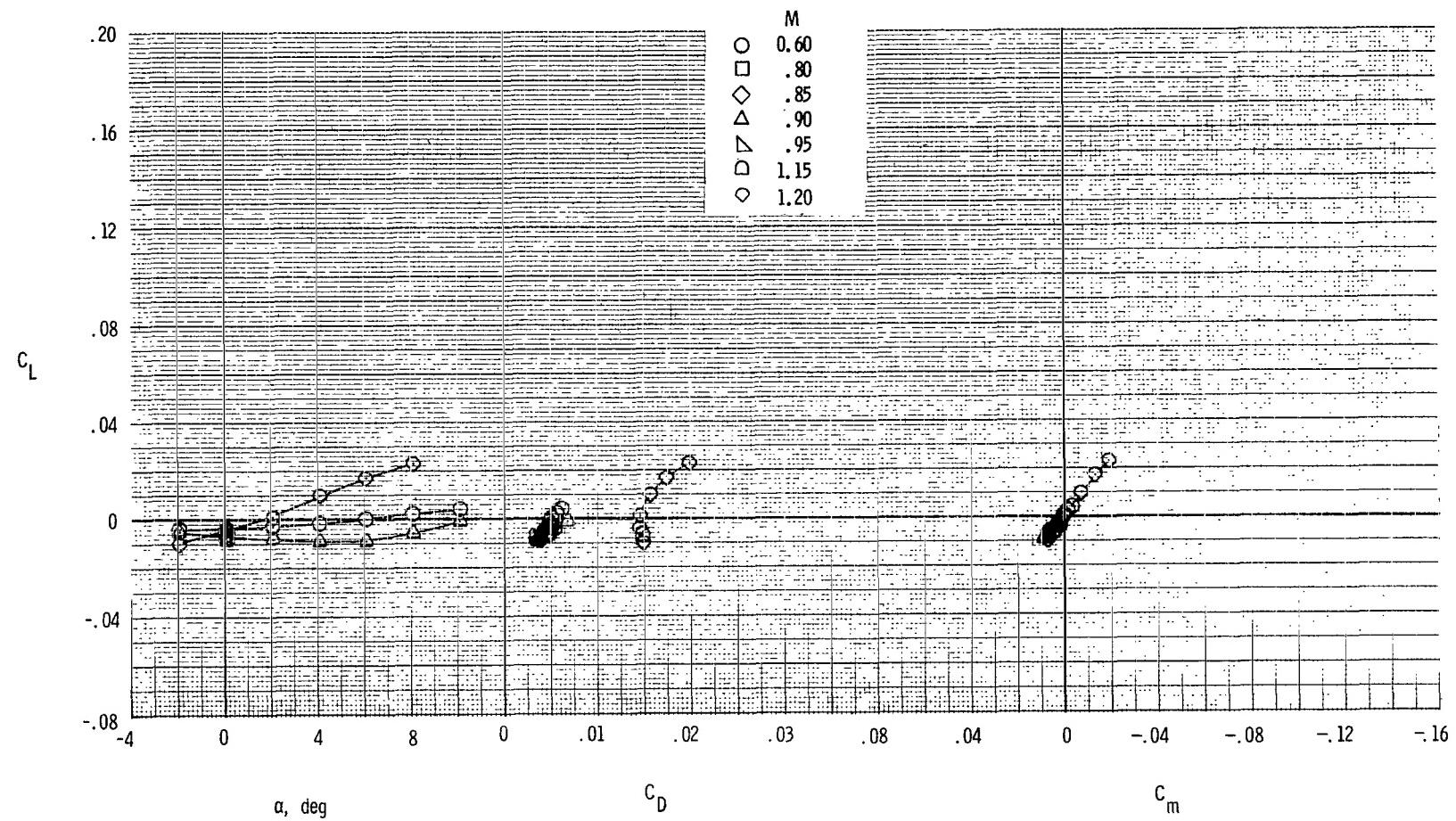
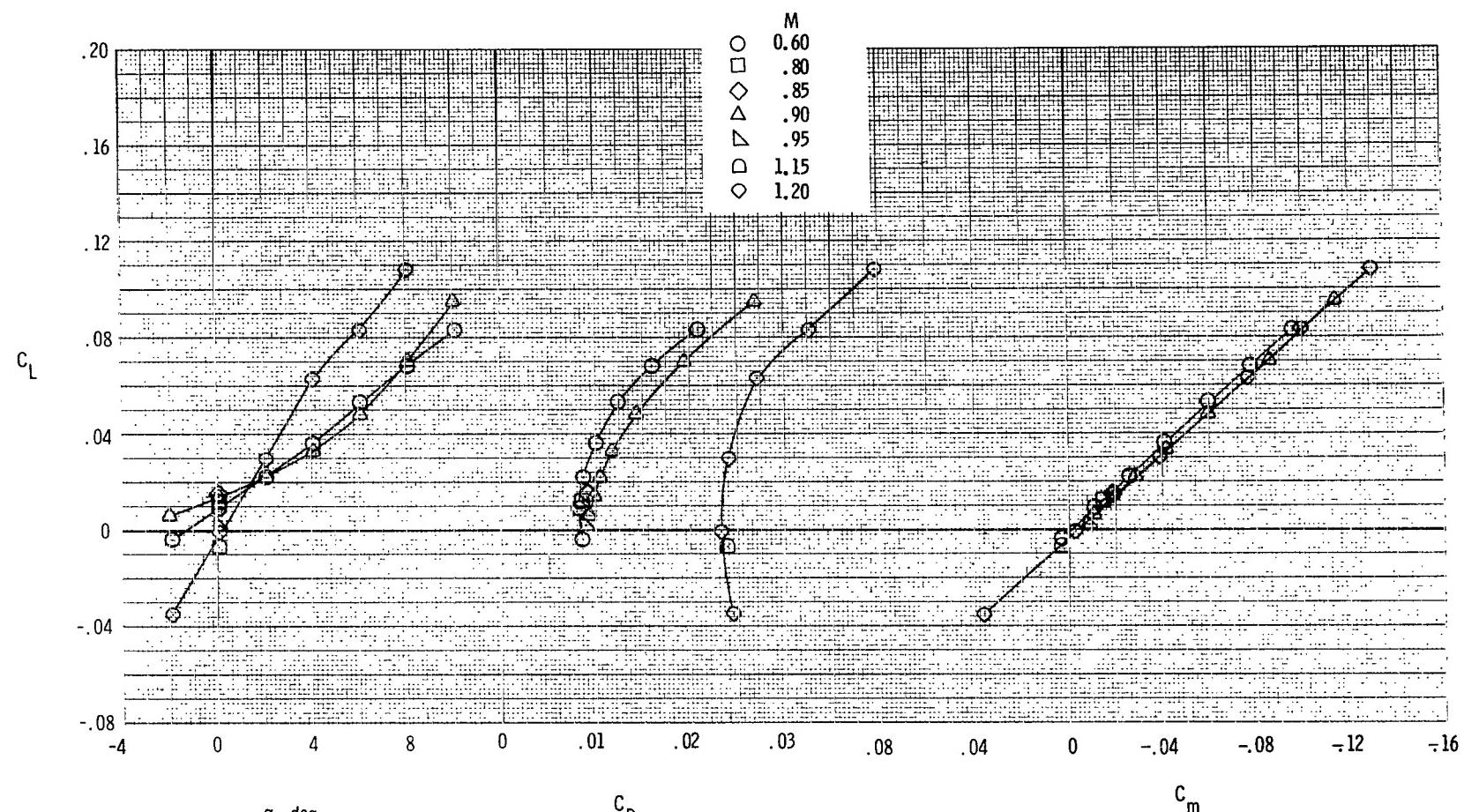
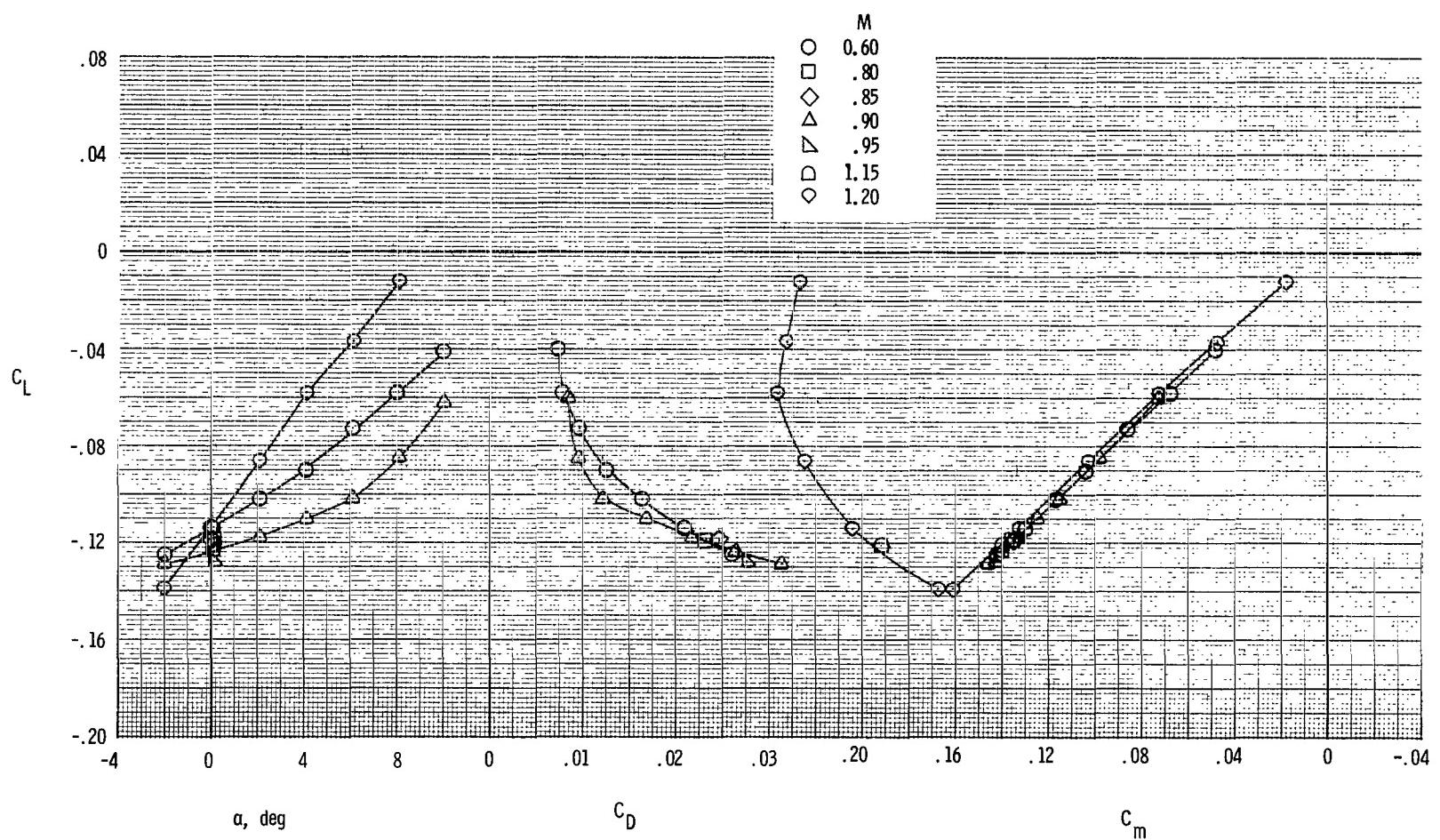


Figure 6.- Basic longitudinal aerodynamic characteristics at various Mach numbers for twin-engine tail interference afterbody model with jet off ( $p_{t,j}/p_\infty = 1.0$ ), dry power nozzles, booms off, and tails off.



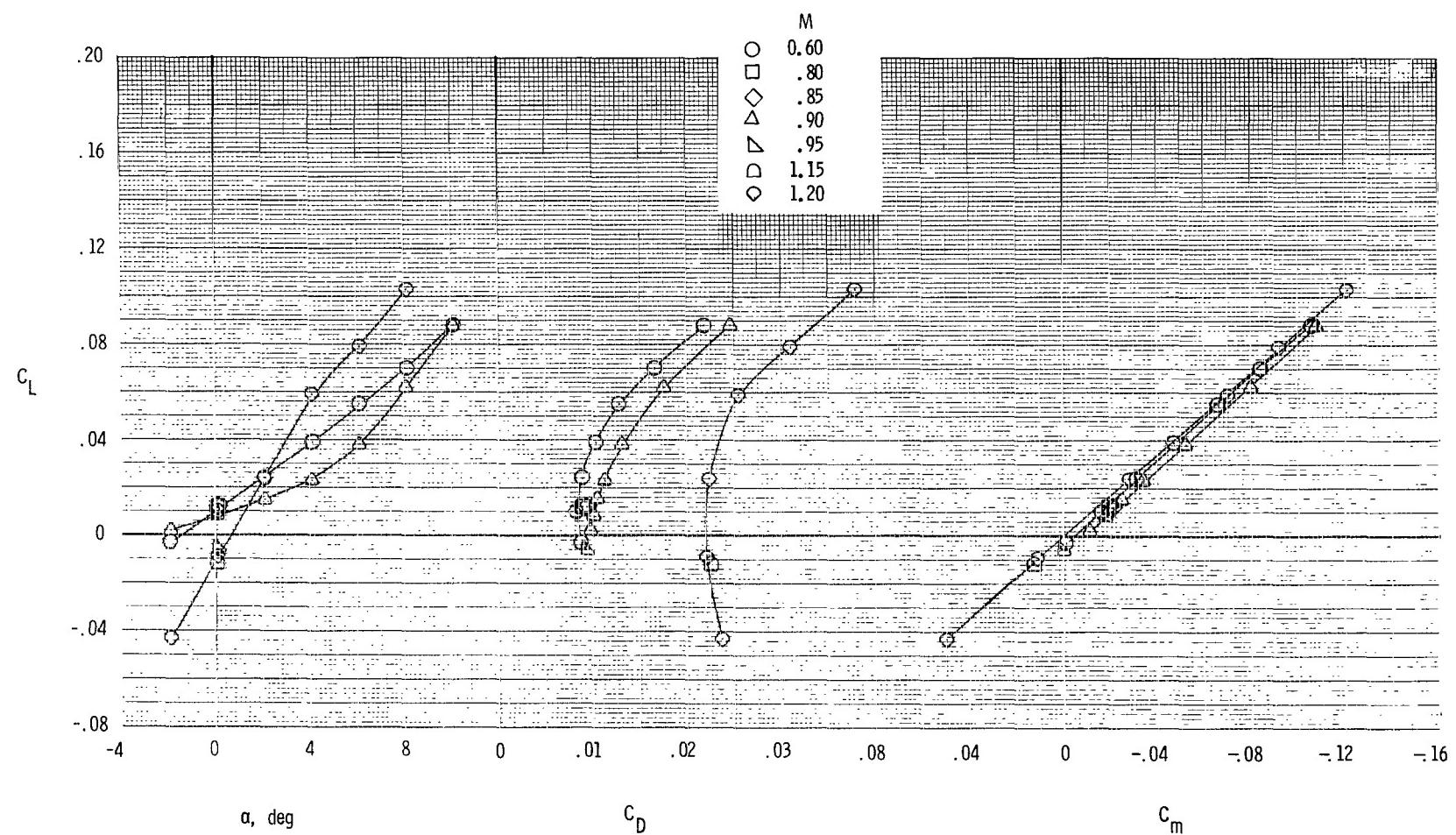
(a) Horizontal tails forward; vertical tails forward;  $\delta_h = 0^\circ$ .

Figure 7.- Basic longitudinal aerodynamic characteristics at various Mach numbers for twin-engine tail interference afterbody model with jet off ( $p_{t,j}/p_\infty = 1.0$ ), dry power nozzles, booms off, and twin vertical tails.



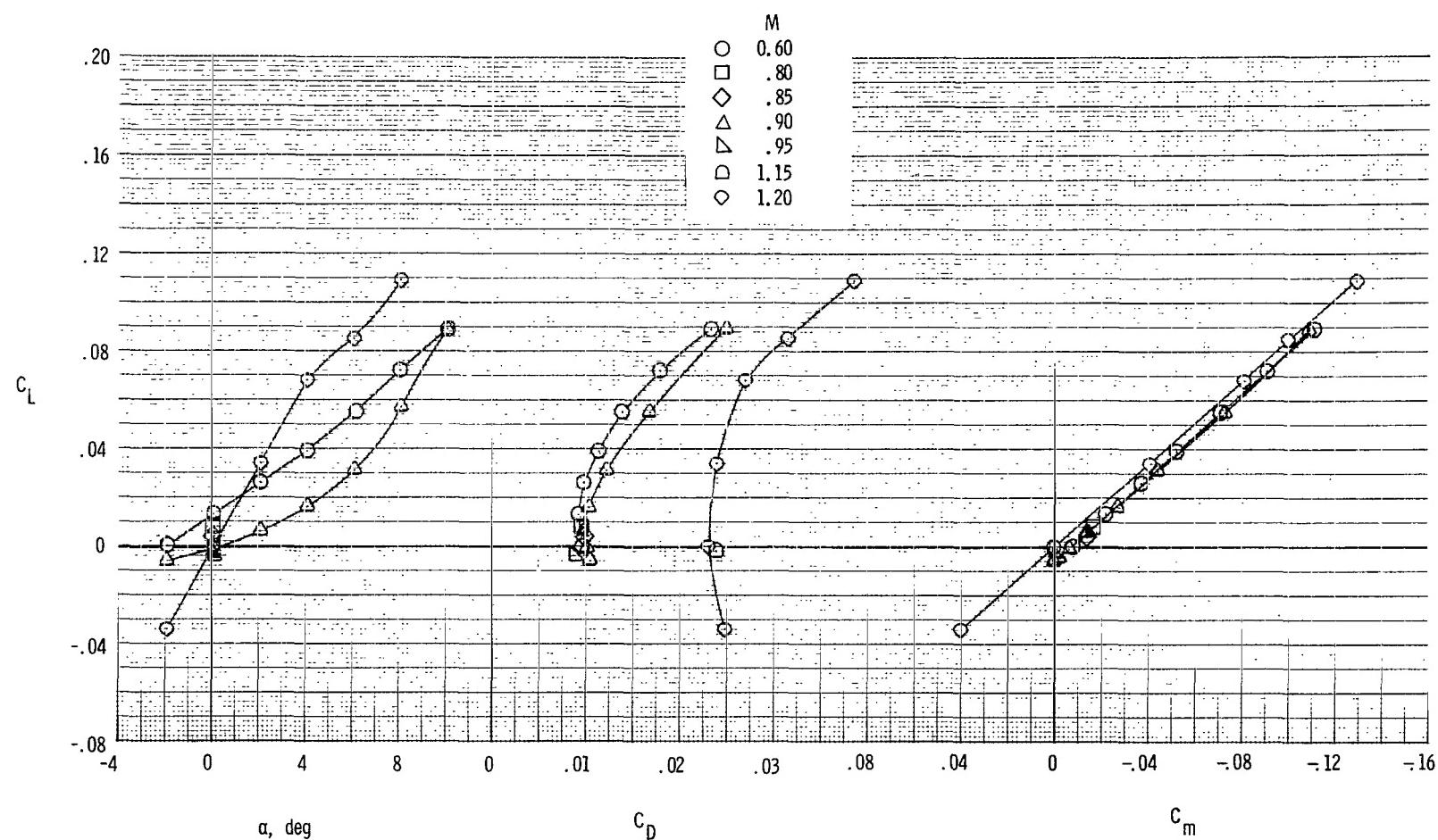
(b) Horizontal tails forward; vertical tails forward;  $\delta_h = -10^\circ$ .

Figure 7.- Continued.



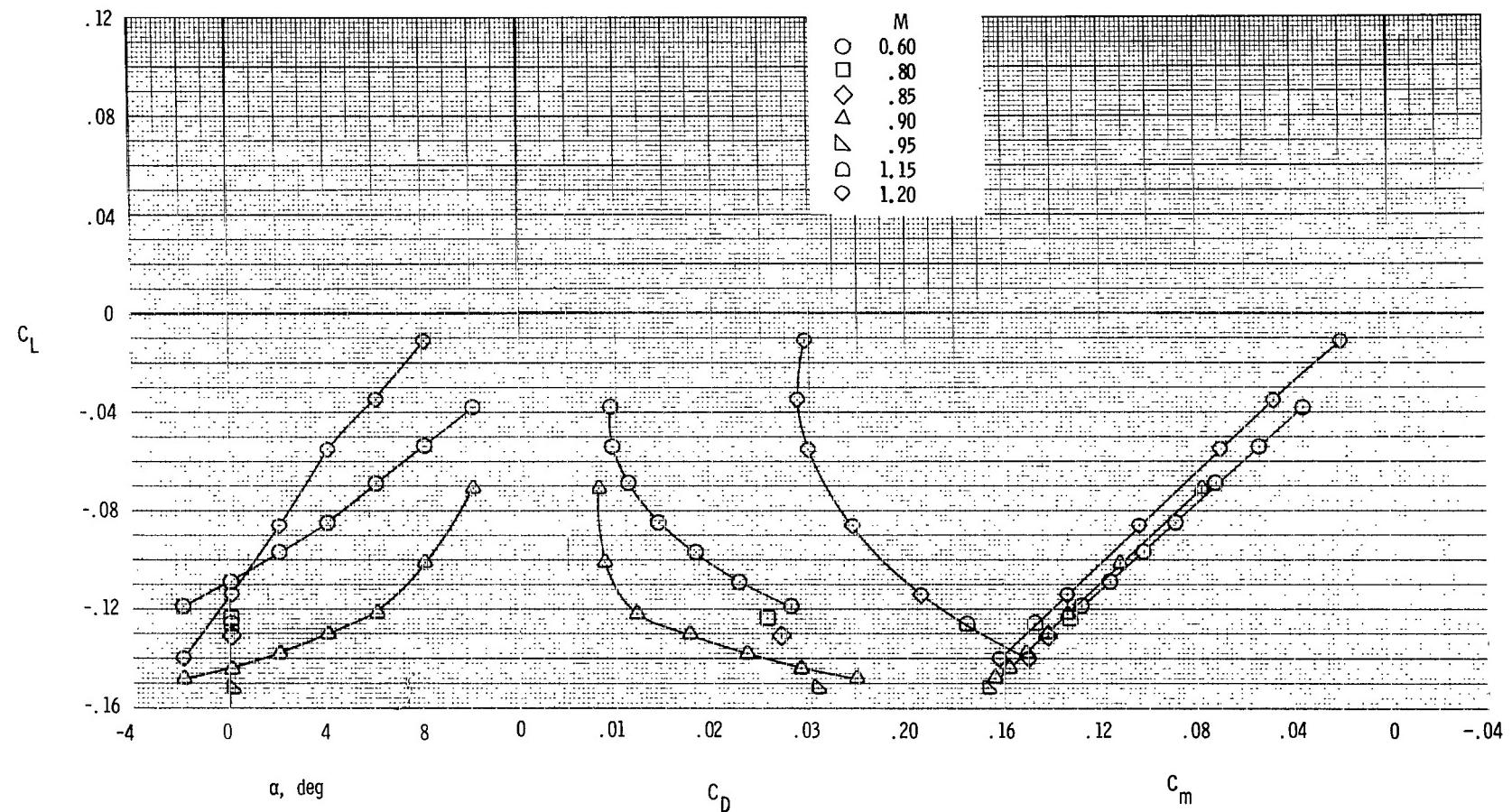
(c) Horizontal tails forward; vertical tails mid;  $\delta_h = 0^\circ$ .

Figure 7.- Continued.



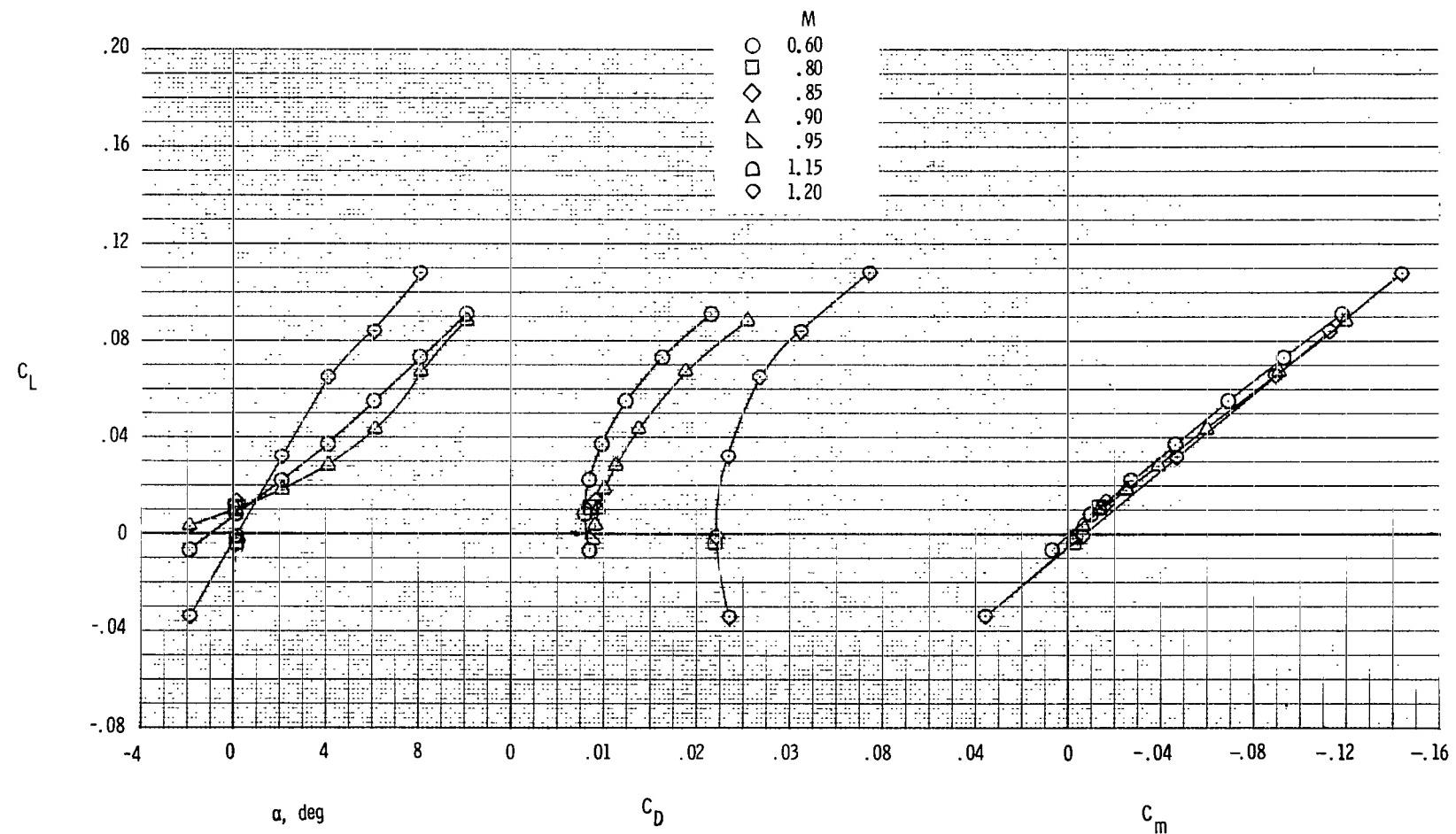
(d) Horizontal tails forward; vertical tails aft;  $\delta_h = 0^\circ$ .

Figure 7.- Continued.



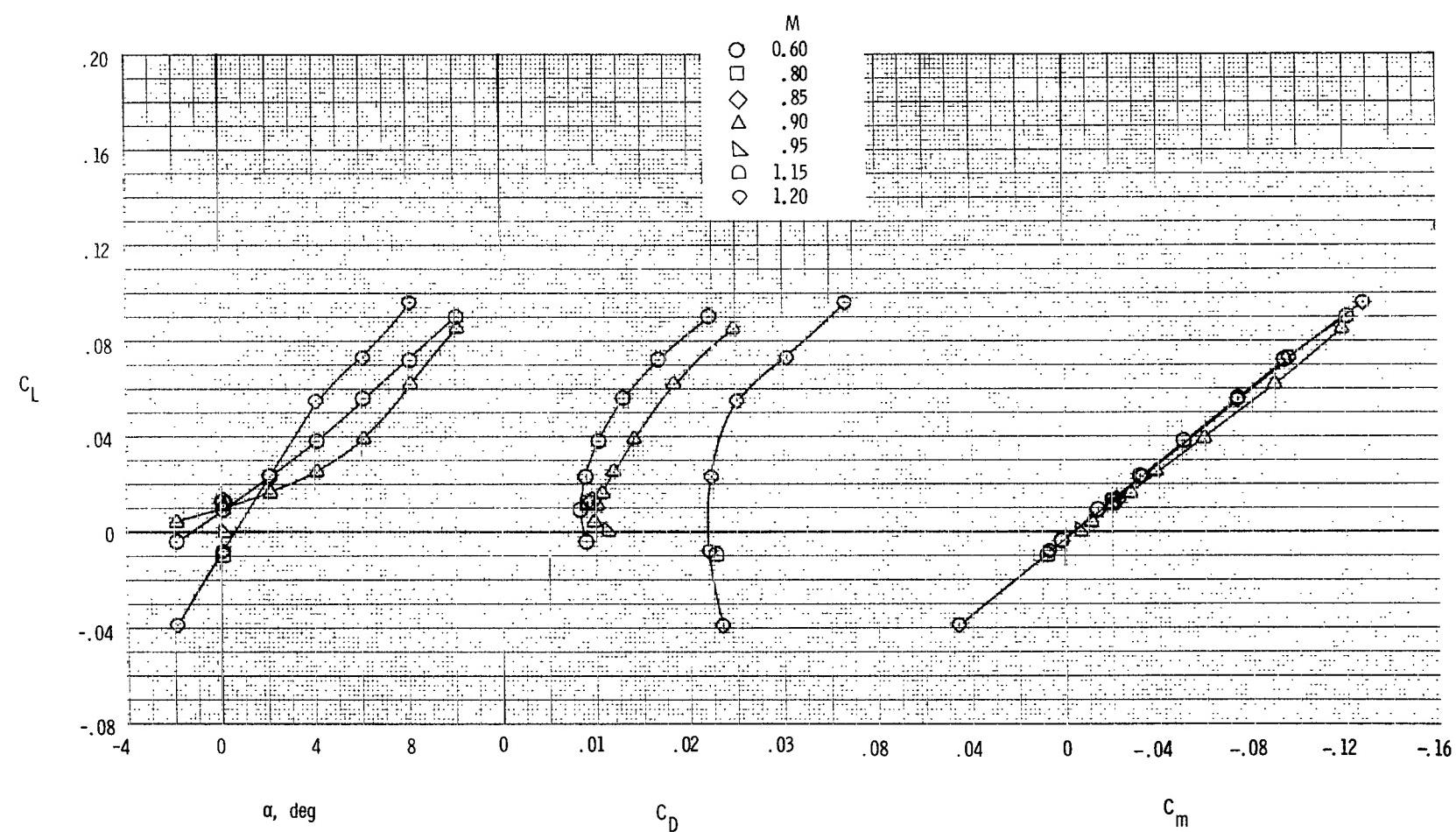
(e) Horizontal tails forward; vertical tails aft;  $\delta_h = -10^\circ$ .

Figure 7.- Continued.



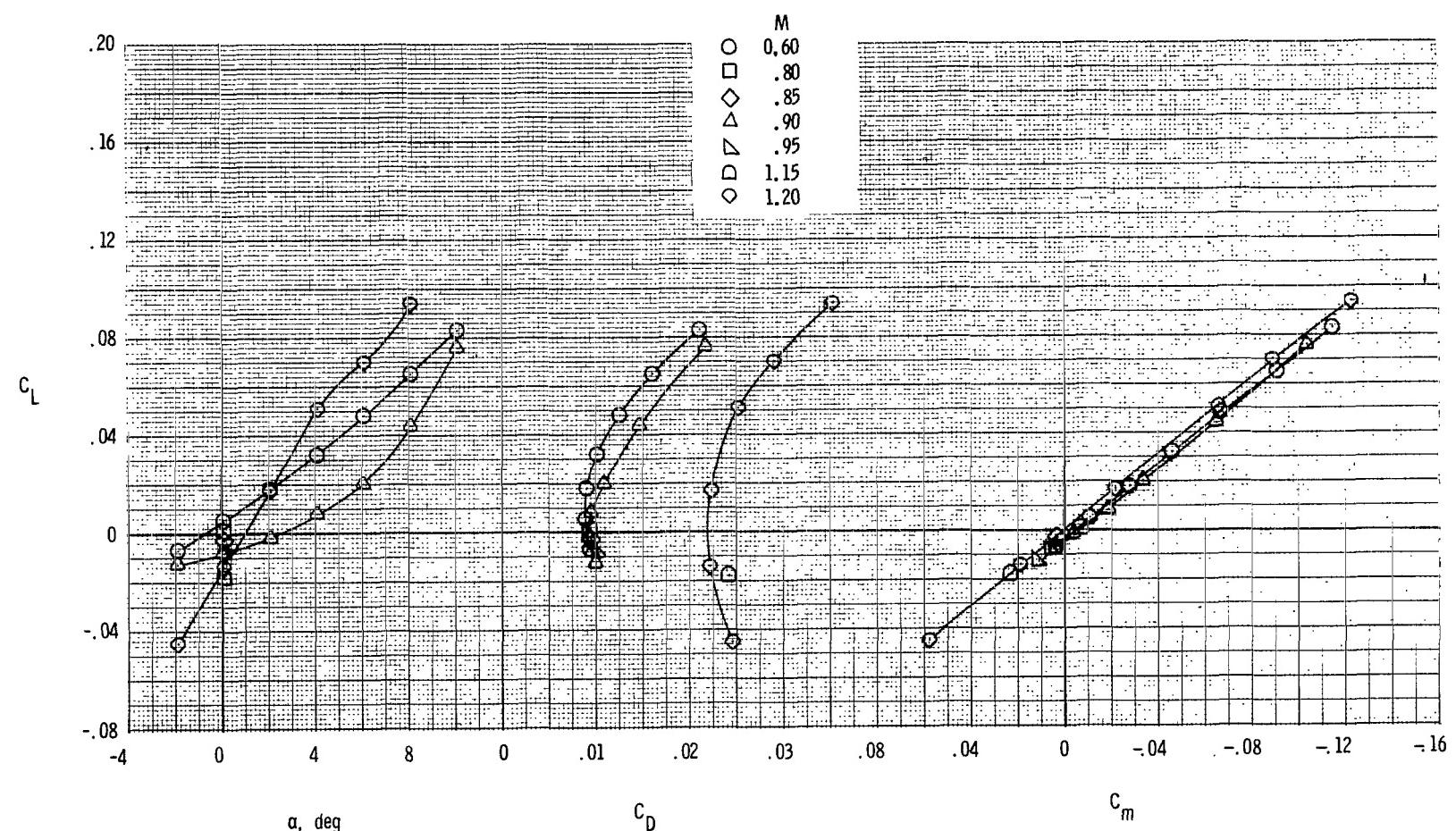
(f) Horizontal tails mid; vertical tails forward;  $\delta_h = 0^\circ$ .

Figure 7.- Continued.



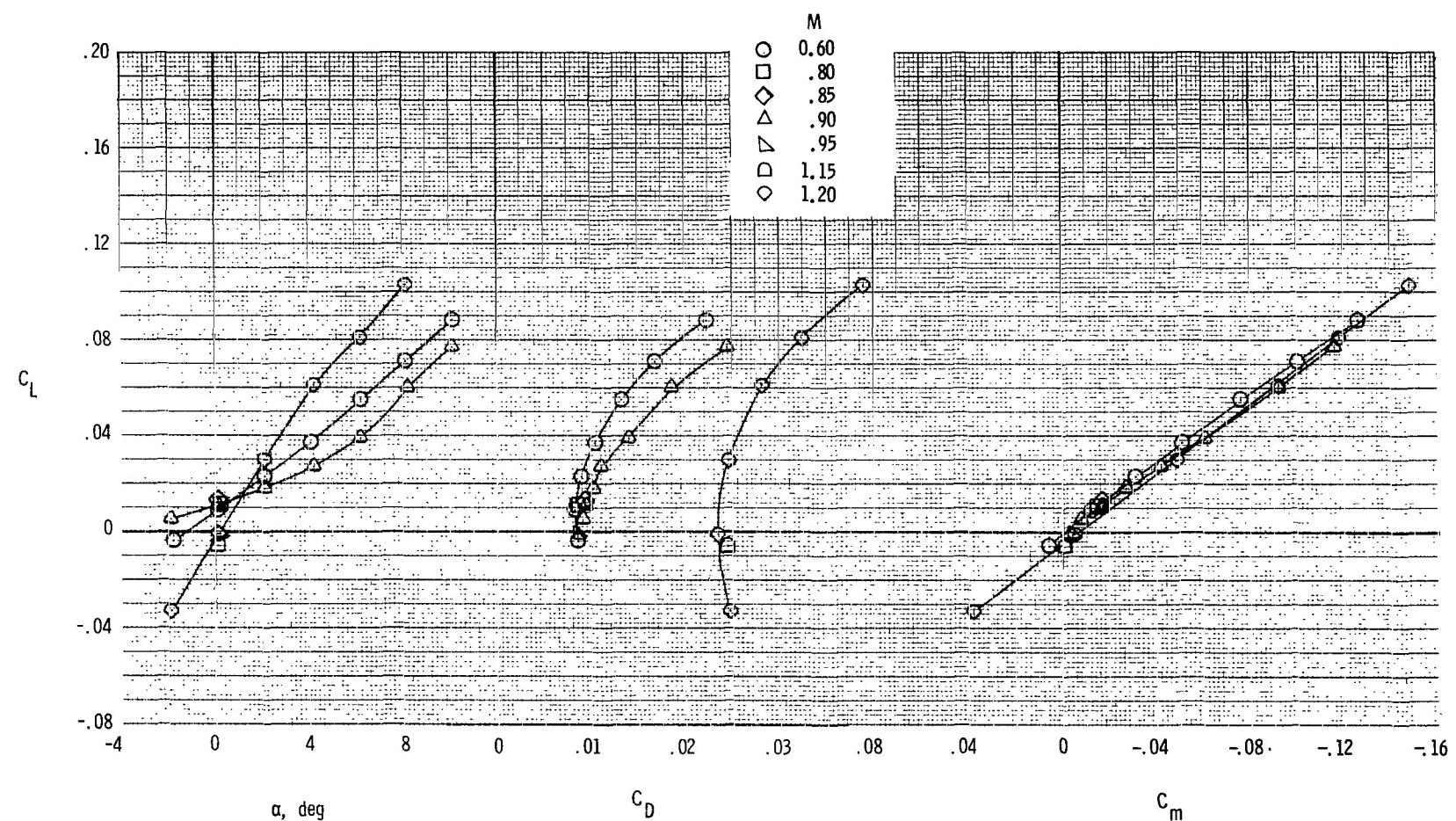
(g) Horizontal tails mid; vertical tails mid;  $\delta_h = 0^\circ$ .

Figure 7.- Continued.



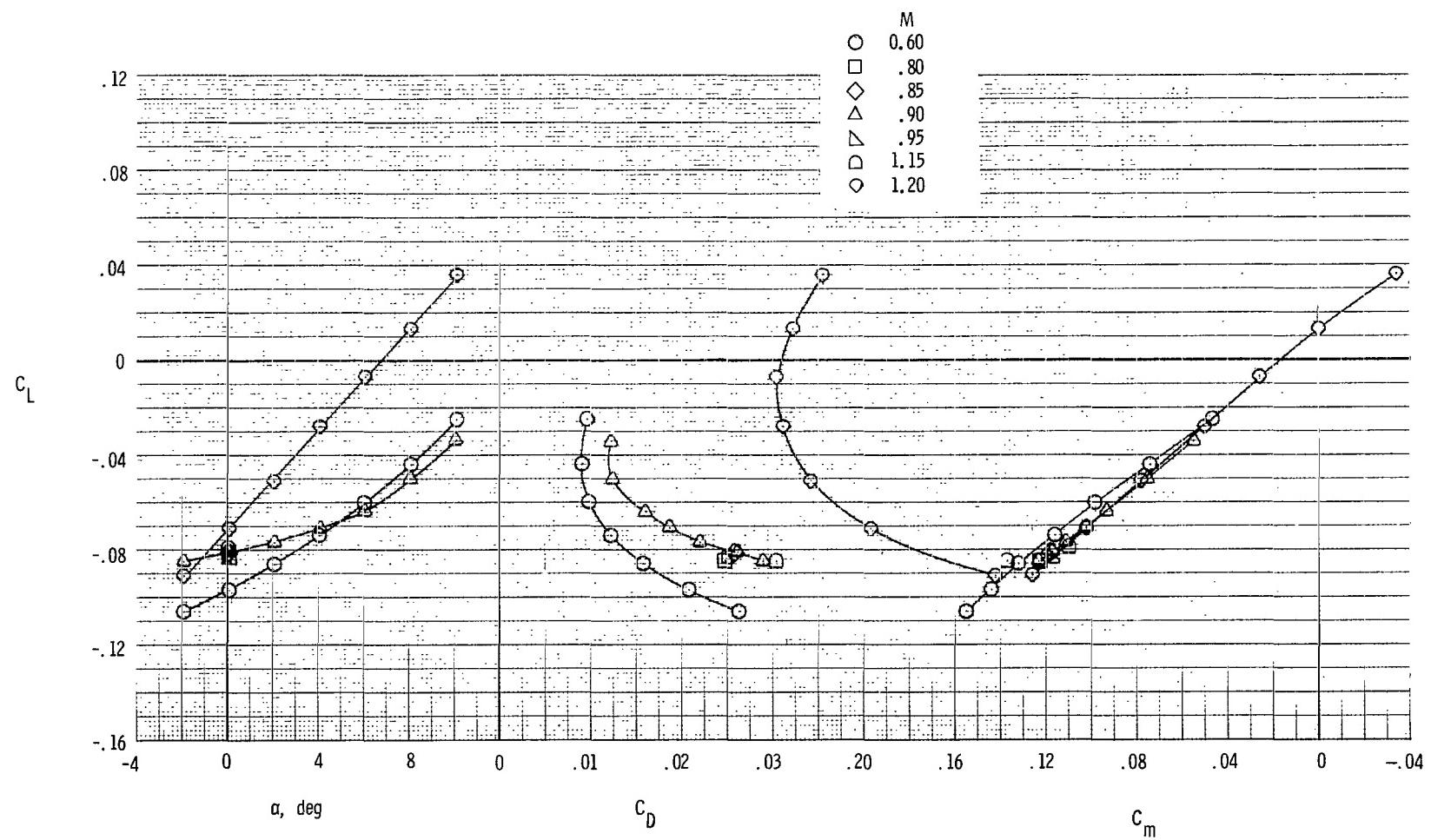
(h) Horizontal tail mid; vertical tails aft;  $\delta_h = 0^\circ$ .

Figure 7.- Continued.



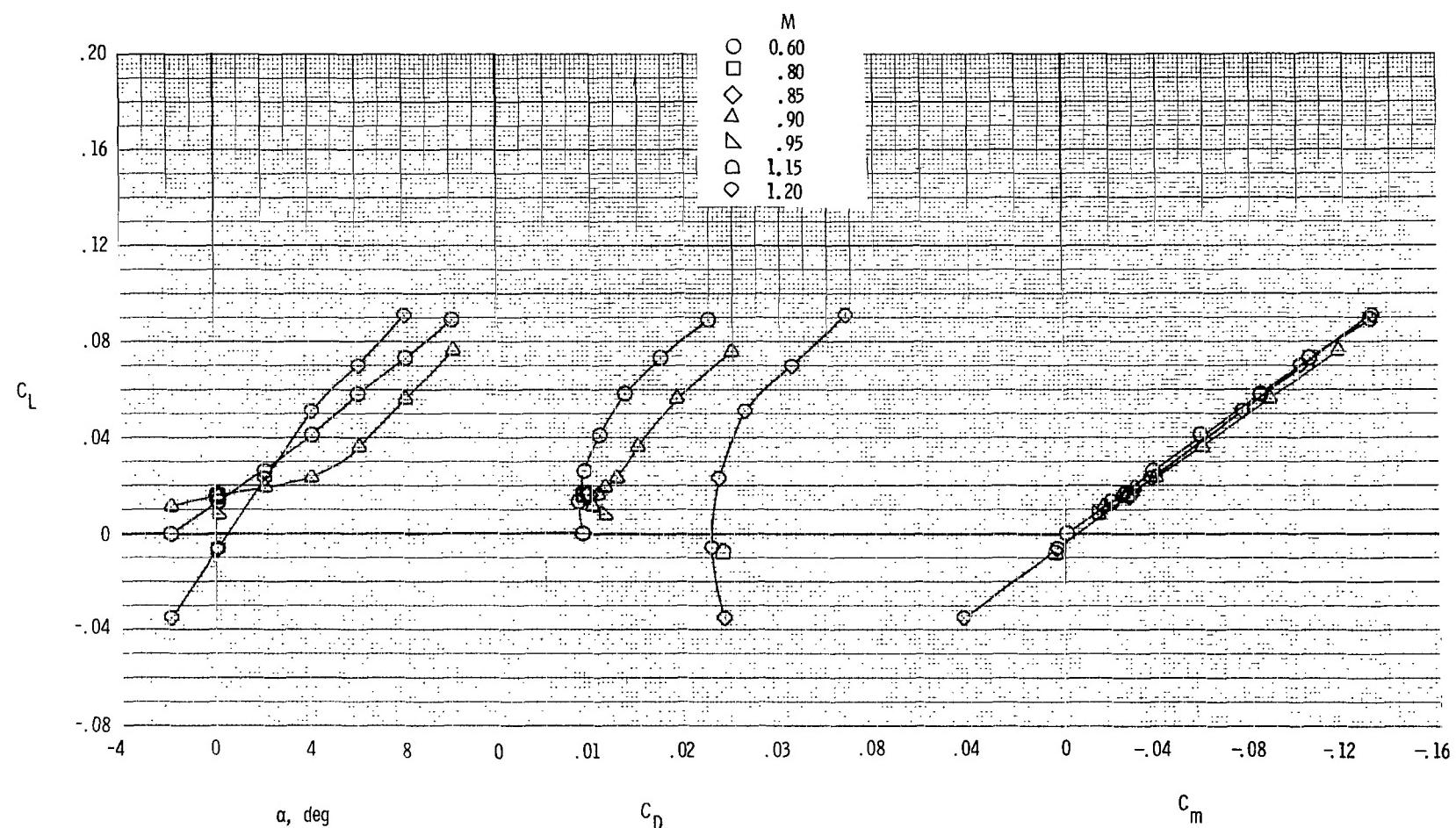
(i) Horizontal tails aft; vertical tails forward;  $\delta_h = 0^\circ$ .

Figure 7.- Continued.



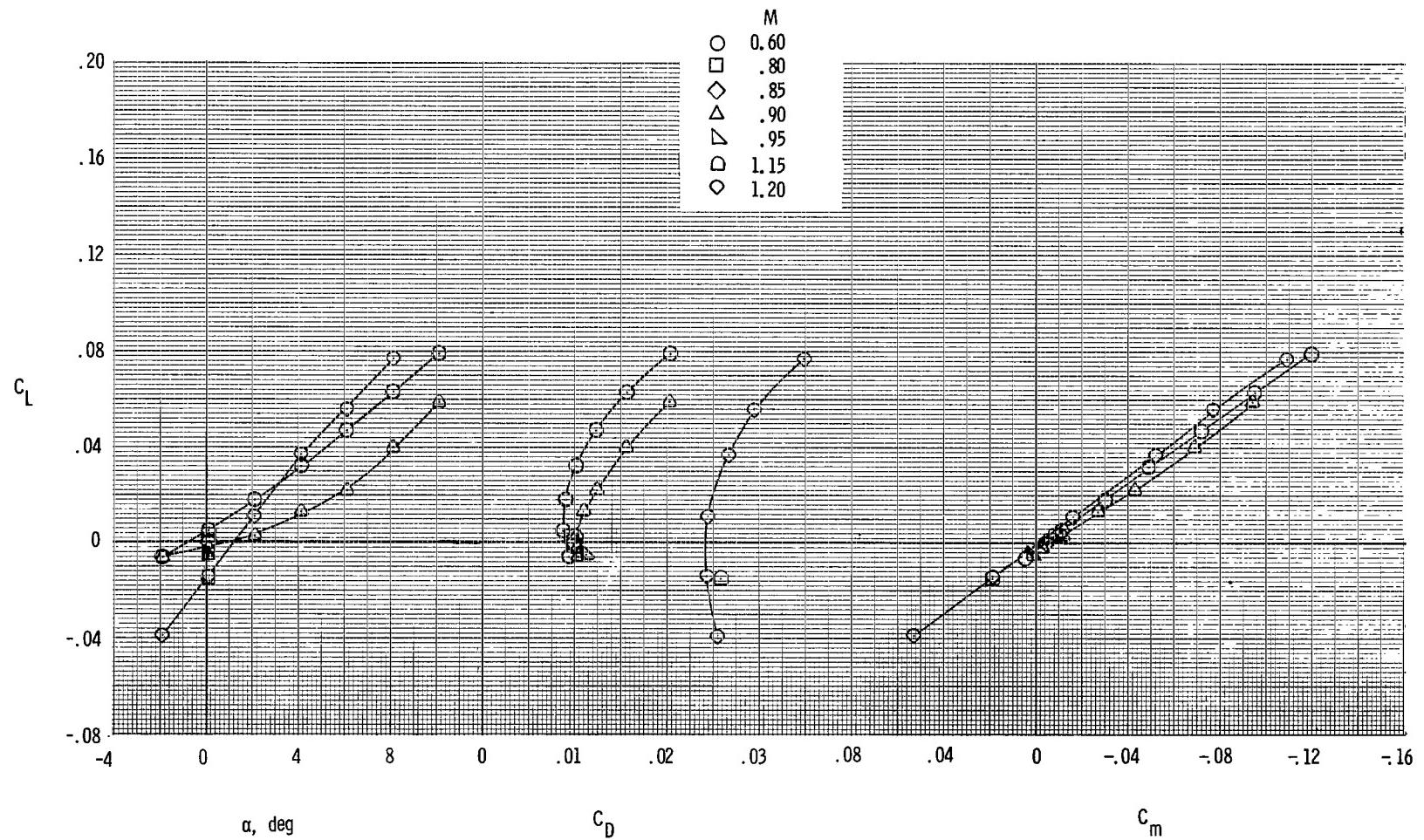
(j) Horizontal tails aft; vertical tails forward;  $\delta_h = -10^\circ$ .

Figure 7.- Continued.



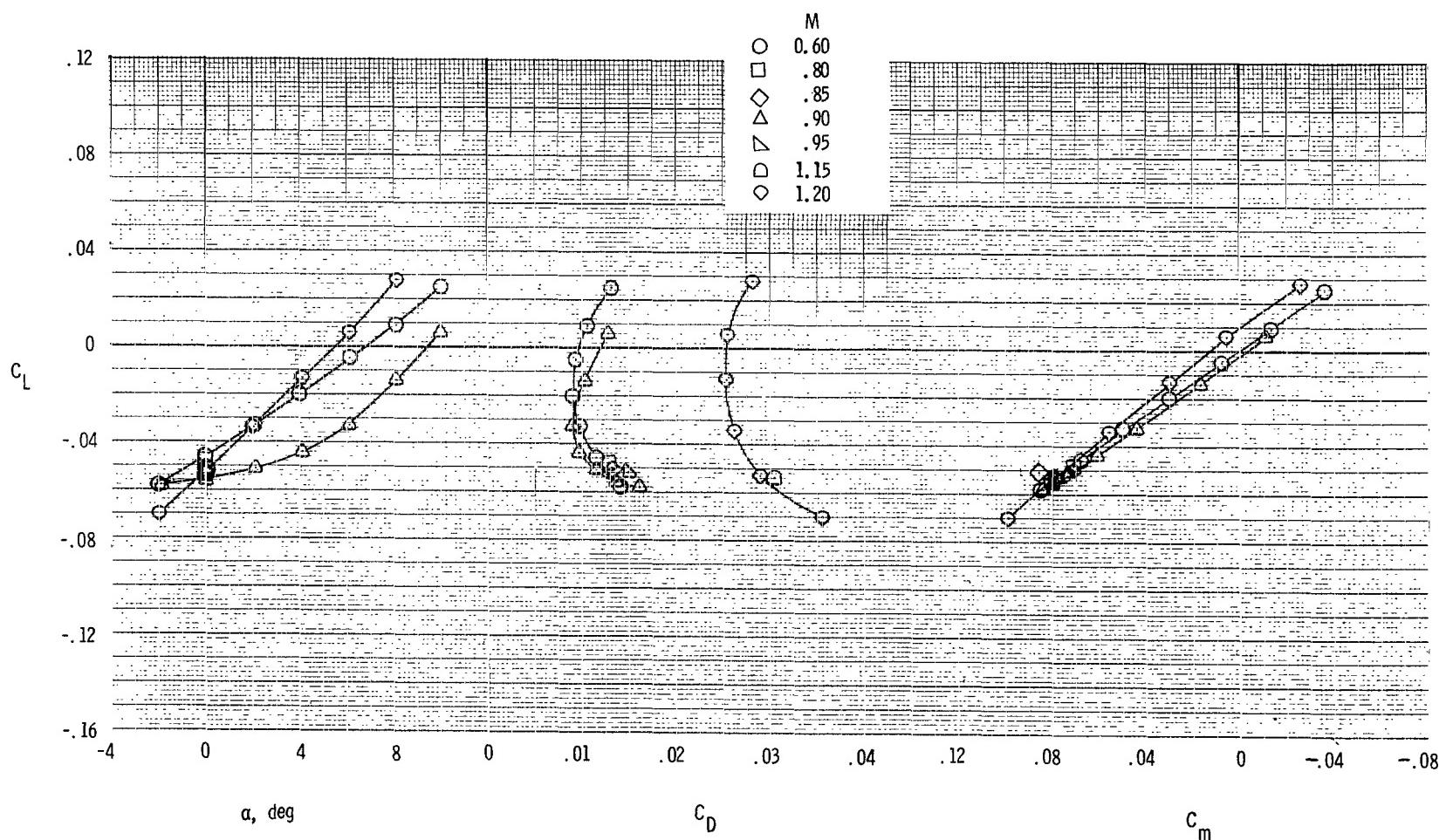
(k) Horizontal tails aft; vertical tails mid;  $\delta_h = 0^\circ$ .

Figure 7.- Continued.



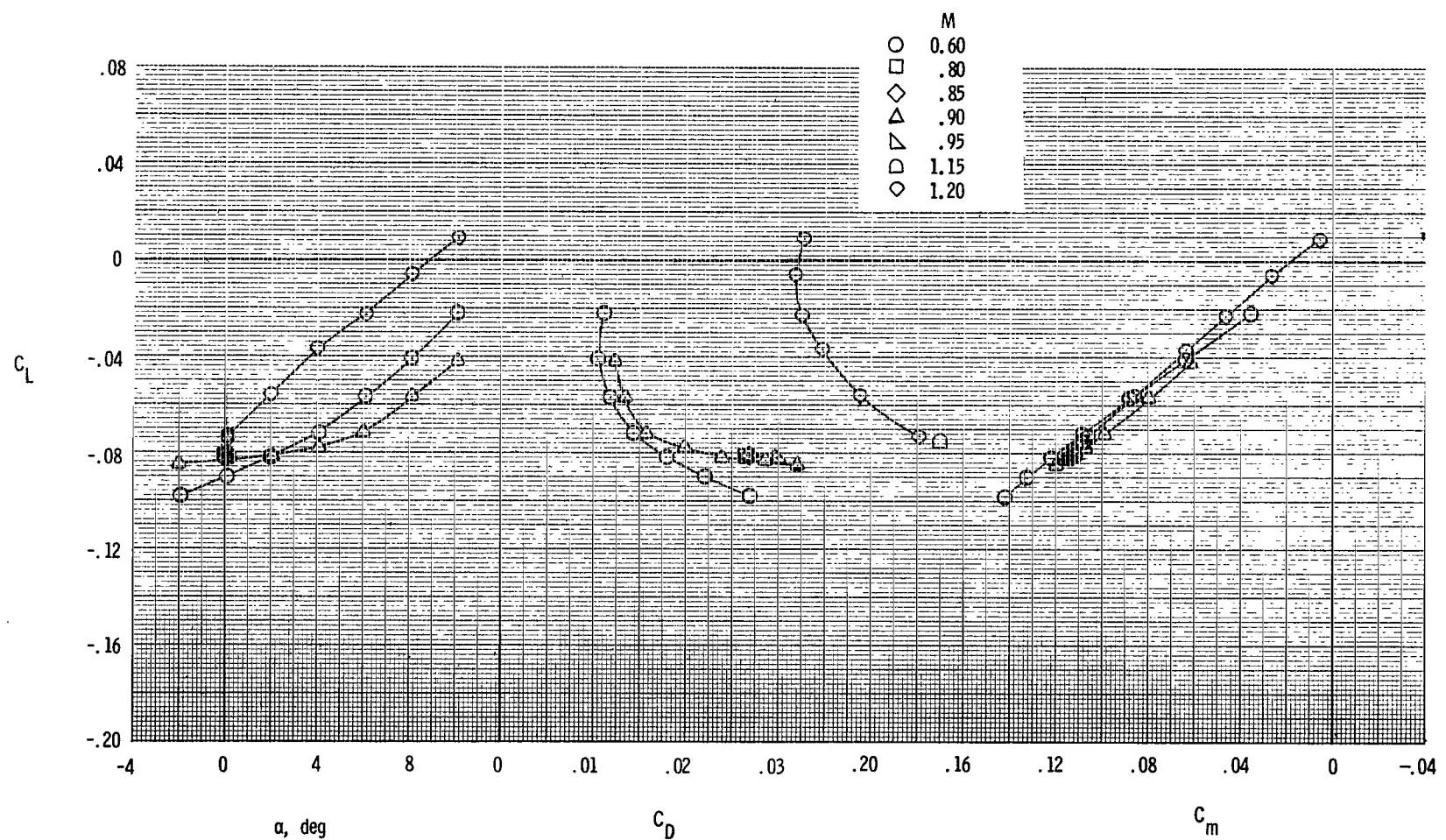
(1) Horizontal tails aft; vertical tails aft;  $\delta_h = 0^\circ$ .

Figure 7.- Continued.



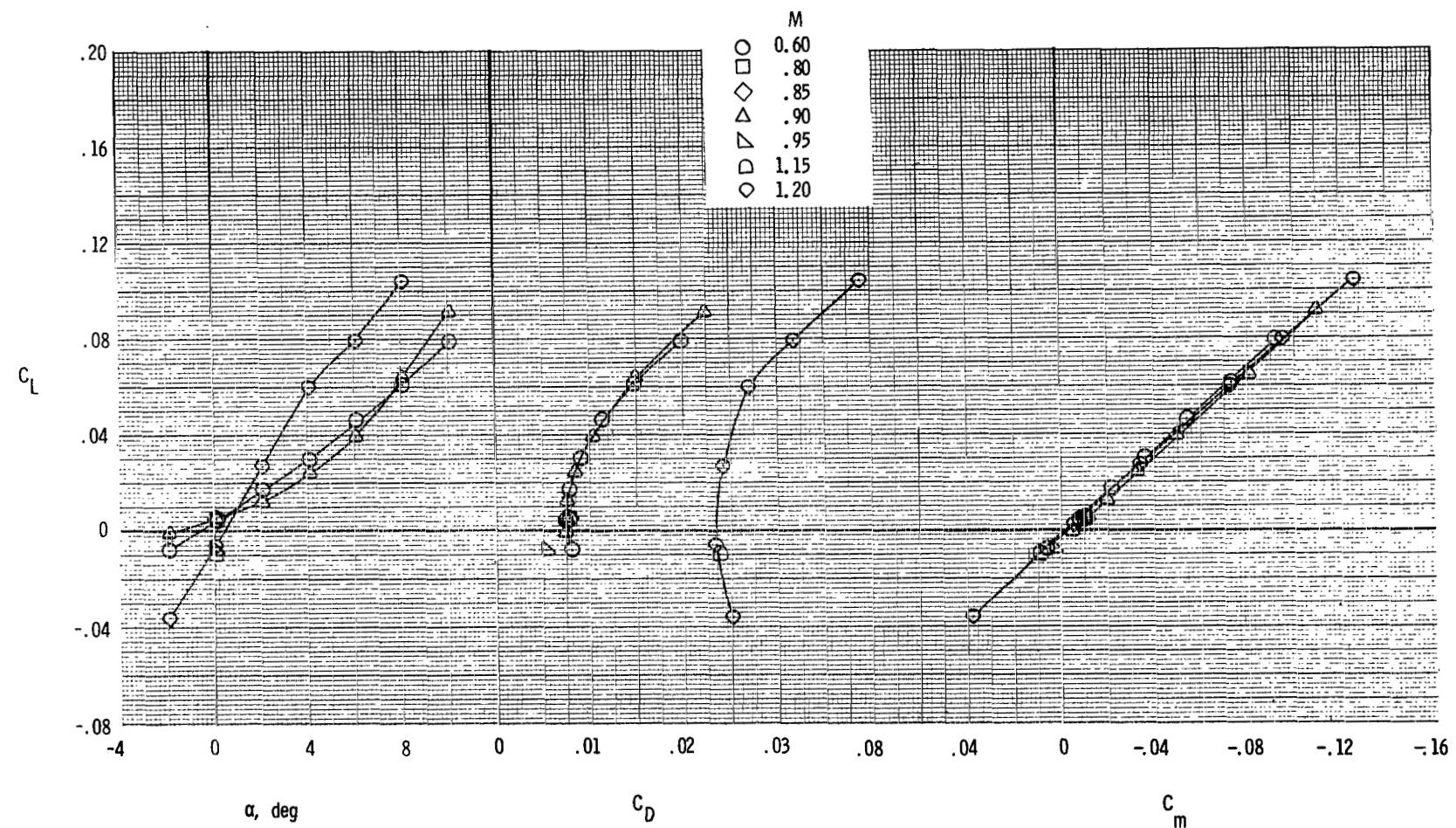
(m) Horizontal tails aft; vertical tails aft;  $\delta_h = -5^\circ$ .

Figure 7.- Continued.



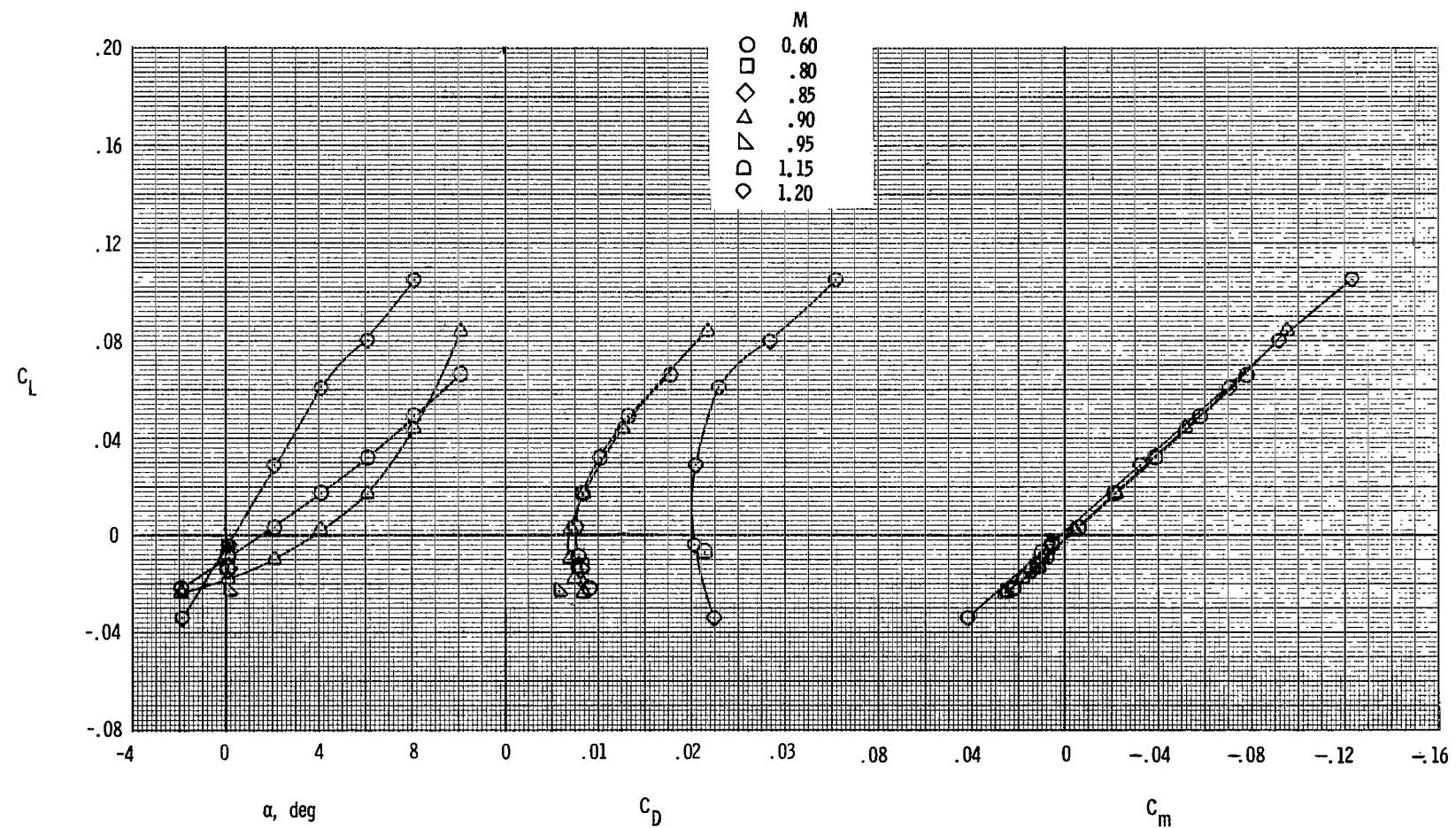
(n) Horizontal tails aft; vertical tails aft;  $\delta_h = -10^\circ$ .

Figure 7.- Concluded.



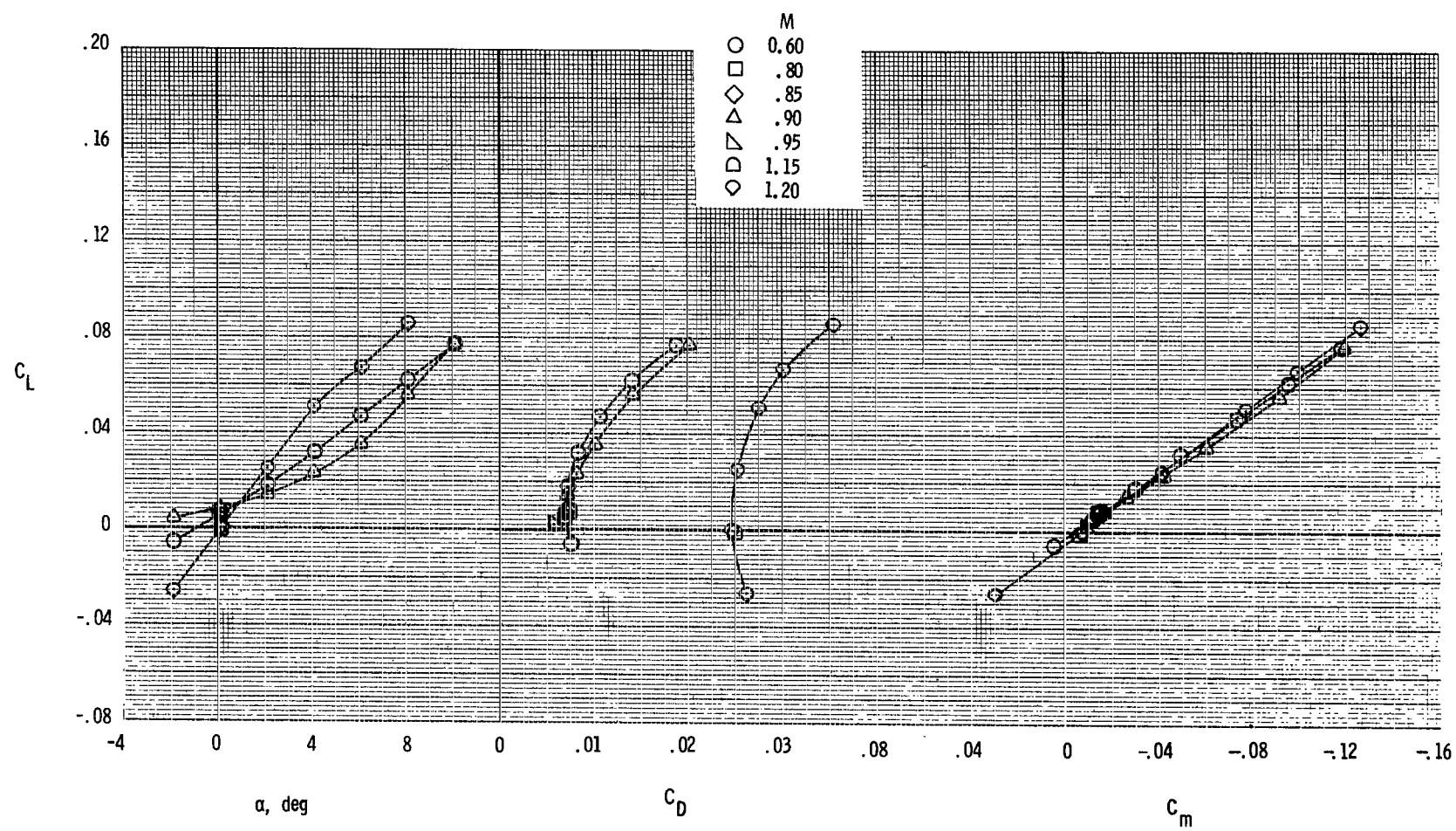
(a) Horizontal tails forward; vertical tail forward;  $\delta_h = 0^\circ$ .

Figure 8.- Basic longitudinal aerodynamic characteristics at various Mach numbers for twin-engine tail interference afterbody model with jet off ( $p_{t,j}/p_\infty = 1.0$ ), dry power nozzles, booms off, and single vertical tail.



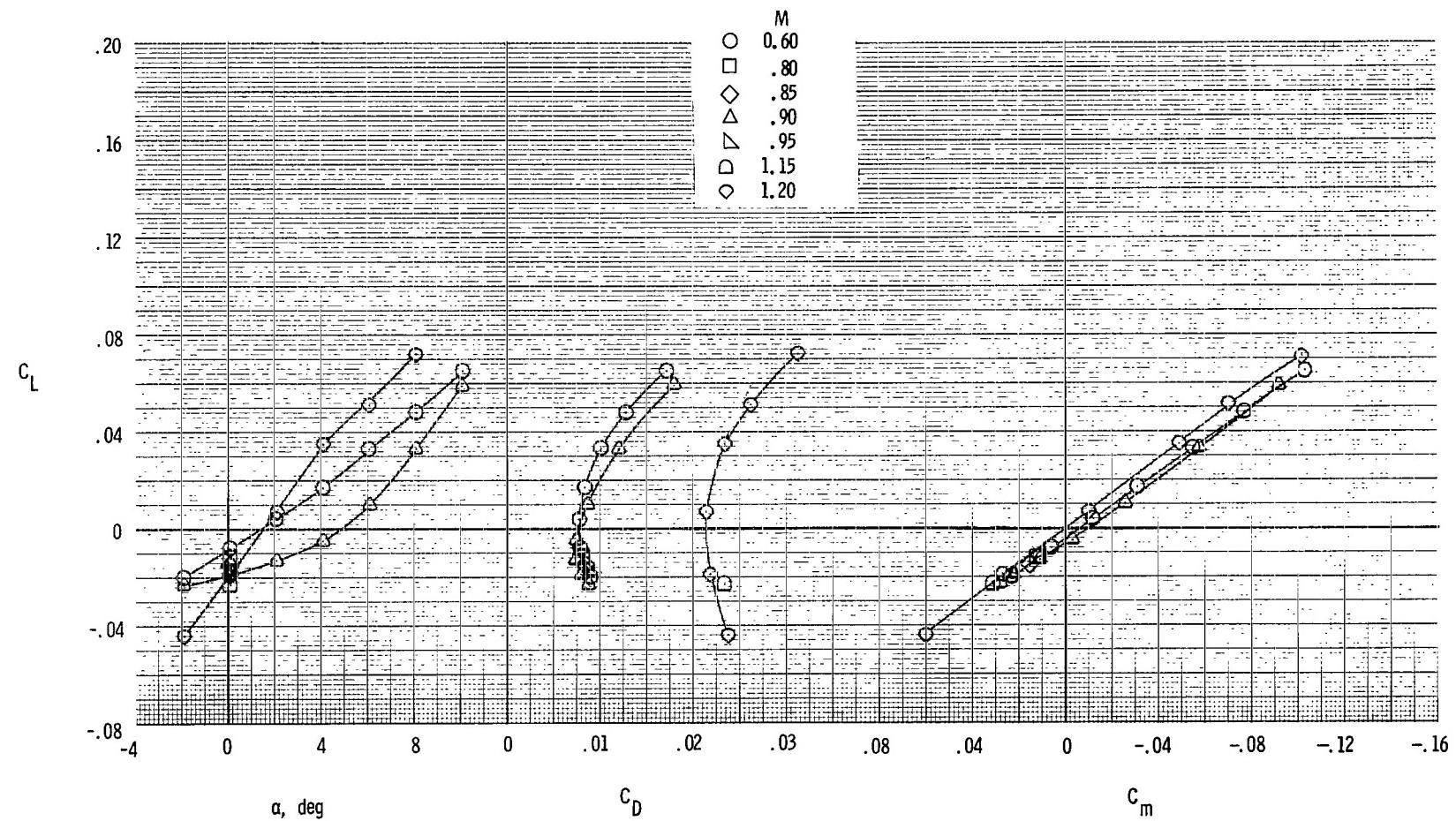
(b) Horizontal tails forward; vertical tail aft;  $\delta_h = 0^\circ$ .

Figure 8.- Continued.



(c) Horizontal tails aft; vertical tail forward;  $\delta_h = 0^\circ$ .

Figure 8.- Continued.



(d) Horizontal tails aft; vertical tail aft;  $\delta_h = 0^\circ$ .

Figure 8.- Concluded.

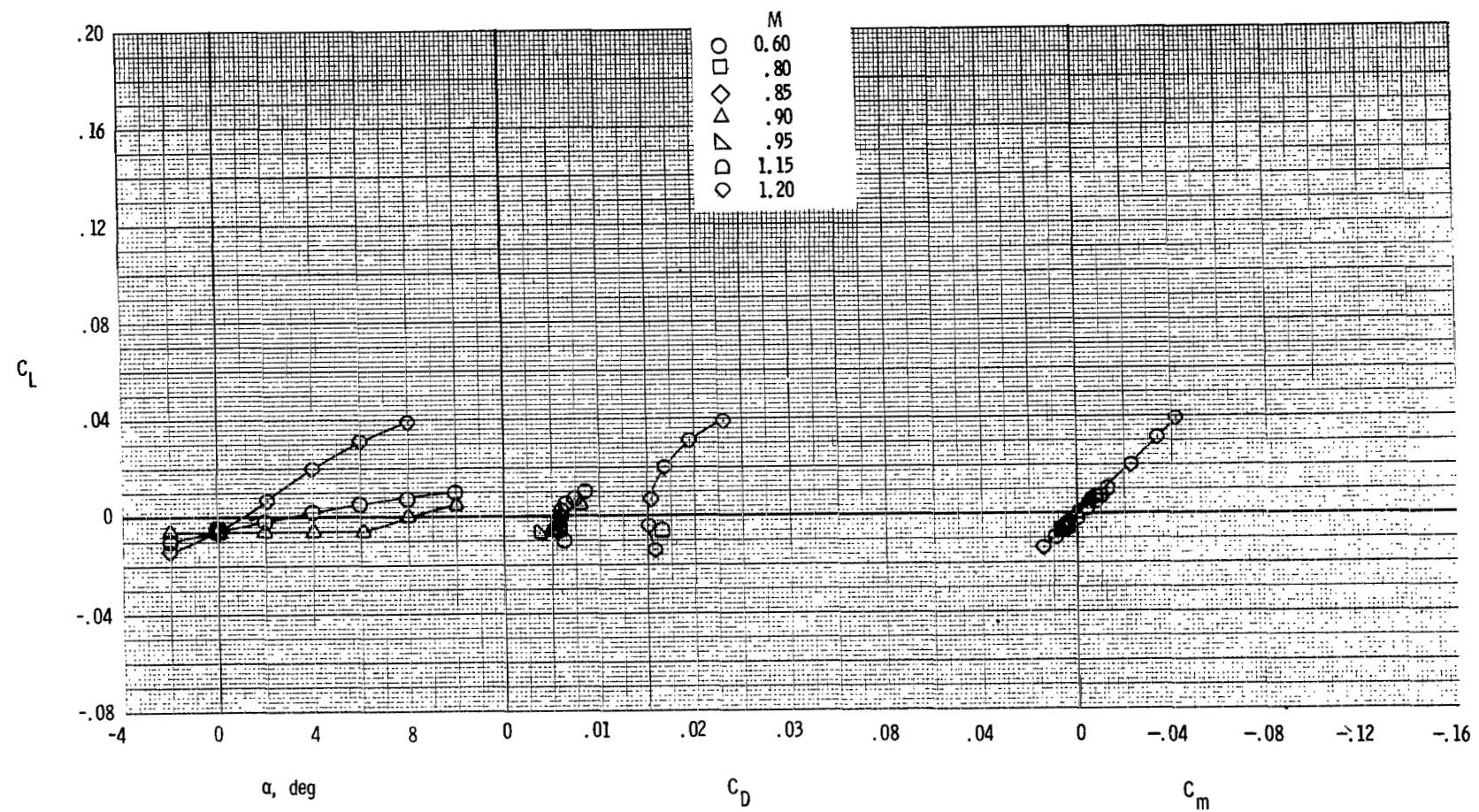
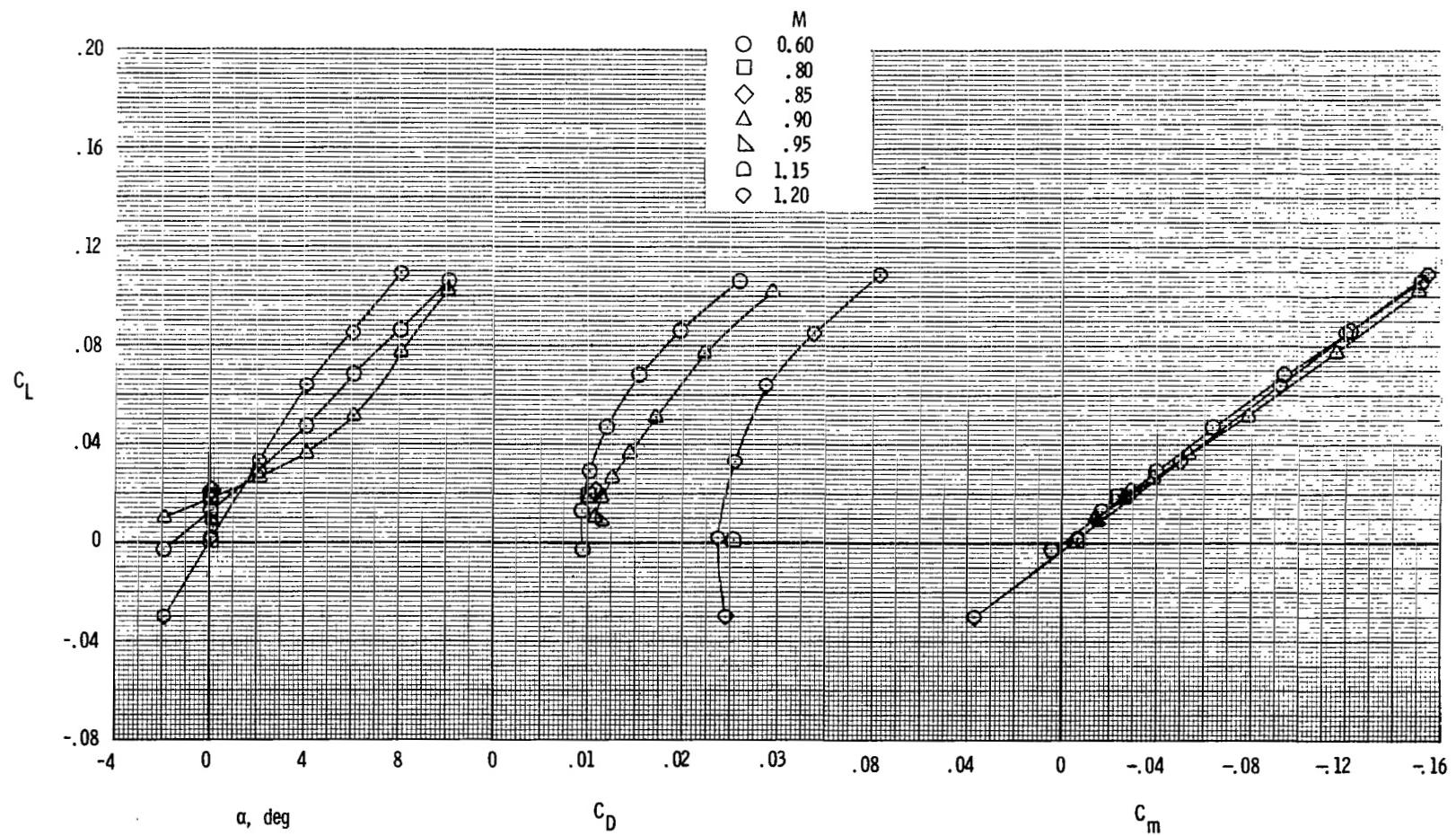
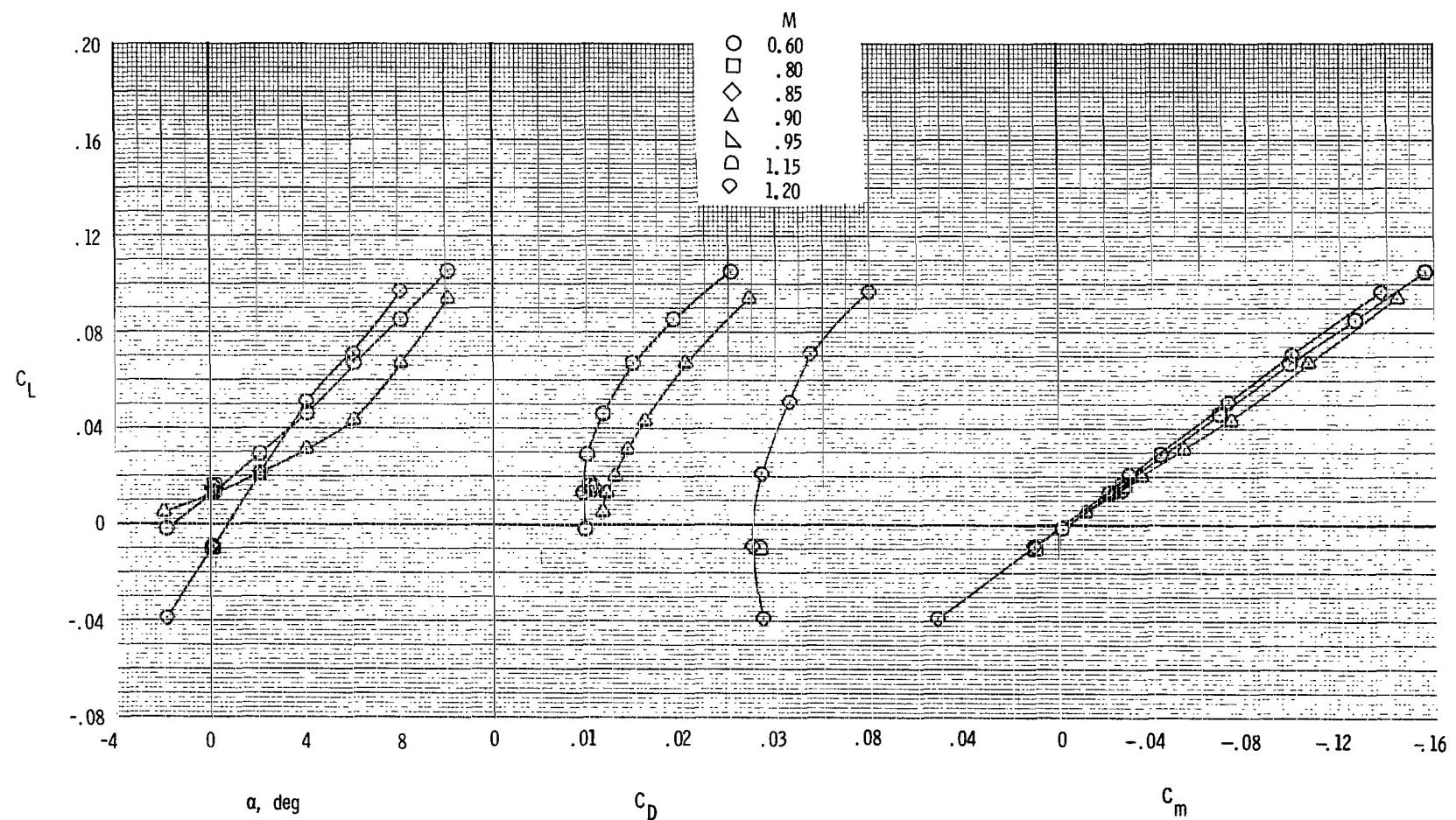


Figure 9.- Basic longitudinal aerodynamic characteristics at various Mach numbers for twin-engine tail interference afterbody model with jet off ( $p_{t,j}/p_\infty = 1.0$ ), dry power nozzles, booms on, and tails off.



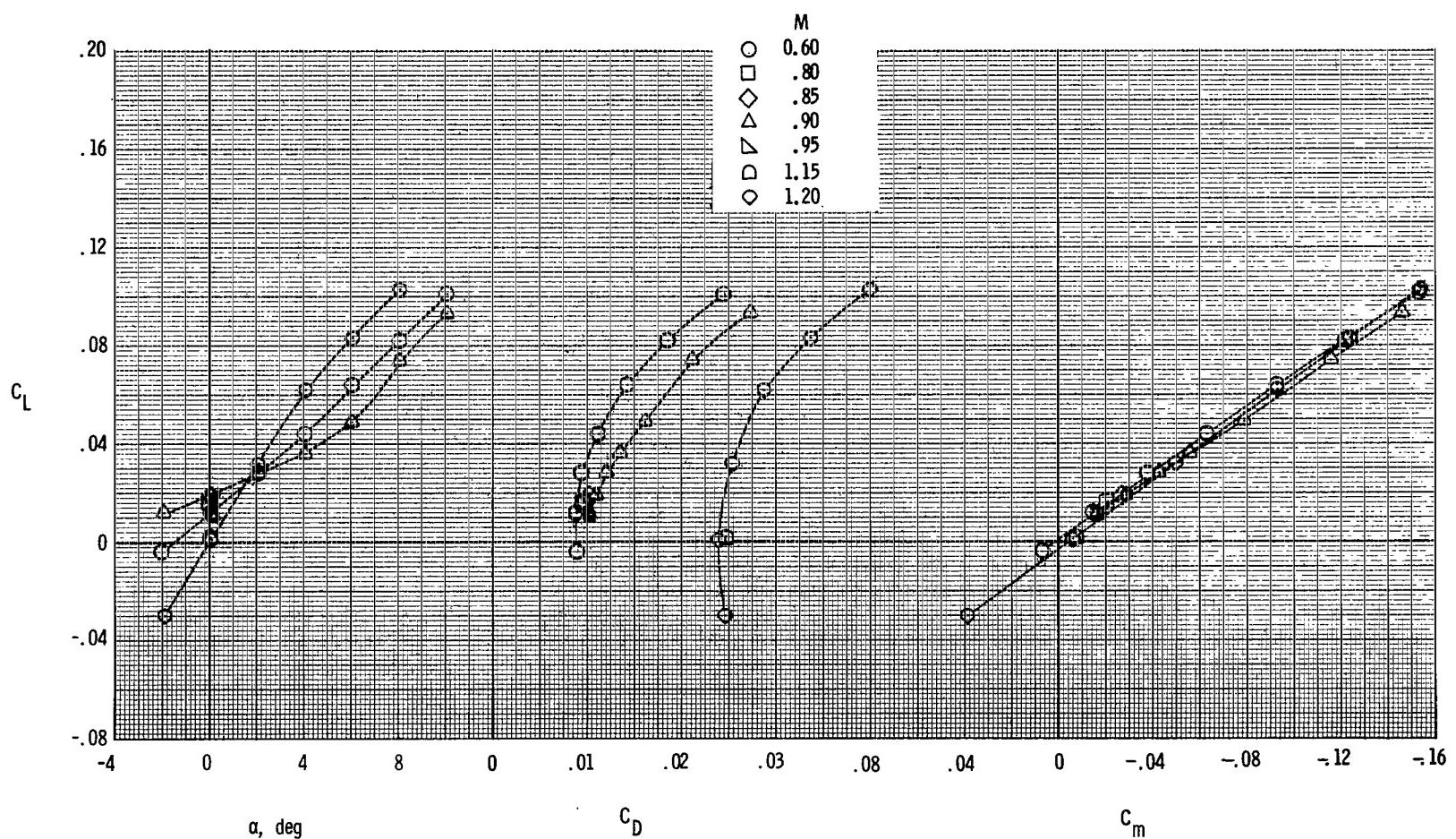
(a) Horizontal tails forward on boom; vertical tails forward on boom;  $\delta_h = 0^\circ$ .

Figure 10.- Basic longitudinal aerodynamic characteristics at various Mach numbers for twin-engine tail interference afterbody model with jet off ( $p_{t,j}/p_\infty = 1.0$ ), dry power nozzles, booms on, and twin vertical tails.



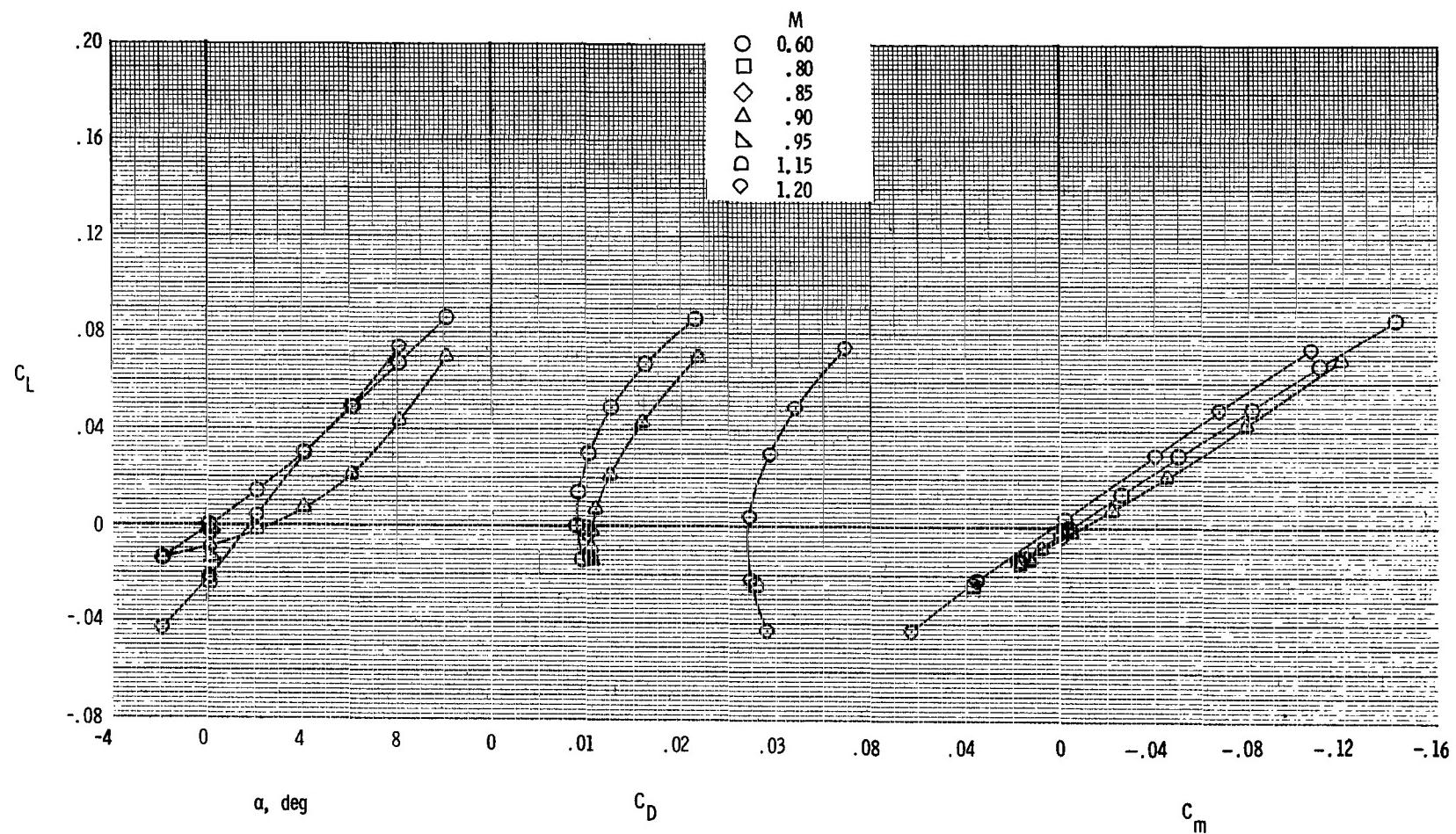
(b) Horizontal tails forward on boom, vertical tails mid on boom;  $\delta_h = 0^\circ$ .

Figure 10.- Continued.



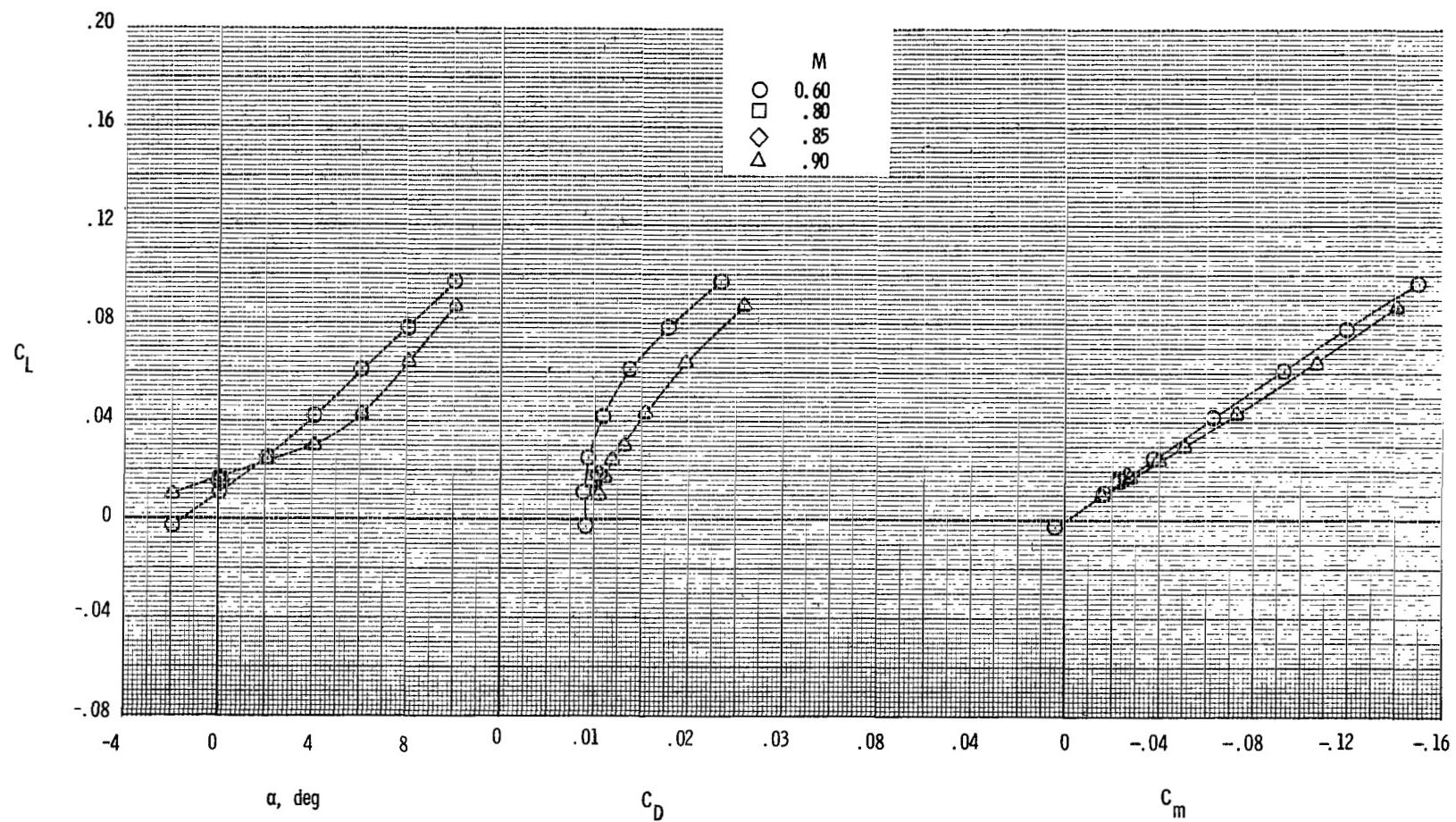
(c) Horizontal tails aft on boom; vertical tails forward on boom;  $\delta_h = 0^\circ$ .

Figure 10.- Continued.



(d) Horizontal tails aft on boom; vertical tails aft on boom;  $\delta_h = 0^\circ$ .

Figure 10.- Continued.



(e) Horizontal tails aft on boom, vertical tails mid on fuselage;  $\delta_h = 0^\circ$ .

Figure 10.- Concluded.

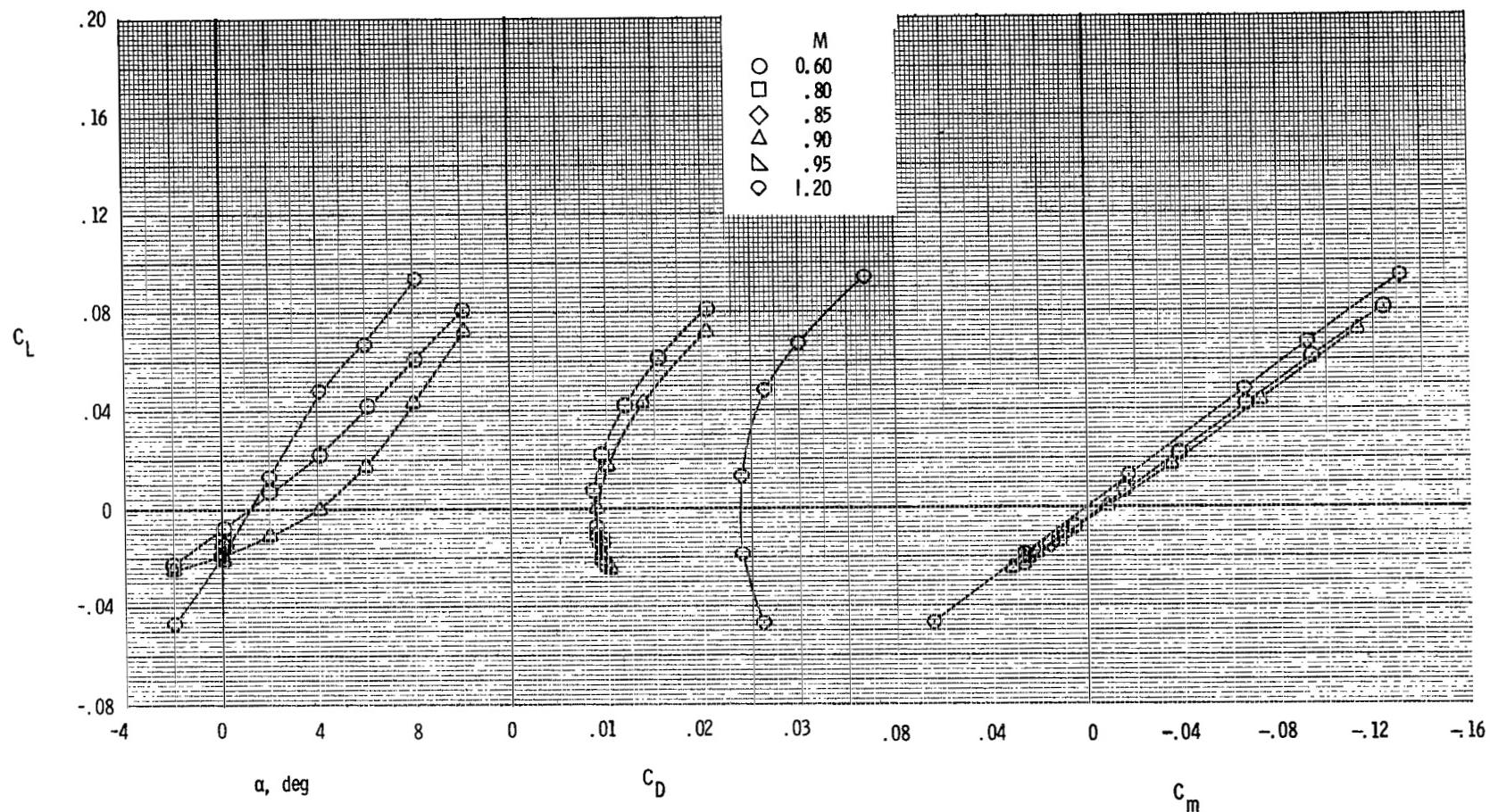


Figure 11.- Basic longitudinal aerodynamic characteristics at various Mach numbers for twin-engine tail interference afterbody model with jet off ( $p_{t,j}/p_\infty = 1.0$ ), dry power nozzles, booms on, horizontal tail forward on boom, single vertical tail aft on fuselage, and  $\delta_h = 0^\circ$ .

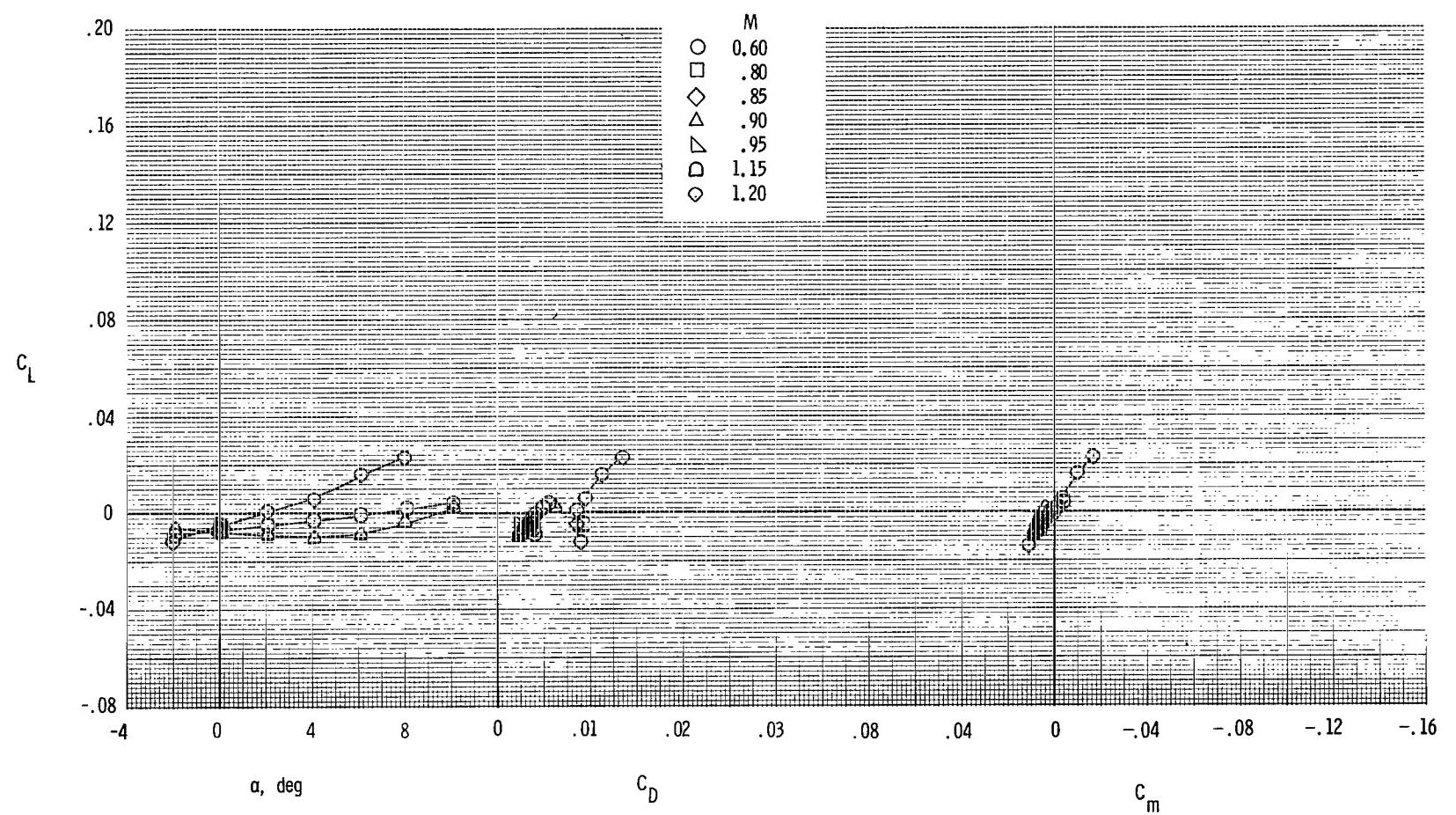
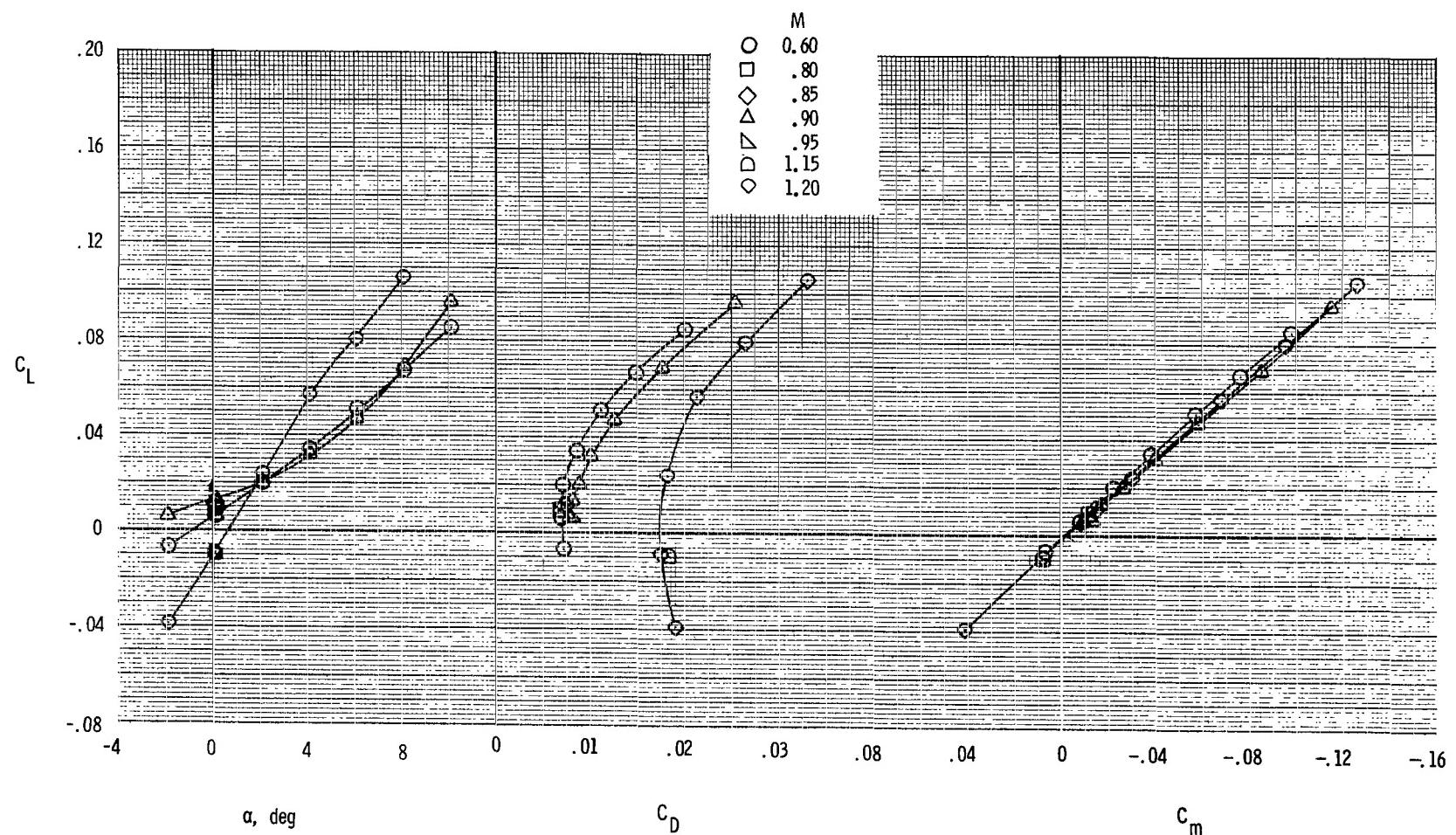
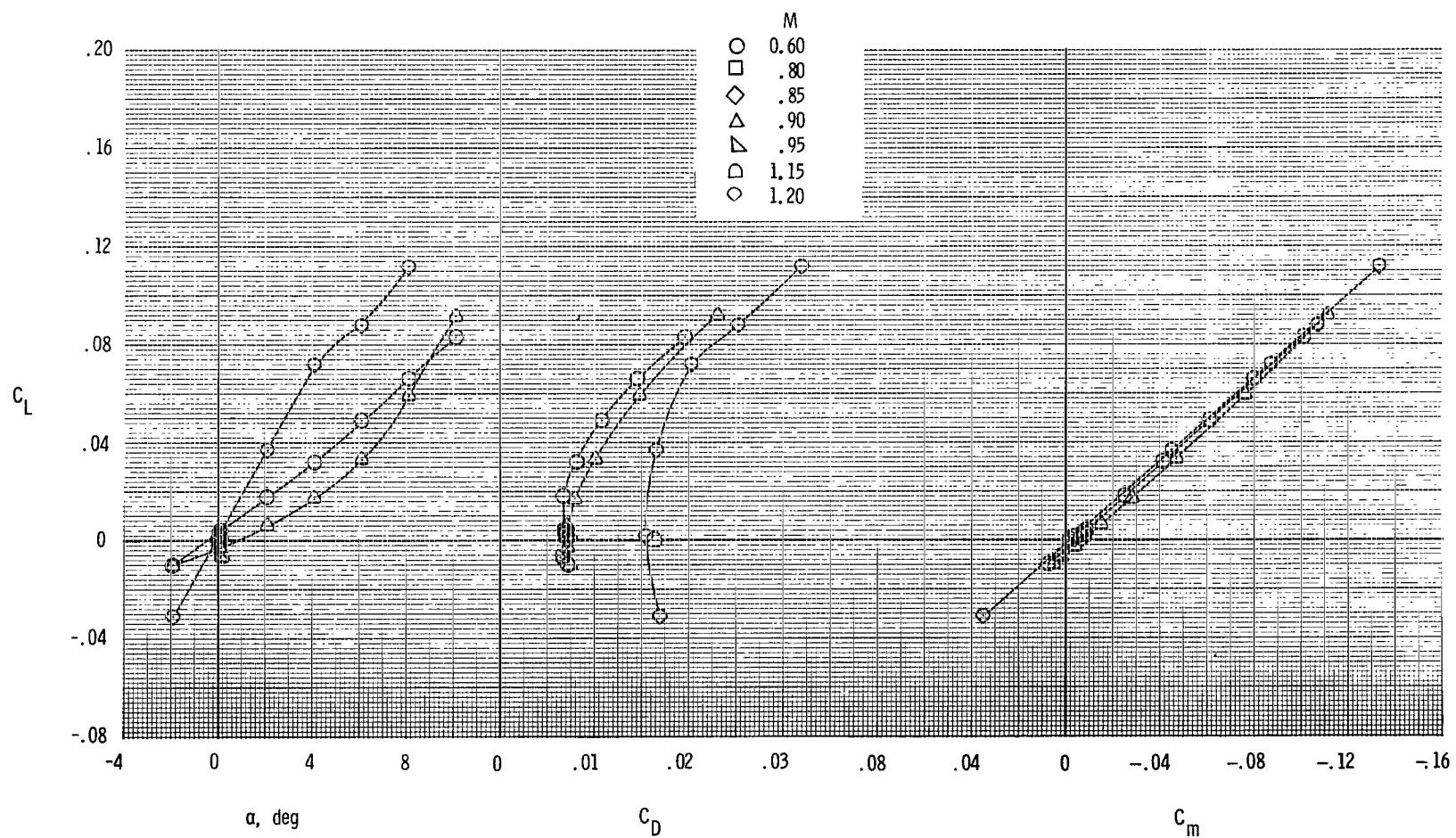


Figure 12.- Basic longitudinal aerodynamic characteristics at various Mach numbers for twin-engine tail interference afterbody model with jet off ( $p_{t,j}/p_\infty = 1.0$ ), A/B nozzles, booms off, and tails off.



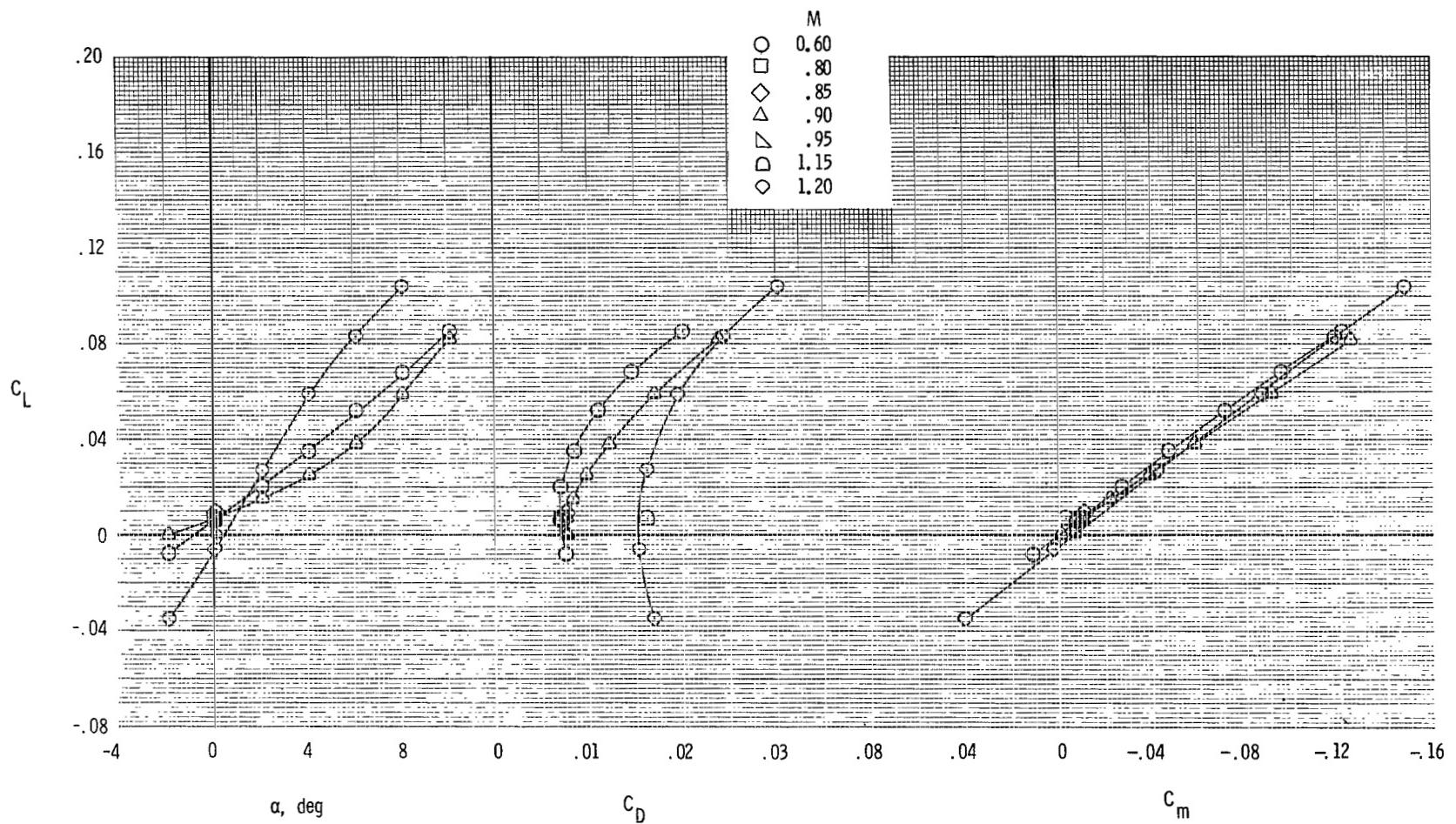
(a) Horizontal tails forward; vertical tails forward;  $\delta_h = 0^\circ$ .

Figure 13.- Basic longitudinal aerodynamic characteristics at various Mach numbers for twin-engine tail interference afterbody model with jet off ( $p_{t,j}/p_\infty = 1.0$ ), A/B nozzles, booms off, and twin vertical tails.



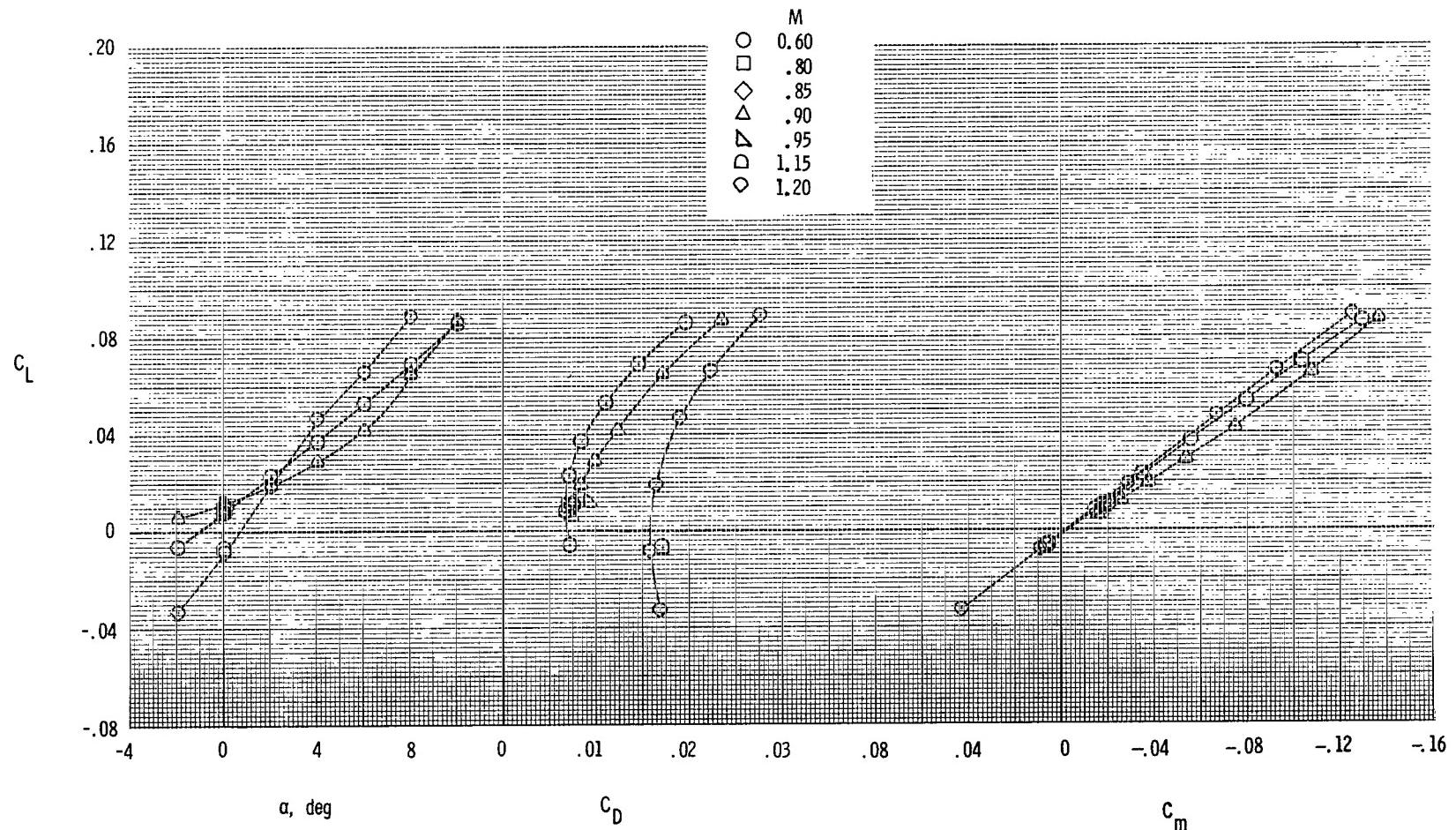
(b) Horizontal tails forward; vertical tails aft;  $\delta_h = 0^\circ$ .

Figure 13.- Continued.



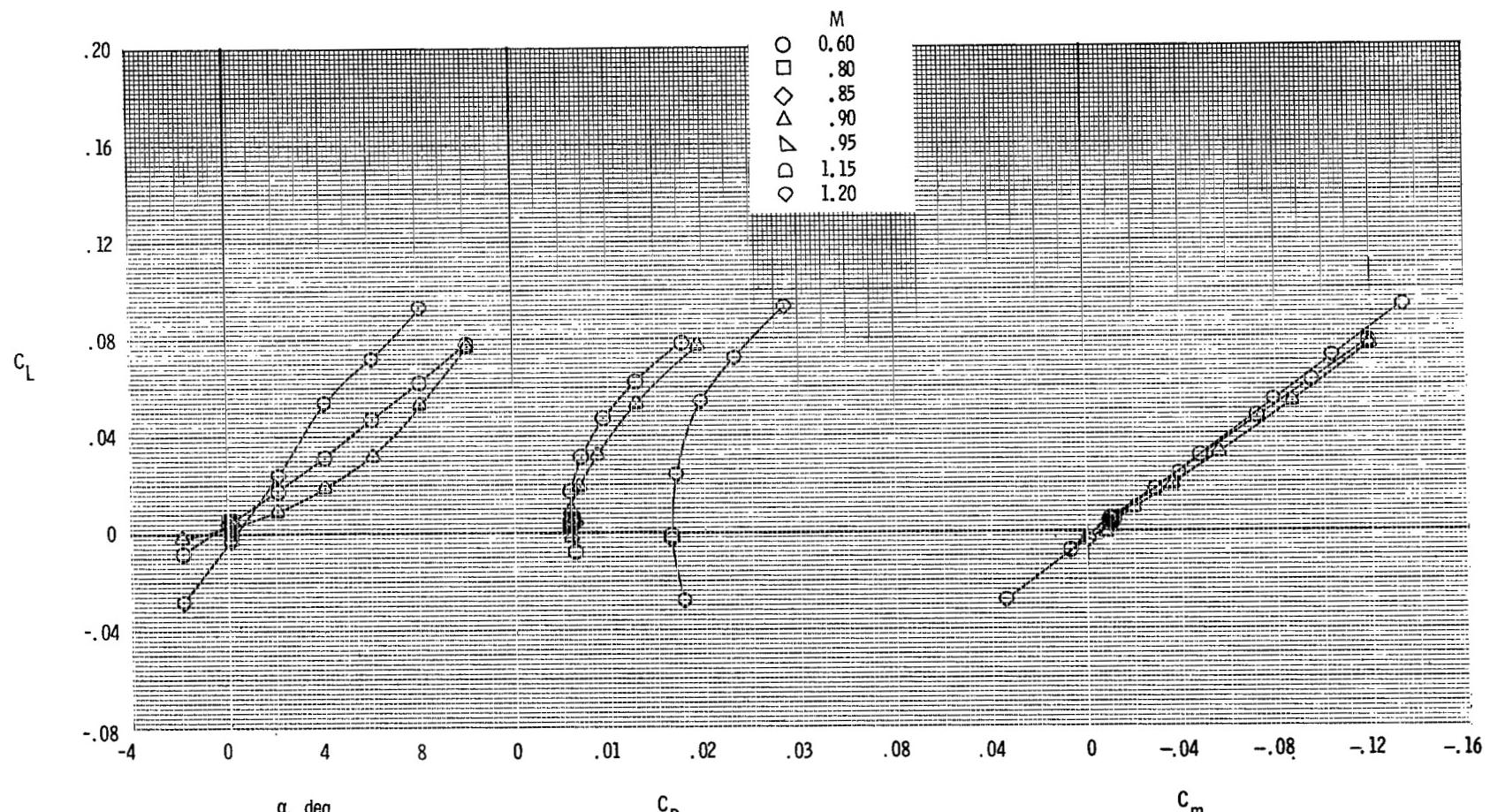
(c) Horizontal tails aft; vertical tails forward;  $\delta_h = 0^\circ$ .

Figure 13.- Continued.



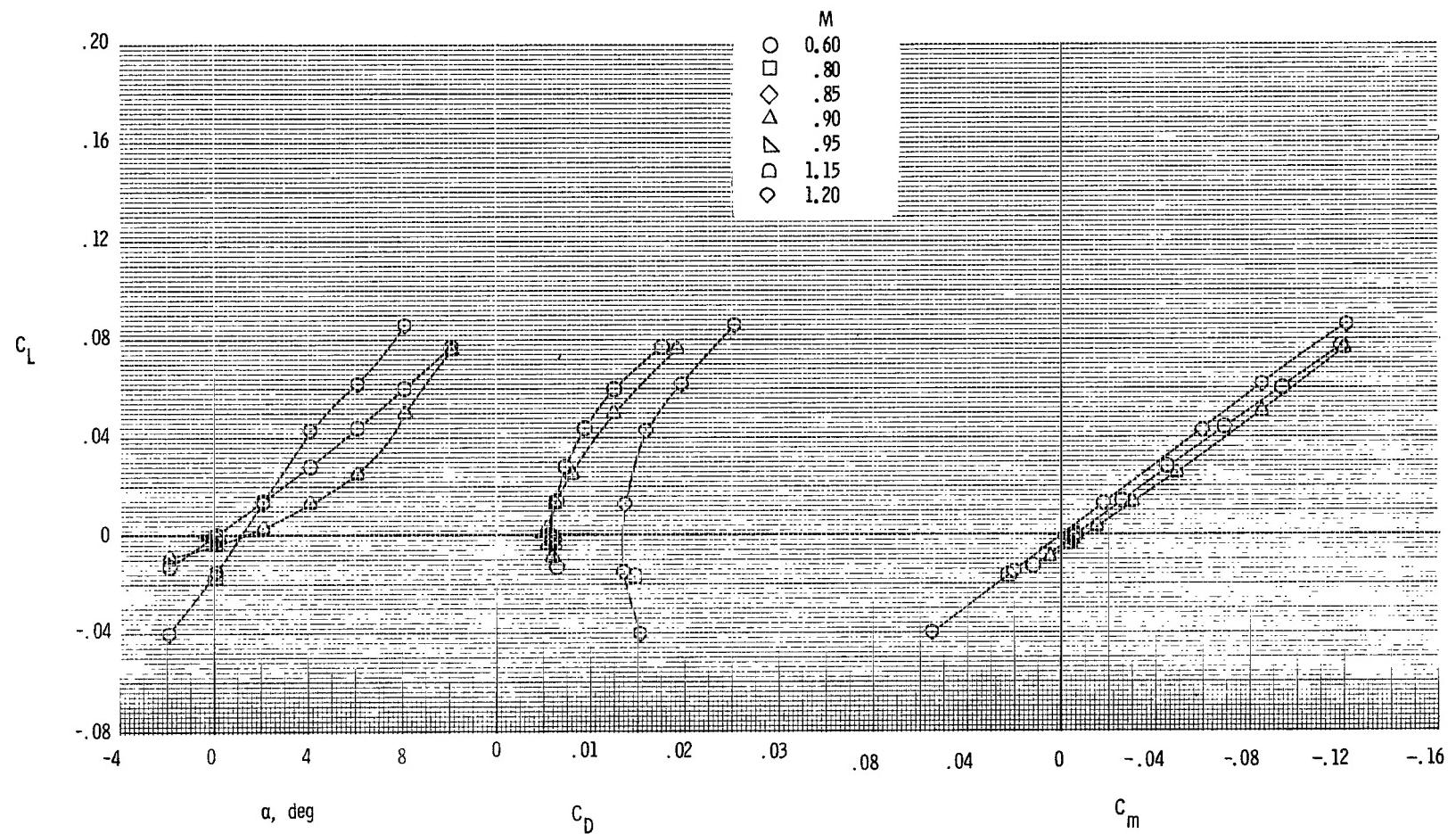
(d) Horizontal tails aft; vertical tails aft;  $\delta_h = 0^\circ$ .

Figure 13.- Concluded.



(a) Horizontal tails aft; vertical tail forward;  $\delta_h = 0^\circ$ .

Figure 14.- Basic longitudinal aerodynamic characteristics at various Mach numbers for twin-engine tail interference afterbody model with jet off ( $p_{t,j}/p_\infty = 1.0$ ), A/B nozzles, booms off, and single vertical tail.



(b) Horizontal tails aft; vertical tail aft;  $\delta_h = 0^\circ$ .

Figure 14.- Concluded.

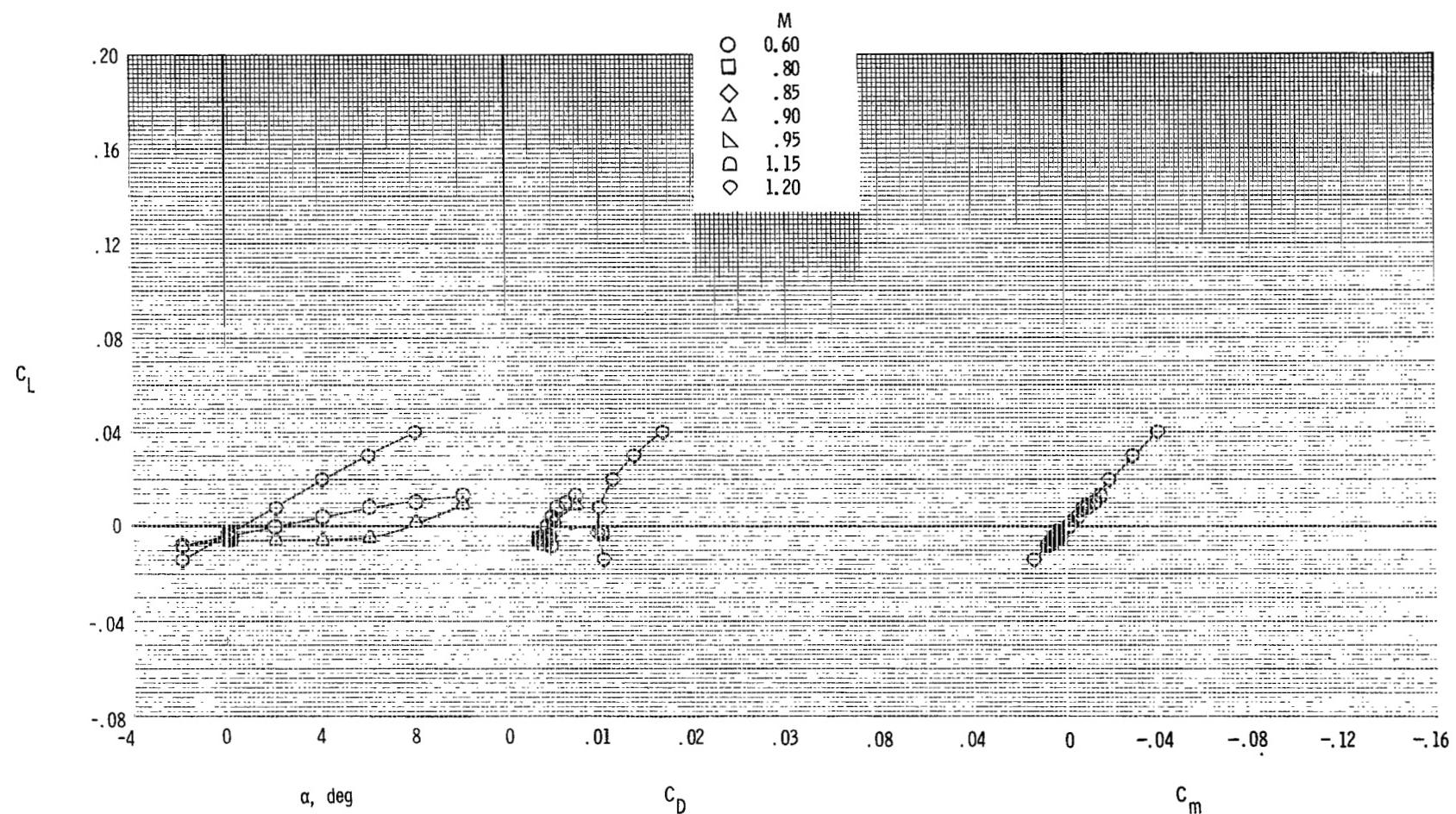
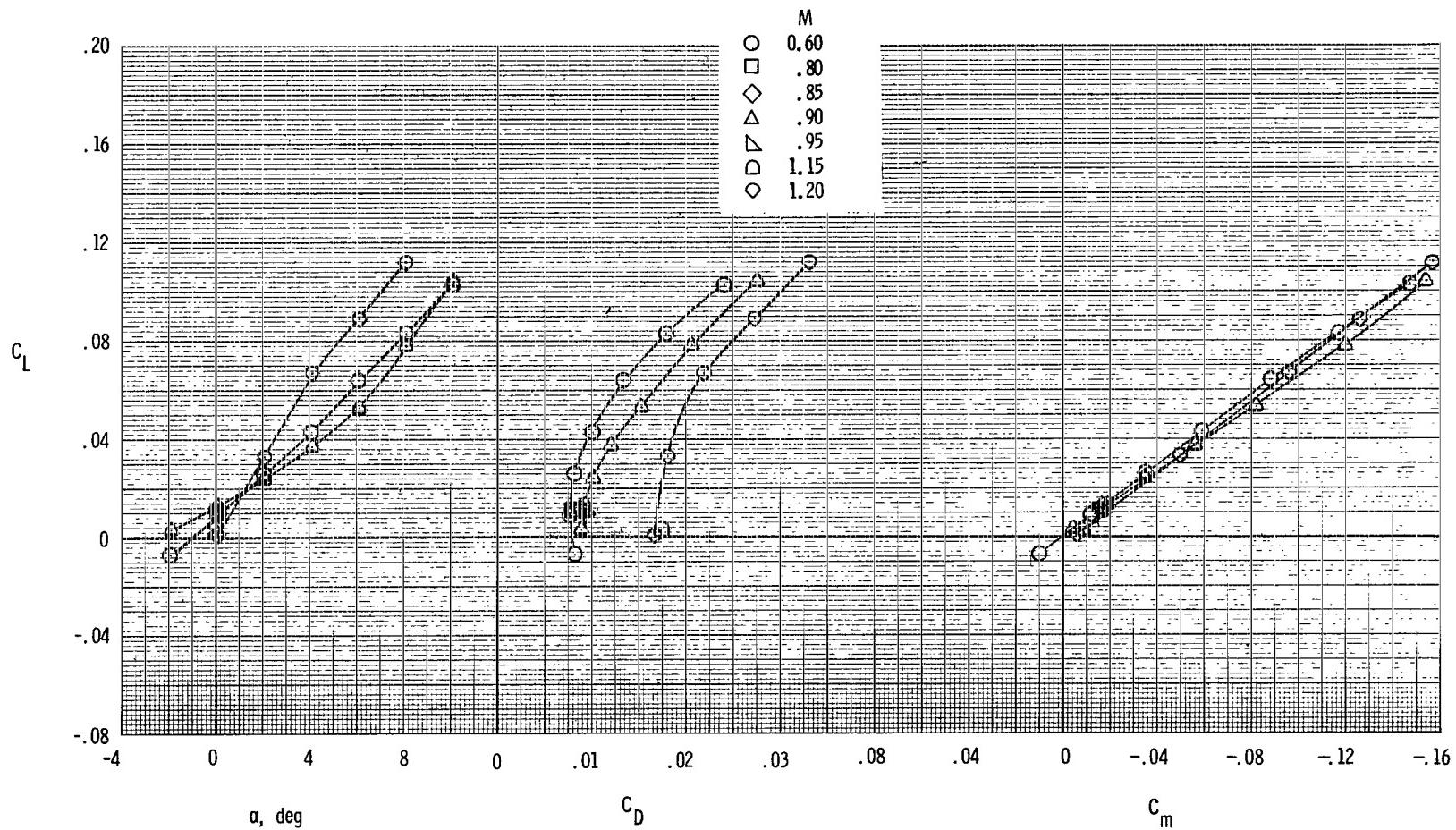
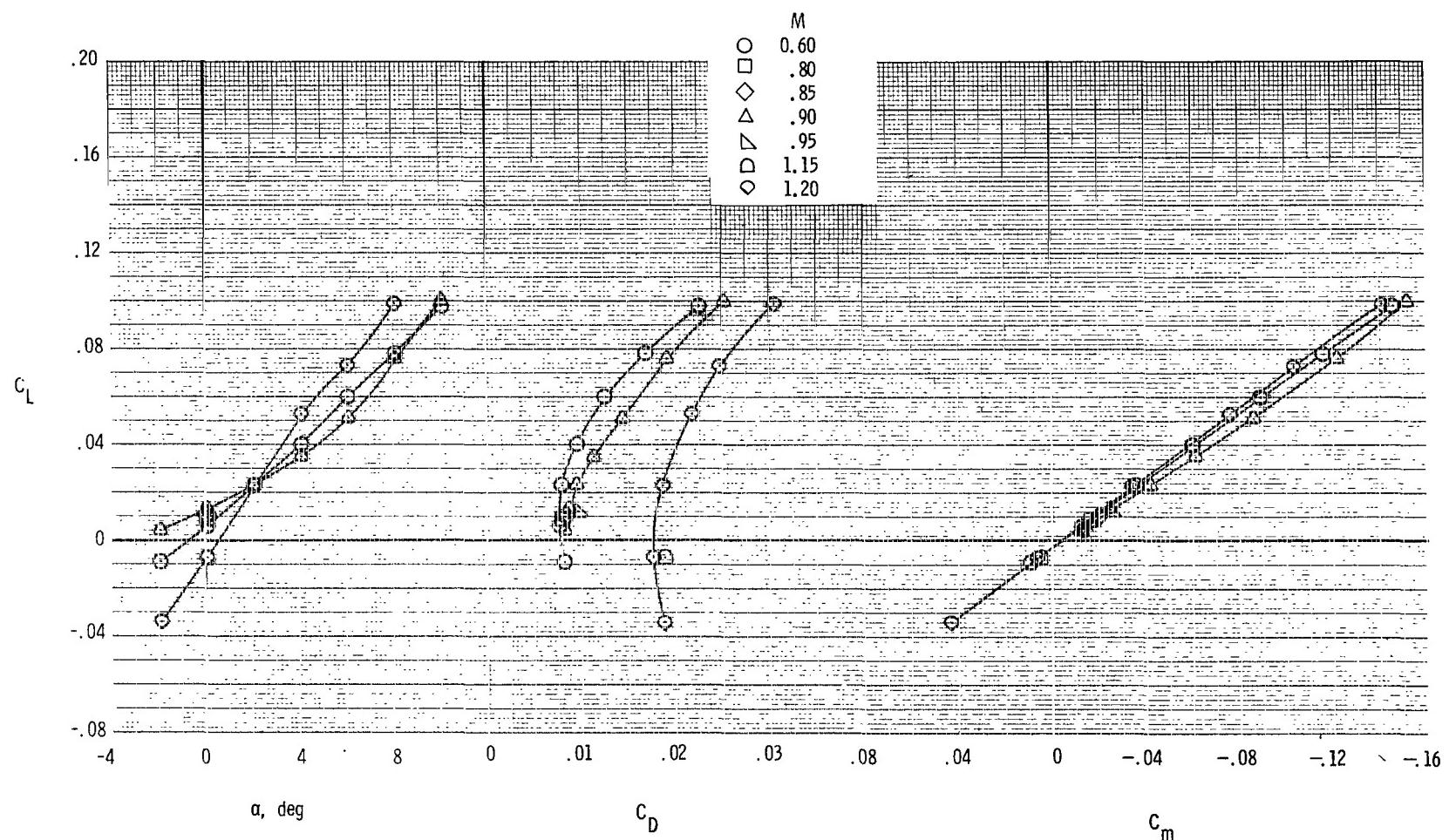


Figure 15.- Basic longitudinal aerodynamic characteristics at various Mach numbers for twin-engine tail interference afterbody model with jet off ( $p_{t,j}/p_\infty = 1.0$ ), A/B nozzles, booms on, and tails off.



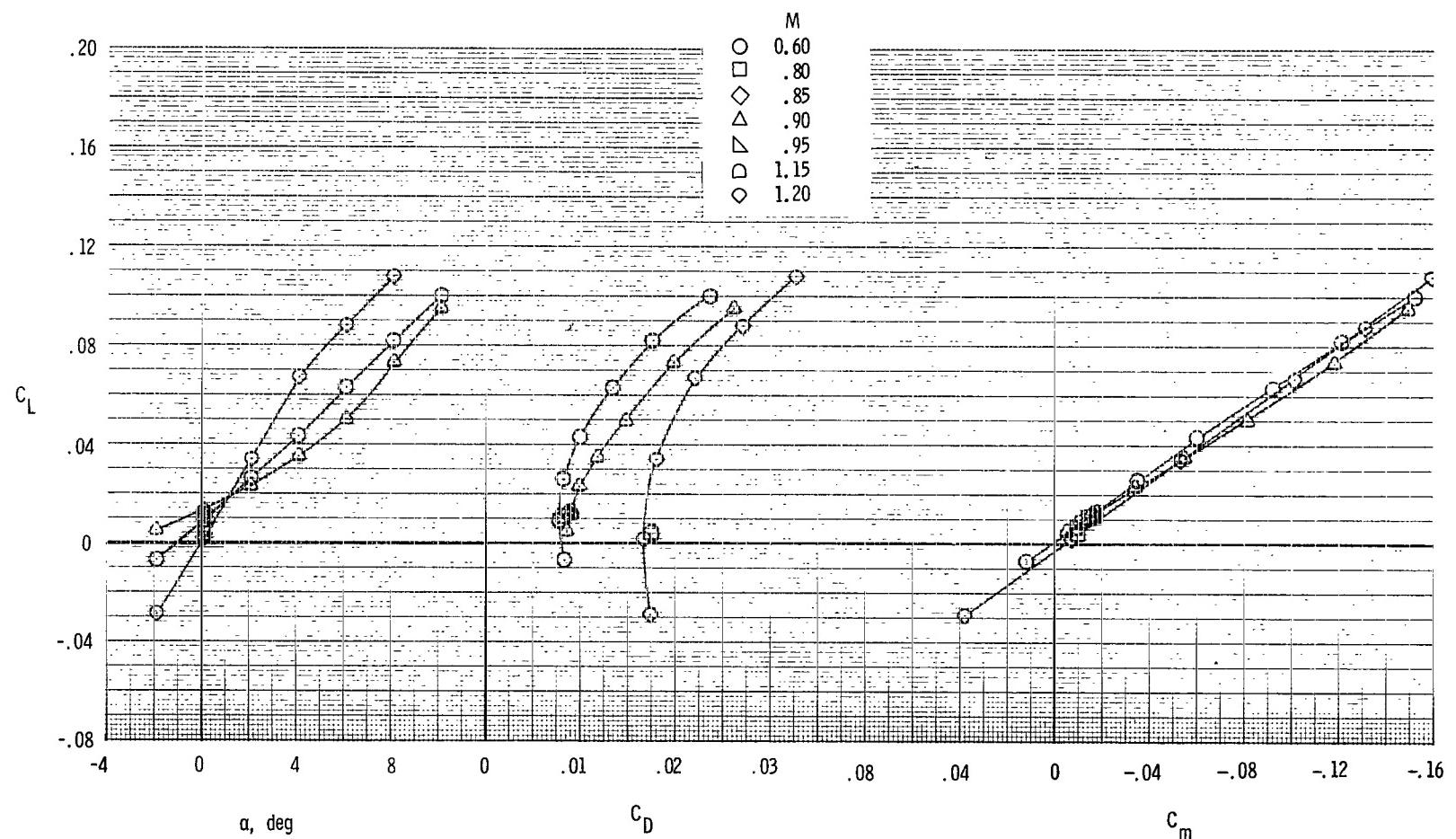
(a) Horizontal tails forward on boom; vertical tails forward on boom,  $\delta_h = 0^\circ$ .

Figure 16.- Basic longitudinal aerodynamic characteristics at various Mach numbers for twin-engine tail interference afterbody model with jet off ( $p_{t,j}/p_\infty = 1.0$ ), A/B nozzles, booms on, and twin vertical tails.



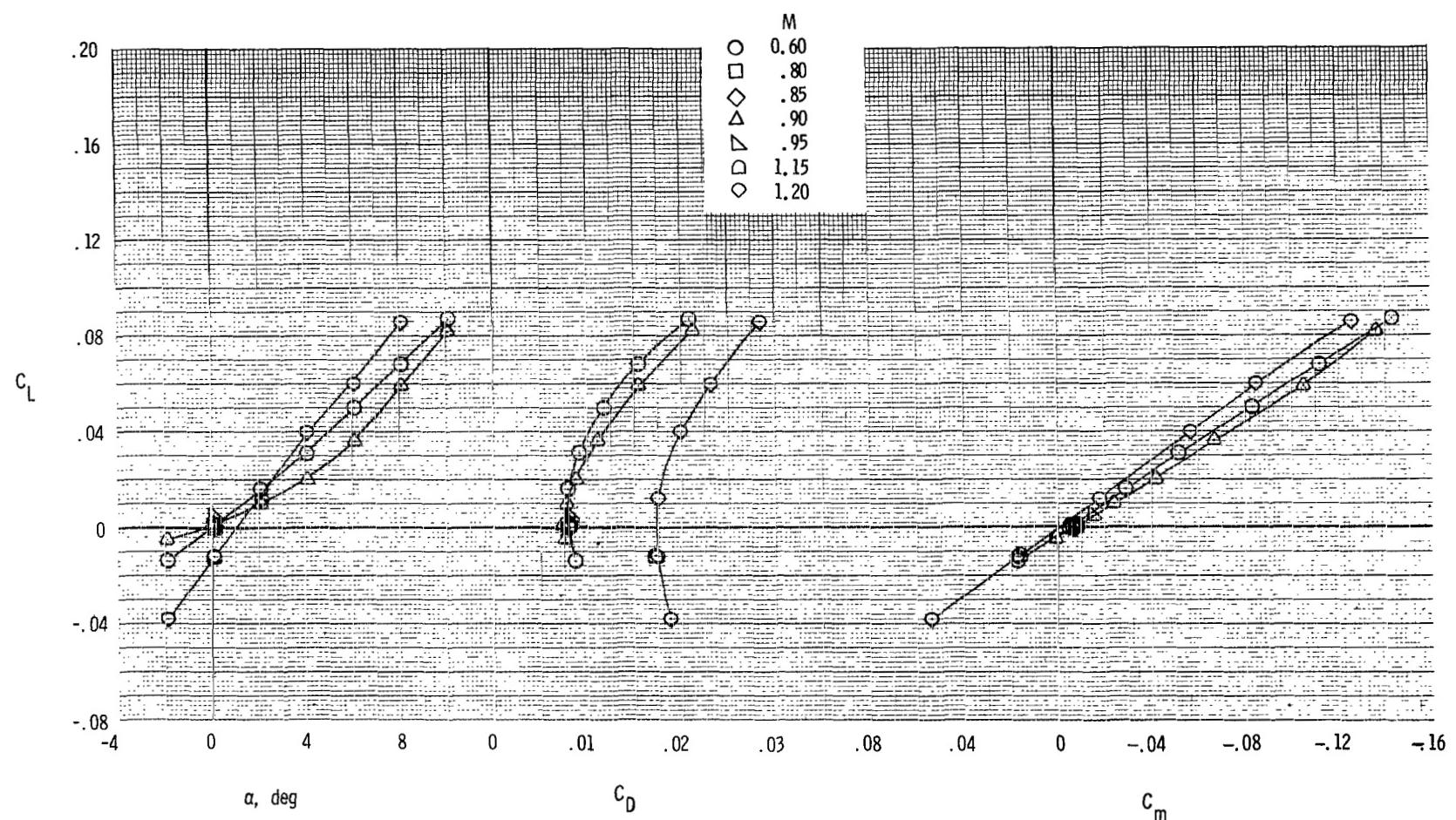
(b) Horizontal tails forward on boom; vertical tails mid on boom;  $\delta_h = 0^\circ$ .

Figure 16.- Continued.



(c) Horizontal tails aft on boom; vertical tails forward on boom;  $\delta_h = 0^\circ$ .

Figure 16.- Continued.



(d) Horizontal tails aft on boom; vertical tails aft on boom;  $\delta_h = 0^\circ$ .

Figure 16.- Concluded.

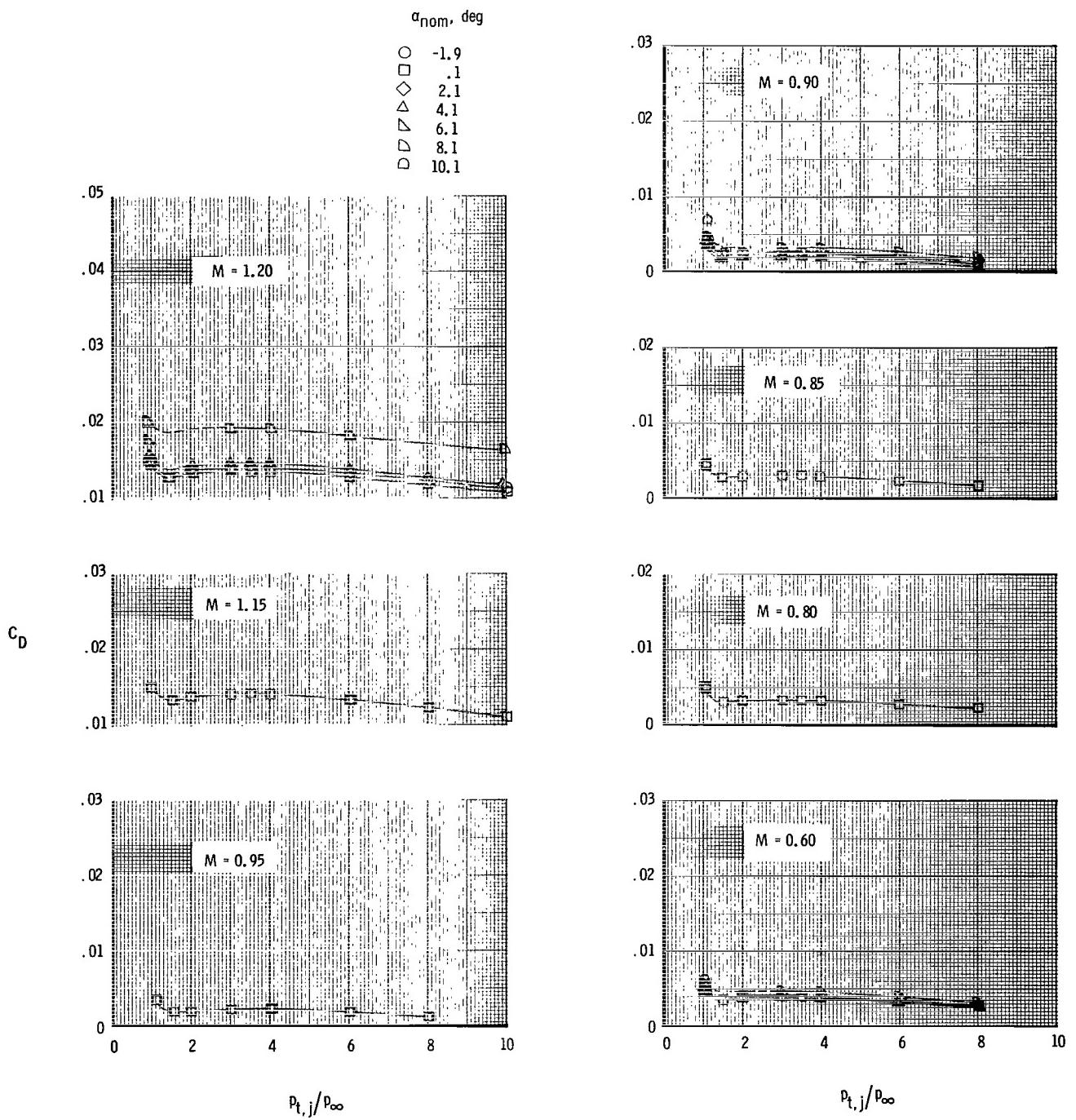
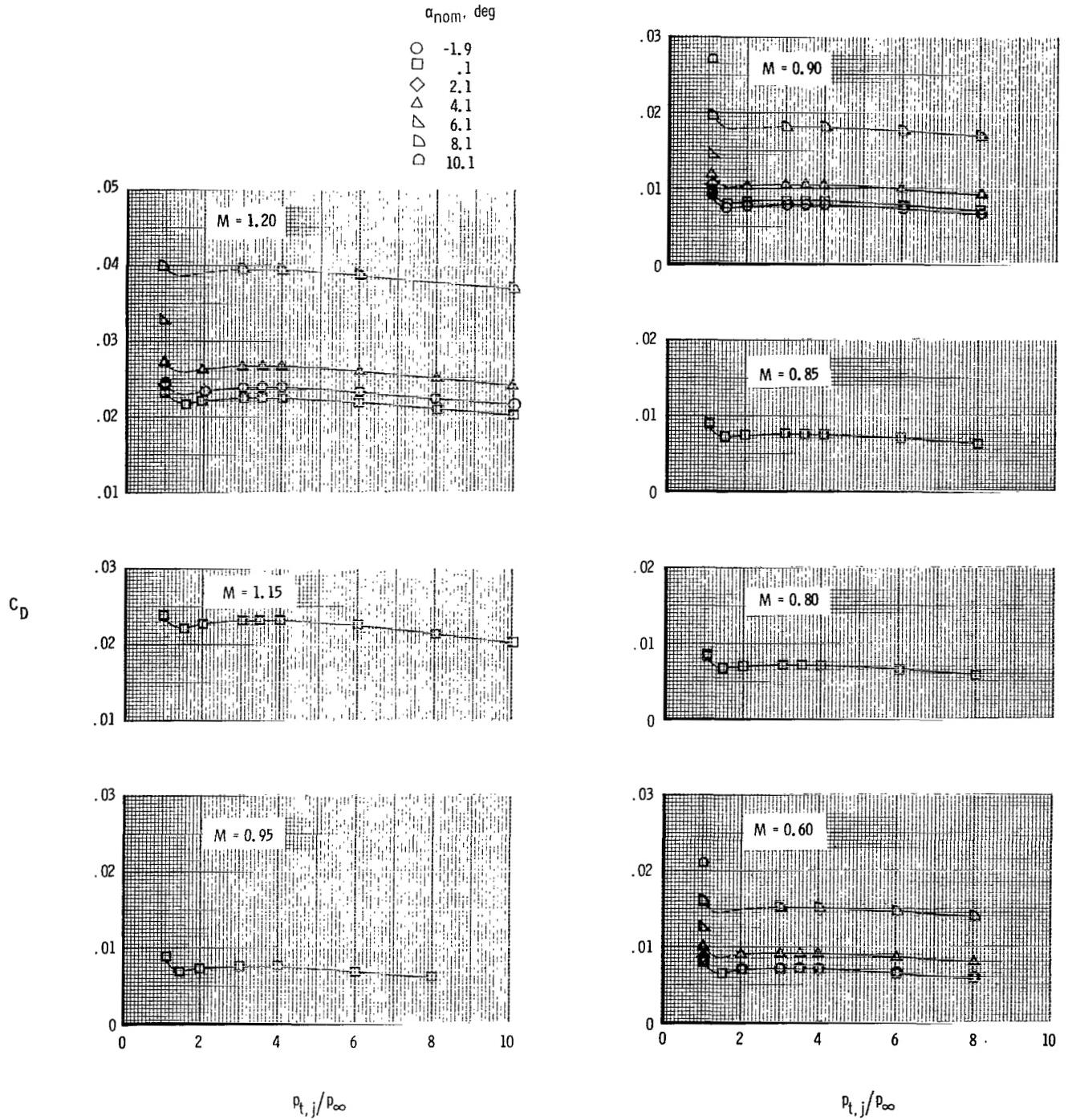
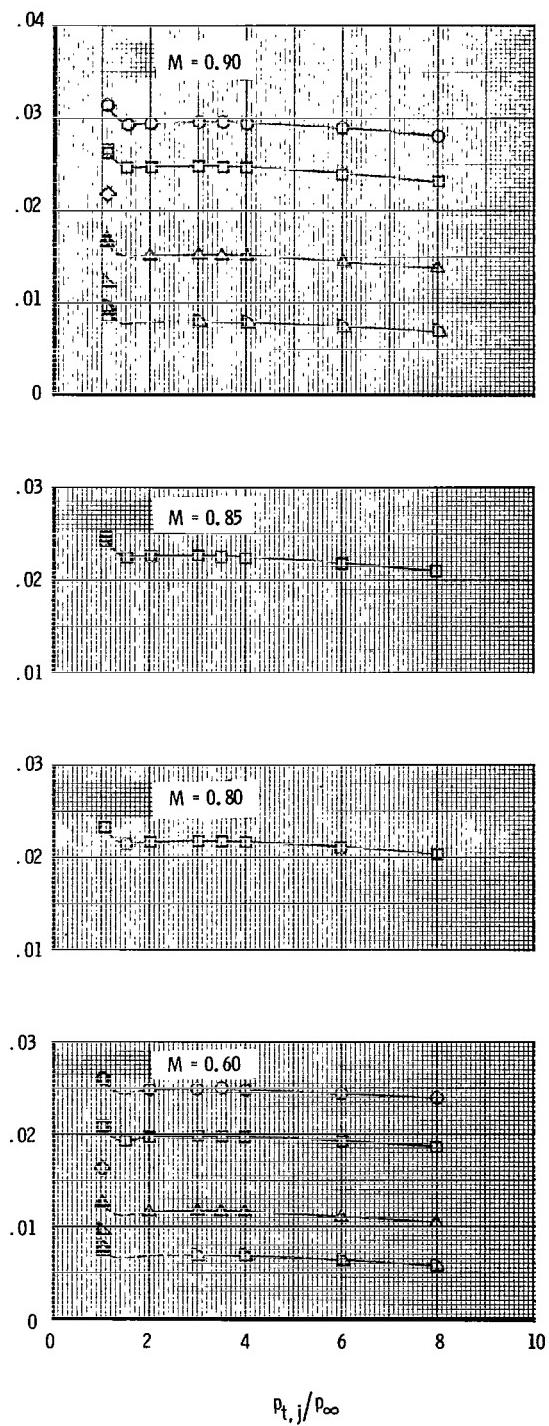
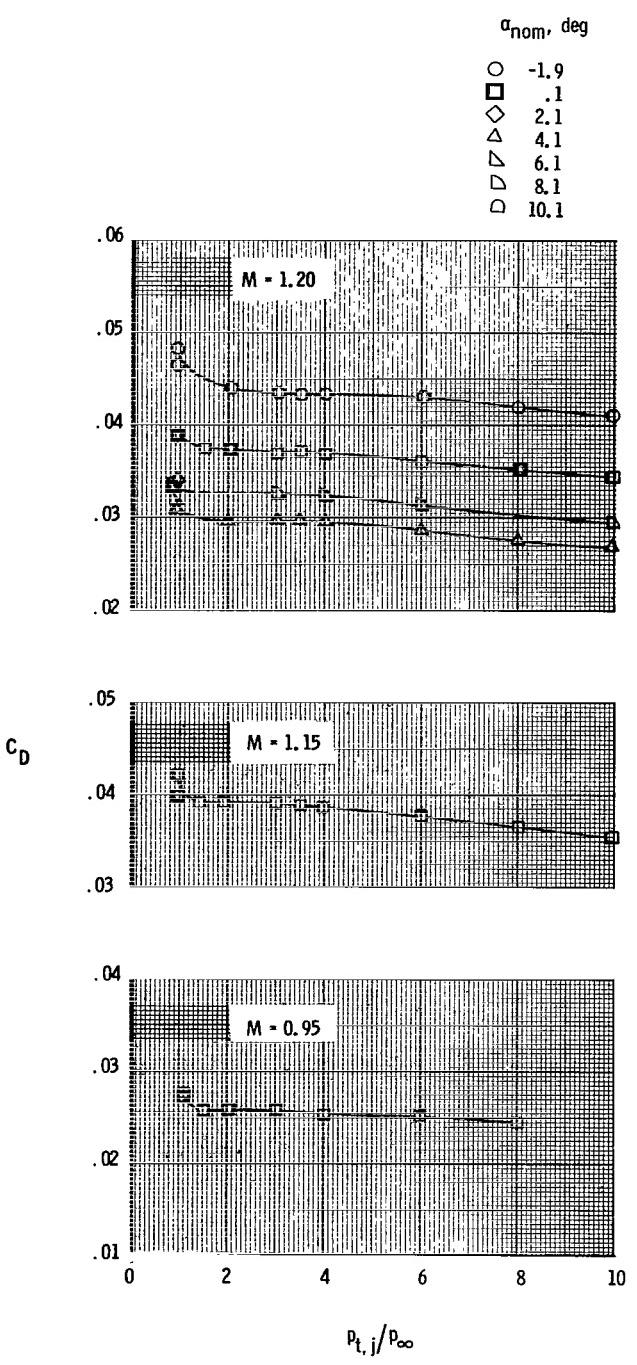


Figure 17.— Variation of total measured afterbody drag coefficient with jet total-pressure ratio for various Mach numbers for twin-engine tail interference afterbody model with dry power nozzles, booms off, and tails off.



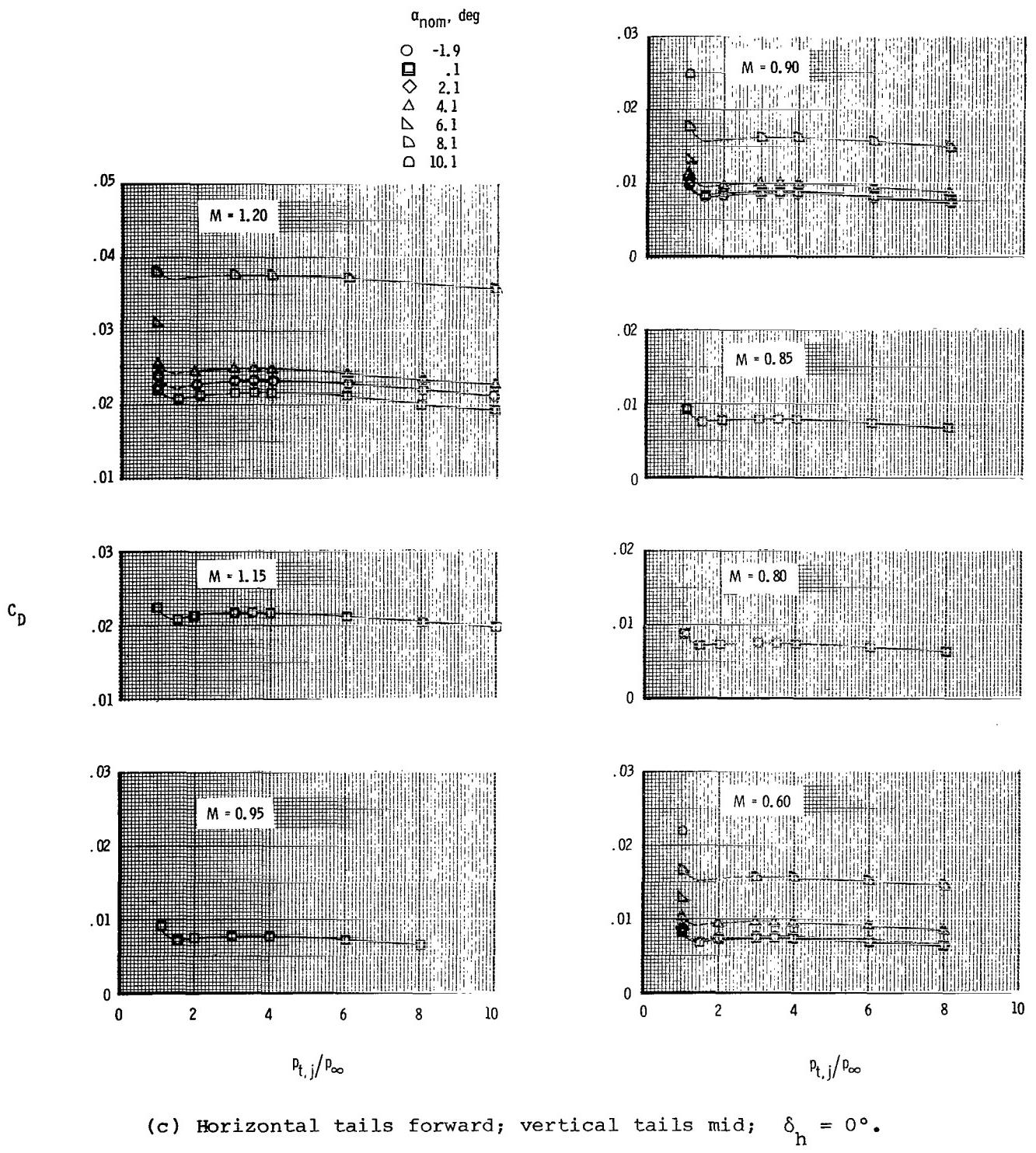
(a) Horizontal tails forward; vertical tails forward;  $\delta_h = 0^\circ$ .

Figure 18.- Variation of total measured afterbody drag coefficient with jet total-pressure ratio for various Mach numbers for twin-engine tail interference afterbody model with dry power nozzles, booms off, and twin vertical tails.



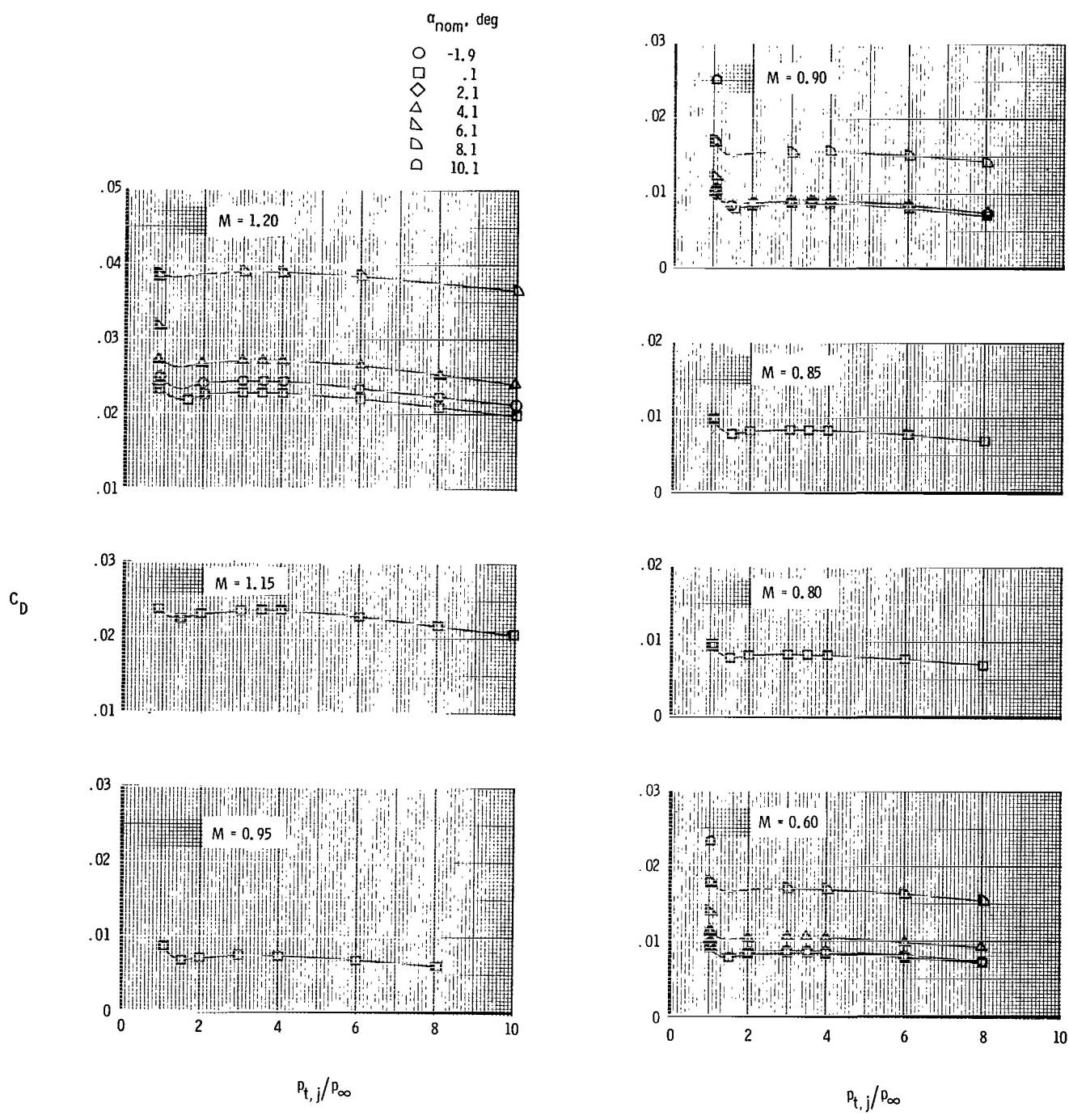
(b) Horizontal tails forward; vertical tails forward;  $\delta_h = -10^\circ$ .

Figure 18.- Continued.



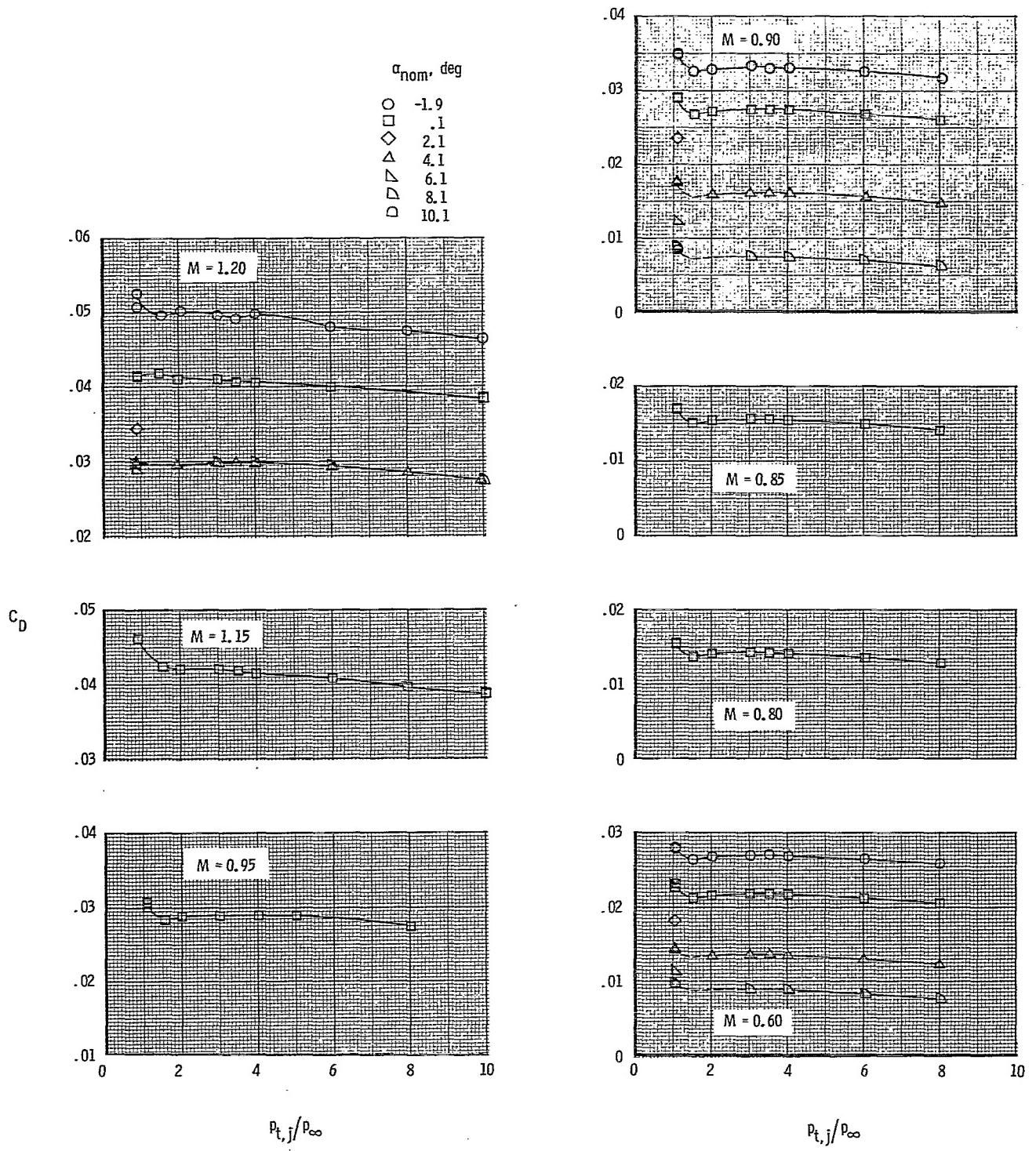
(c) Horizontal tails forward; vertical tails mid;  $\delta_h = 0^\circ$ .

Figure 18.- Continued.



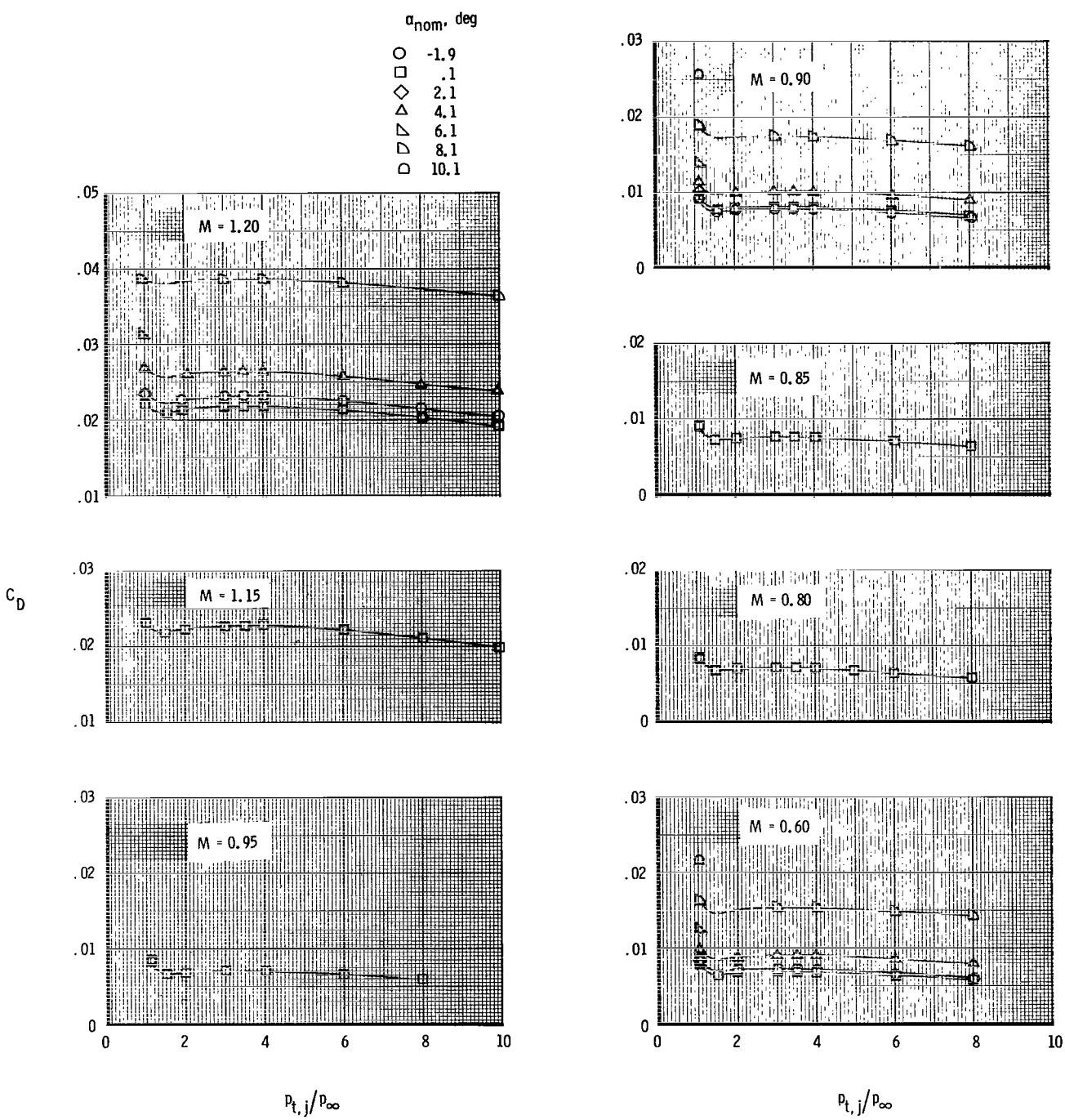
(d) Horizontal tails forward; vertical tails aft;  $\delta_h = 0^\circ$ .

Figure 18.- Continued.



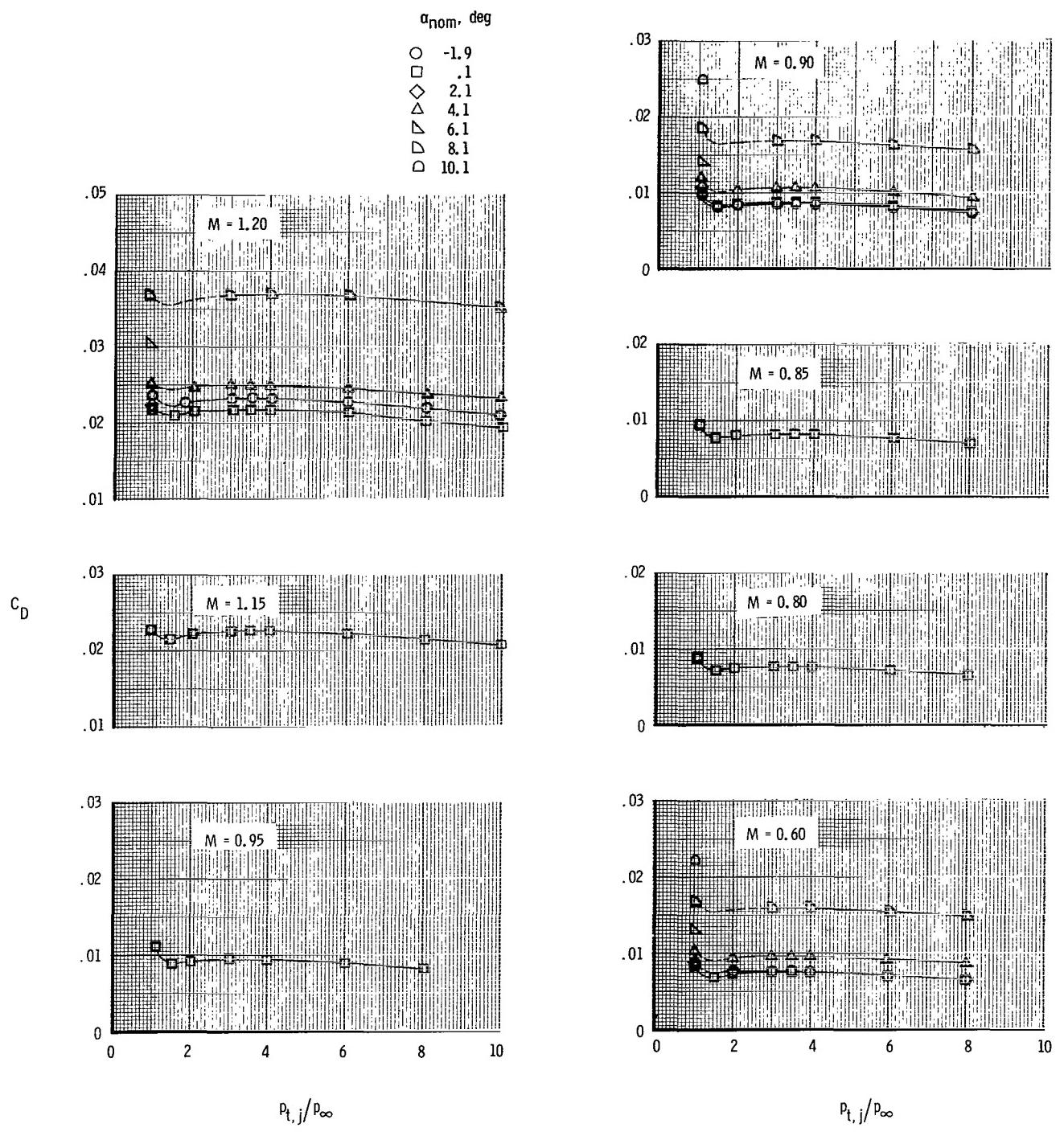
(e) Horizontal tails forward; vertical tails aft;  $\delta_h = -10^\circ$ .

Figure 18.- Continued.



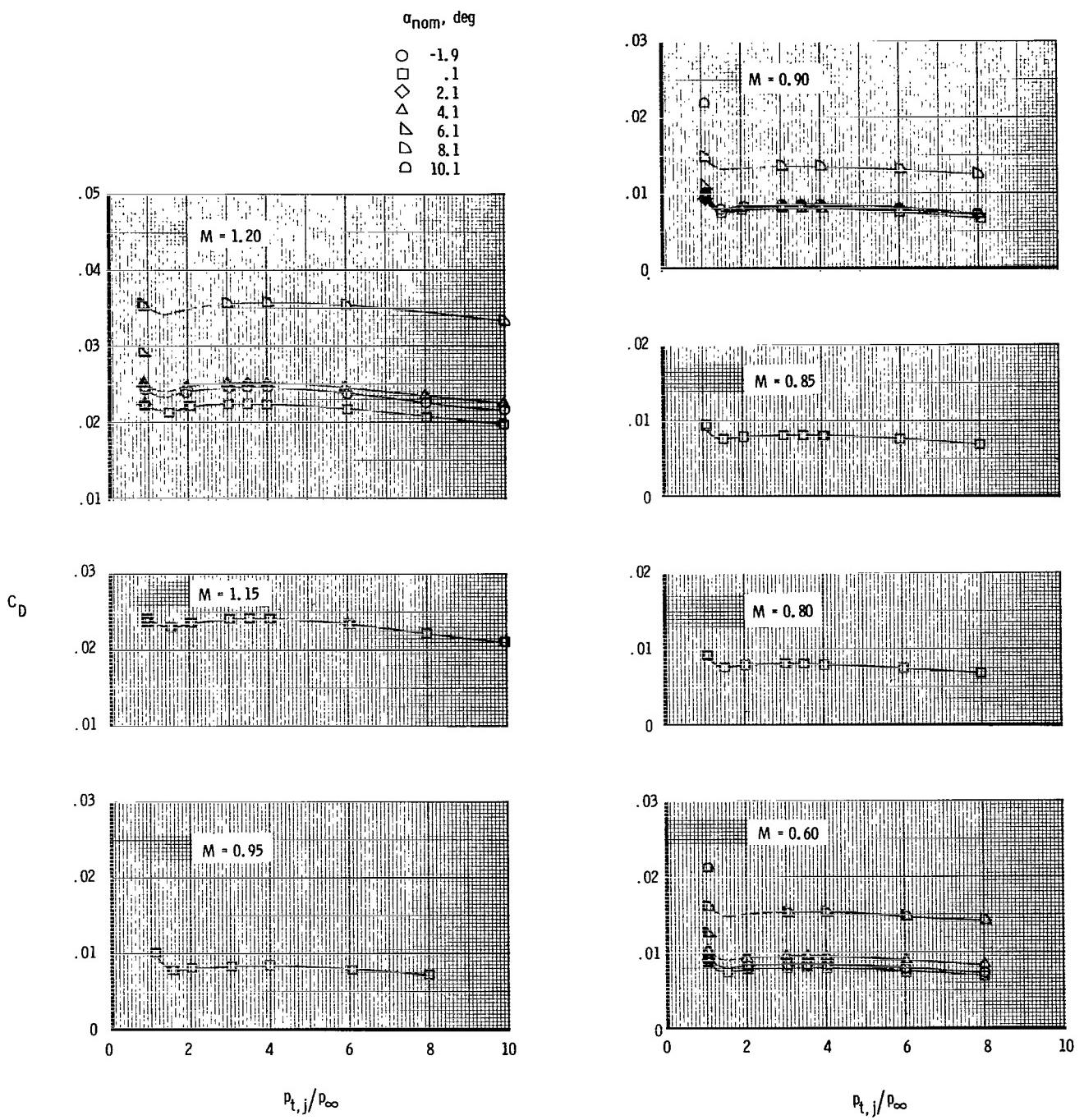
(f) Horizontal tails mid; vertical tails forward;  $\delta_h = 0^\circ$ .

Figure 18.- Continued.



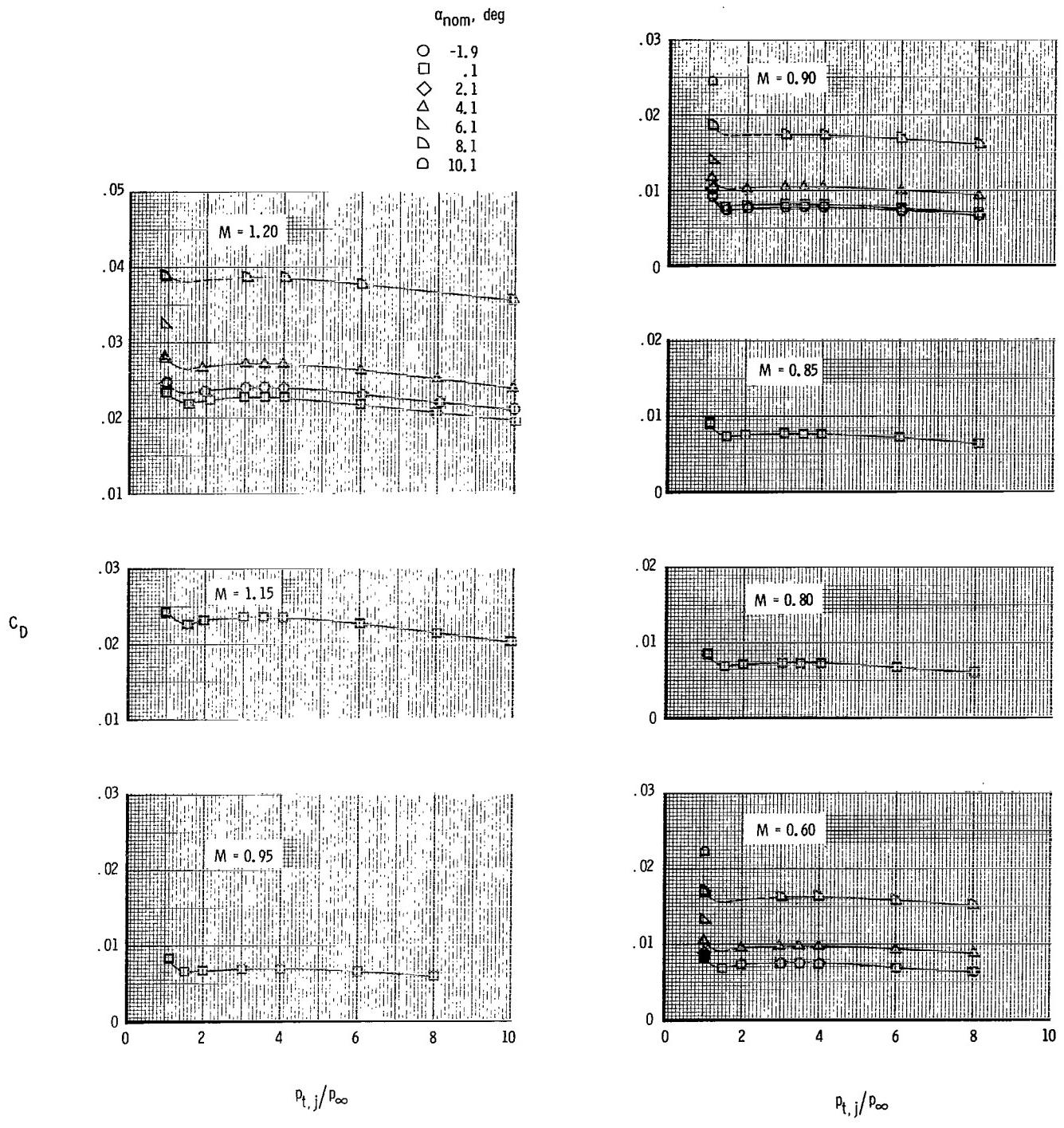
(g) Horizontal tails mid; vertical tails mid;  $\delta_h = 0^\circ$ .

Figure 18.- Continued.



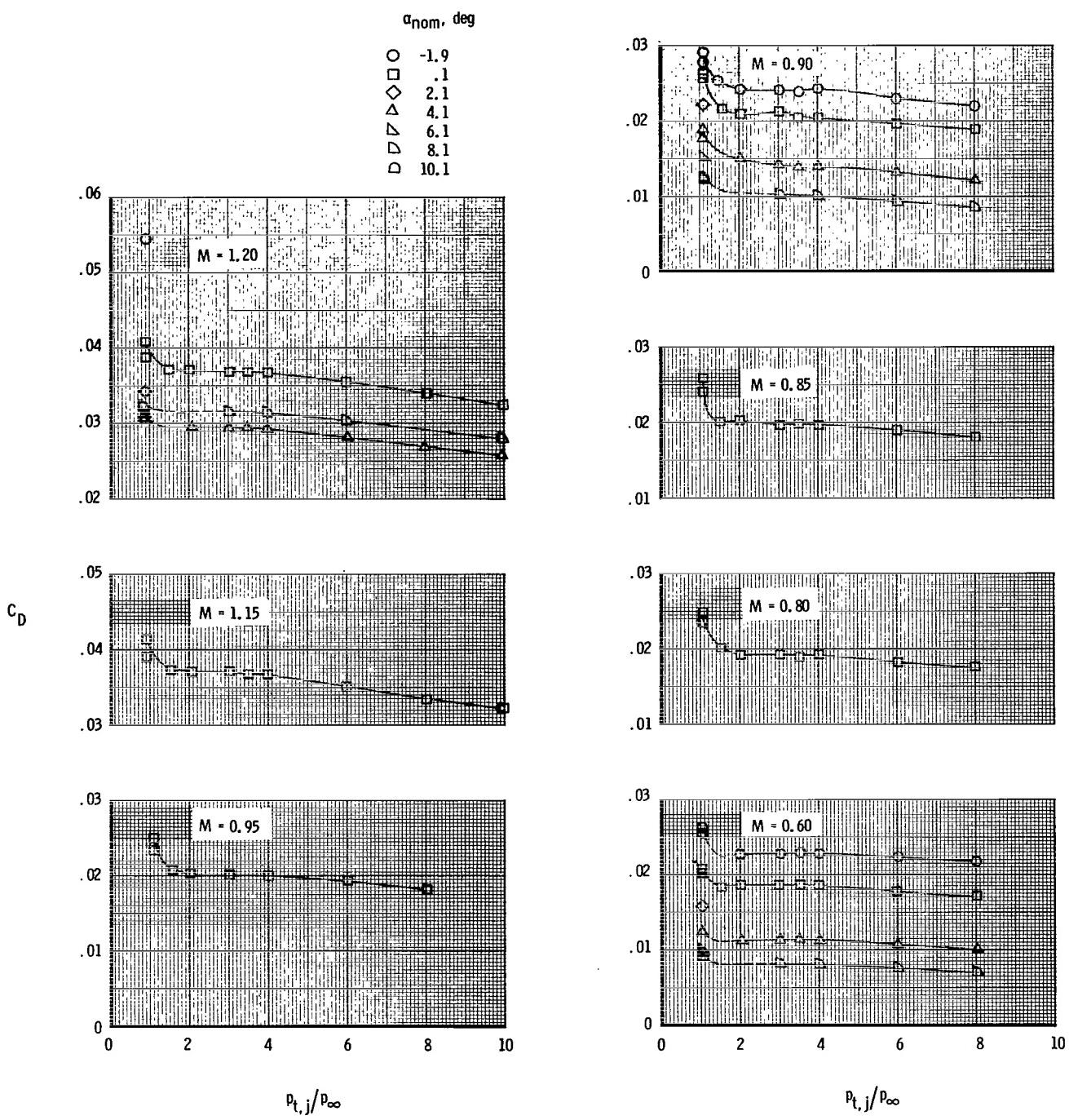
(h) Horizontal tails mid; vertical tails aft;  $\delta_h = 0^\circ$ .

Figure 18.- Continued.



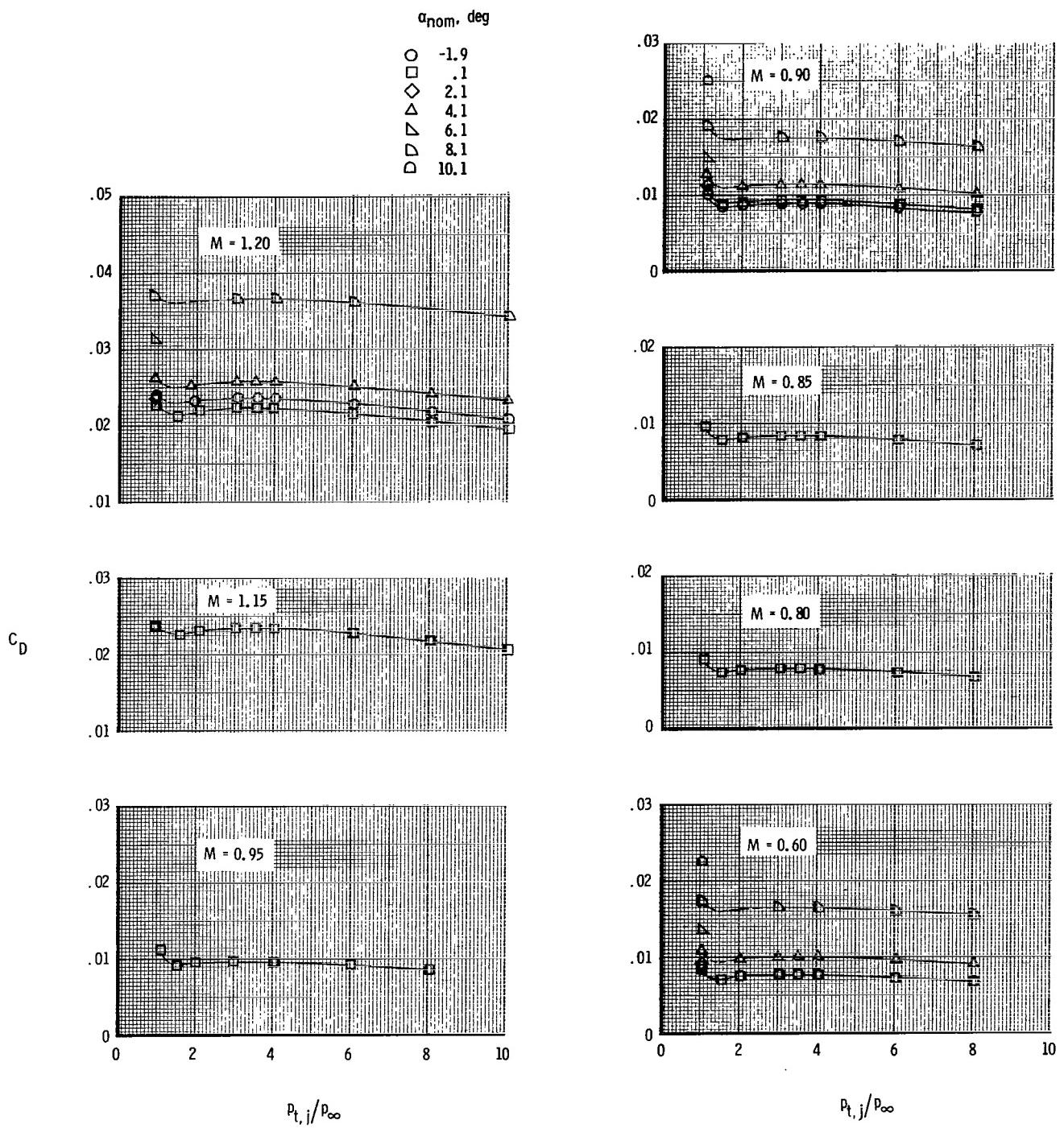
(i) Horizontal tails aft; vertical tails forward;  $\delta_h = 0^\circ$ .

Figure 18.- Continued.



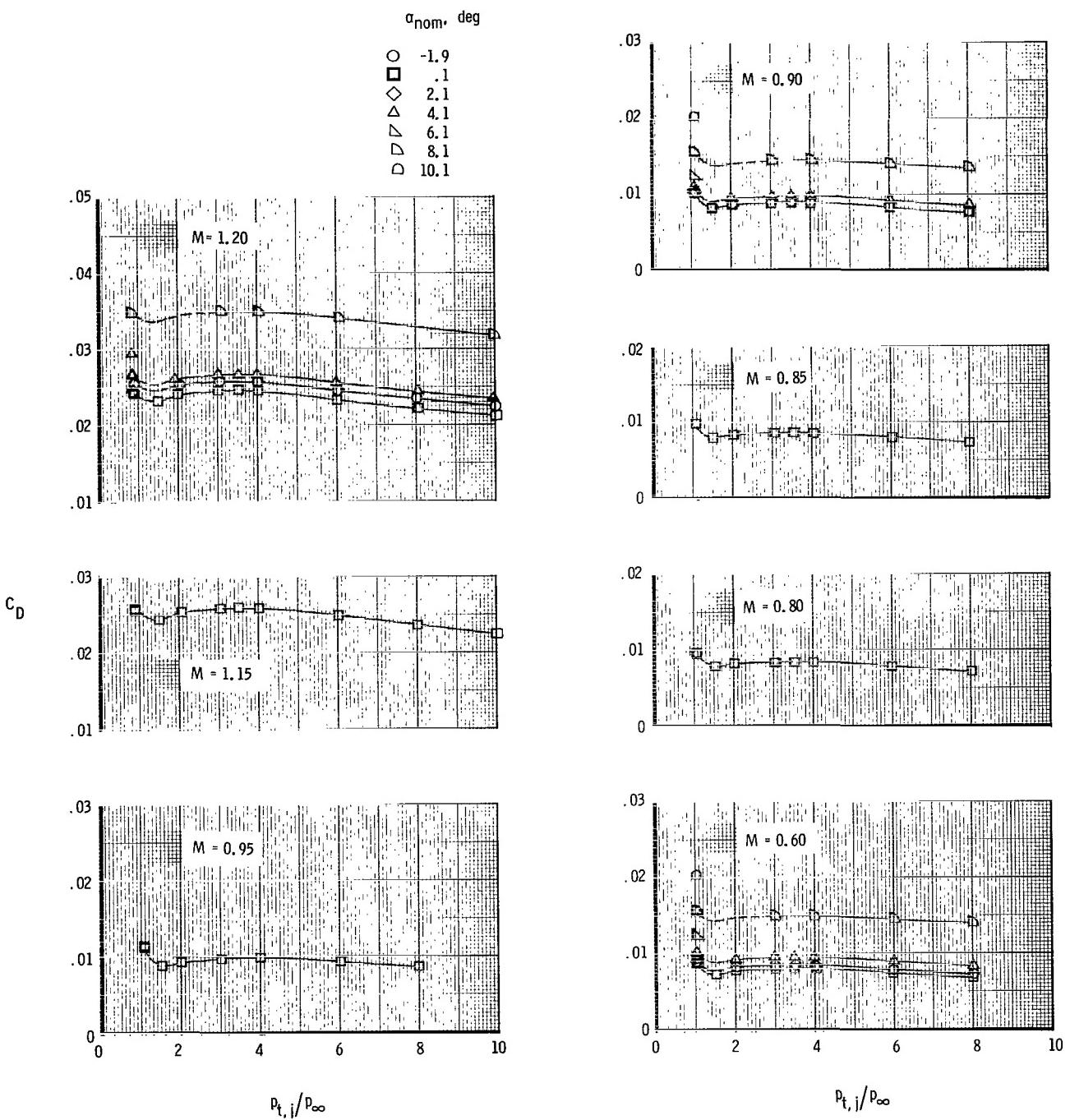
(j) Horizontal tails aft; vertical tails forward;  $\delta_h = -10^\circ$ .

Figure 18.- Continued.



(k) Horizontal tails aft; vertical tails mid;  $\delta_h = 0^\circ$ .

Figure 18.- Continued.



(1) Horizontal tails aft; vertical tails aft;  $\delta_h = 0^\circ$ .

Figure 18.- Continued.

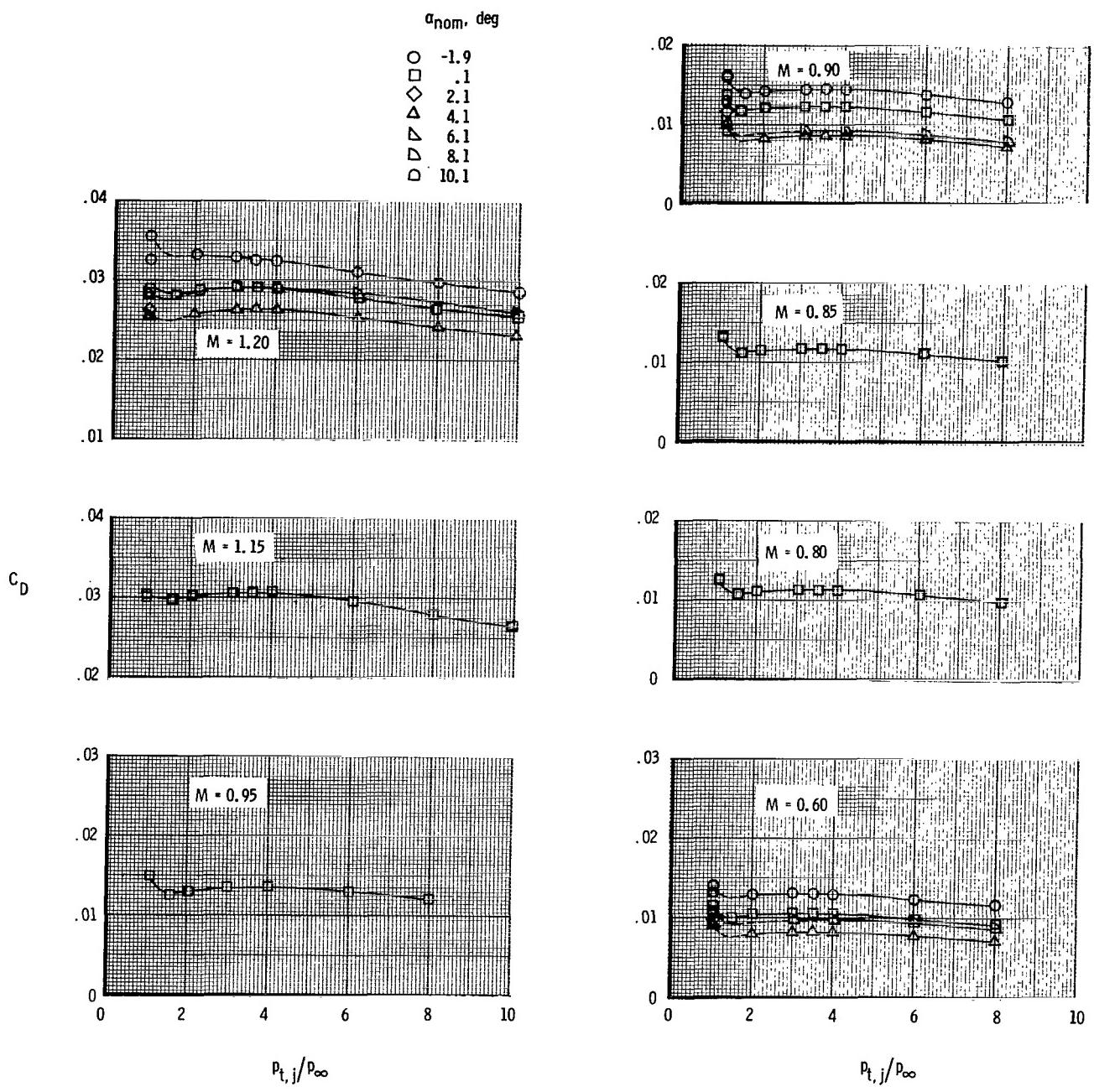
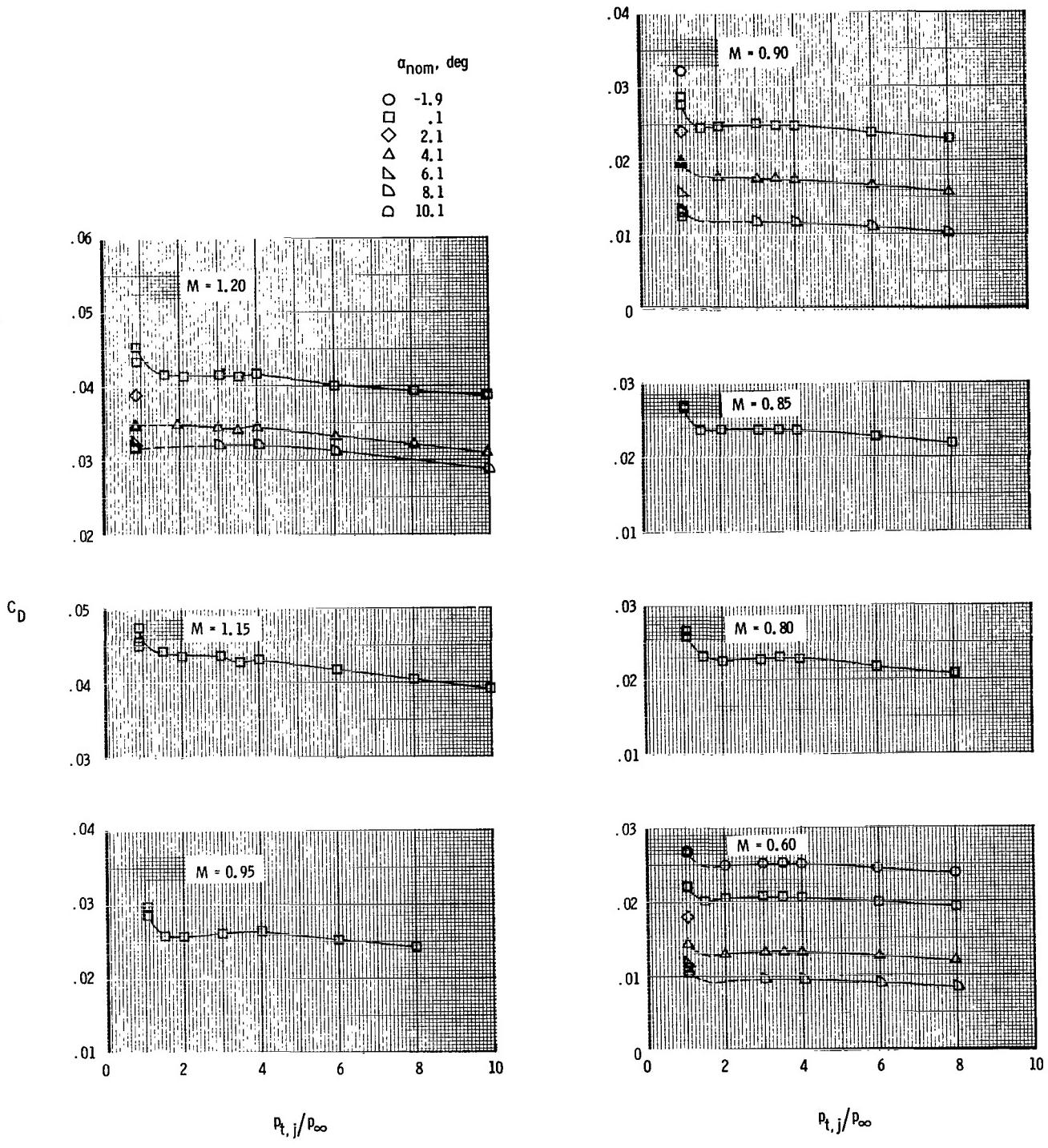
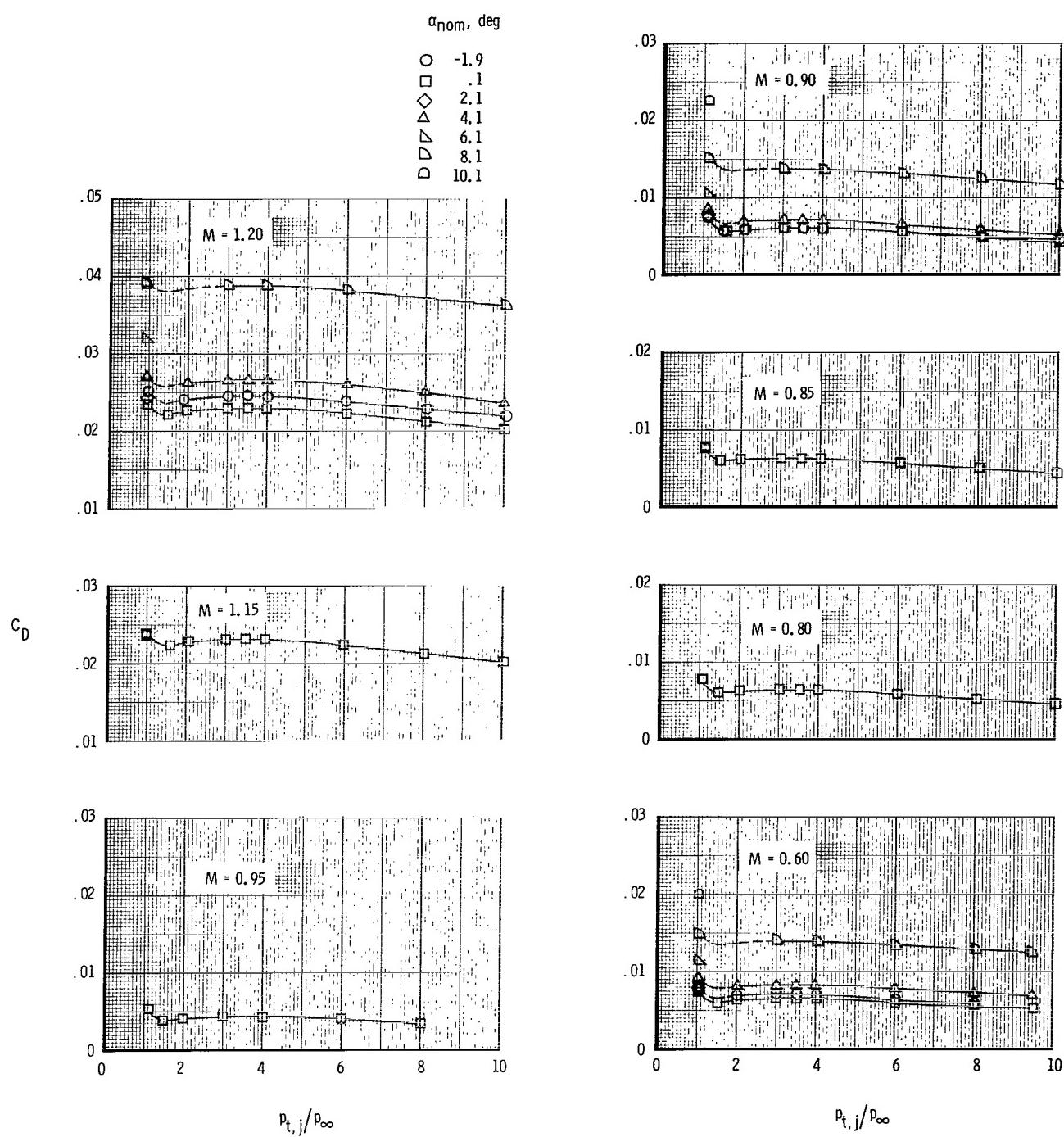


Figure 18.- Continued.



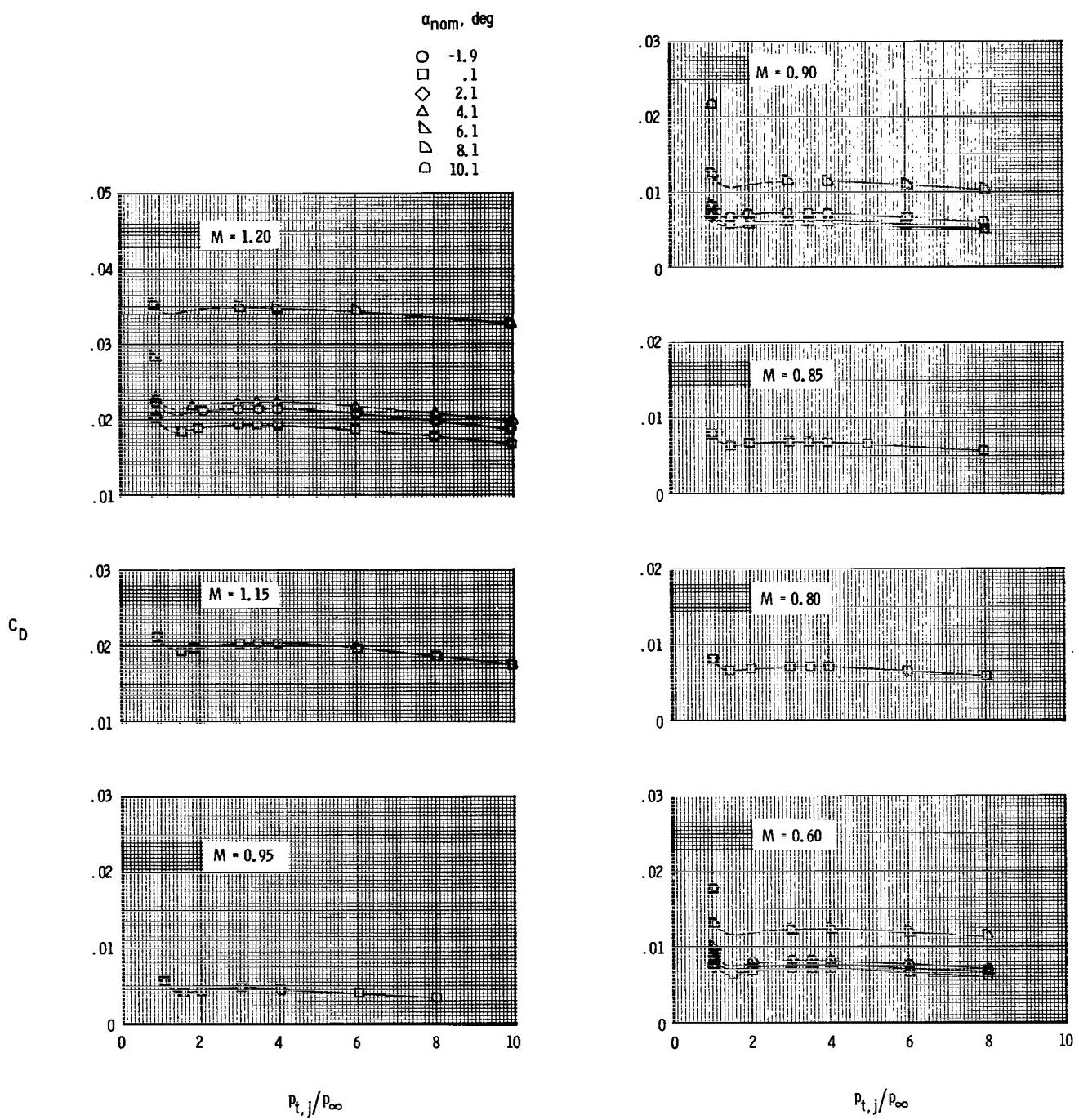
(n) Horizontal tails aft; vertical tails aft;  $\delta_h = -10^\circ$ .

Figure 18.- Concluded.



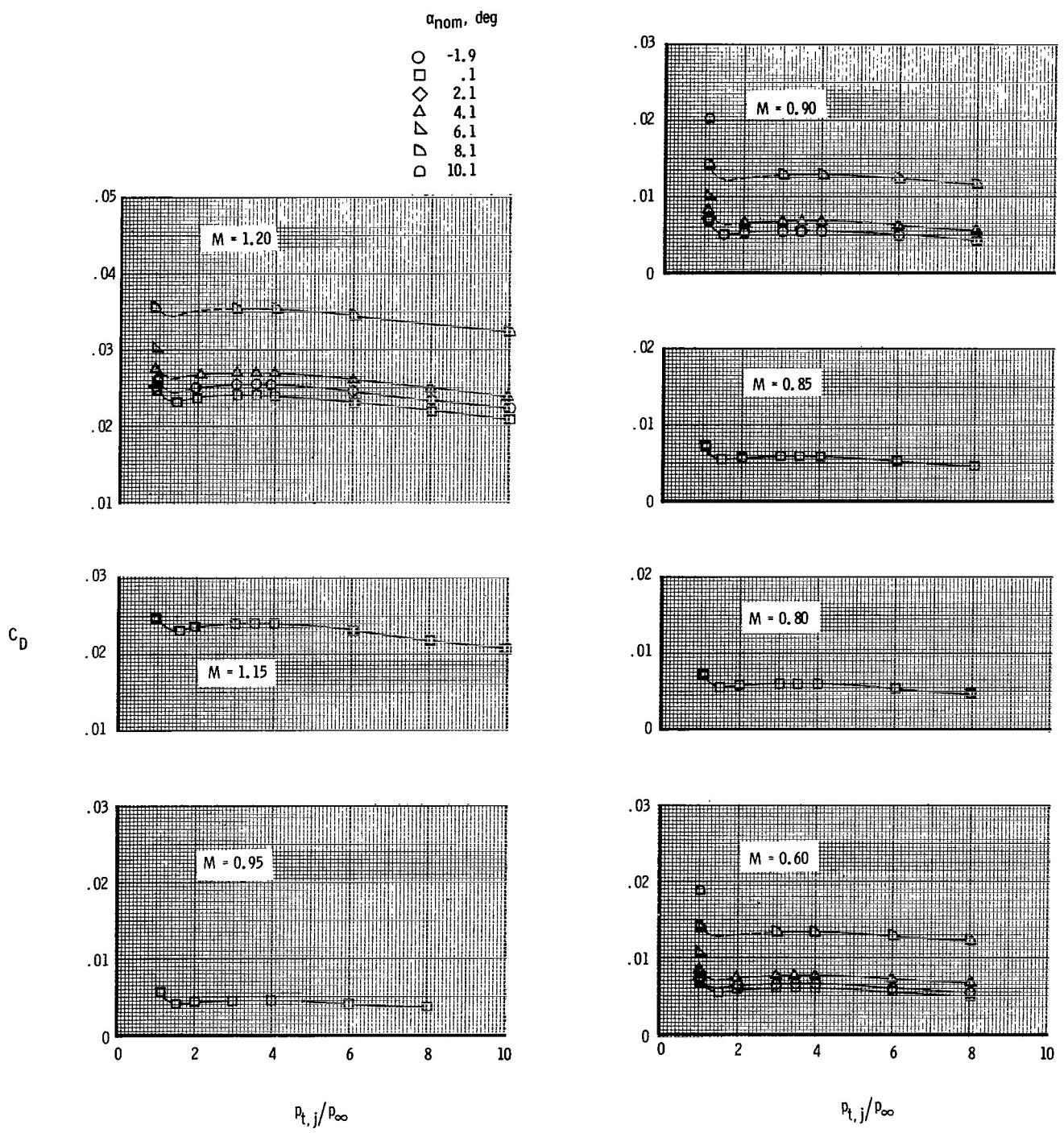
(a) Horizontal tails forward; vertical tail forward;  $\delta_h = 0^\circ$ .

Figure 19.- Variation of total measured afterbody drag coefficient with jet total-pressure ratio for various Mach numbers for twin-engine tail interference afterbody model with dry power nozzles, booms off, and single vertical tail.



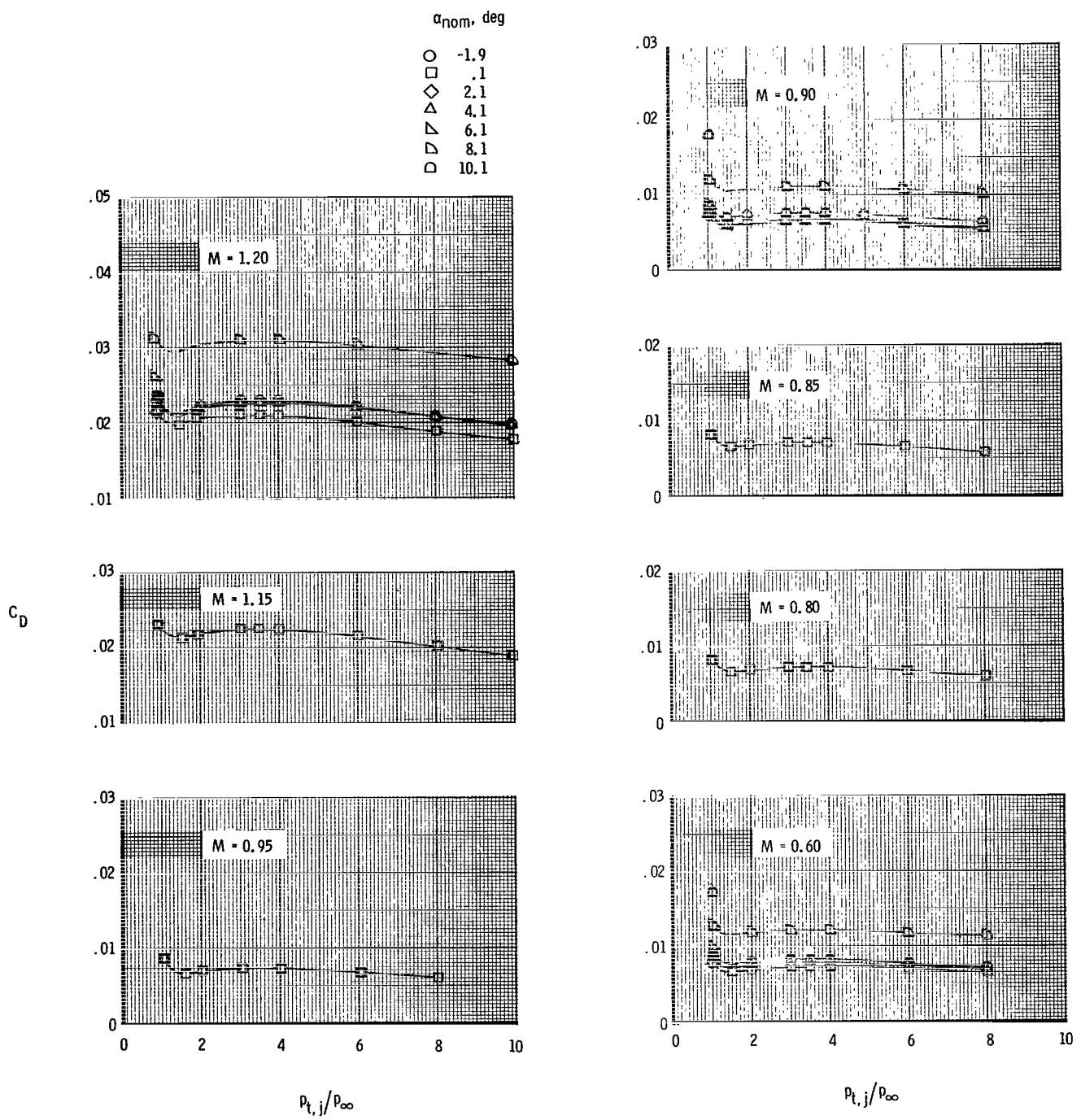
(b) Horizontal tails forward; vertical tail aft;  $\delta_h = 0^\circ$ .

Figure 19.- Continued.



(c) Horizontal tails aft; vertical tail forward;  $\delta_h = 0^\circ$ .

Figure 19.- Continued.



(d) Horizontal tails aft; vertical tail aft;  $\delta_h = 0^\circ$ .

Figure 19.- Concluded.

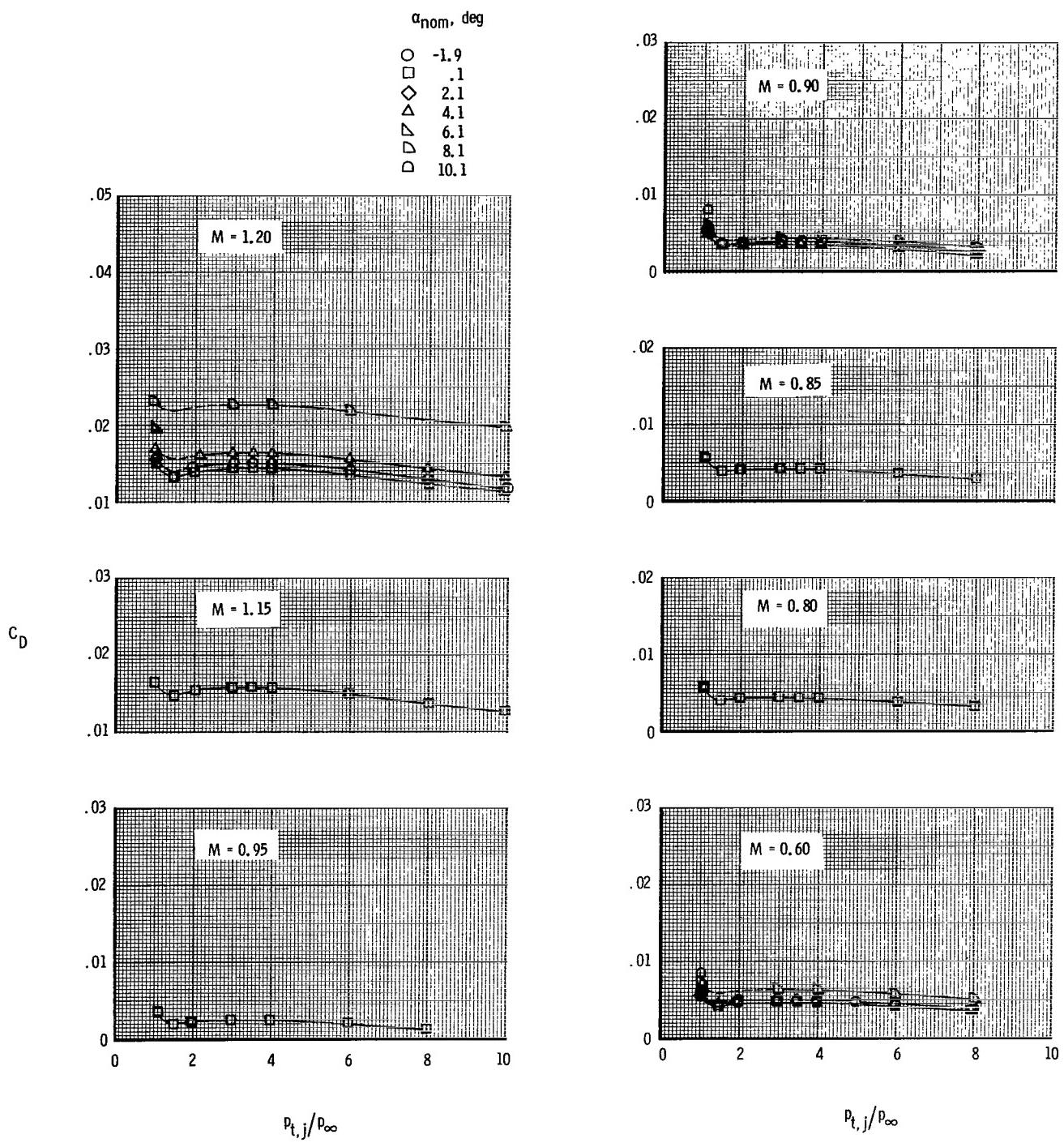
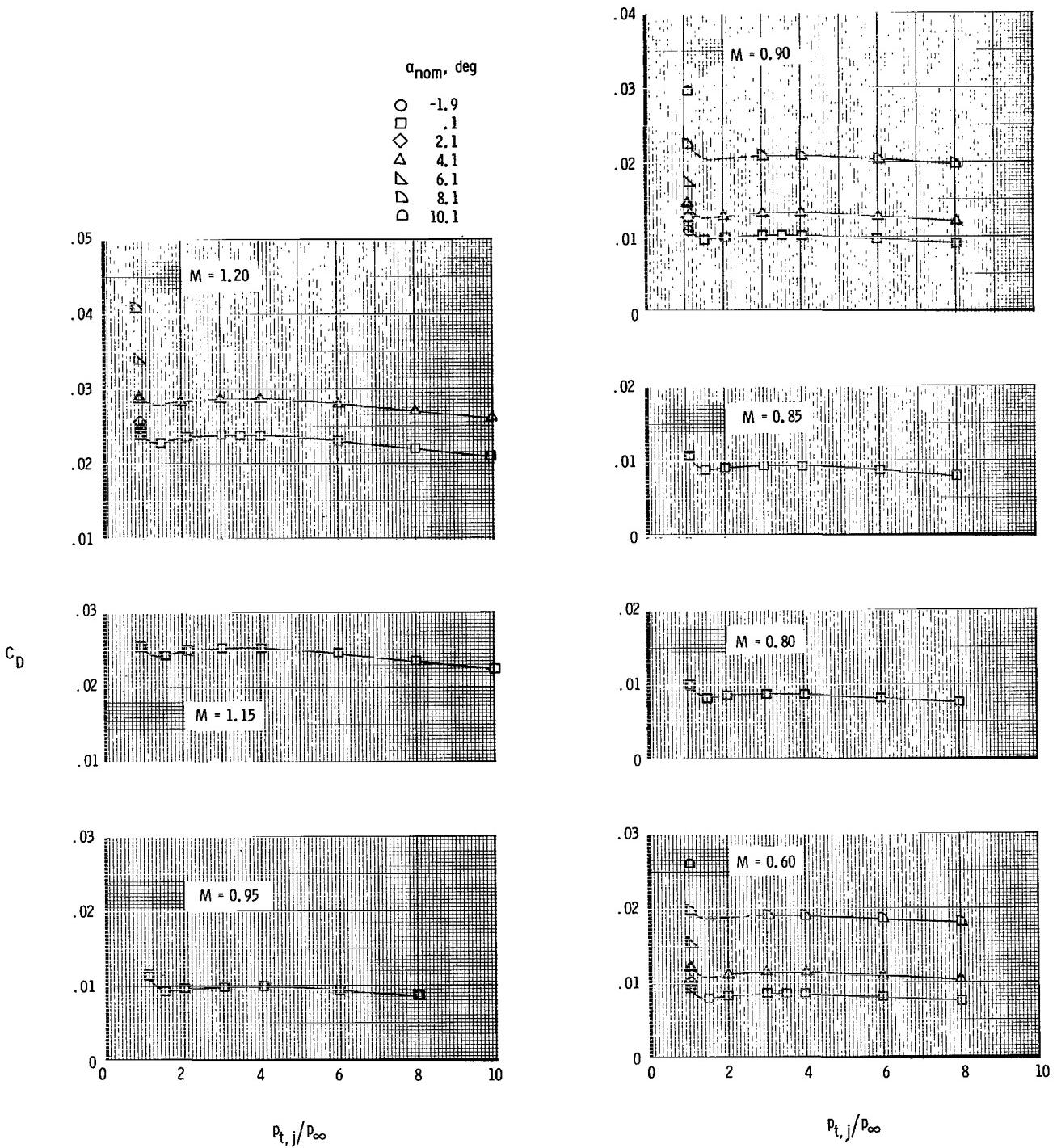
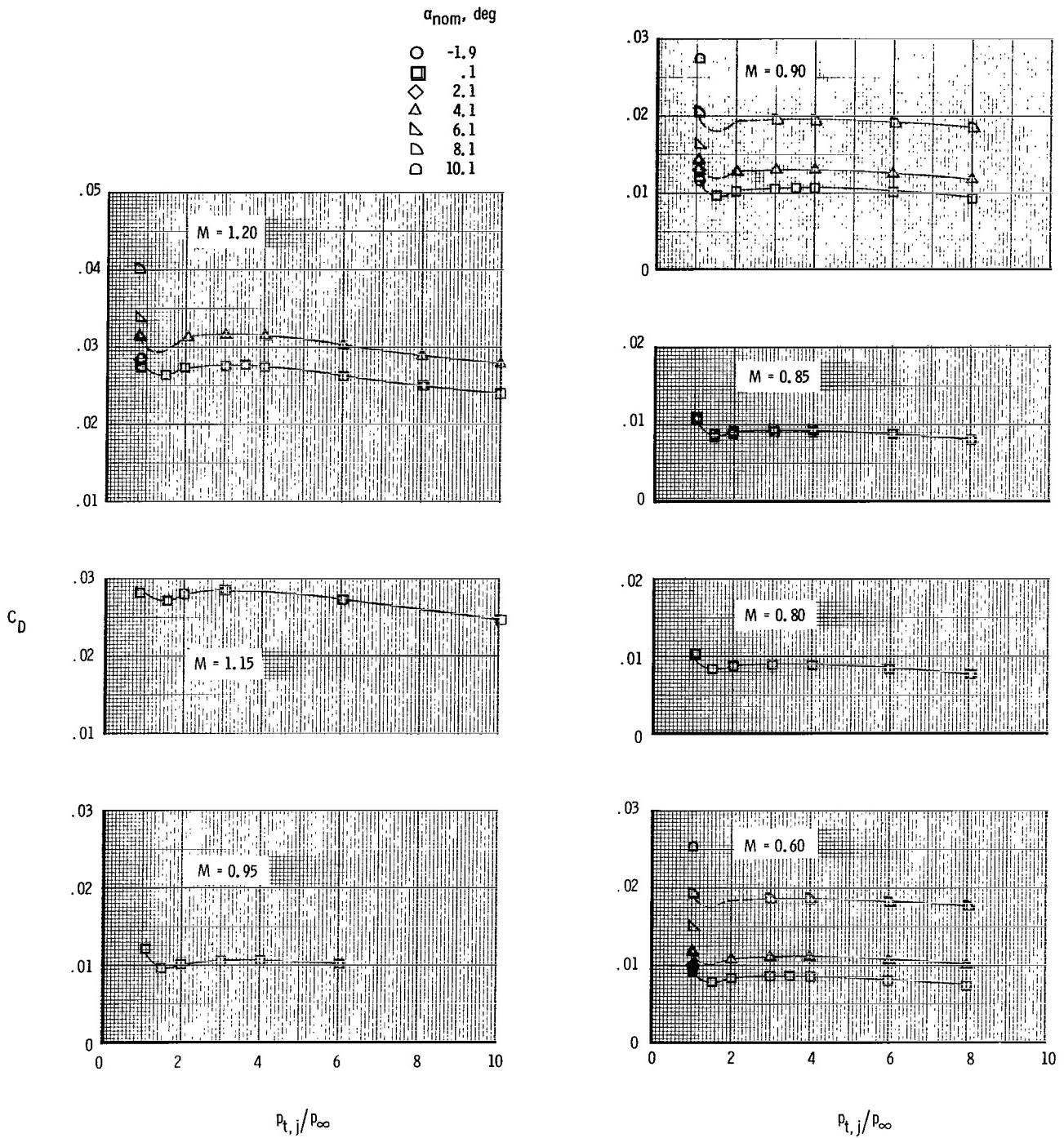


Figure 20.- Variación of total measured afterbody drag coefficient with jet total-pressure ratio for various Mach numbers for twin-engine tail interference afterbody model with dry power nozzles, booms on, and tails off.



(a) Horizontal tails forward on boom; vertical tails forward on boom;  $\delta_h = 0^\circ$ .

Figure 21.- Variation of total measured afterbody drag coefficient with jet total-pressure ratio for various Mach numbers for twin-engine tail interference afterbody model with dry power nozzles, booms on, and twin vertical tails.



(b) Horizontal tails forward on boom; vertical tails mid on boom;  $\delta_h = 0^\circ$ .

Figure 21.- Continued.

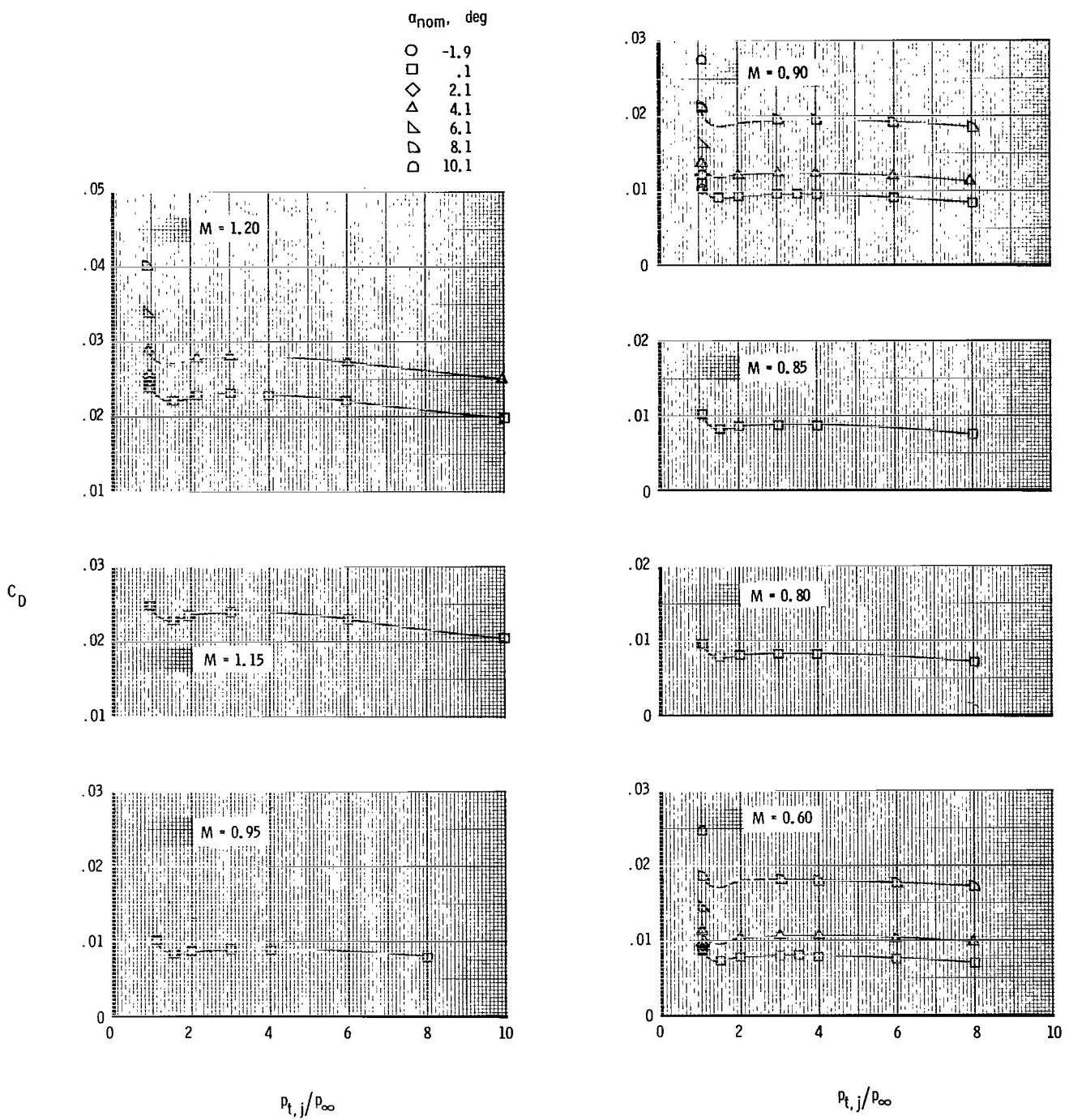
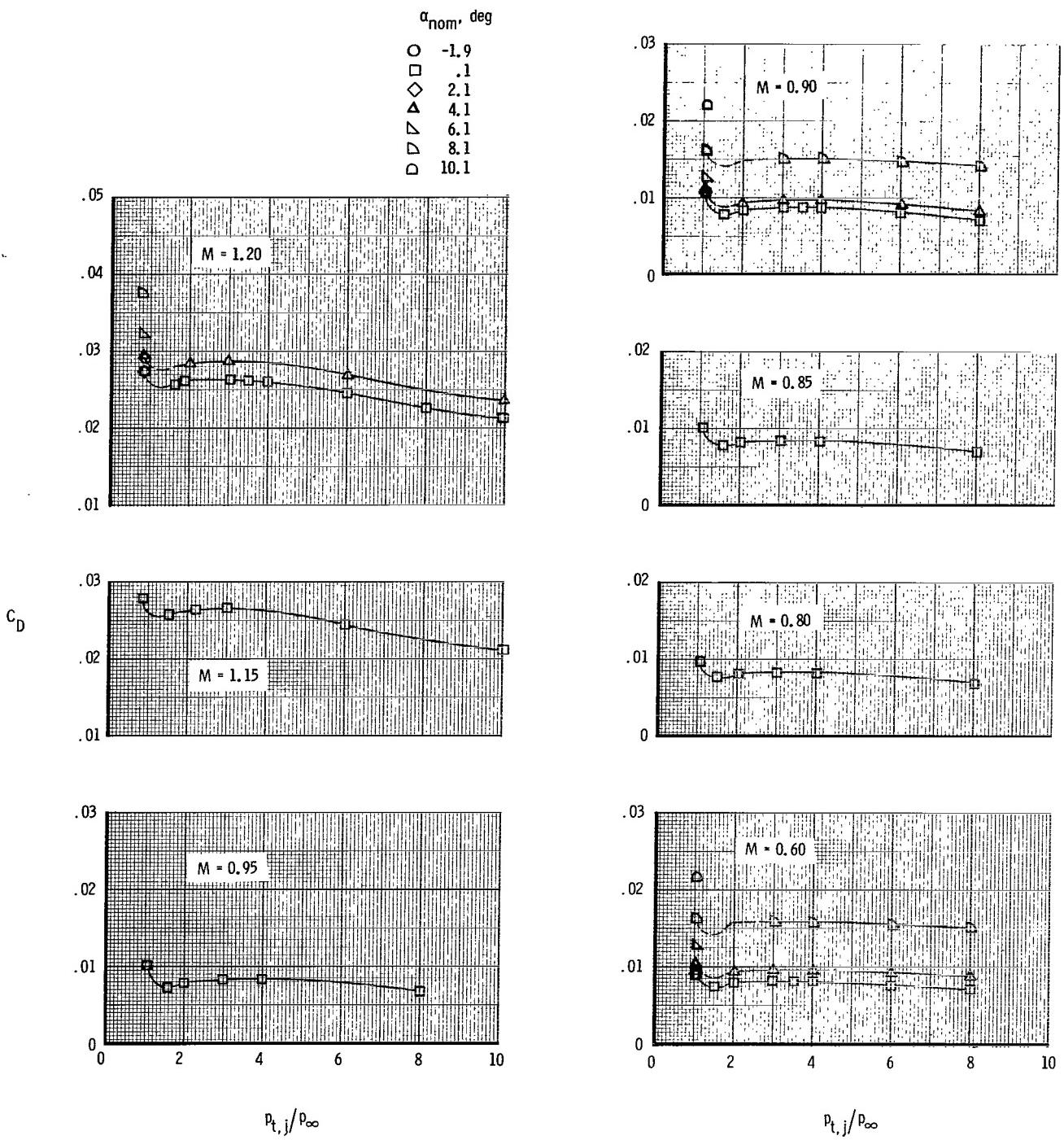
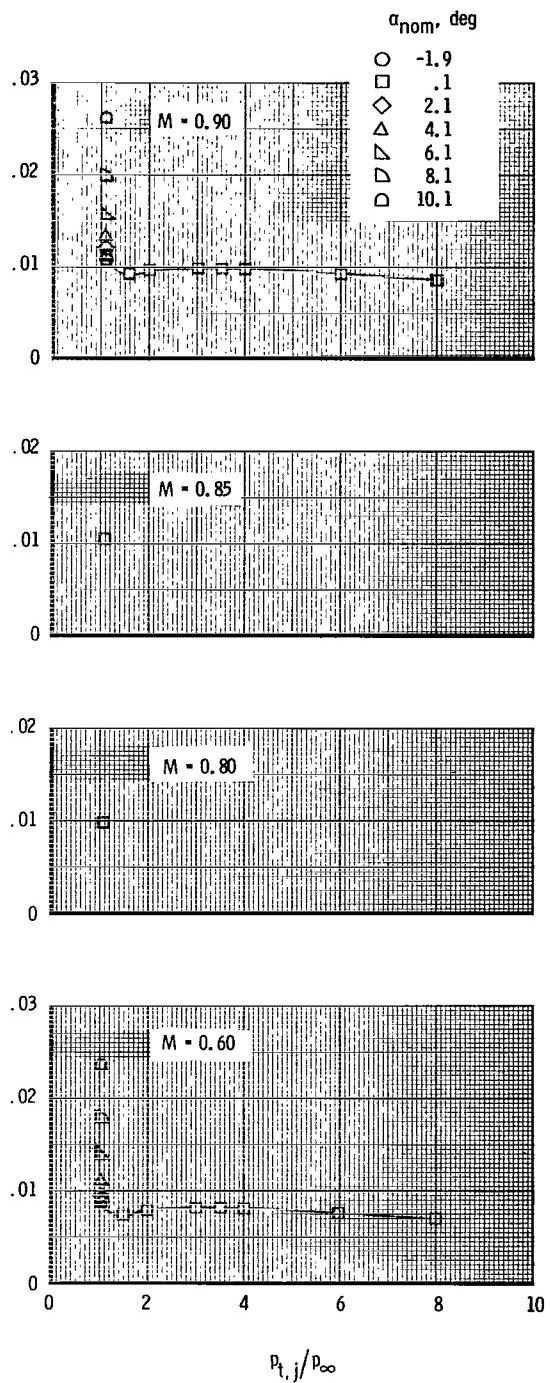


Figure 21.- Continued.



(d) Horizontal tails aft on boom; vertical tails aft on boom;  $\delta_h = 0^\circ$ .

Figure 21.- Continued.



(e) Horizontal tails aft on boom; vertical tails mid on fuselage;  $\delta_h = 0^\circ$ .

Figure 21.-- Concluded.

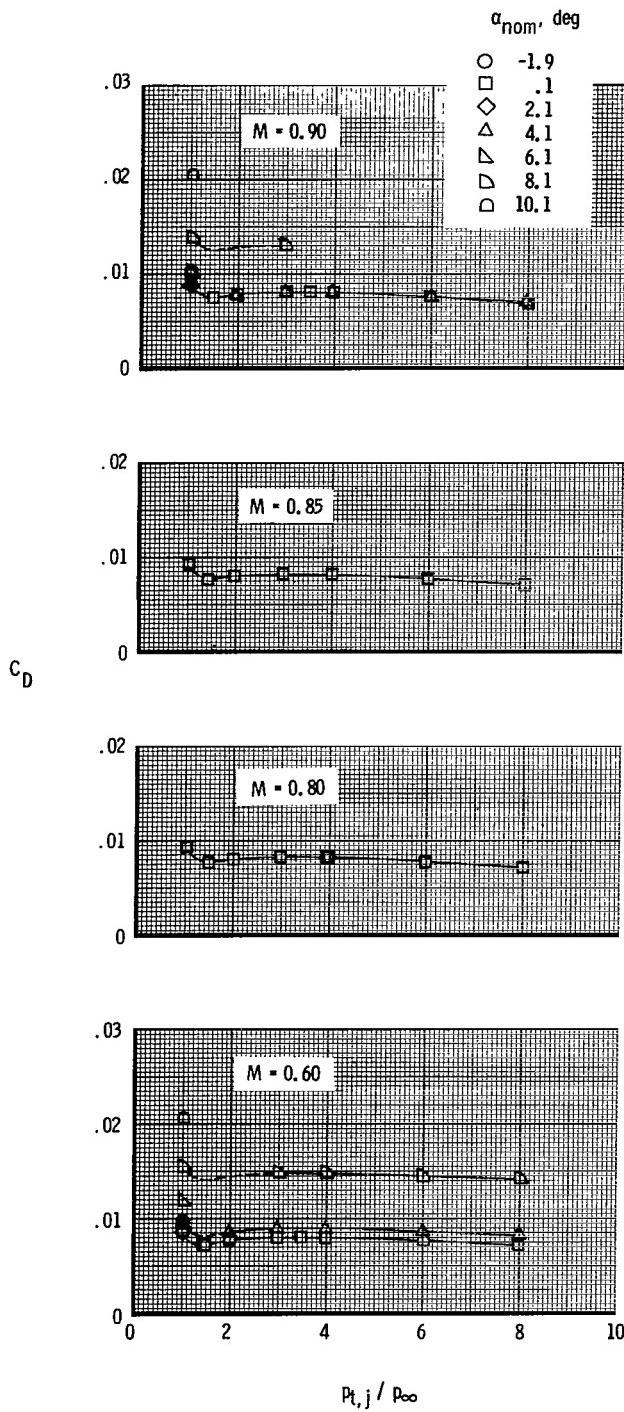


Figure 22.- Variation of total measured afterbody drag coefficient with jet total-pressure ratio for various Mach numbers for twin-engine tail interference afterbody model with dry power nozzles, booms on, horizontal tails forward on boom, single vertical tail aft on fuselage, and  $\delta_h = 0^\circ$ .

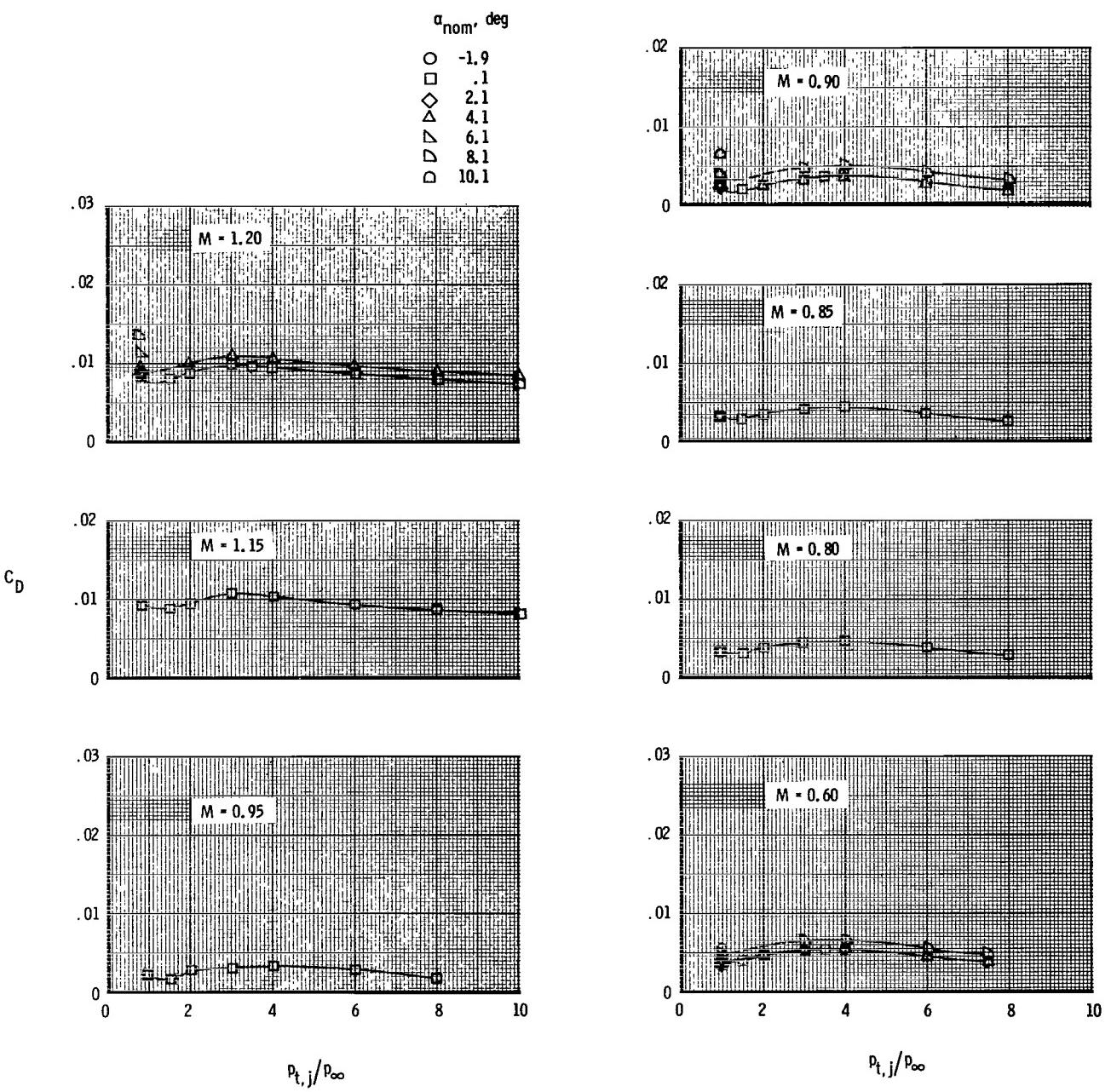
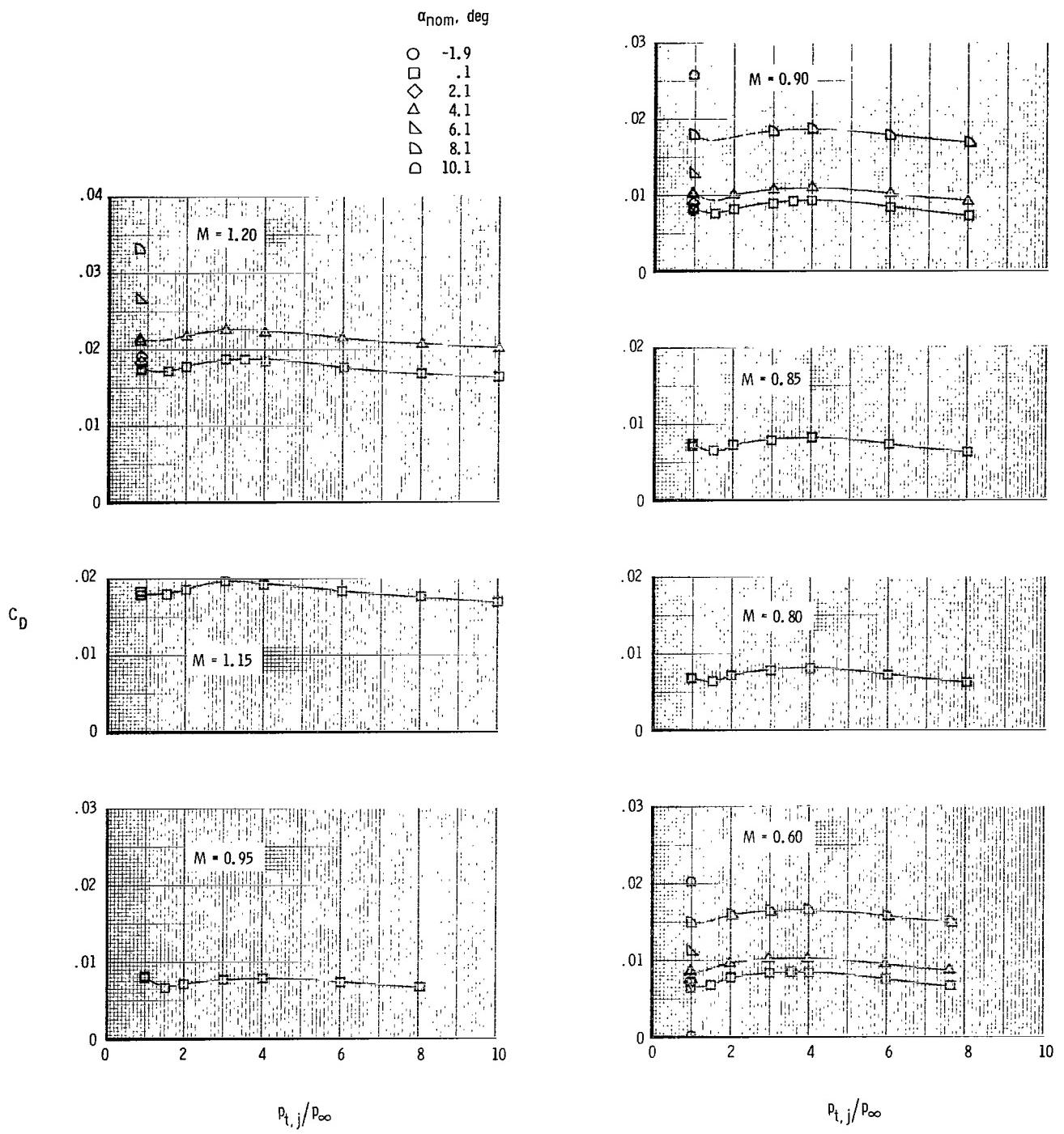
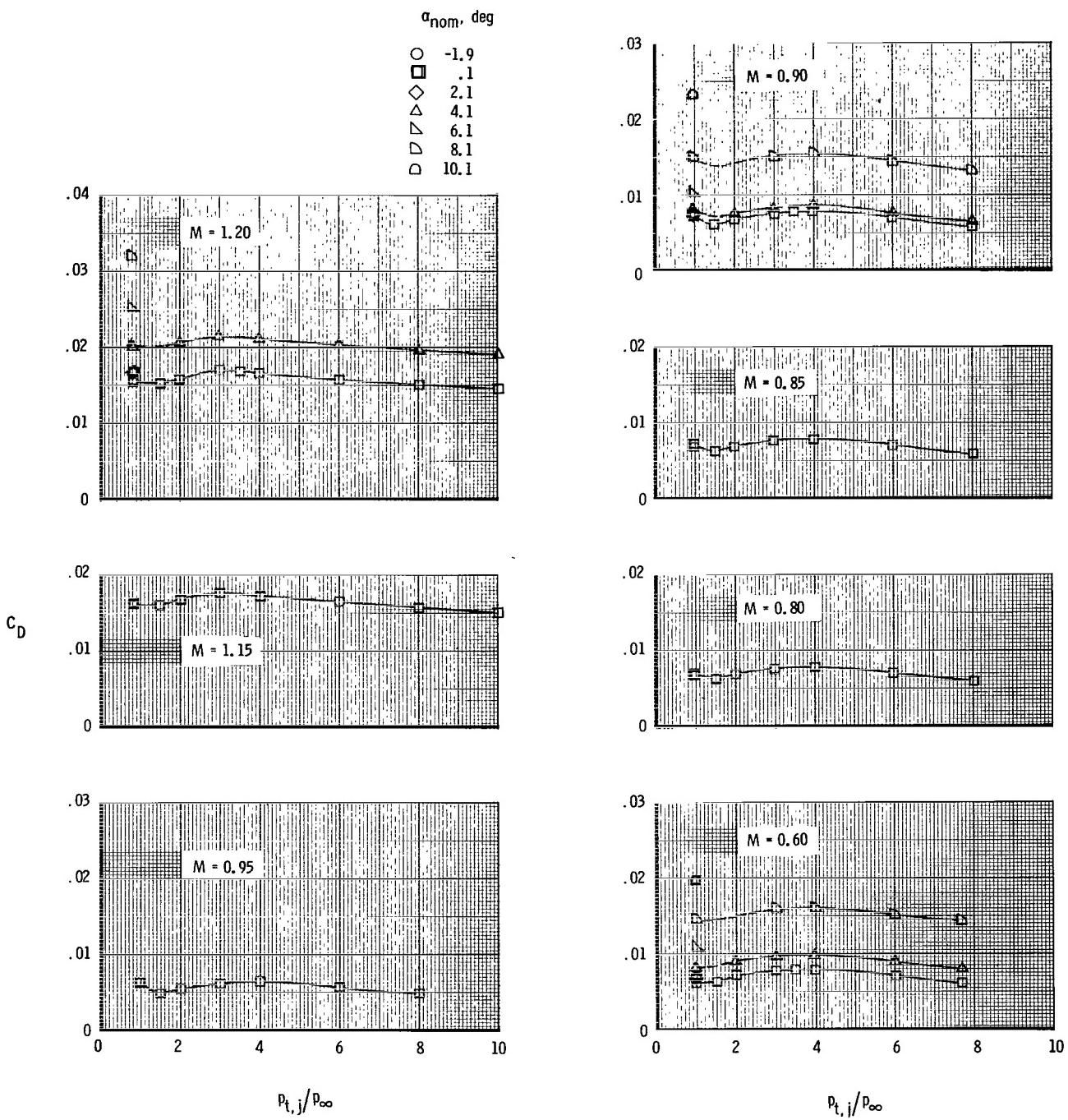


Figure 23.— Variation of total measured afterbody drag coefficient with jet total-pressure ratio for various Mach numbers for twin-engine tail interference afterbody model with A/B nozzles, booms off, and tails off.



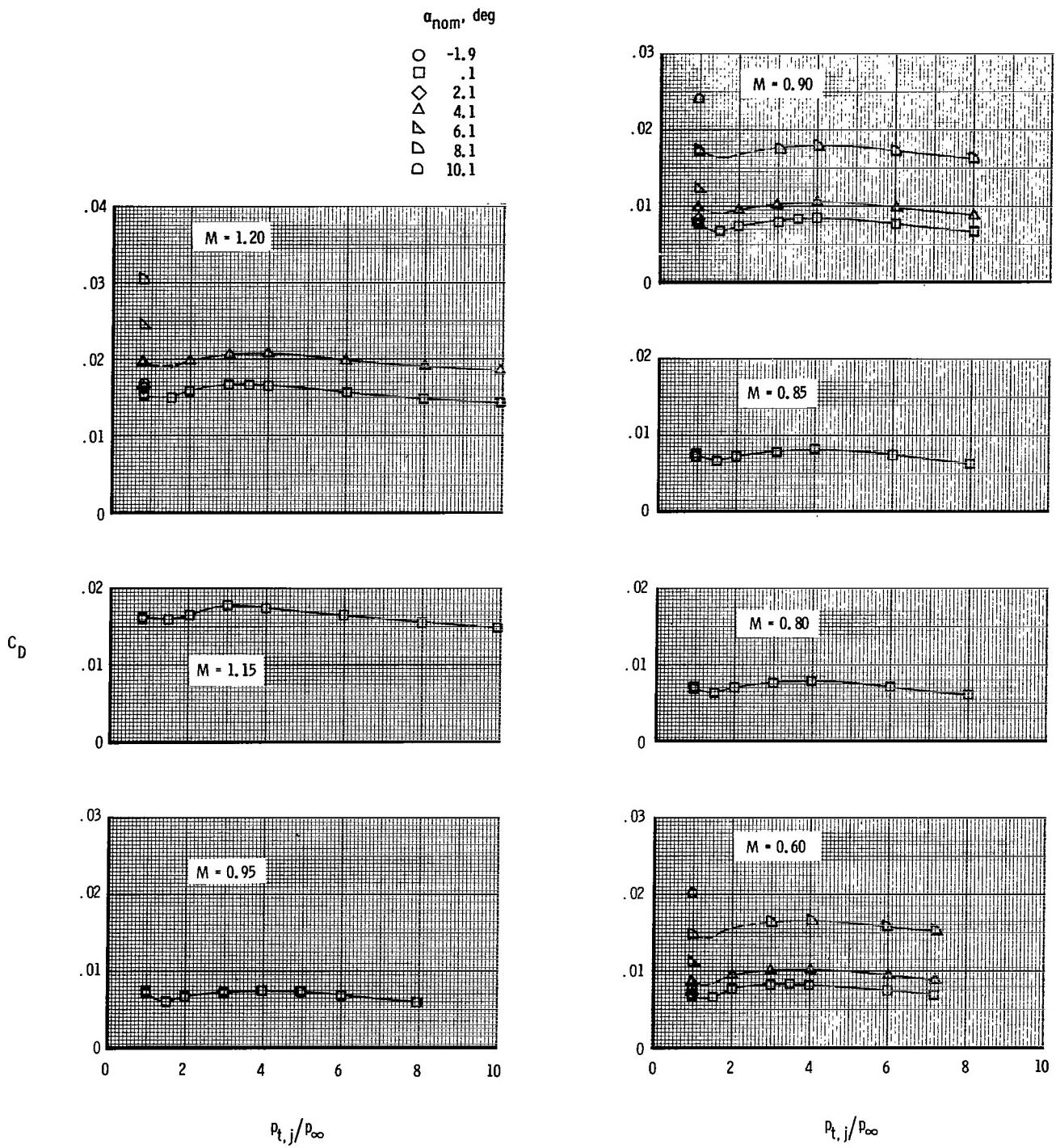
(a) Horizontal tails forward; vertical tails forward;  $\delta_h = 0^\circ$ .

Figure 24.- Variation of total measured afterbody drag coefficient with jet total-pressure ratio for various Mach numbers for twin-engine tail interference afterbody model with A/B nozzles, booms off, and twin vertical tails.



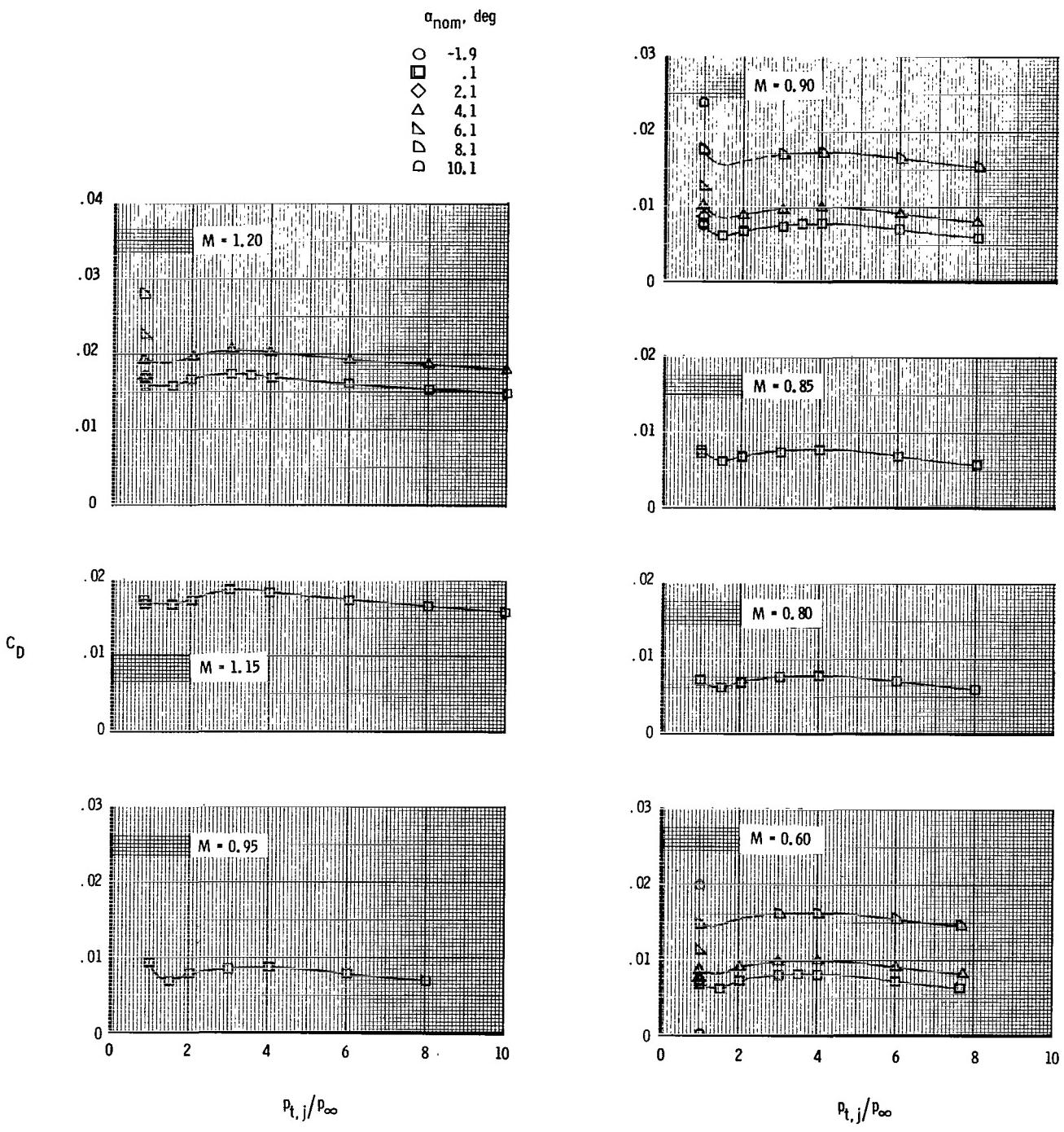
(b) Horizontal tails forward; vertical tails aft;  $\delta_h = 0^\circ$ .

Figure 24.- Continued.



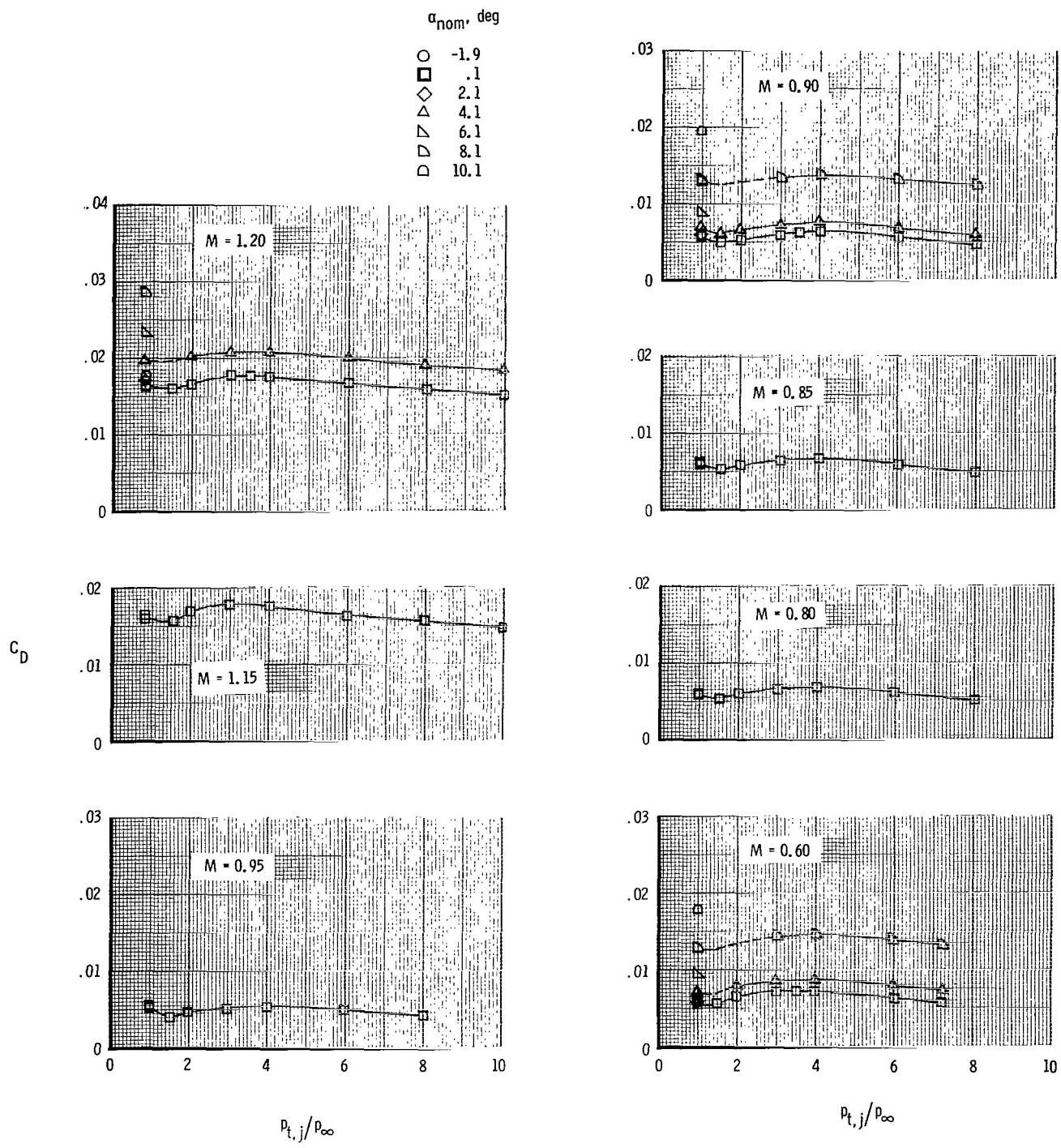
(c) Horizontal tails aft; vertical tails forward;  $\delta_h = 0^\circ$ .

Figure 24.- Continued.



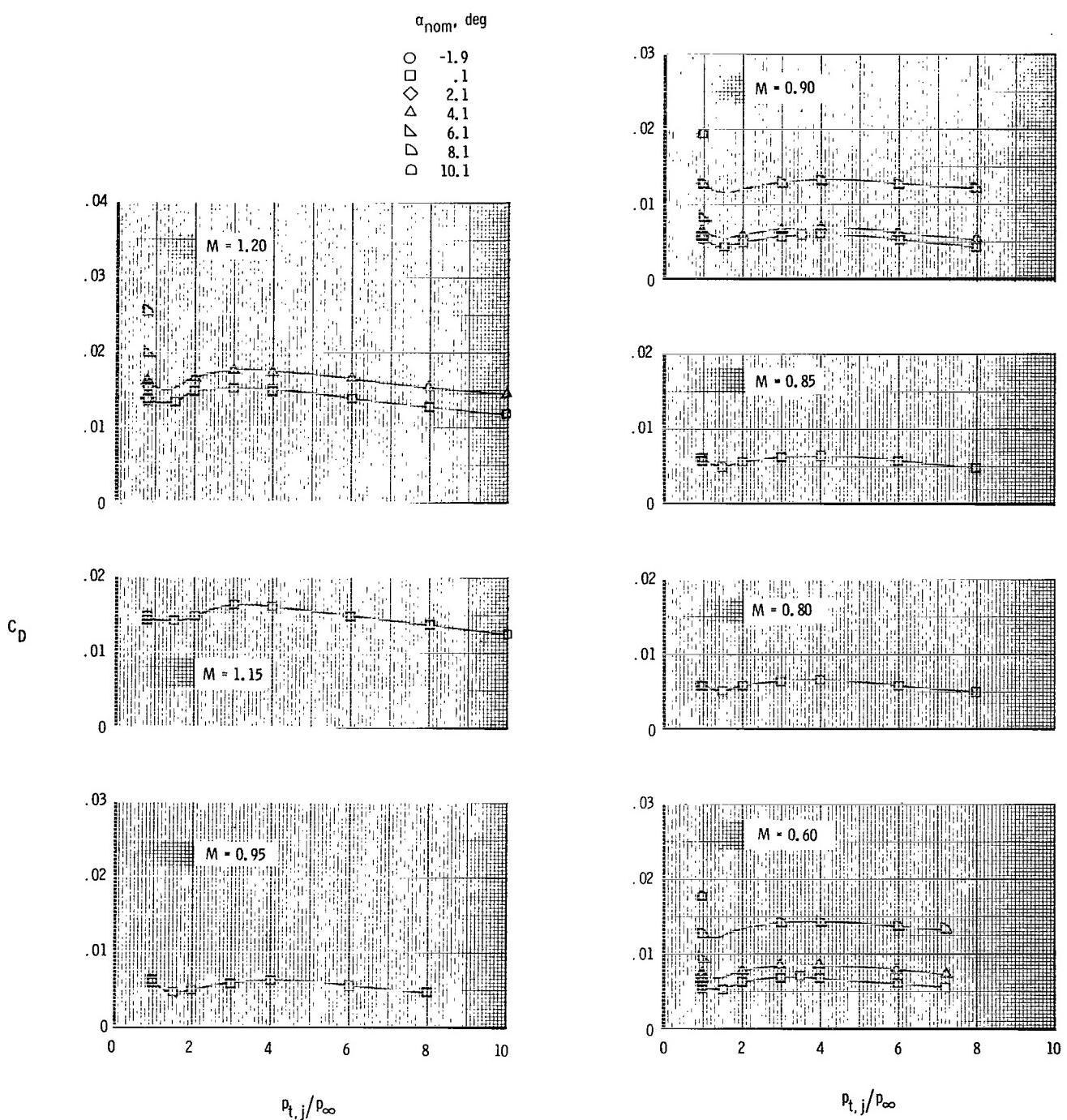
(d) Horizontal tails aft; vertical tails aft;  $\delta_h = 0^\circ$ .

Figure 24.- Concluded.



(a) Horizontal tails aft; vertical tail forward;  $\delta_h = 0^\circ$ .

Figure 25.- Variation of total measured afterbody drag coefficient with jet total-pressure ratio for various Mach numbers for twin-engine tail interference afterbody model with A/B nozzles, booms off, and single vertical tail.



(b) Horizontal tails aft; vertical tail aft;  $\delta_h = 0^\circ$ .

Figure 25.- Concluded.

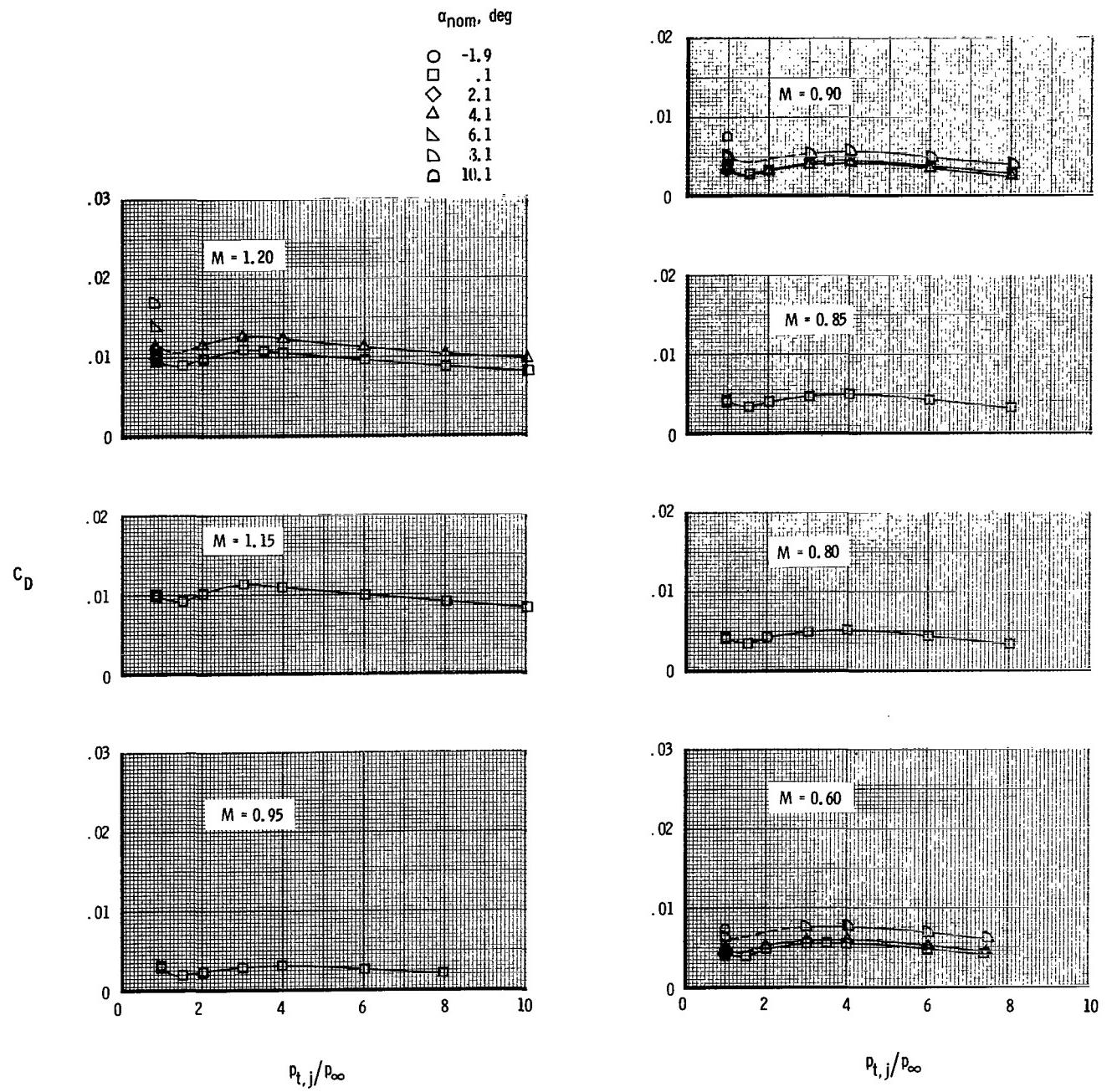
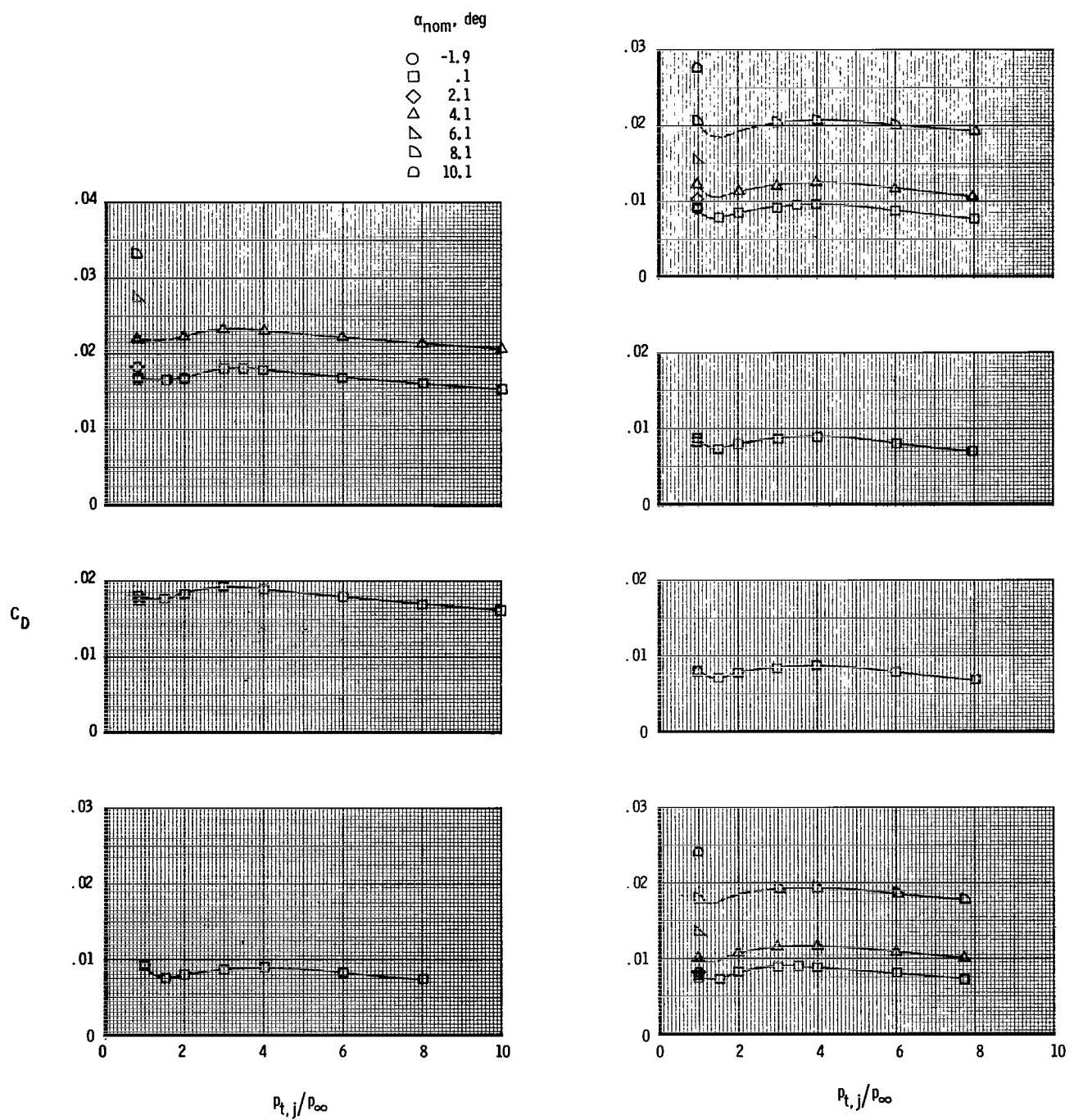
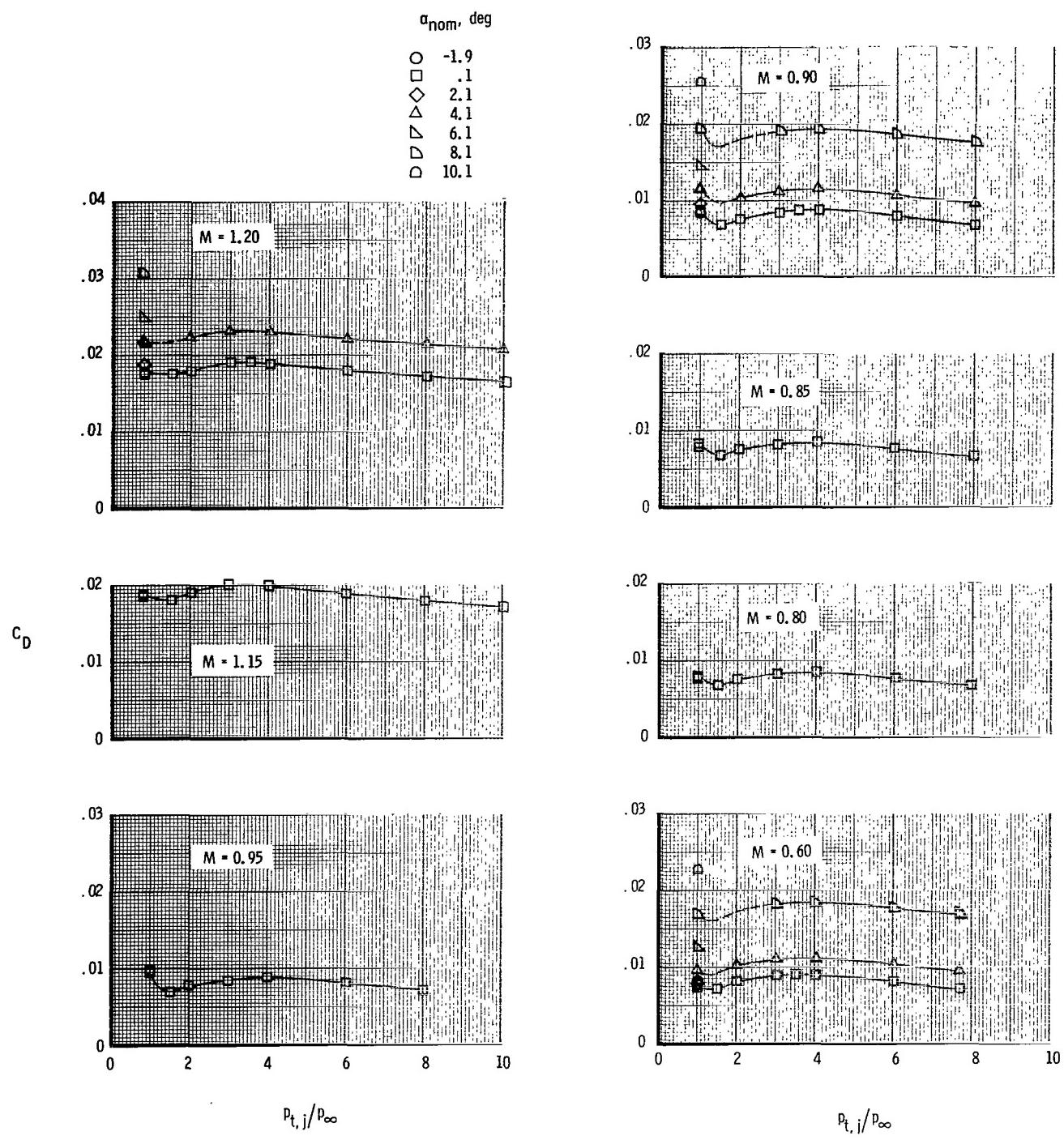


Figure 26.- Variation of total measured afterbody drag coefficient with jet total-pressure ratio for various Mach numbers for twin-engine tail interference afterbody model with A/B nozzles, booms on, and tails off.



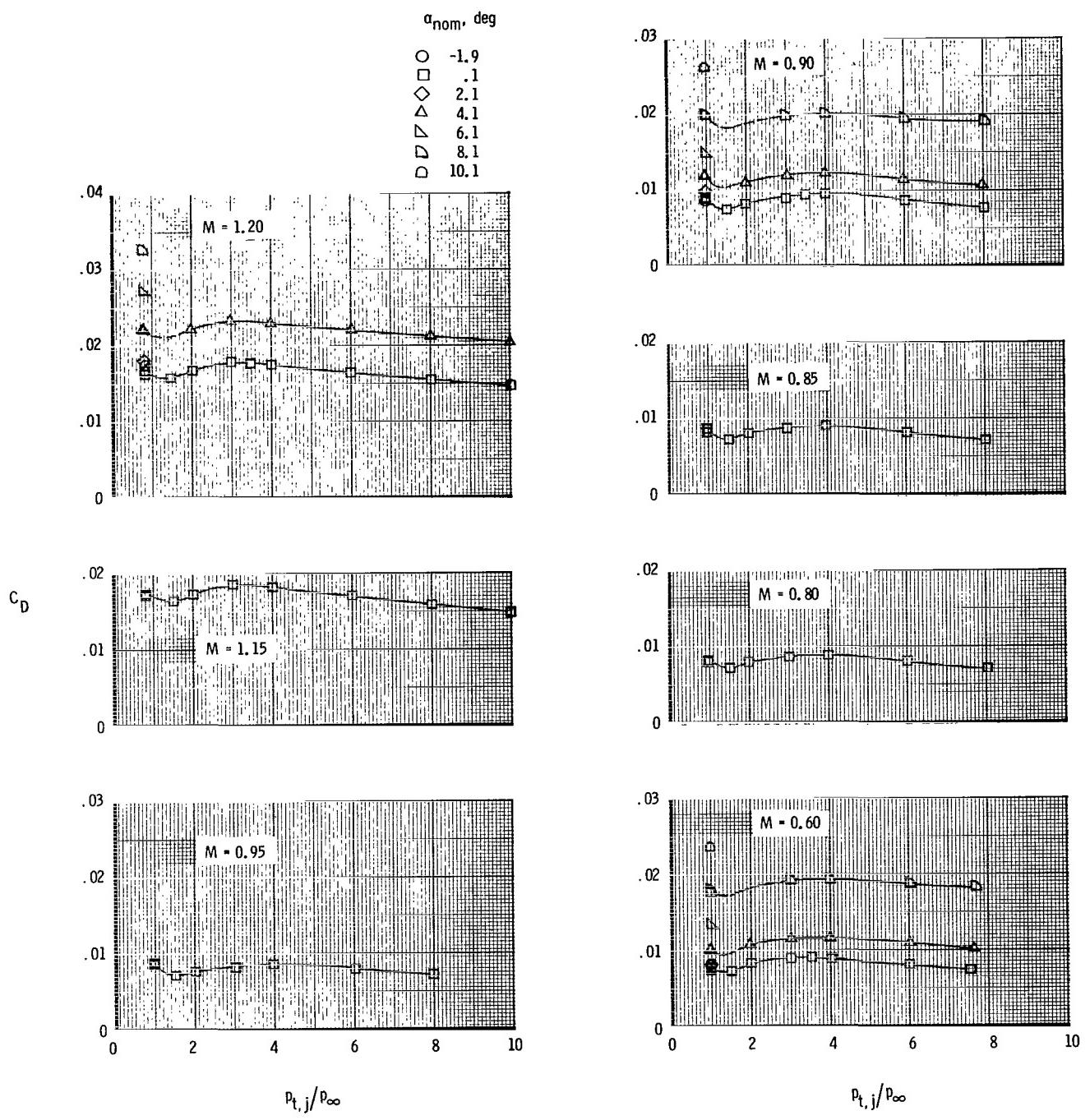
(a) Horizontal tails forward on boom; vertical tails forward on boom;  $\delta_h = 0^\circ$ .

Figure 27.- Variation of total measured afterbody drag coefficient with jet total-pressure ratio for various Mach numbers for twin-engine tail interference afterbody model with A/B nozzles, booms on, and twin vertical tails.



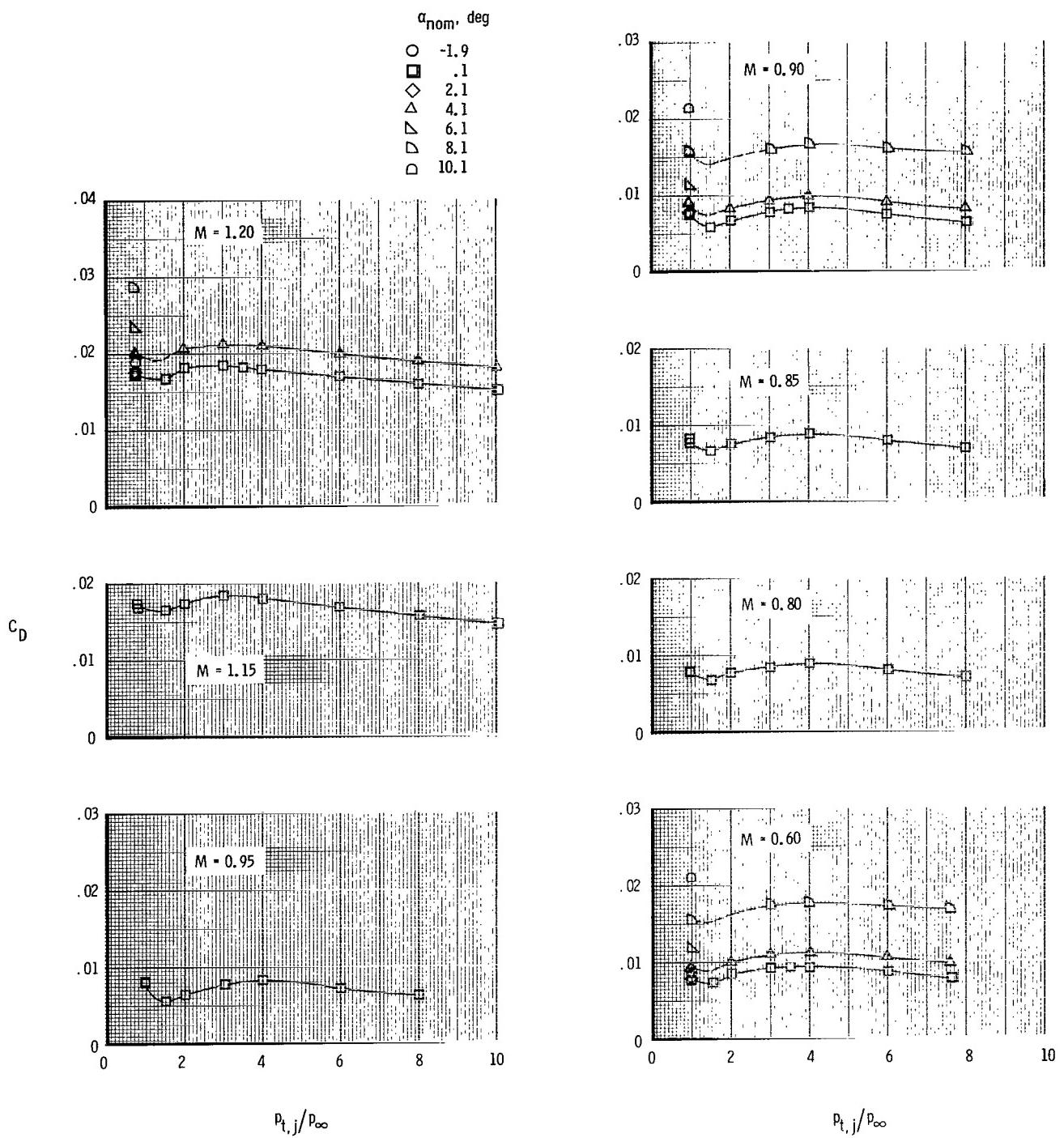
(b) Horizontal tails forward on boom; vertical tails mid on boom;  $\delta_h = 0^\circ$ .

Figure 27.- Continued.



(c) Horizontal tails aft on boom; vertical tails forward on boom;  $\delta_h = 0^\circ$ .

Figure 27.- Continued.



(d) Horizontal tails aft on boom; vertical tails aft on boom;  $\delta_h = 0^\circ$ .

Figure 27.- Concluded.

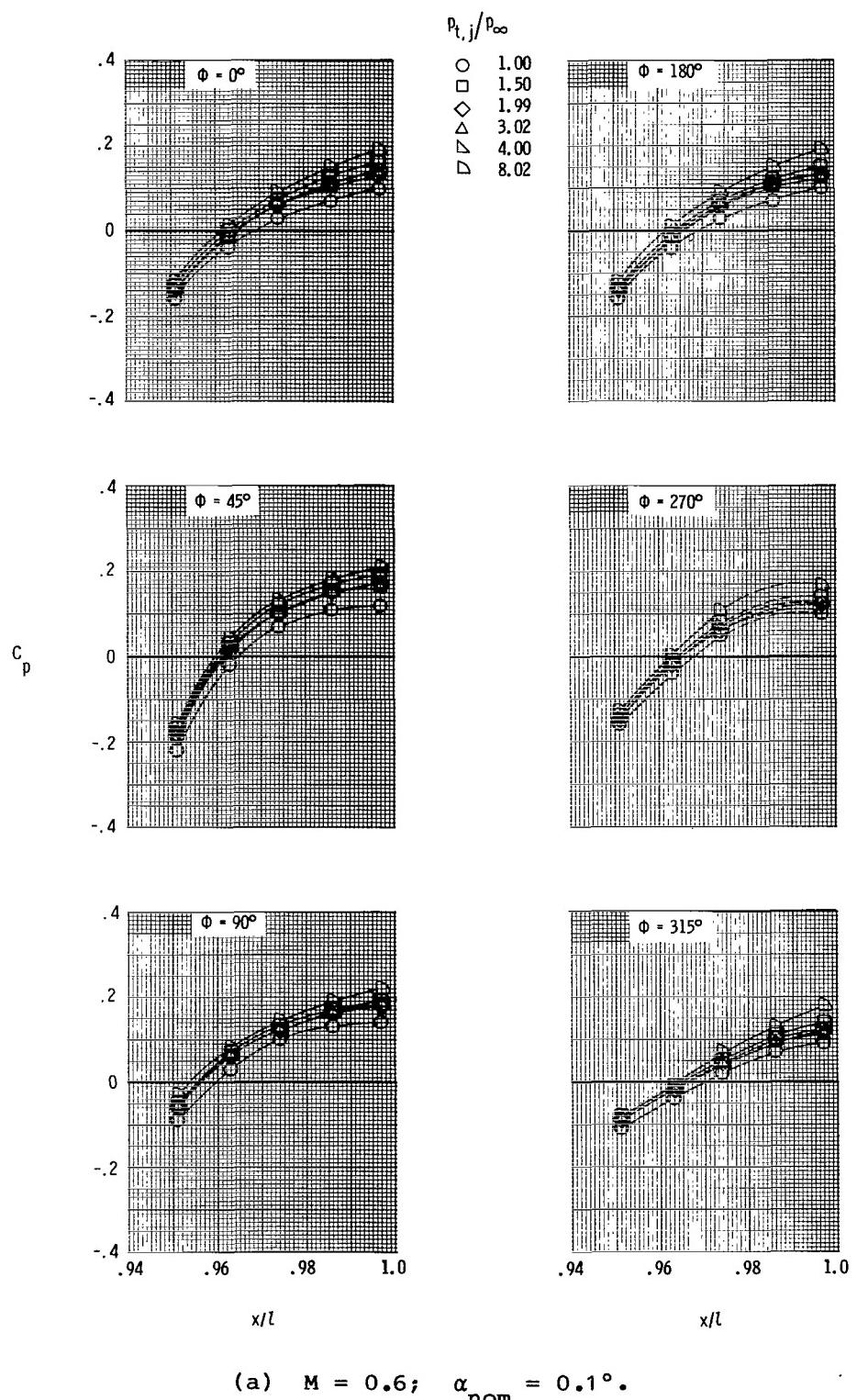
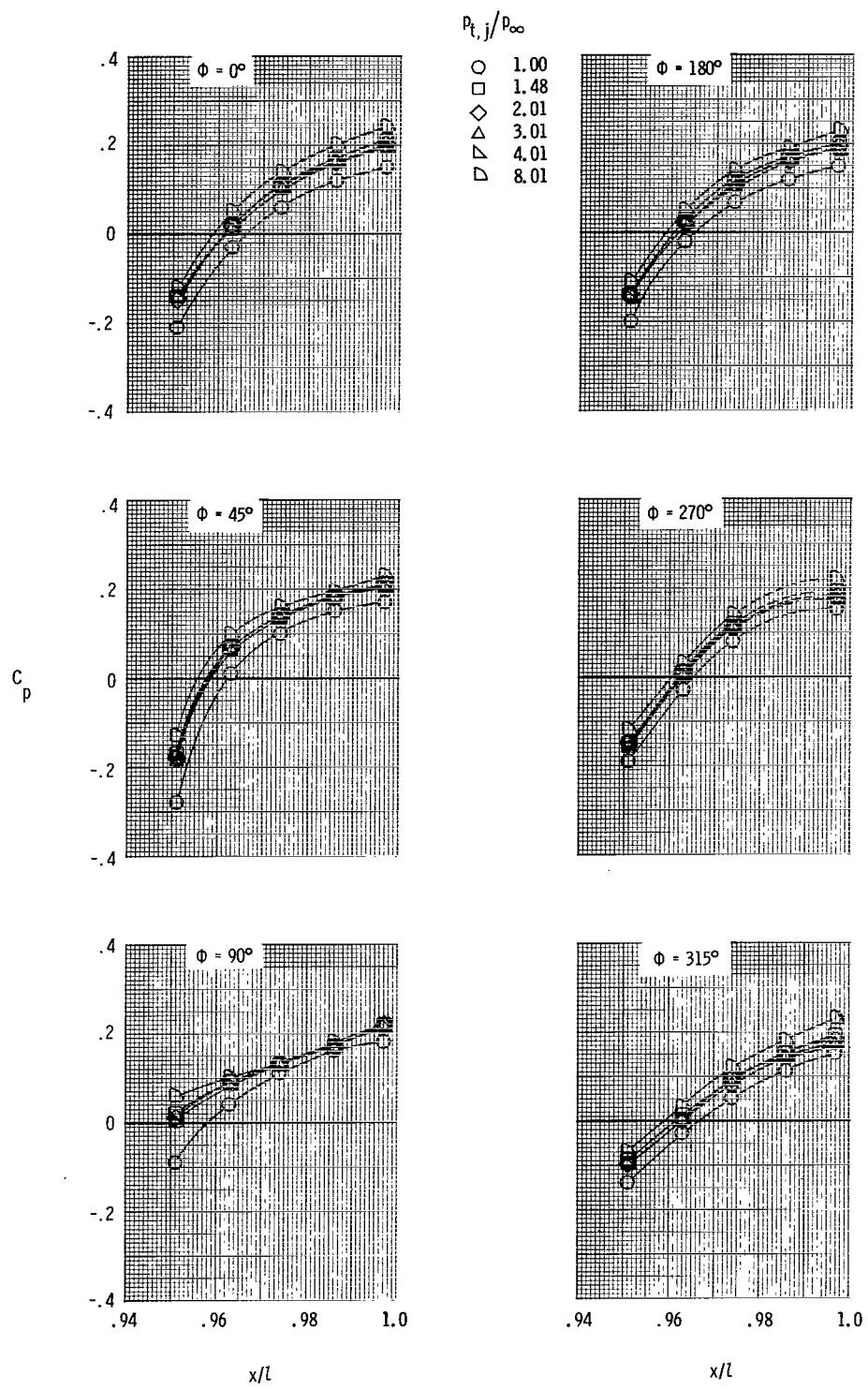
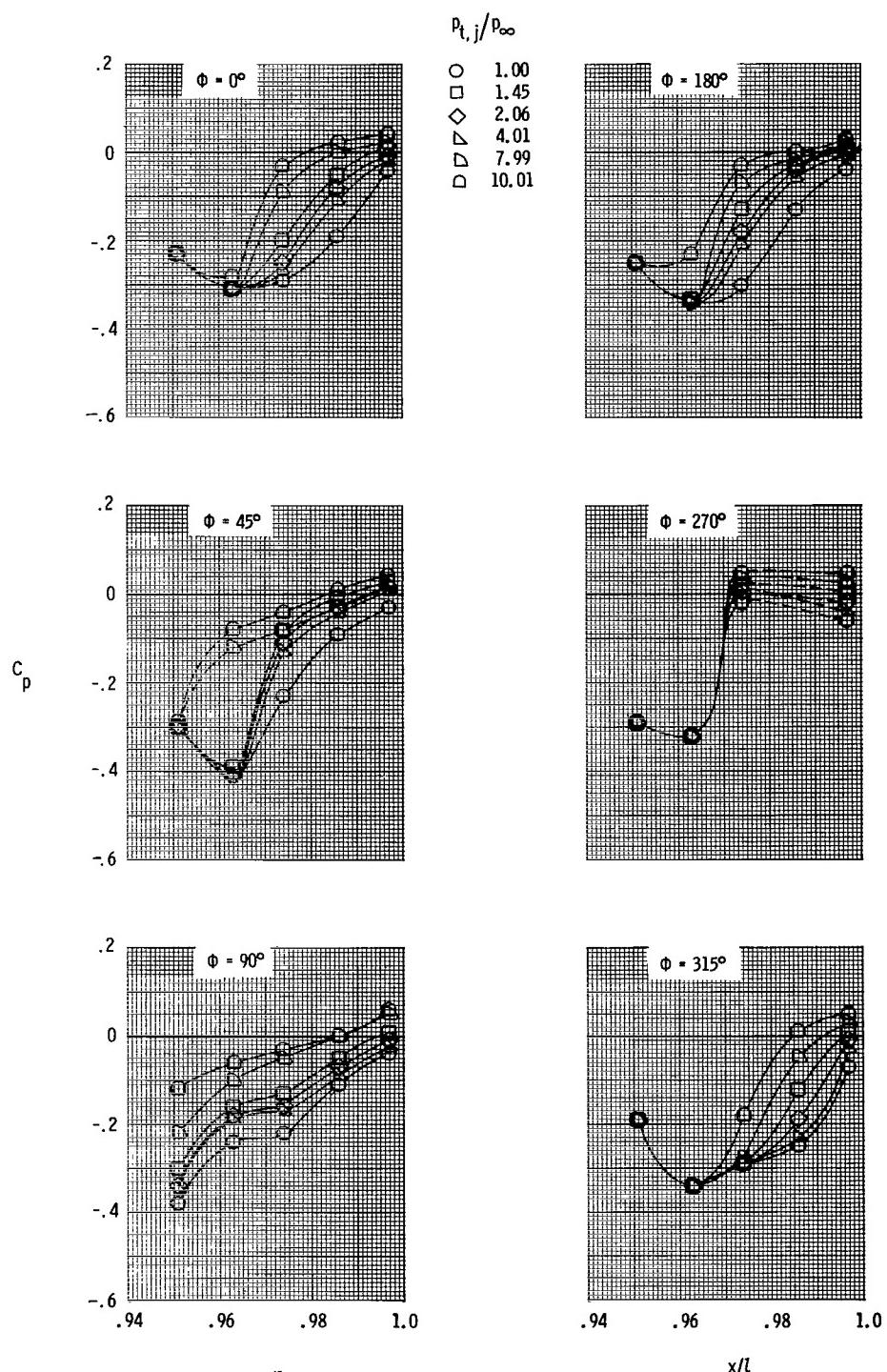


Figure 28.- Effect of jet total-pressure ratio on nozzle pressure distribution with dry power nozzles, booms off, and tails off.



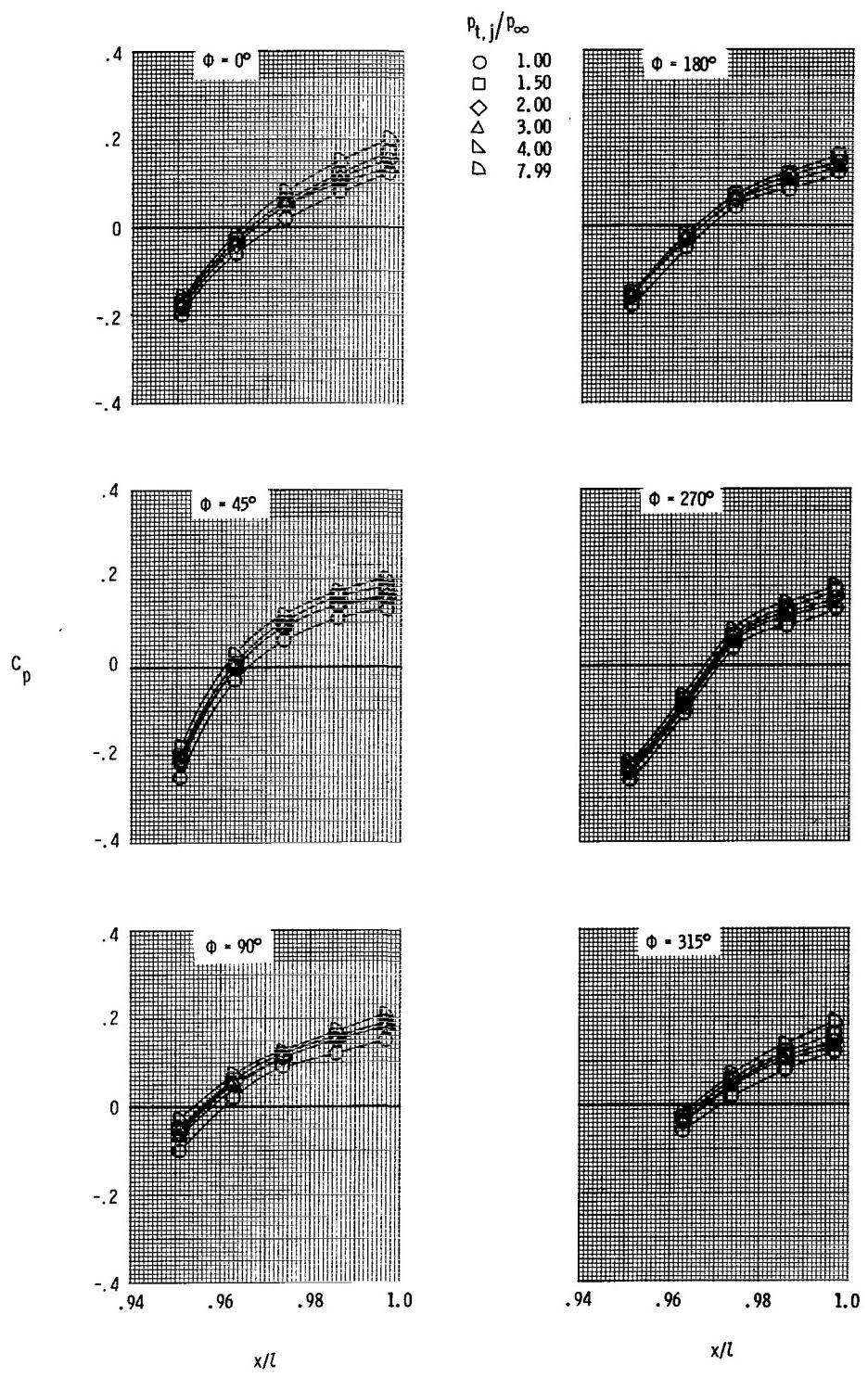
(b)  $M = 0.9$ ;  $\alpha_{\text{nom}} = 0.1^\circ$ .

Figure 28.- Continued.



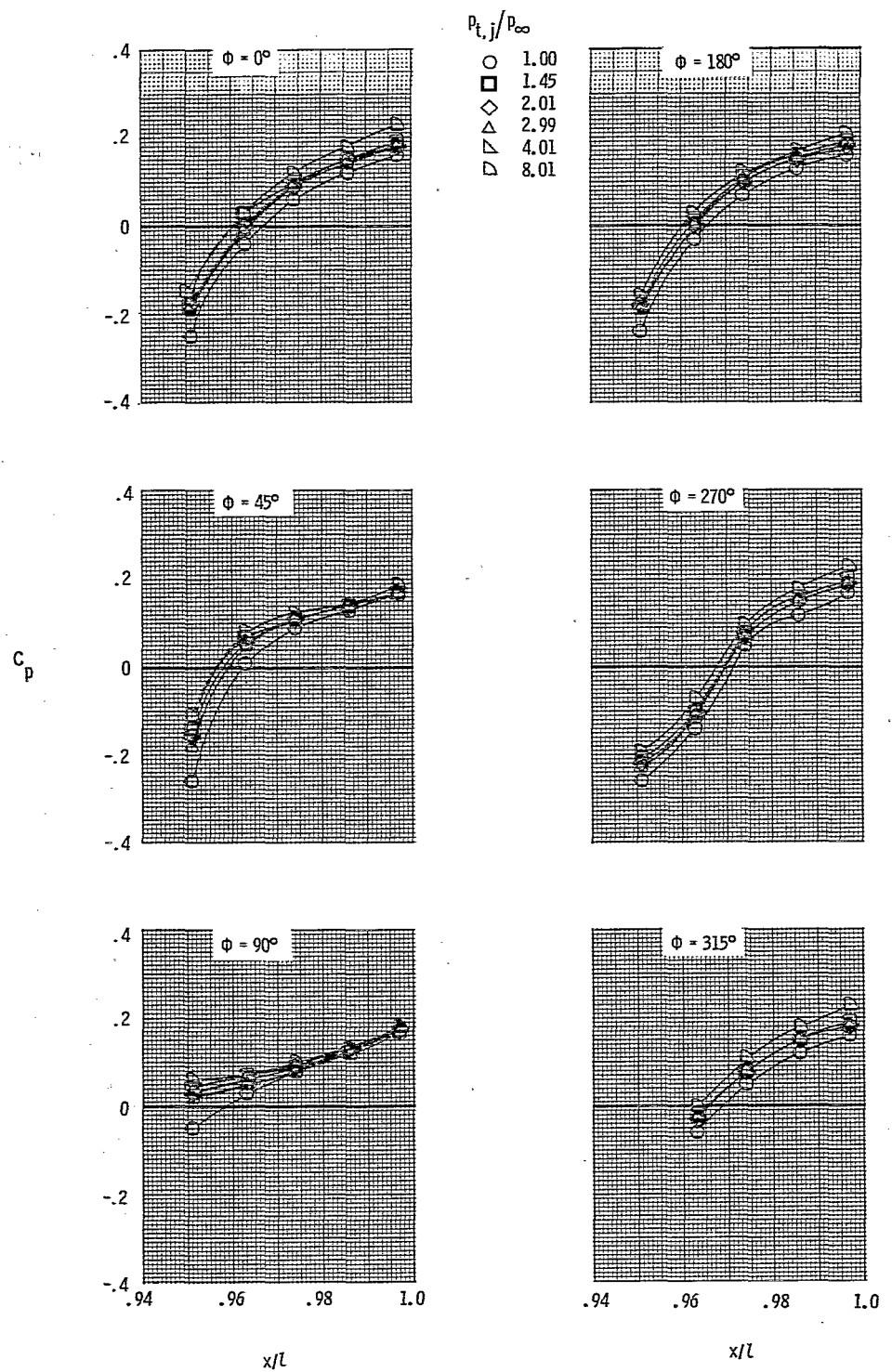
(c)  $M = 1.2; \alpha_{\text{nom}} = 0.1^\circ.$

Figure 28.- Concluded.



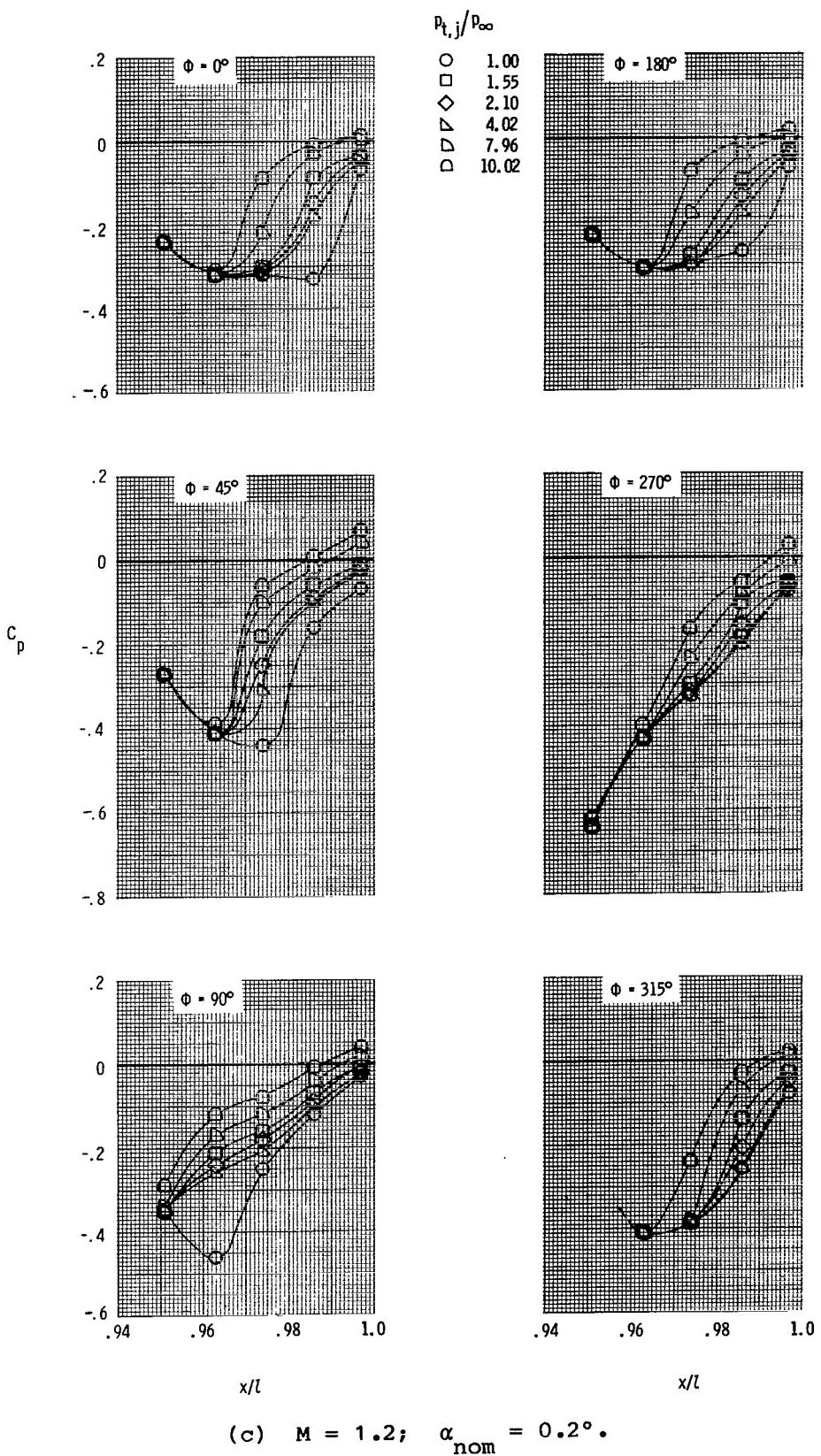
(a)  $M = 0.6$ ;  $\alpha_{nom} = 0.2^\circ$ .

Figure 29.- Effect of jet total-pressure ratio on nozzle pressure distributions with dry power nozzles, booms off, horizontal tails aft, and twin vertical tails forward.



(b)  $M = 0.9$ ;  $\alpha_{\text{nom}} = 0.2^\circ$ .

Figure 29.- Continued.



(c)  $M = 1.2$ ;  $\alpha_{\text{nom}} = 0.2^\circ$ .

Figure 29.-- Concluded.

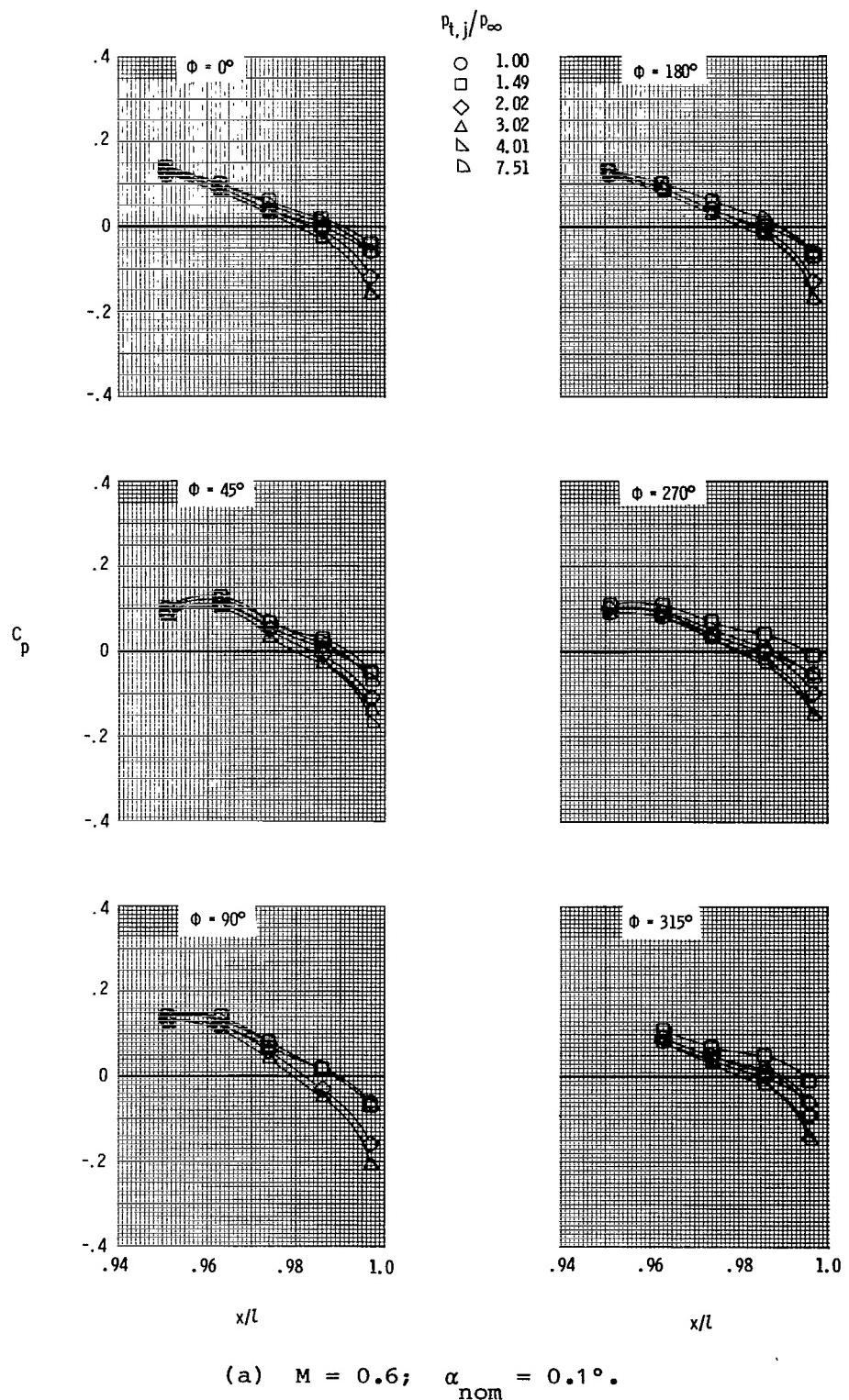
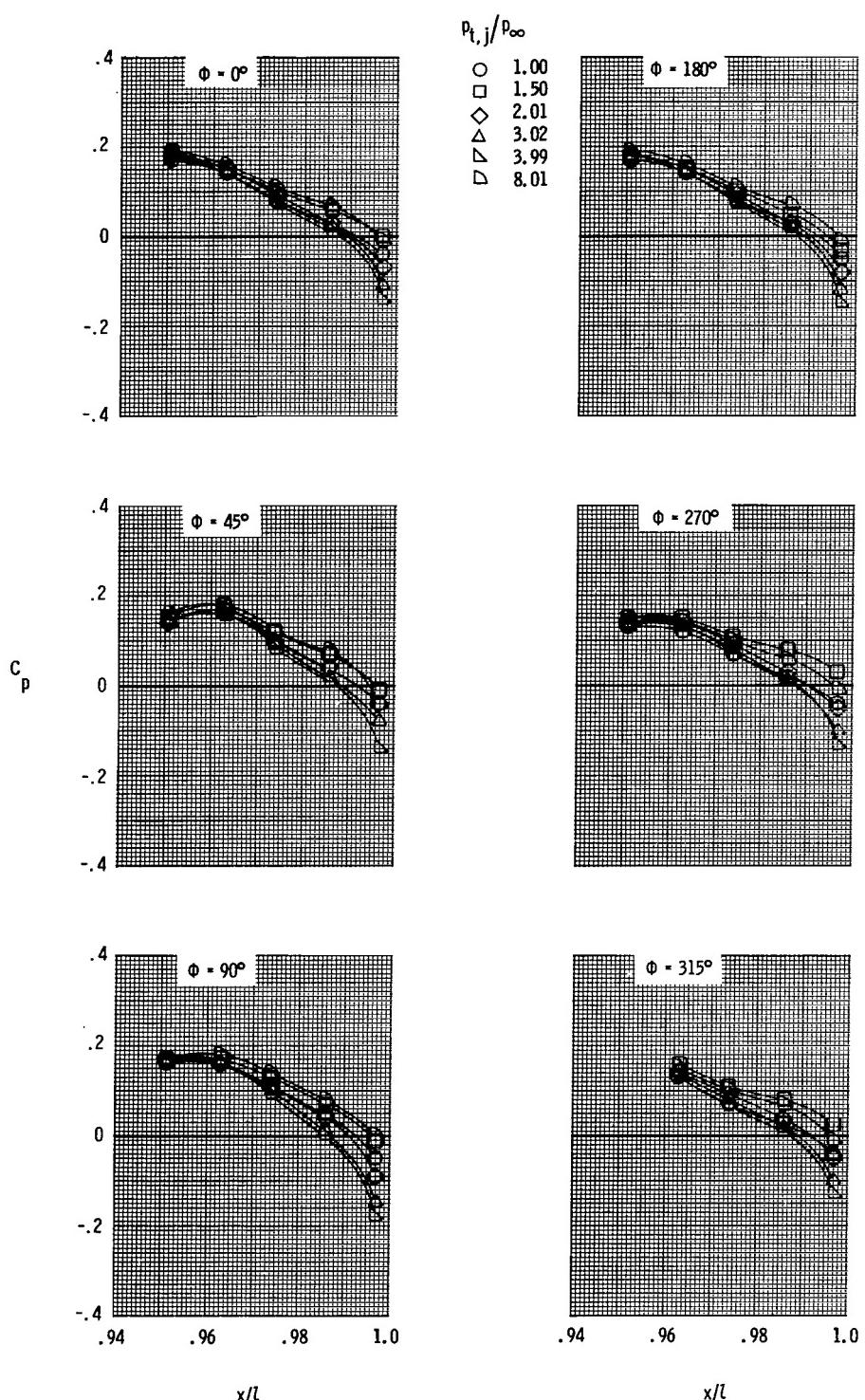
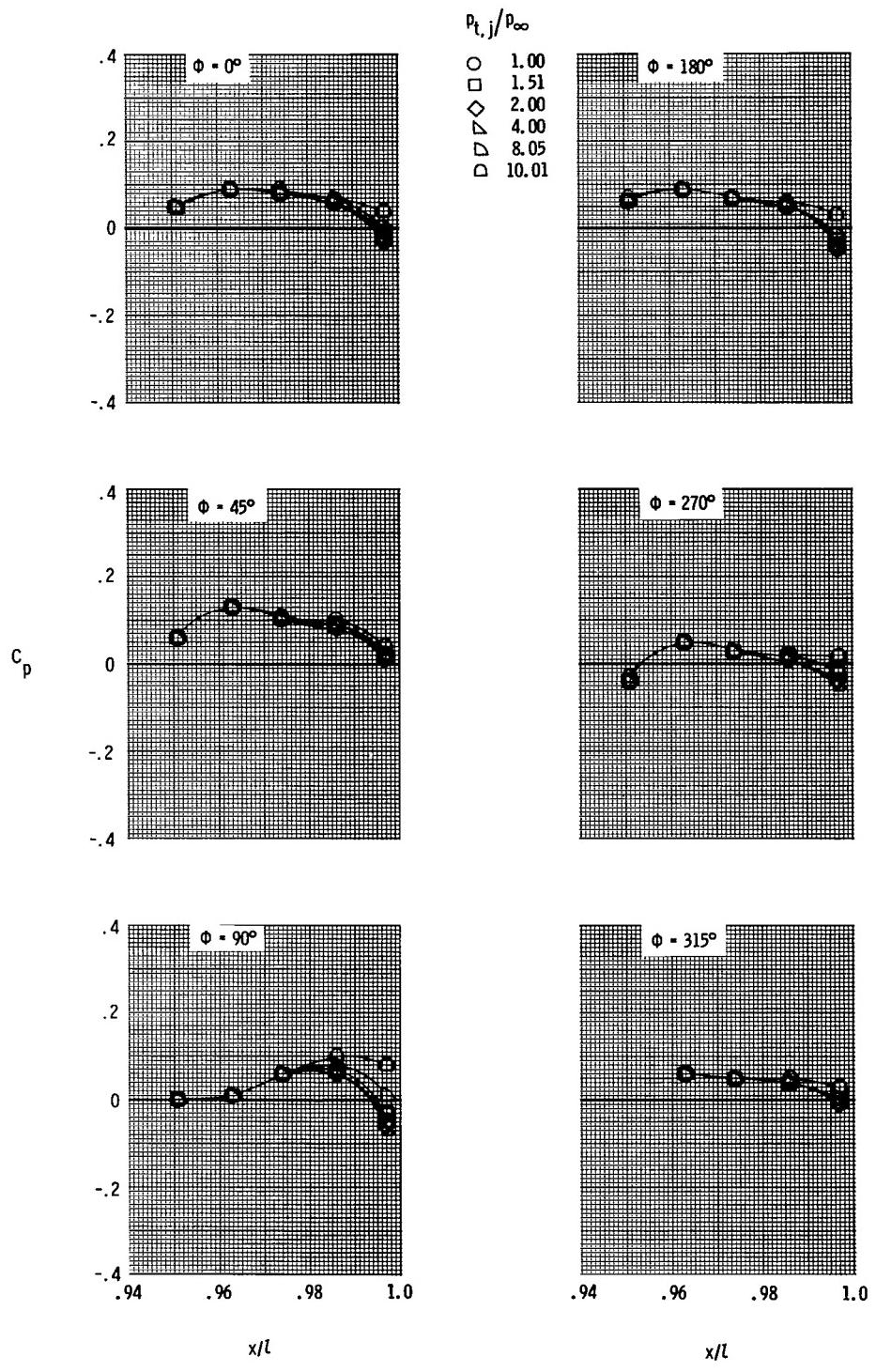


Figure 30.- Effect of jet total-pressure ratio on nozzle pressure distributions with A/B nozzles, booms off, and tails off.



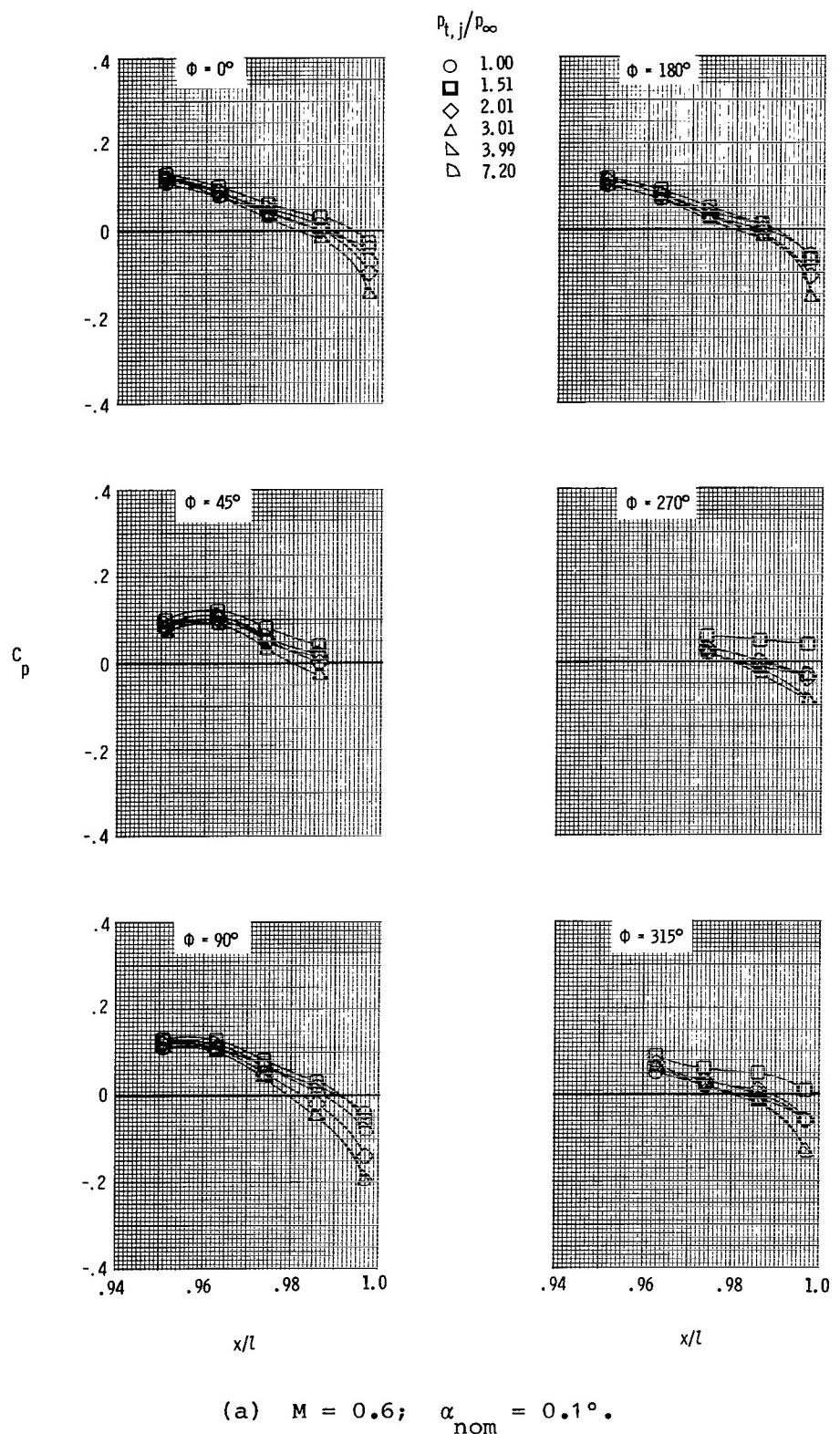
(b)  $M = 0.9$ ;  $\alpha_{\text{nom}} = 0.1^\circ$ .

Figure 30.- Continued.



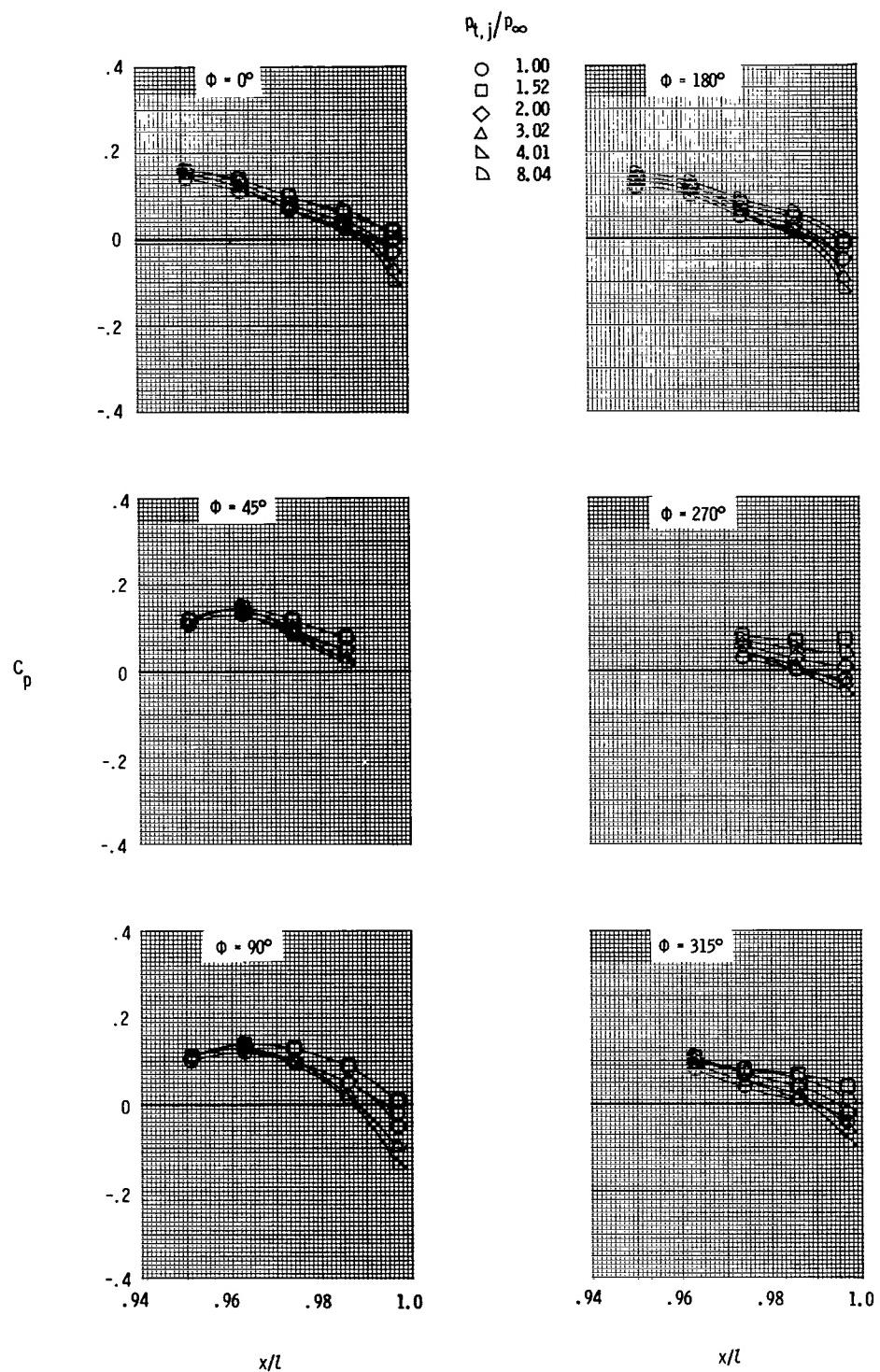
(c)  $M = 1.2$ ;  $\alpha_{\text{nom}} = 0.1^\circ$ .

Figure 30.- Concluded.



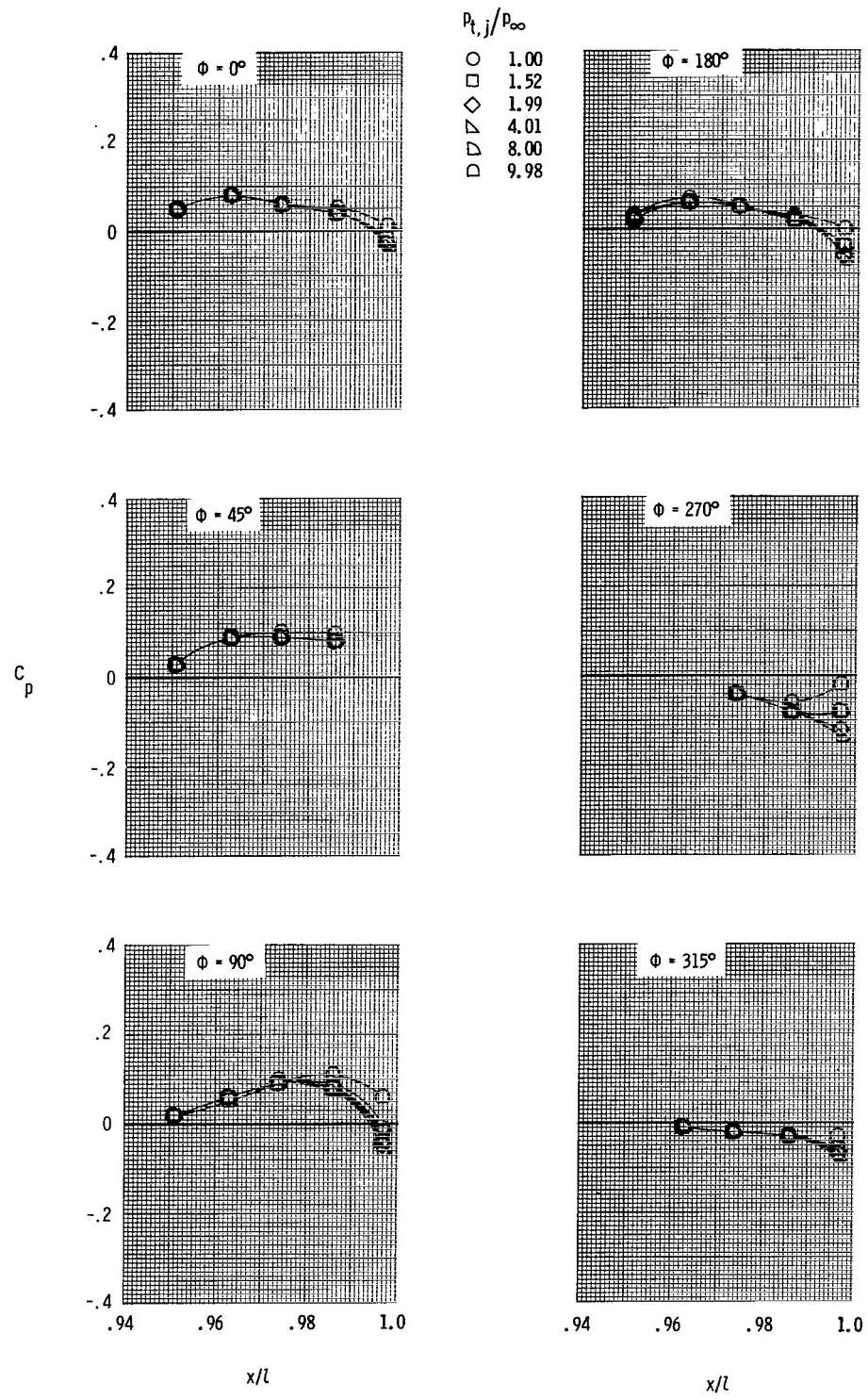
(a)  $M = 0.6$ ;  $\alpha_{nom} = 0.1^\circ$ .

Figure 31.- Effect of jet total-pressure ratio on nozzle pressure distributions with A/B nozzles, booms off, horizontal tails aft, and twin vertical tails forward.



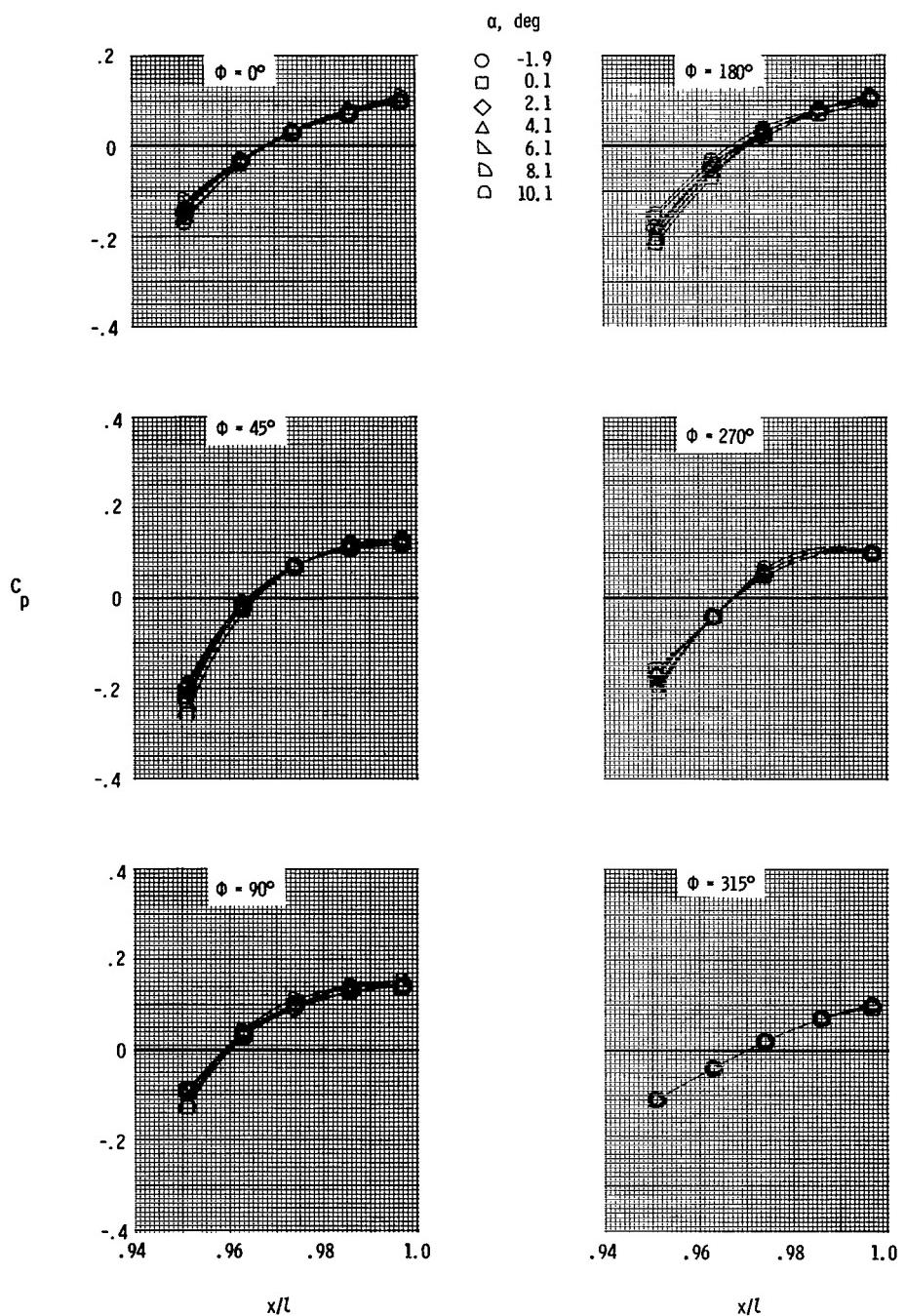
(b)  $M = 0.9$ ;  $\alpha_{\text{nom}} = 0.1^\circ$ .

Figure 31.- Continued.



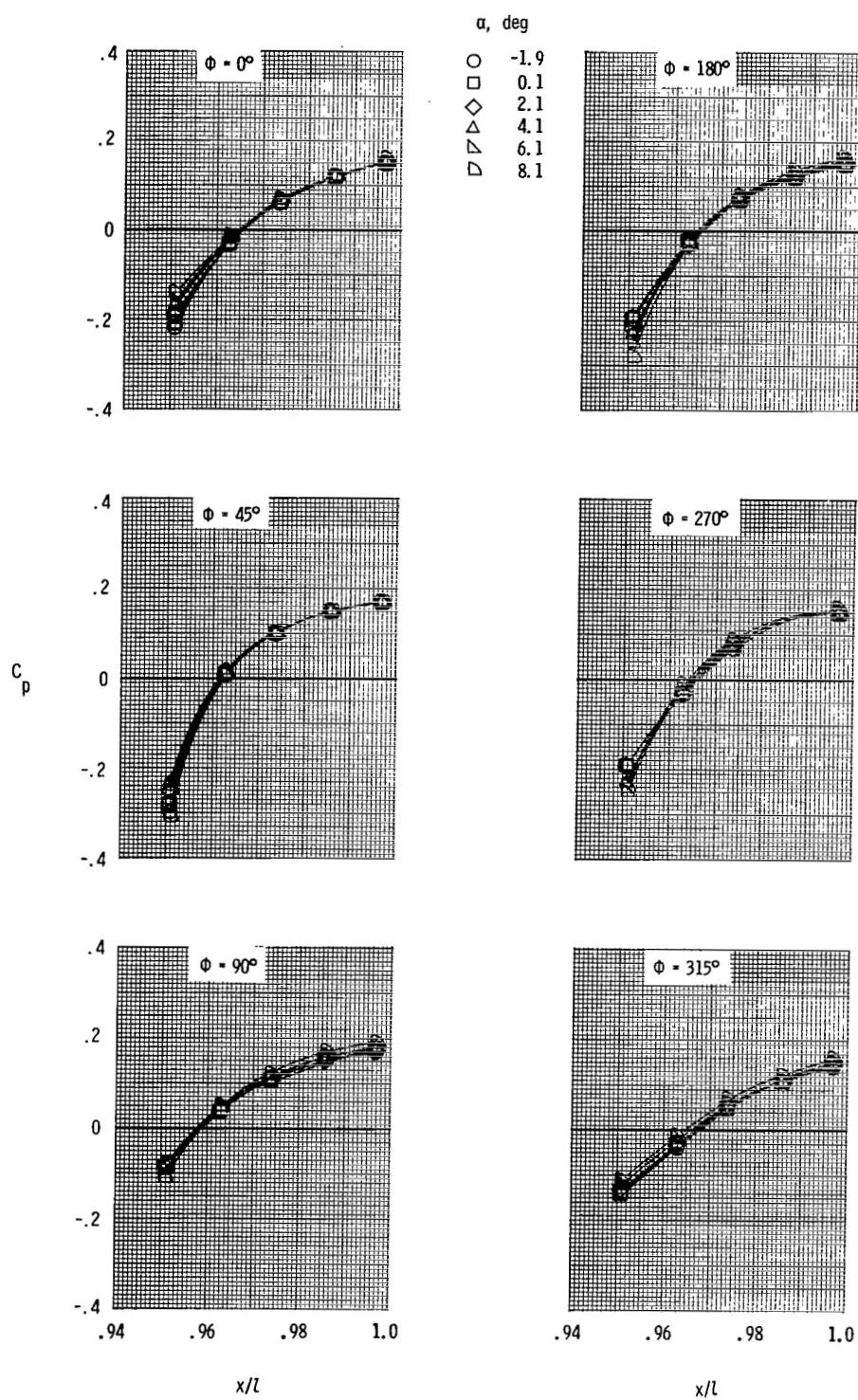
(c)  $M = 1.2$ ;  $\alpha_{\text{nom}} = 0.1^\circ$ .

Figure 31.- Concluded.



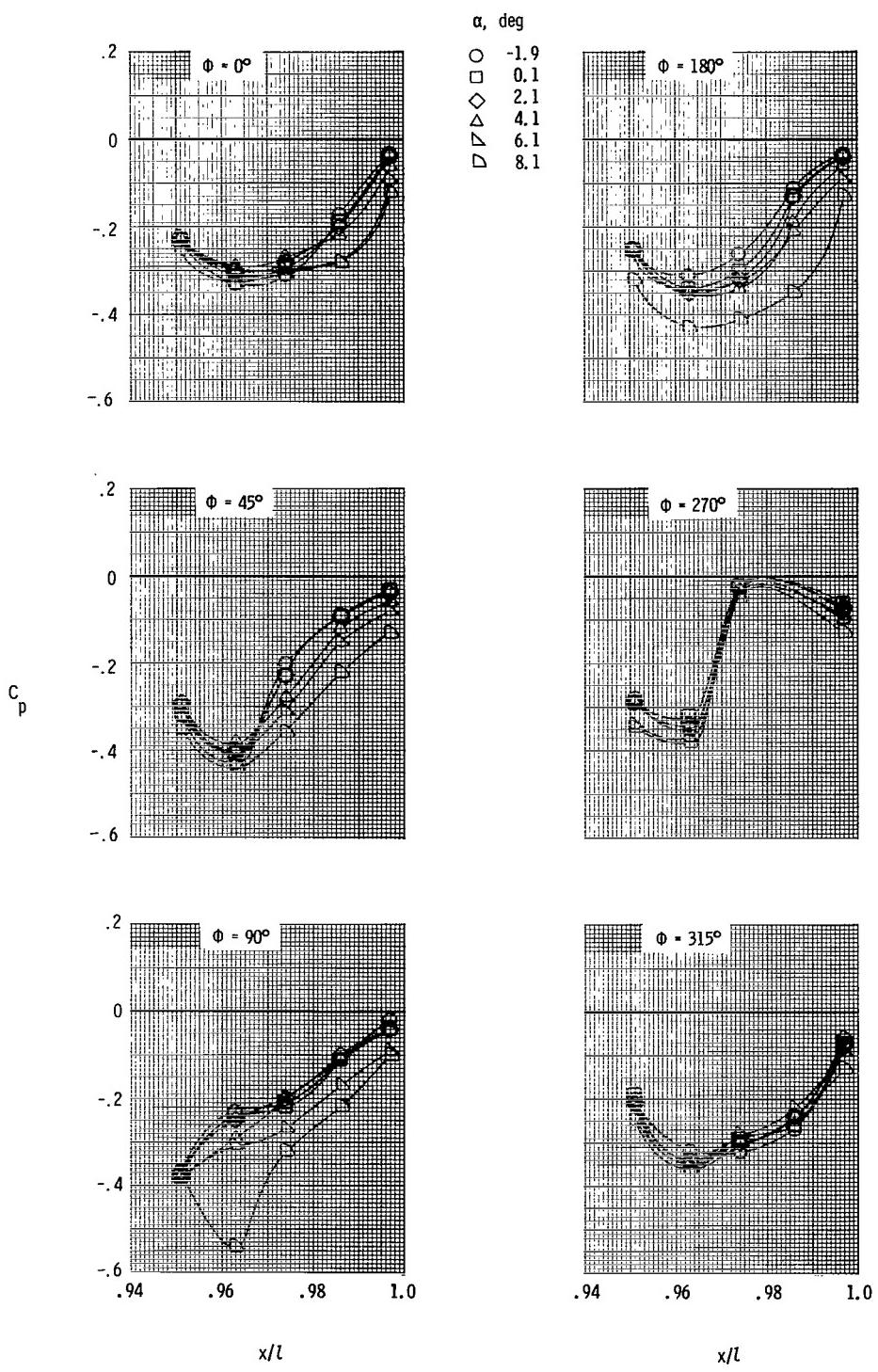
(a)  $M = 0.6$ ;  $p_{t,j}/p_\infty = 1.0$  (jet off).

Figure 32.- Effects of afterbody angle of attack on nozzle pressure distributions with dry power nozzles, booms off, and tails off.



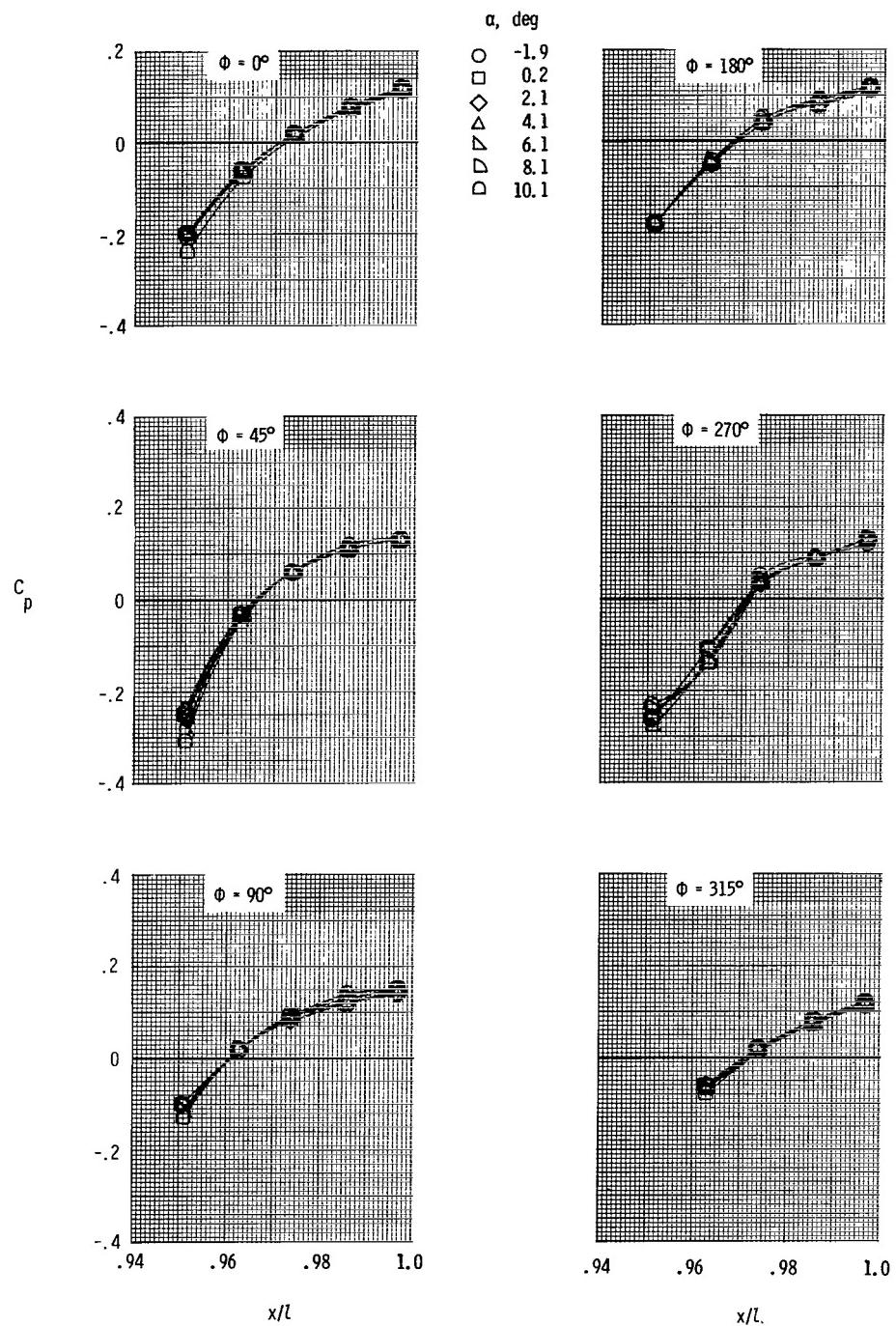
(b)  $M = 0.9$ ;  $p_{t,j}/p_\infty = 1.0$  (jet off).

Figure 32.- Continued.



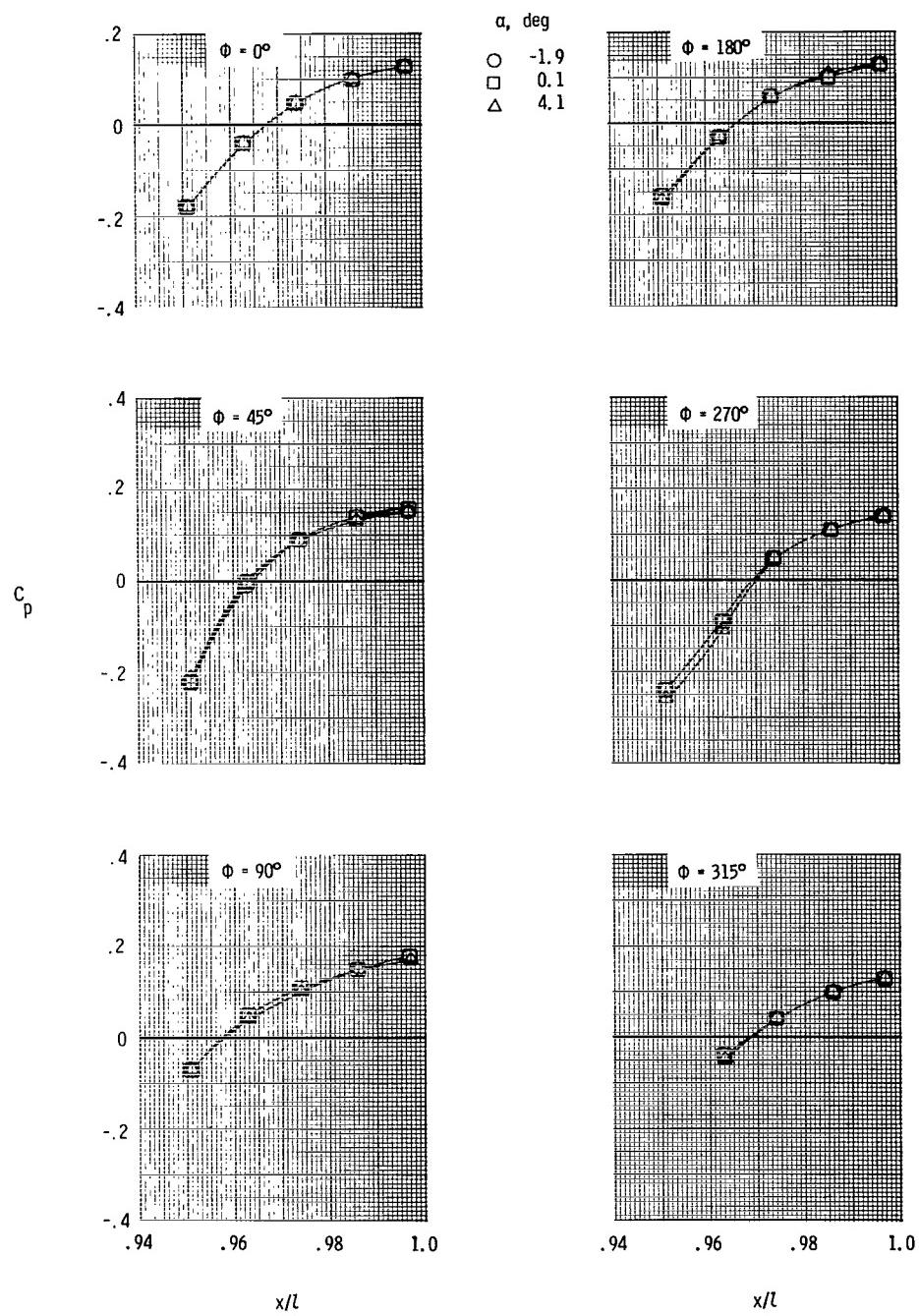
(c)  $M = 1.2$ ;  $p_{t,j}/p_\infty = 1.0$  (jet off).

Figure 32.- Concluded.



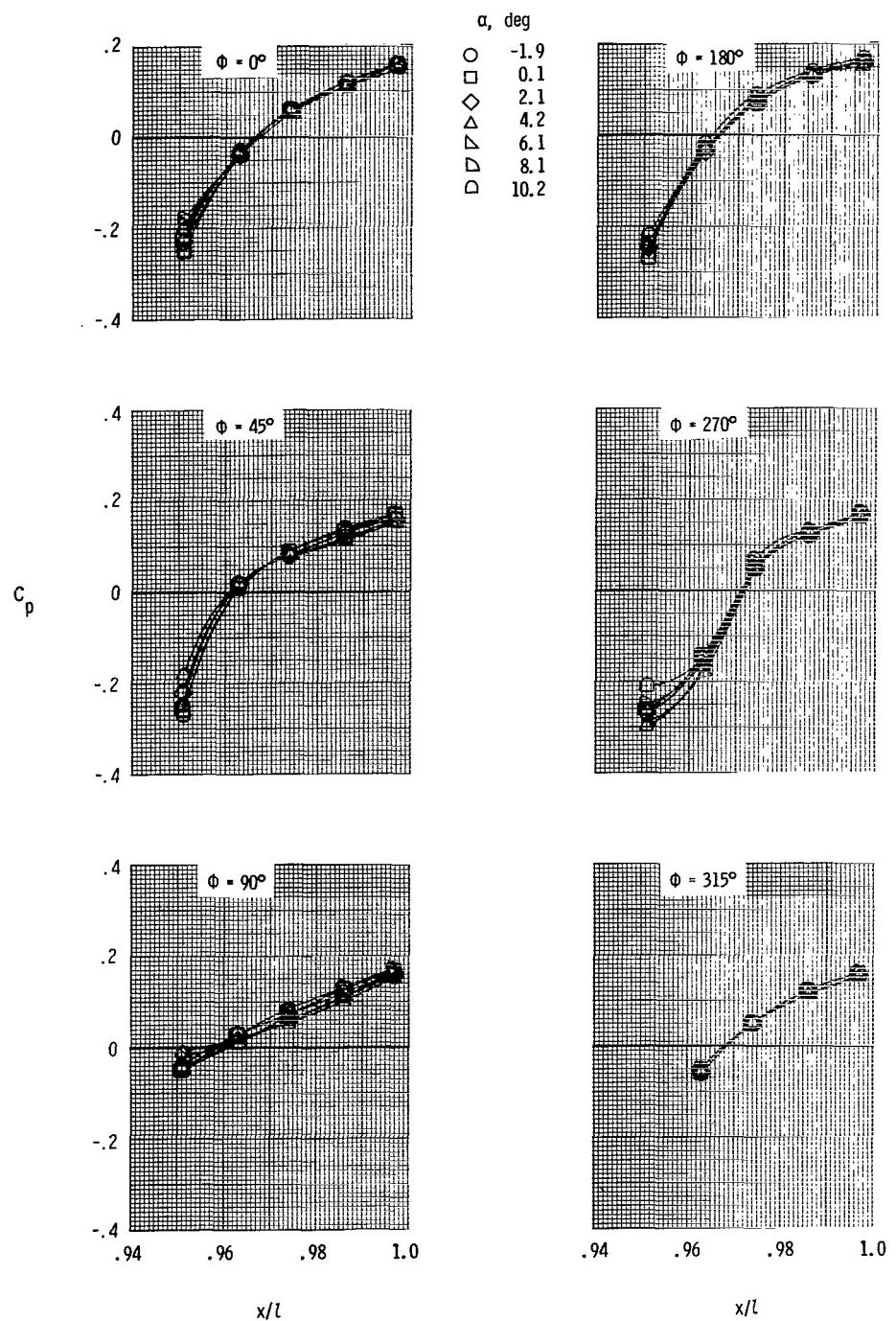
(a)  $M = 0.6$ ;  $p_{t,j}/p_\infty = 1.0$  (jet off).

Figure 33.- Effects of afterbody angle of attack on nozzle pressure distributions with dry power nozzles, booms off, horizontal tails aft, and twin vertical tails forward.



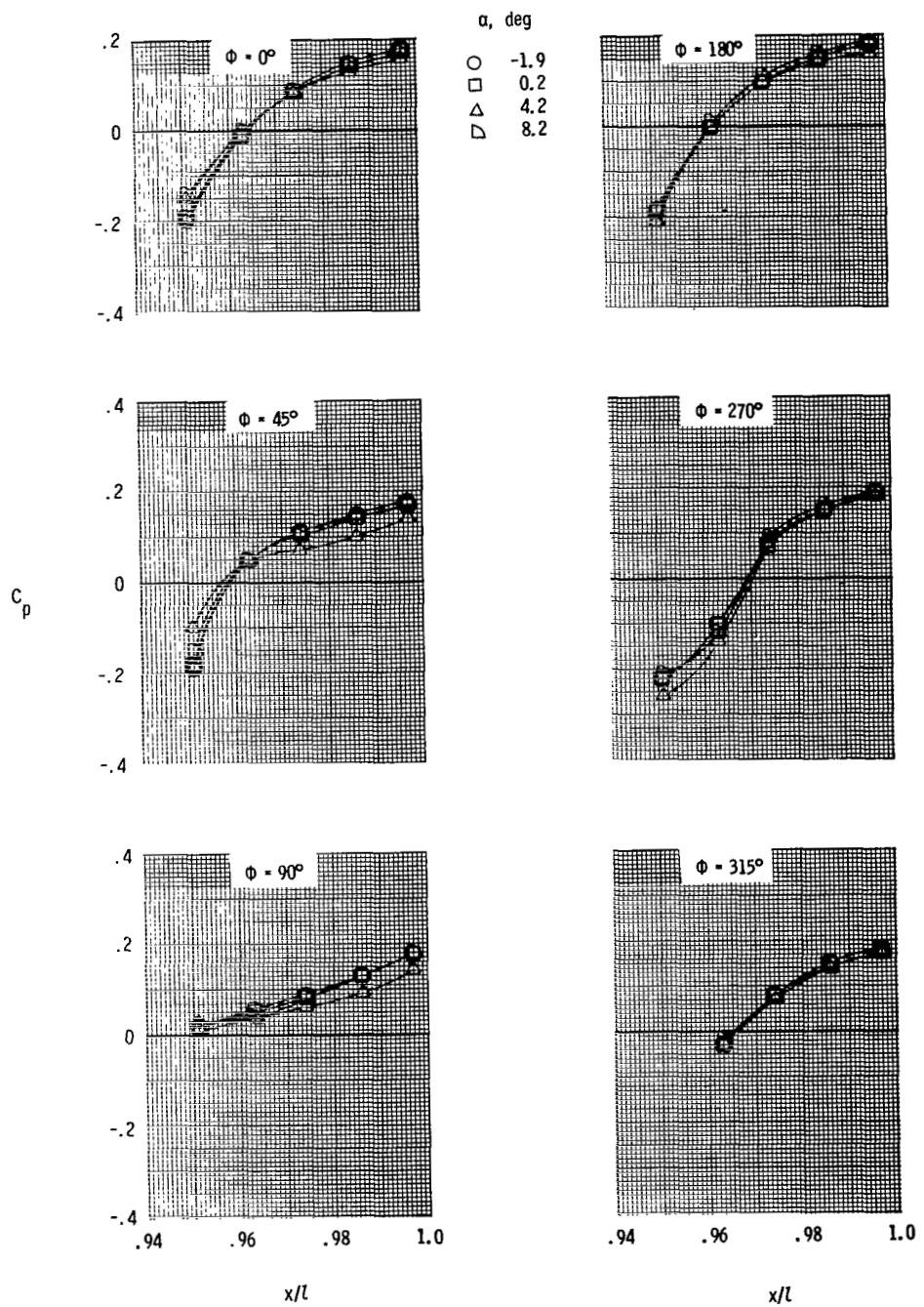
(b)  $M = 0.6$ ;  $p_{t,j}/p_\infty = 3.50$ .

Figure 33.- Continued.



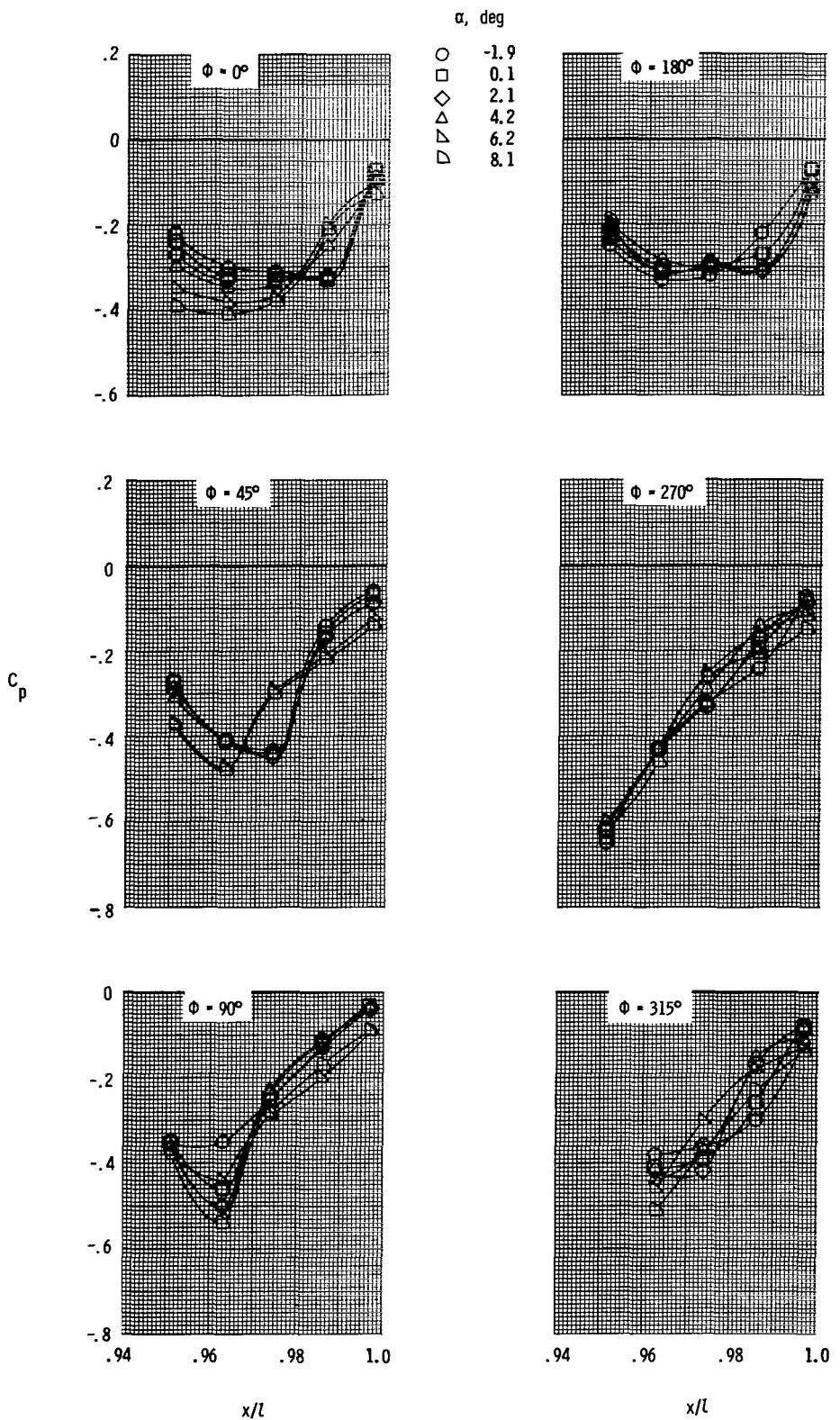
(c)  $M = 0.9$ ;  $p_{t,j}/p_\infty = 1.0$  (jet off).

Figure 33.- Continued.



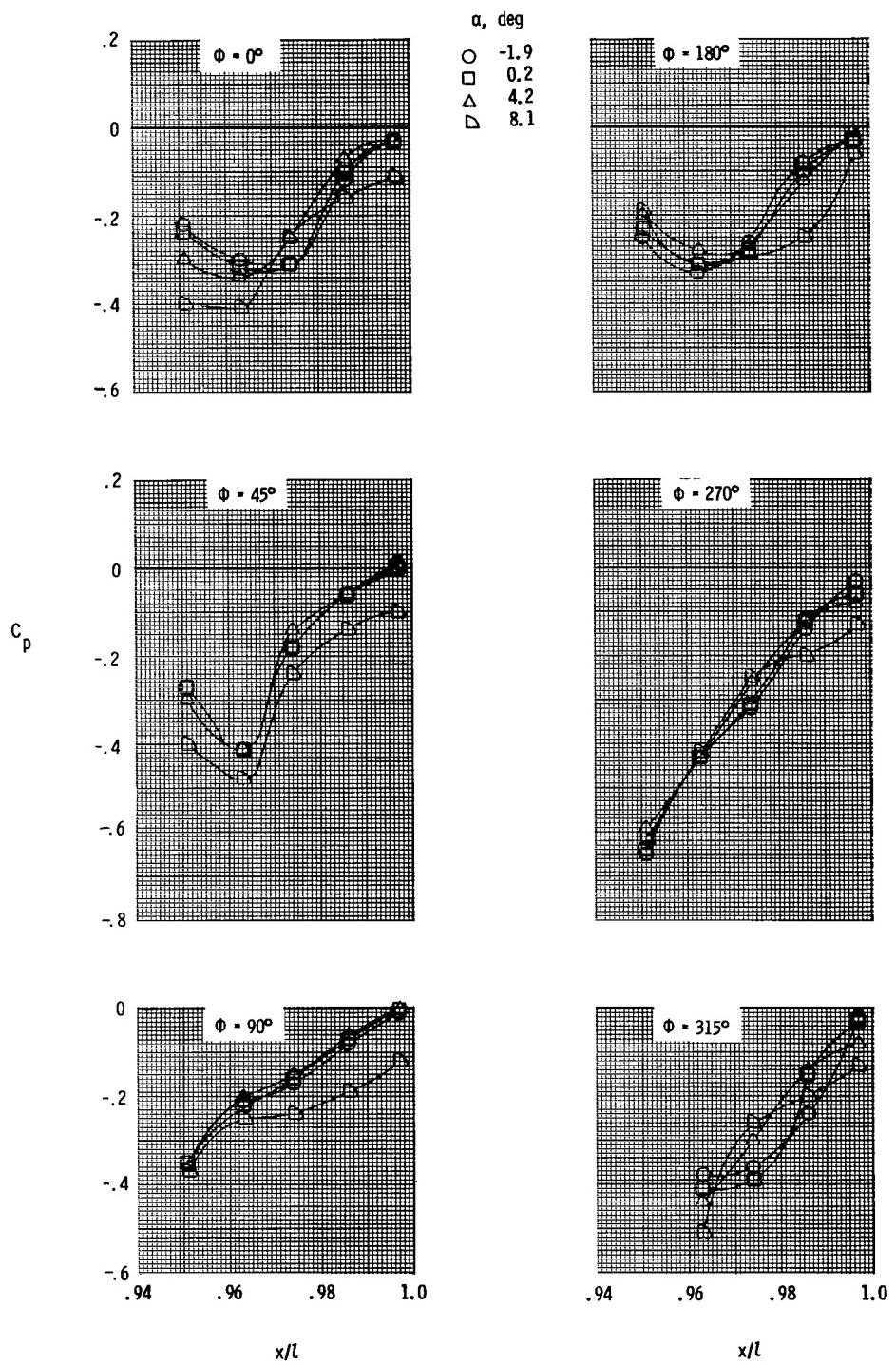
(d)  $M = 0.9$ ;  $p_{t,j}/p_\infty = 4.00$ .

Figure 33.- Continued.



(e)  $M = 1.2$ ;  $p_{t,j}/p_\infty = 1.0$  (jet off).

Figure 33.- Continued.



(f)  $M = 1.2; p_{t,j}/p_\infty = 6.01.$

Figure 33.- Concluded.

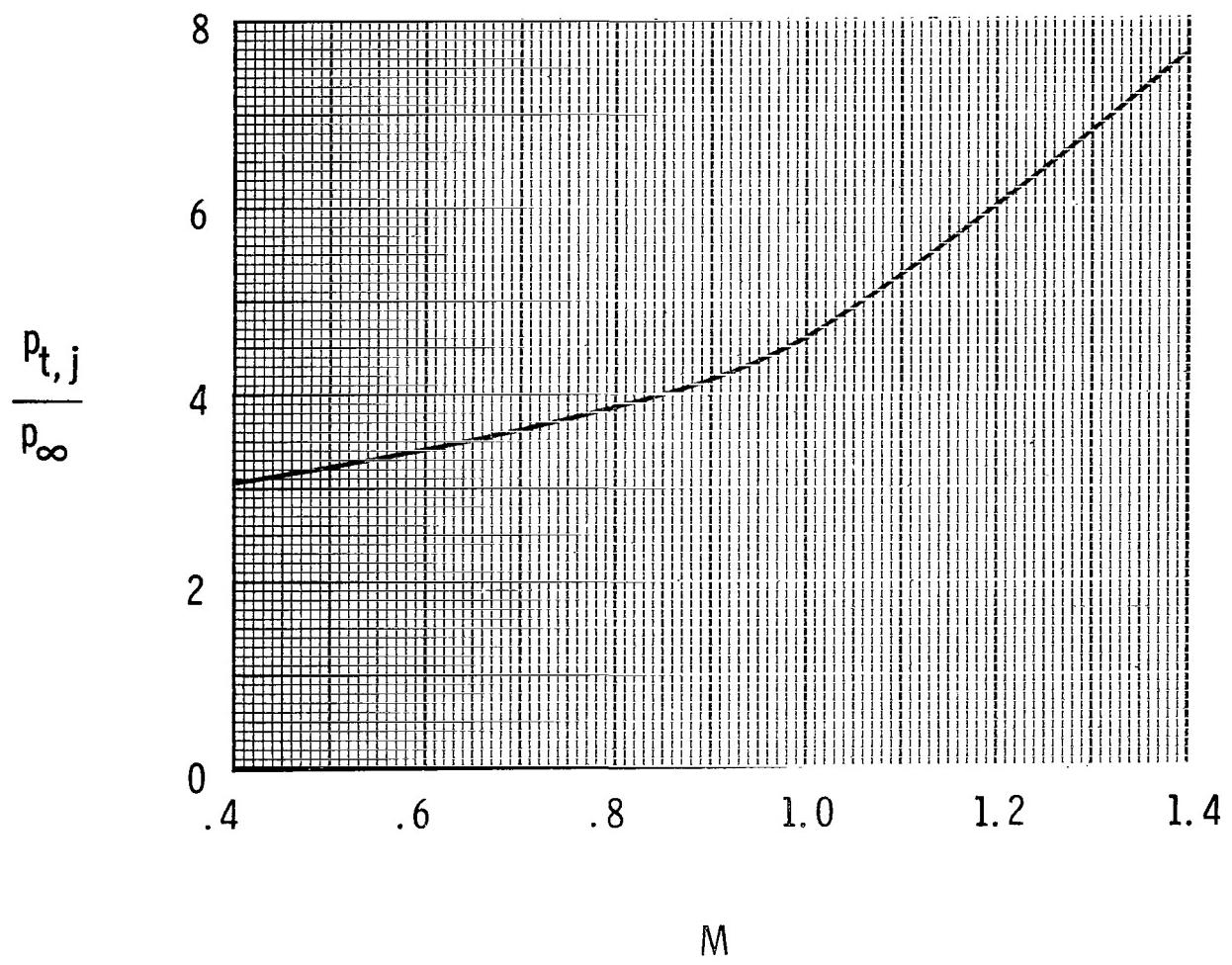
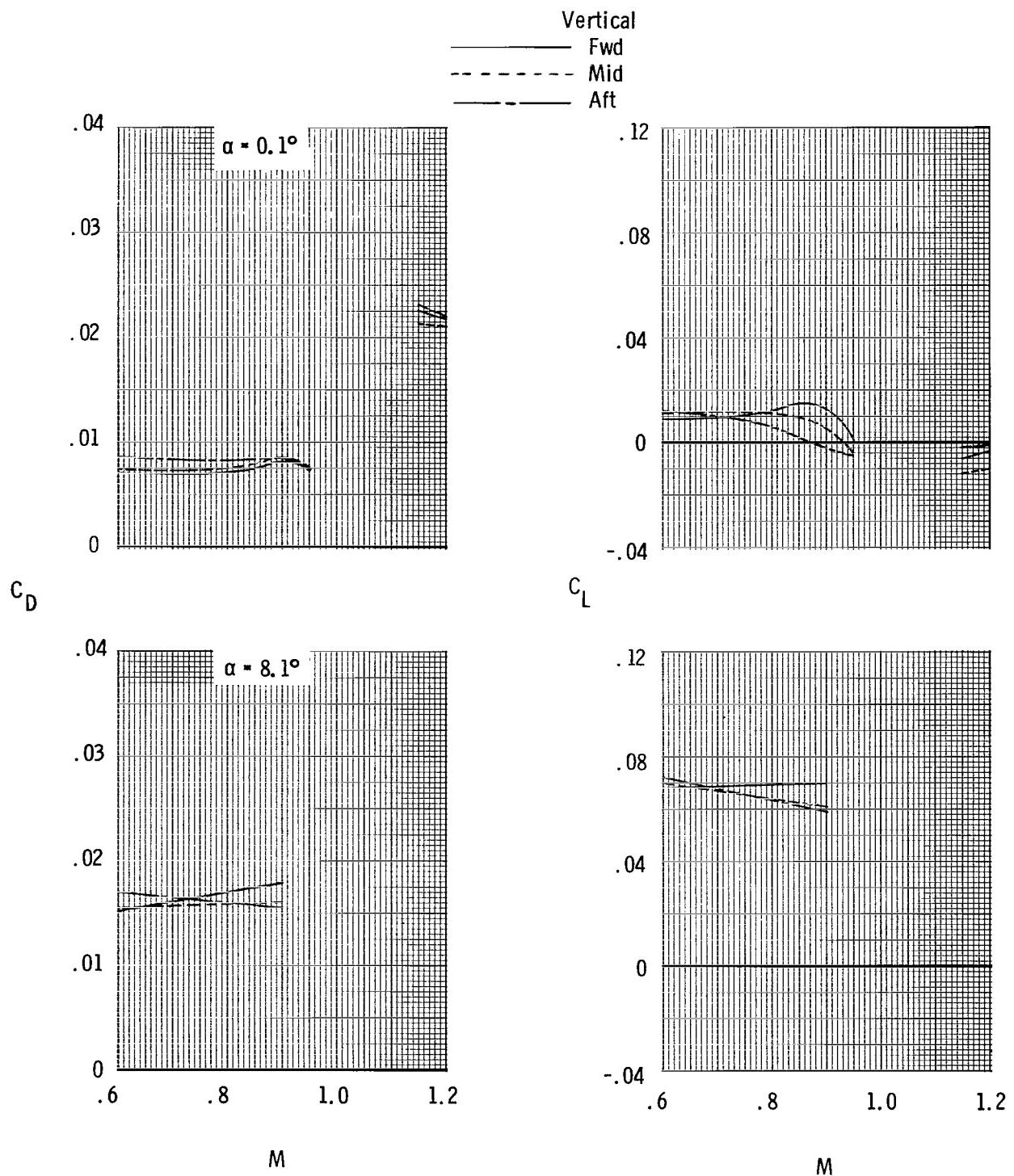
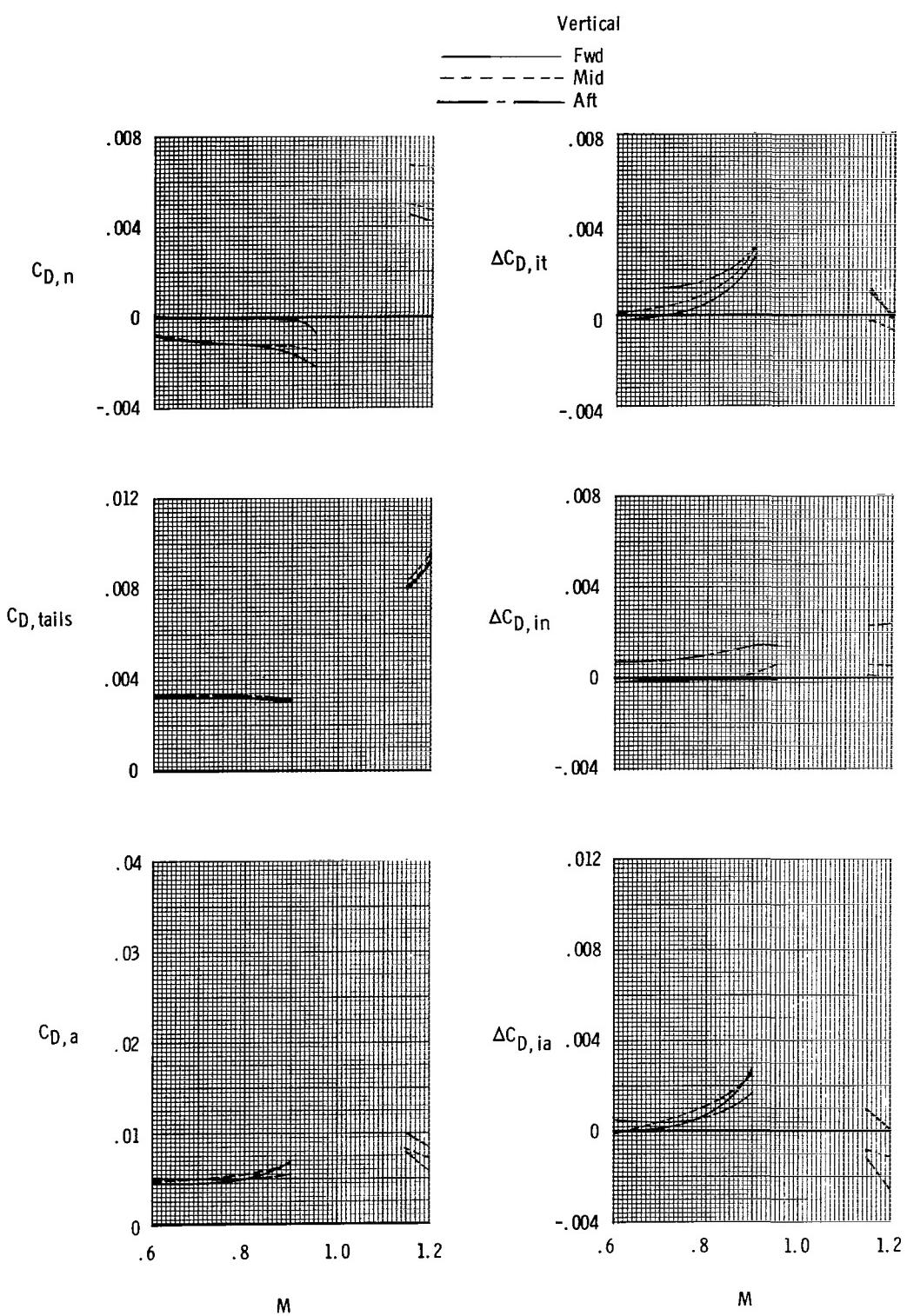


Figure 34.- Typical jet total-pressure ratios for a turbofan engine.



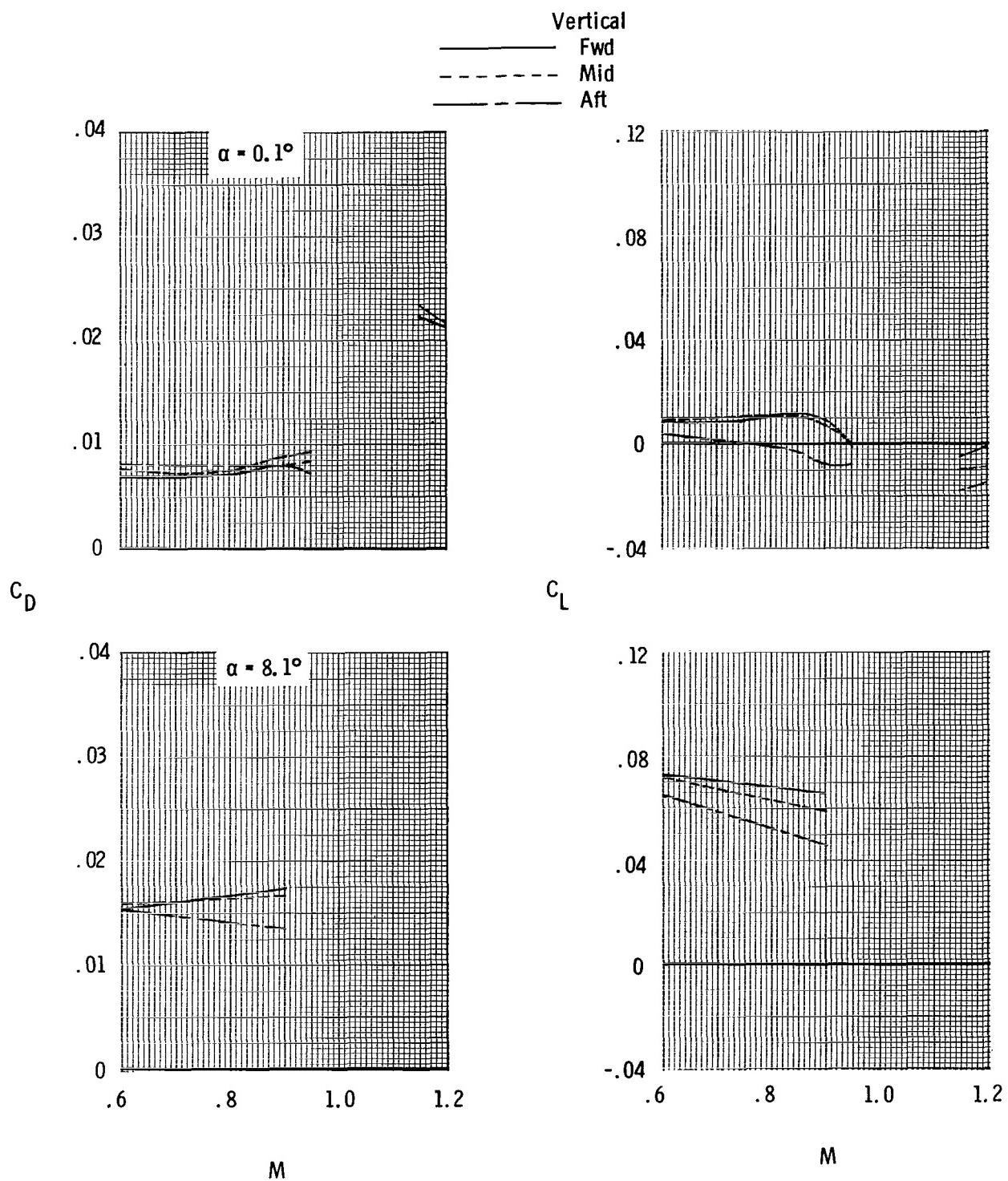
(a) Total aft-end lift and drag coefficient.

Figure 35.- Effect of twin vertical tail location on variation of afterbody characteristics with Mach number for scheduled jet total-pressure ratios with dry power nozzles, booms off, and horizontal tails forward.



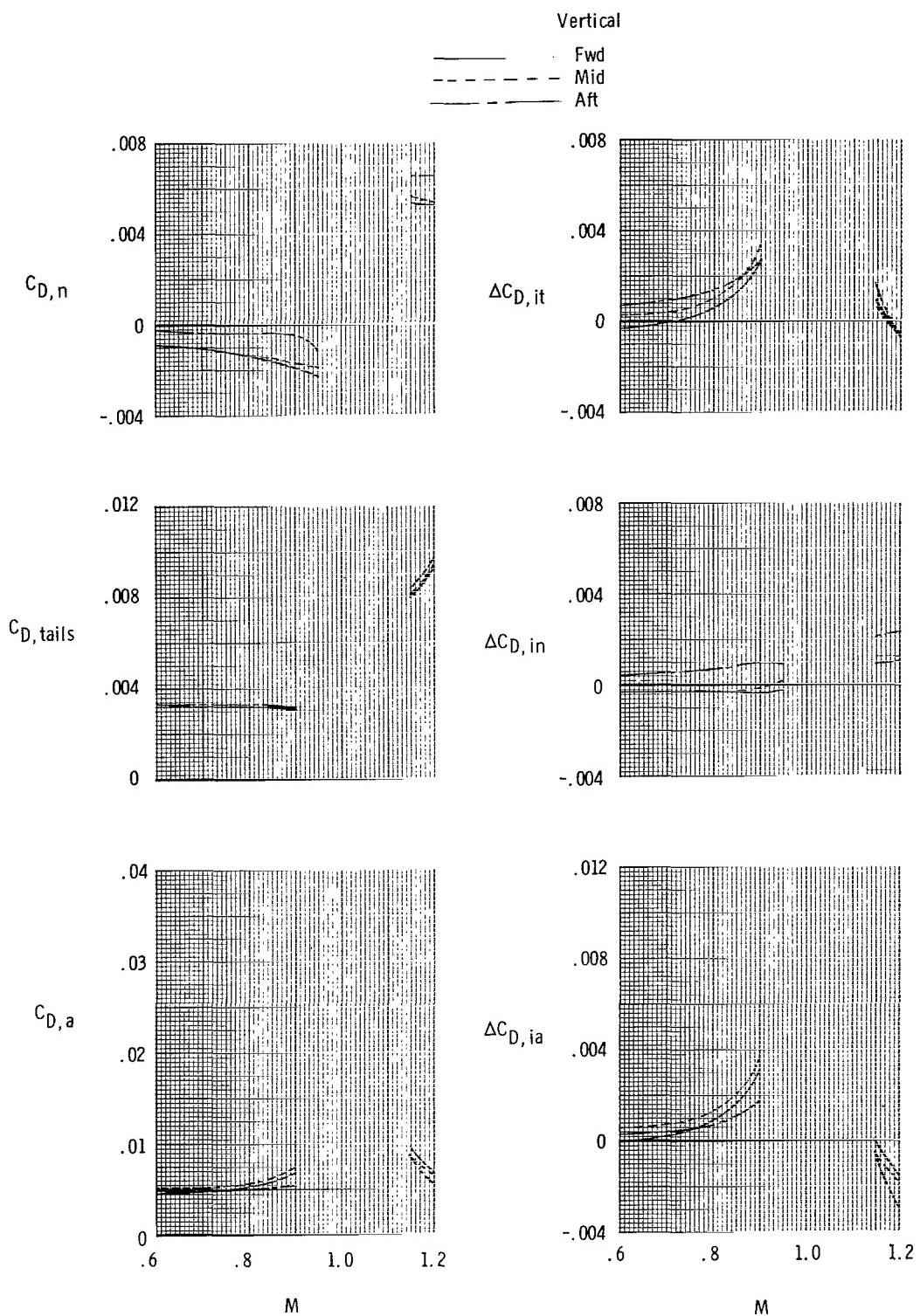
(b) Aft-end drag-coefficient components and tail interference drag-coefficient increments for  $\alpha_{nom} = 0.1^\circ$ .

Figure 35.- Concluded.



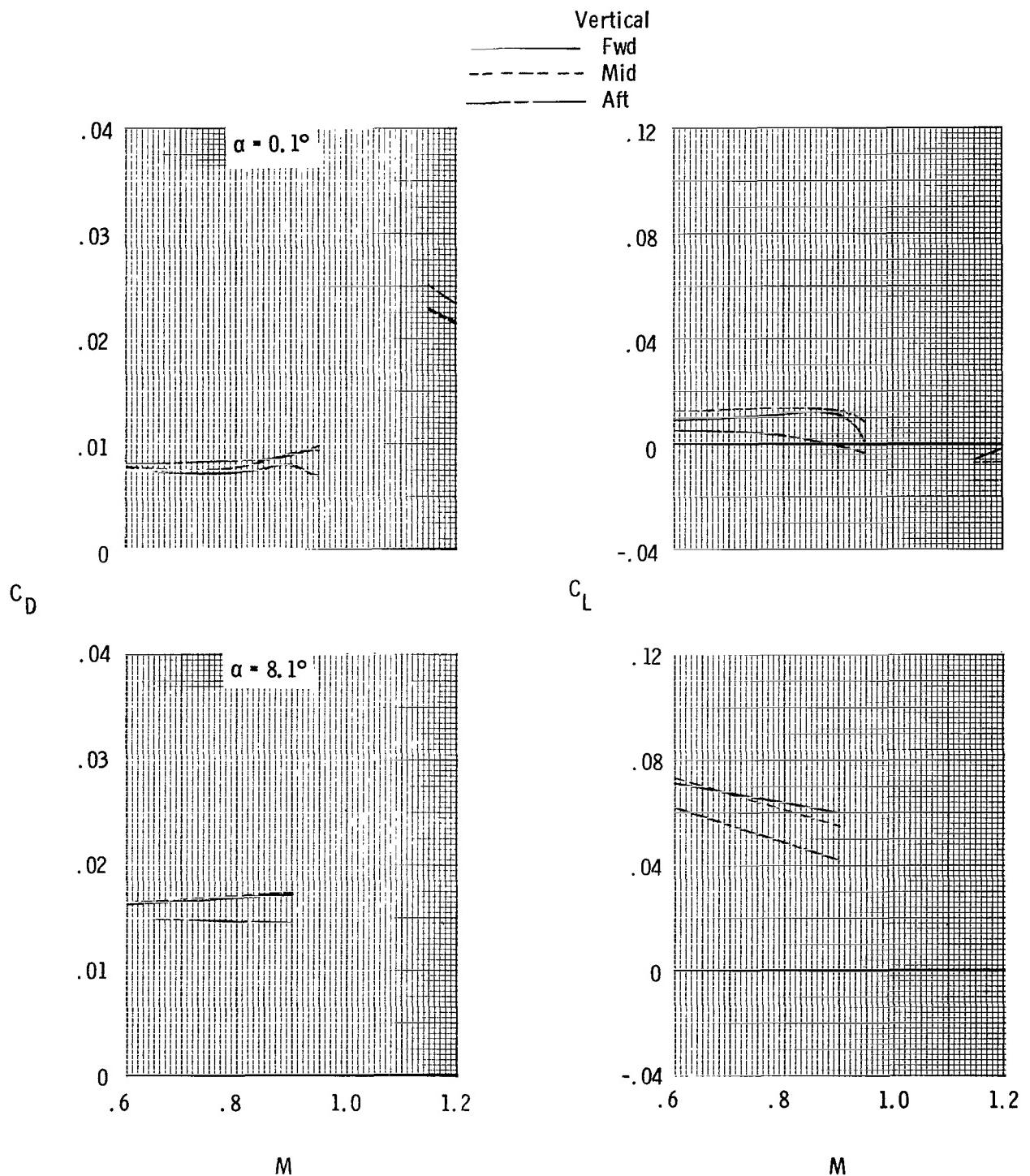
(a) Total aft-end lift and drag coefficient.

Figure 36.- Effect of twin vertical tail location on variation of afterbody characteristics with Mach number for scheduled jet total-pressure ratios with dry power nozzles, booms off, and horizontal tails mid.



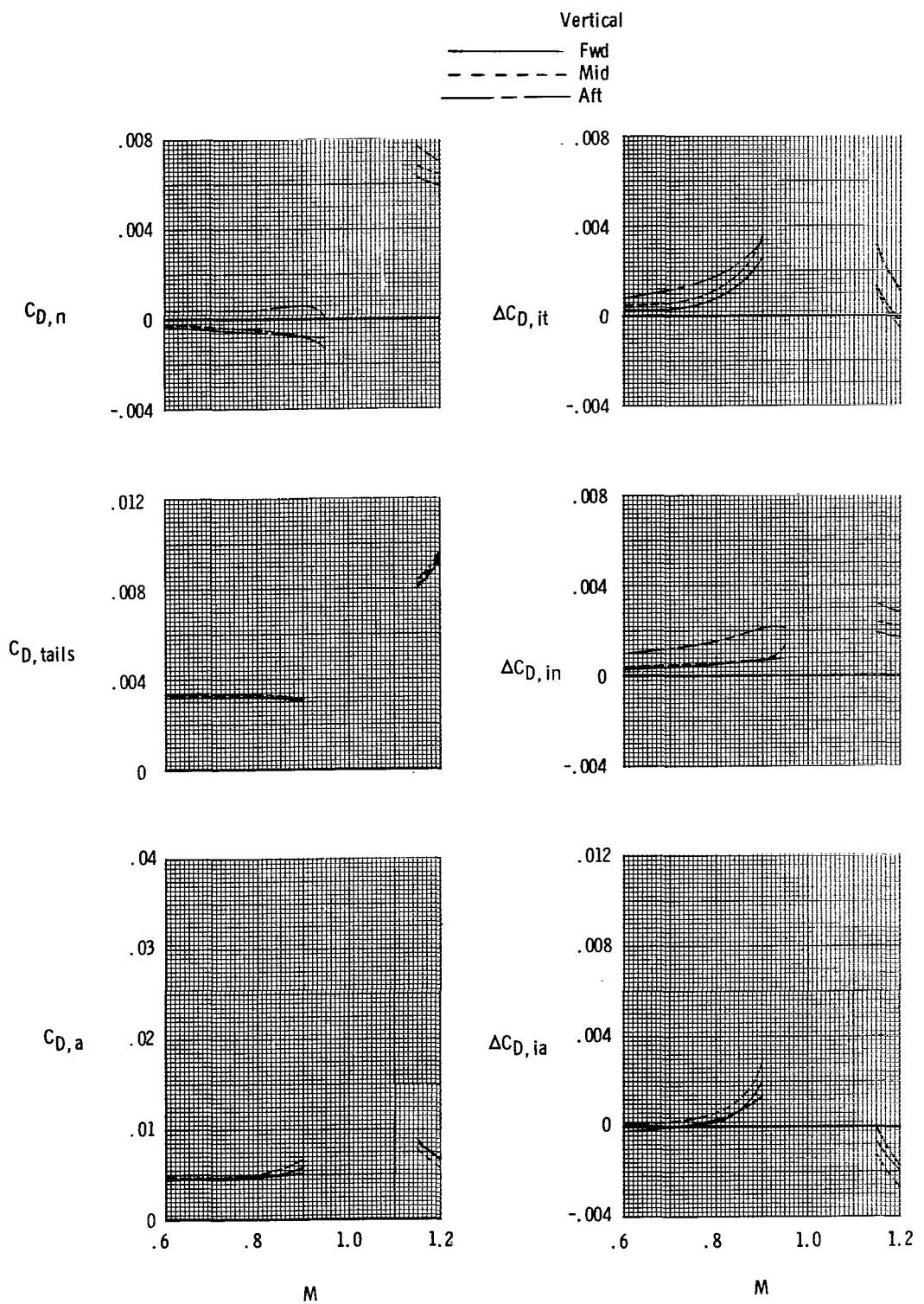
(b) Aft-end drag-coefficient components and tail interference drag-coefficient increments for  $\alpha_{nom} = 0.1^\circ$ .

Figure 36.- Concluded.



(a) Total aft-end lift and drag coefficient.

Figure 37.- Effects of twin vertical tail location on variation of afterbody characteristics with Mach number for scheduled jet total-pressure ratios with dry power nozzles, booms off, and horizontal tails aft.



(b) Aft-end drag-coefficient components and tail interference drag-coefficient increments for  $\alpha_{nom} = 0.1^\circ$ .

Figure 37.-- Concluded.

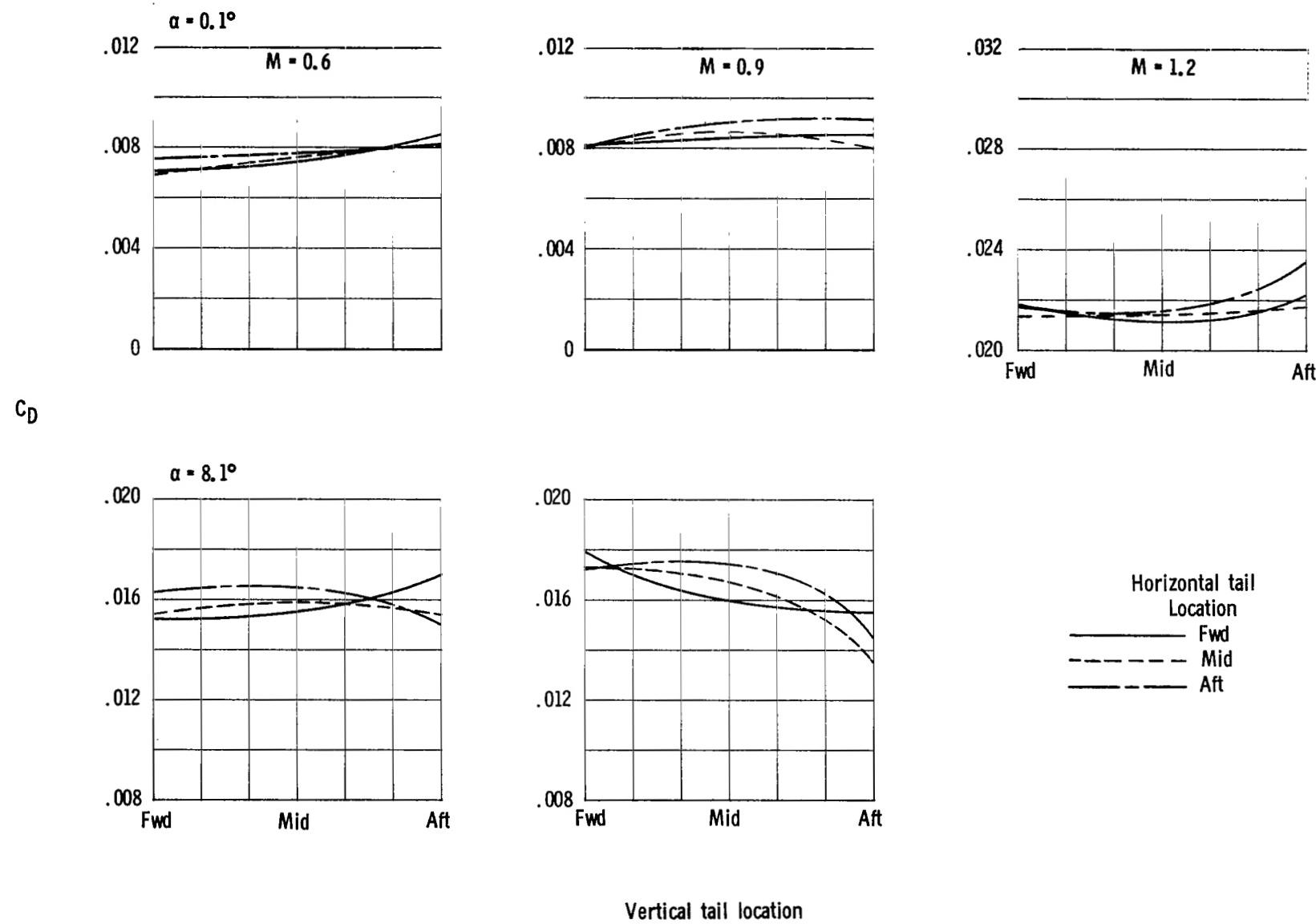
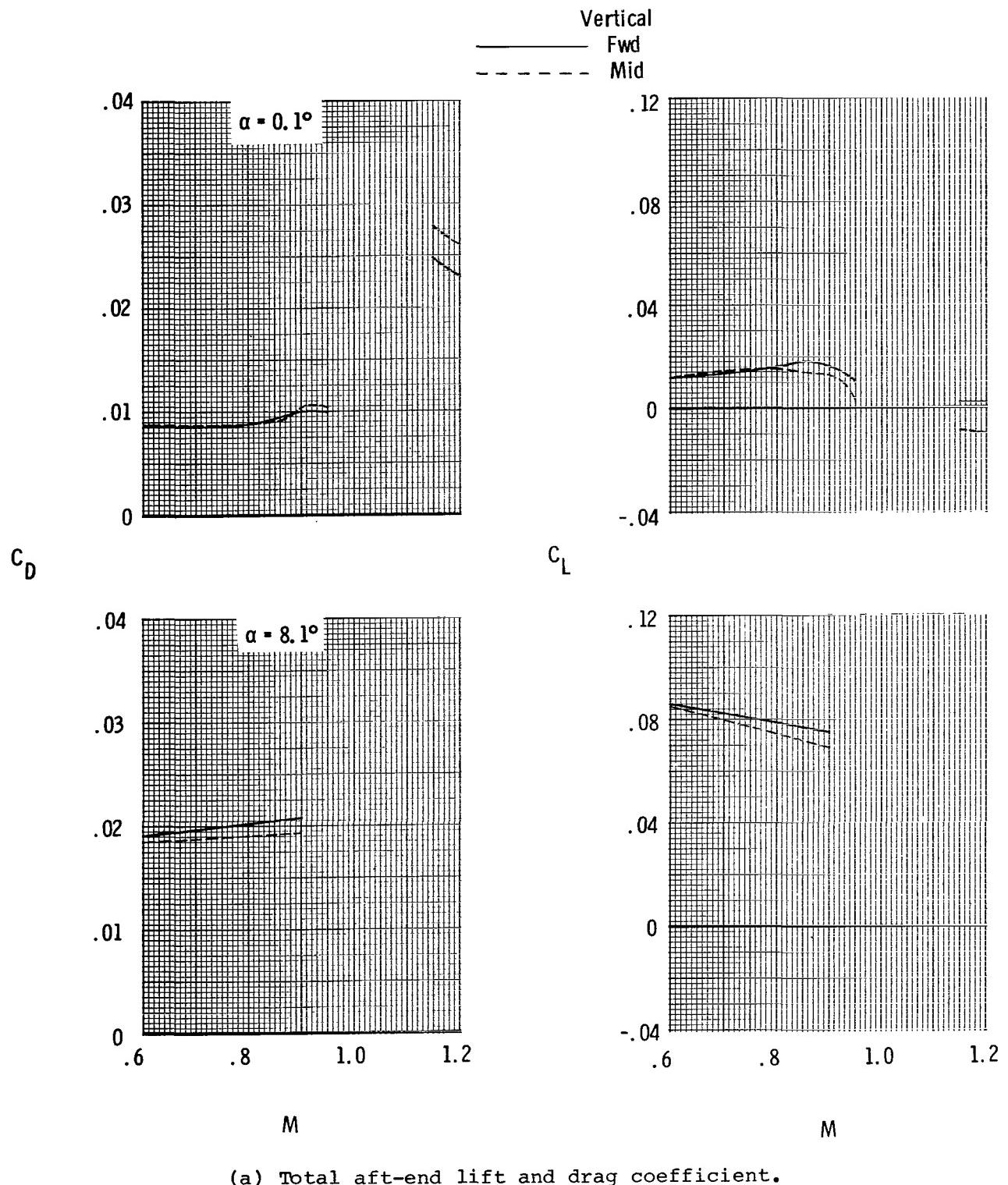
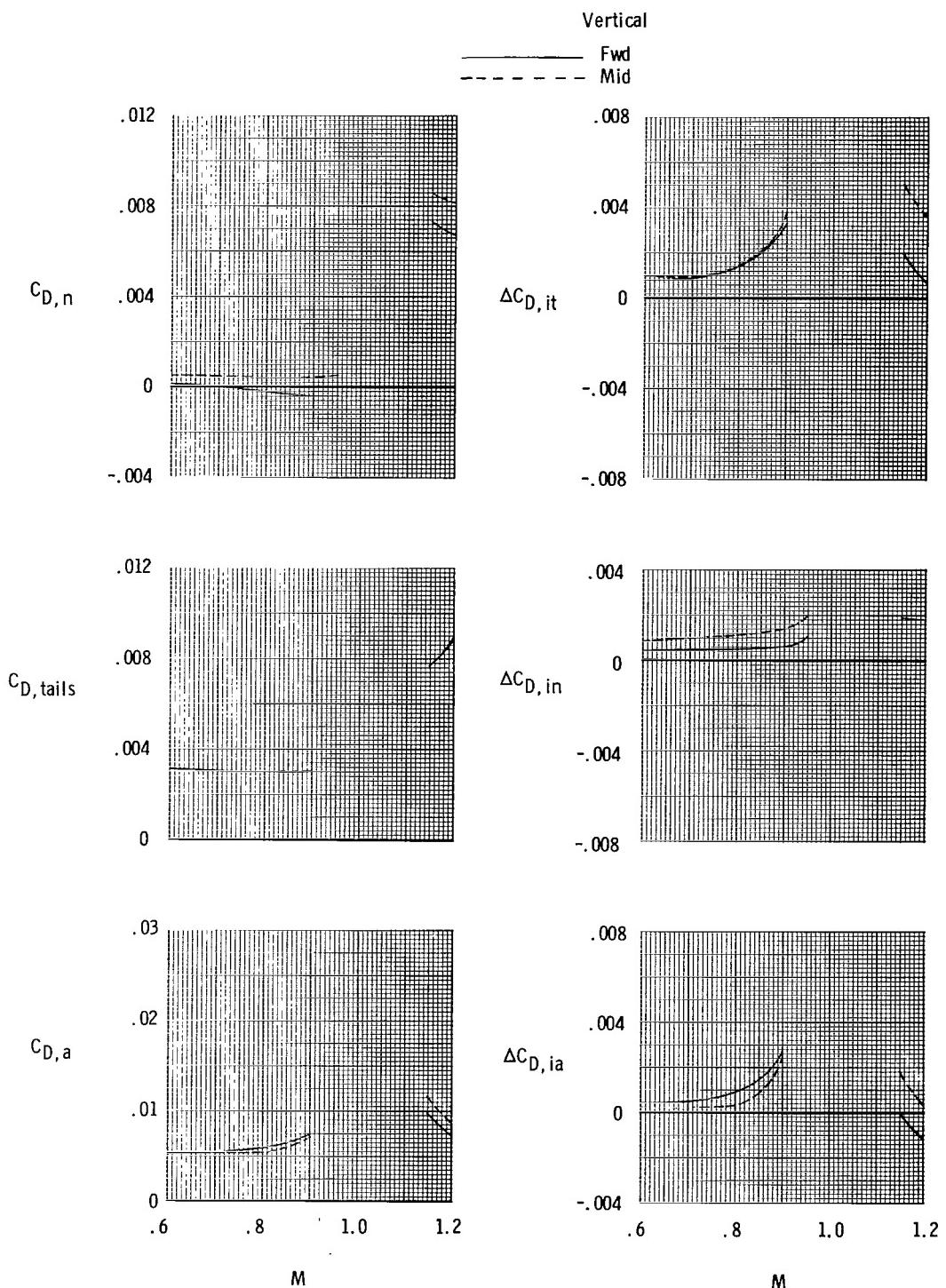


Figure 38.- Summary of effects of twin vertical tail location on total aft-end drag characteristics at scheduled jet total-pressure ratios with dry power nozzles and booms off.



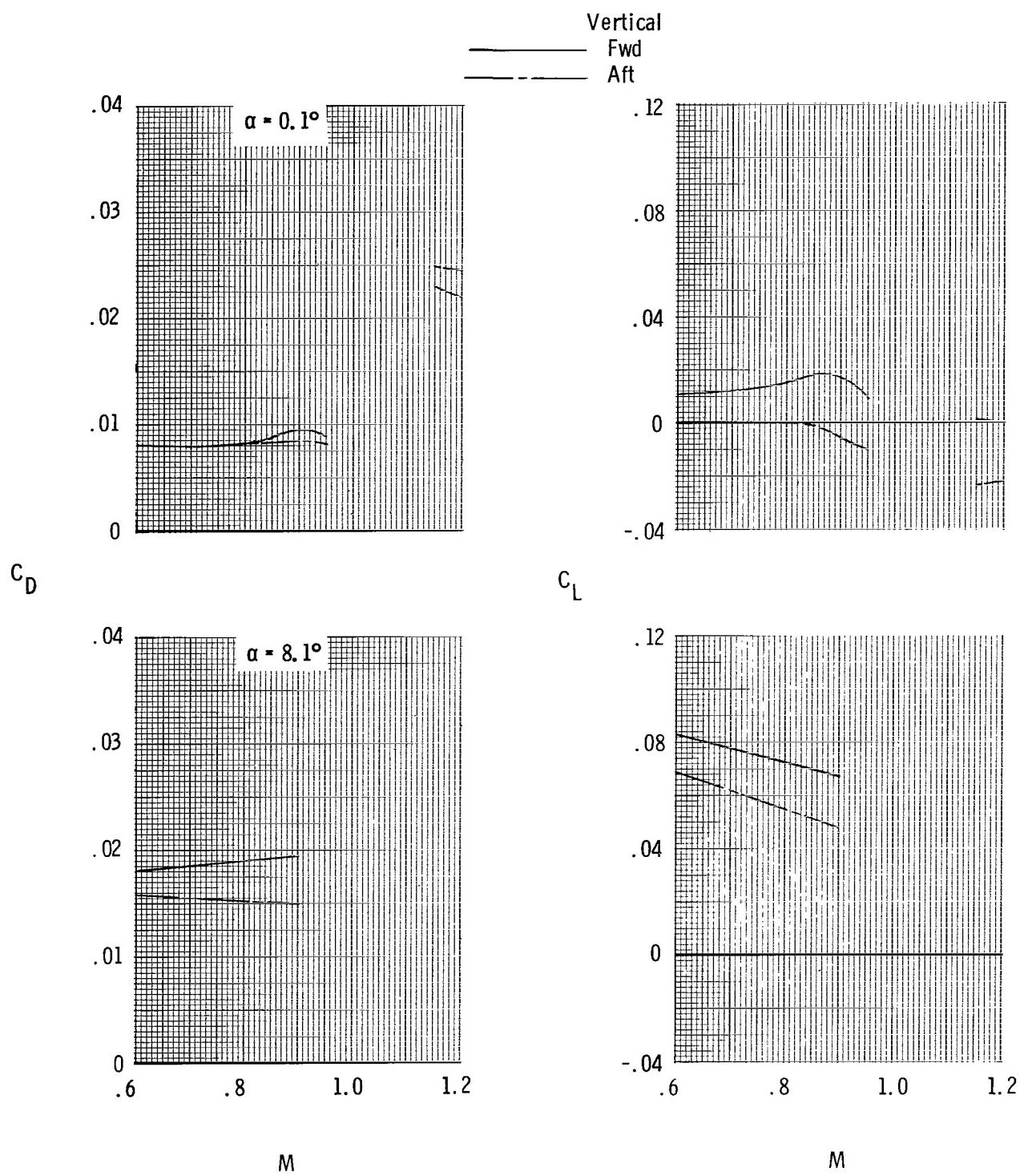
(a) Total aft-end lift and drag coefficient.

Figure 39.- Effects of twin vertical tail location on variation of afterbody characteristics with Mach number for scheduled jet total-pressure ratios with dry power nozzles, booms on, and horizontal tails forward.



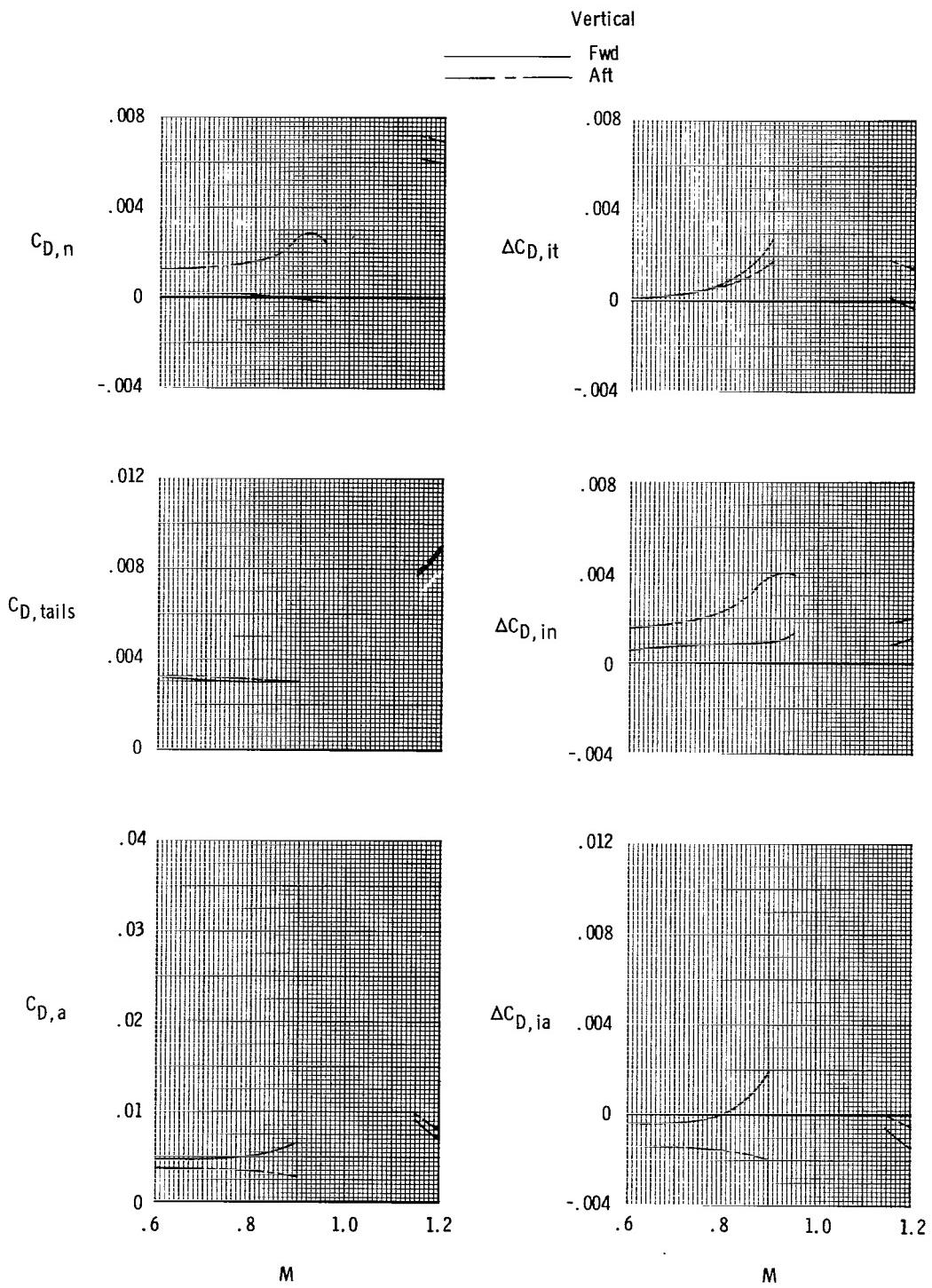
(b) Aft-end drag-coefficient components and tail interference drag-coefficient increments for  $\alpha_{nom} = 0.1^\circ$ .

Figure 39.- Concluded.



(a) Total aft-end lift and drag coefficient.

Figure 40.- Effects of twin vertical tail location on variation of afterbody characteristics with Mach number for scheduled jet total-pressure ratios with dry power nozzles, booms on, and horizontal tails aft.



(b) Aft-end drag-coefficient components and tail interference drag-coefficient increments for  $\alpha_{nom} = 0.1^\circ$ .

Figure 40.- Concluded.

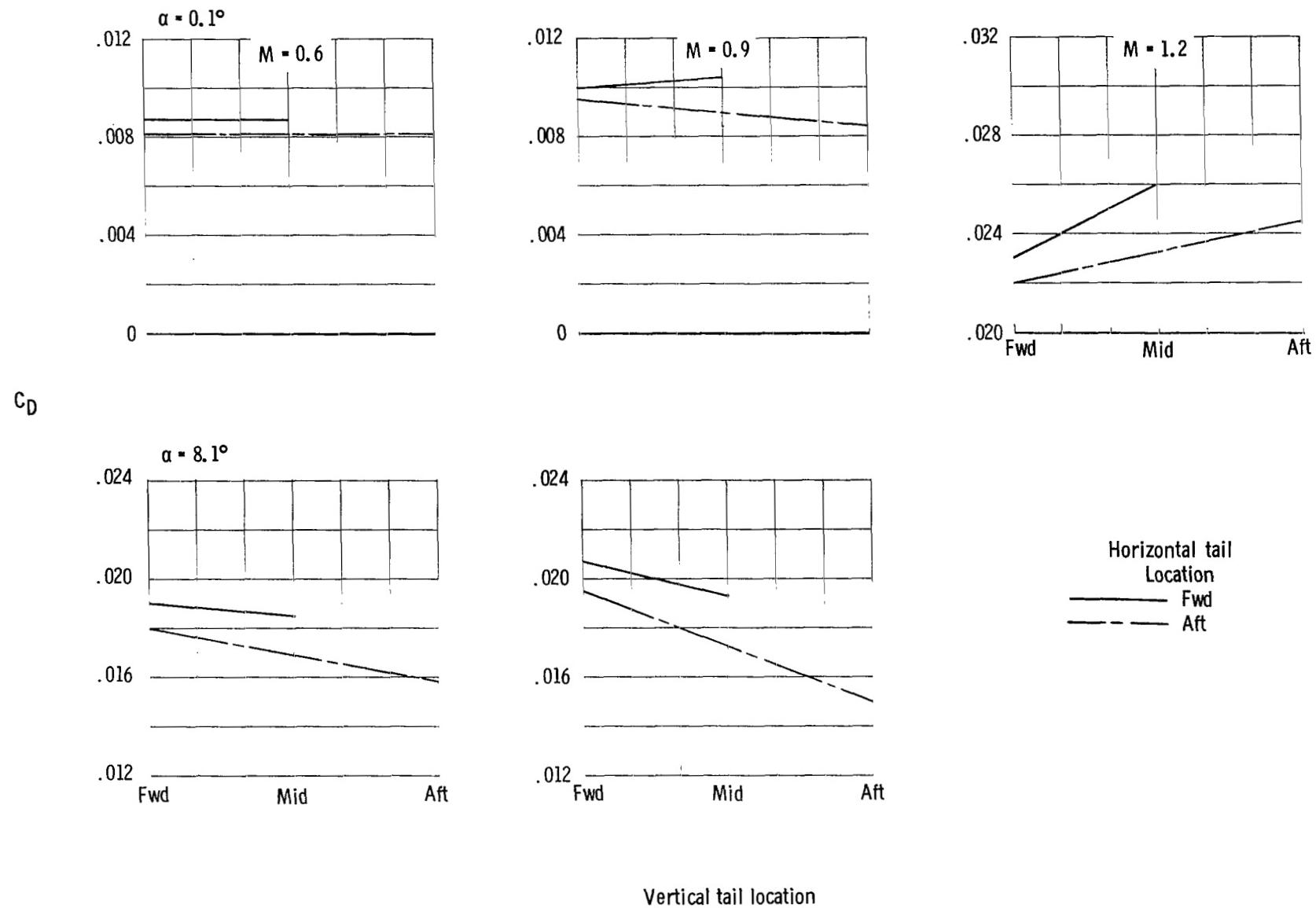
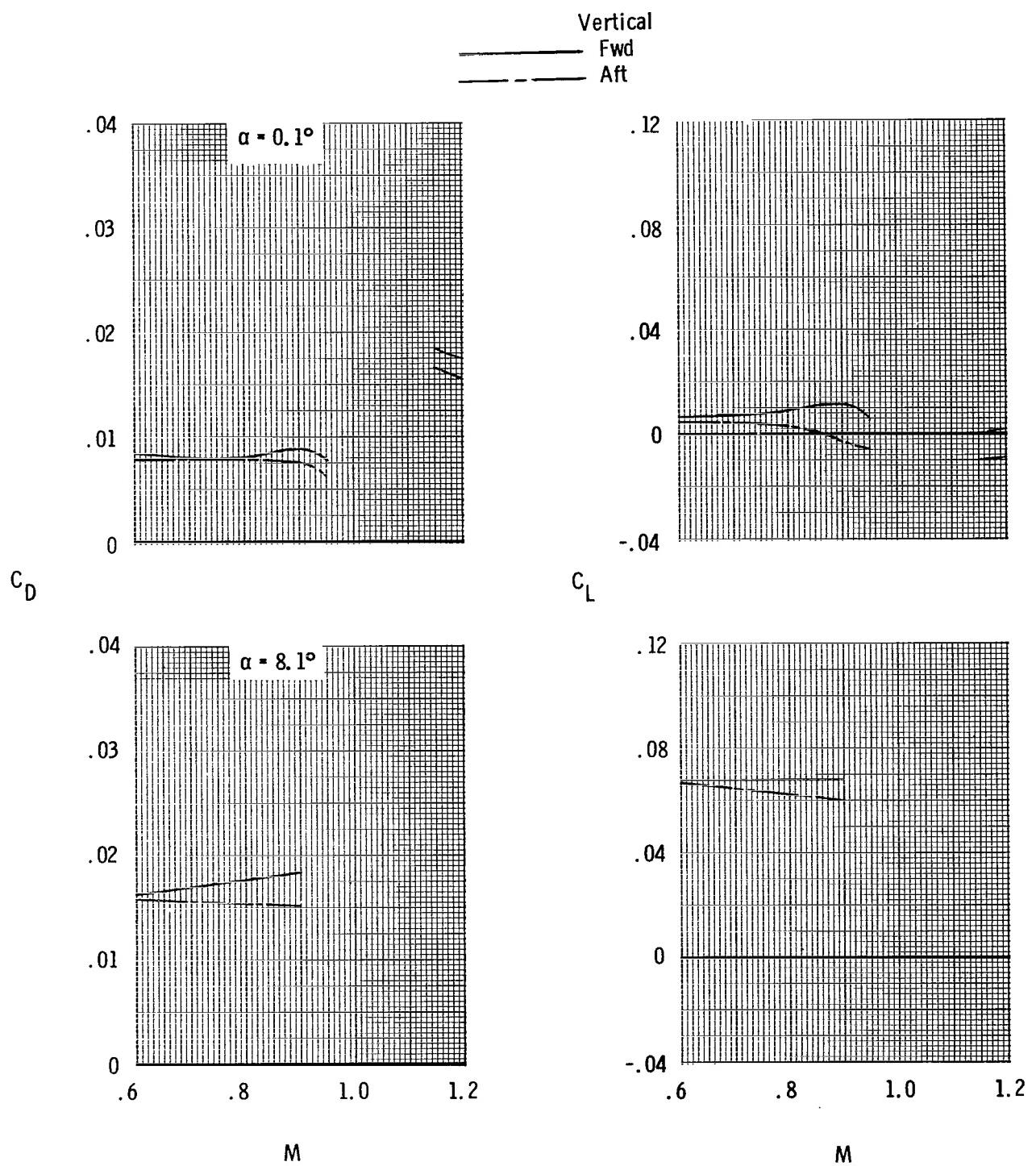
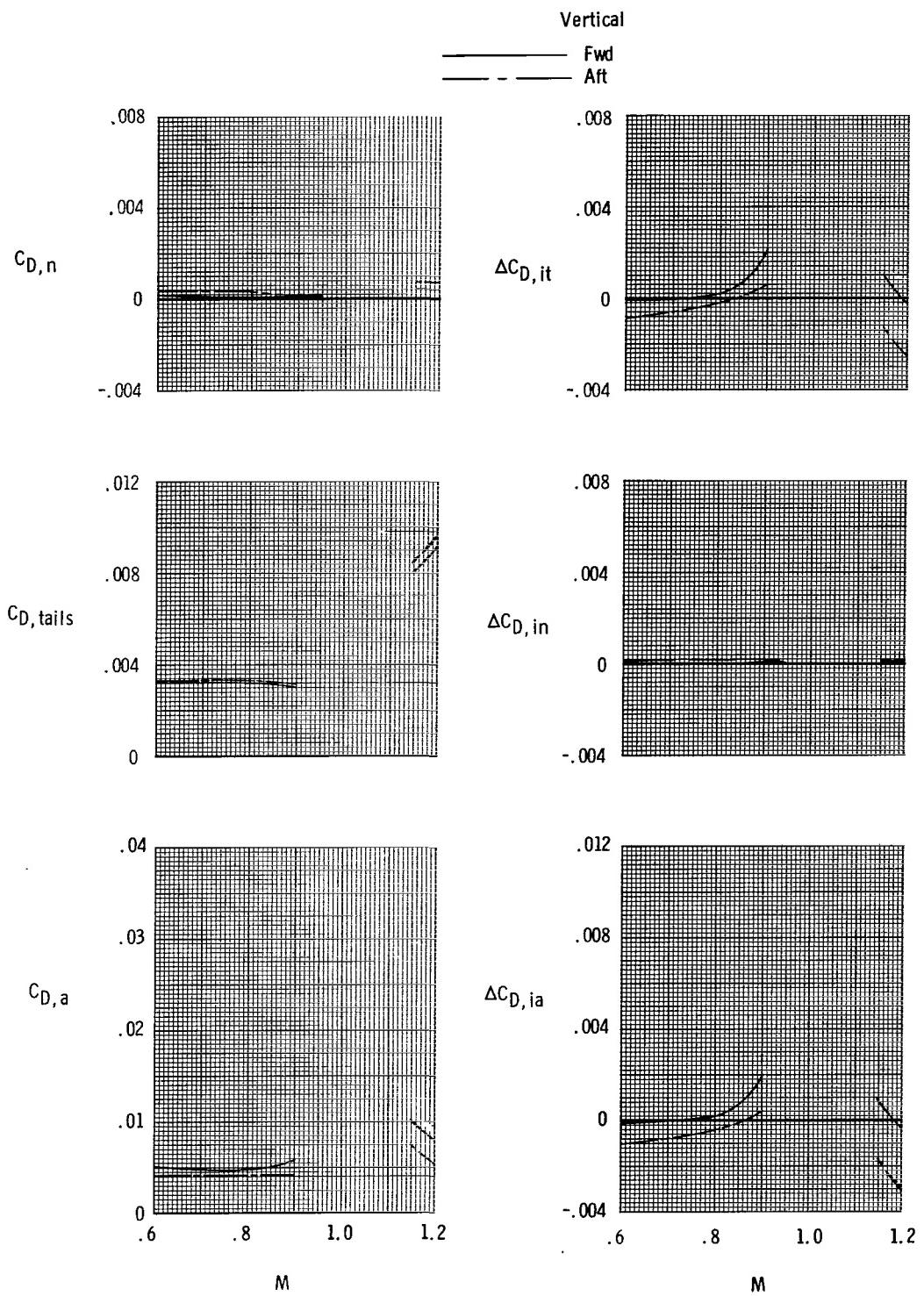


Figure 41.- Summary of effects of twin vertical tail location on total aft-end drag characteristics at scheduled jet total-pressure ratios with dry power nozzles and booms on.



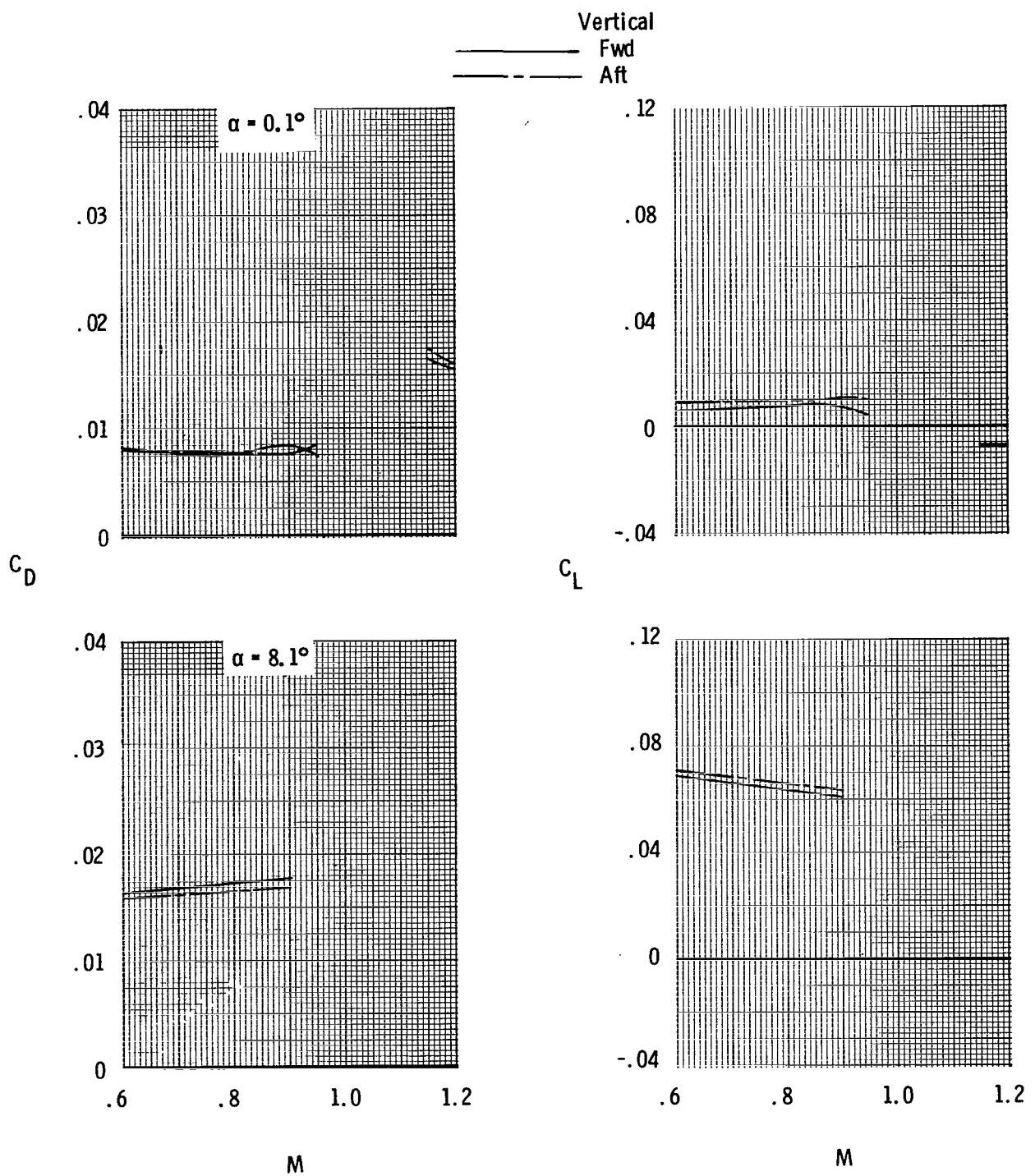
(a) Total aft-end lift and drag coefficient.

Figure 42.- Effects of twin vertical tail location on variation of afterbody characteristics with Mach number for scheduled jet total-pressure ratios with A/B nozzles, booms off, and horizontal tails forward.



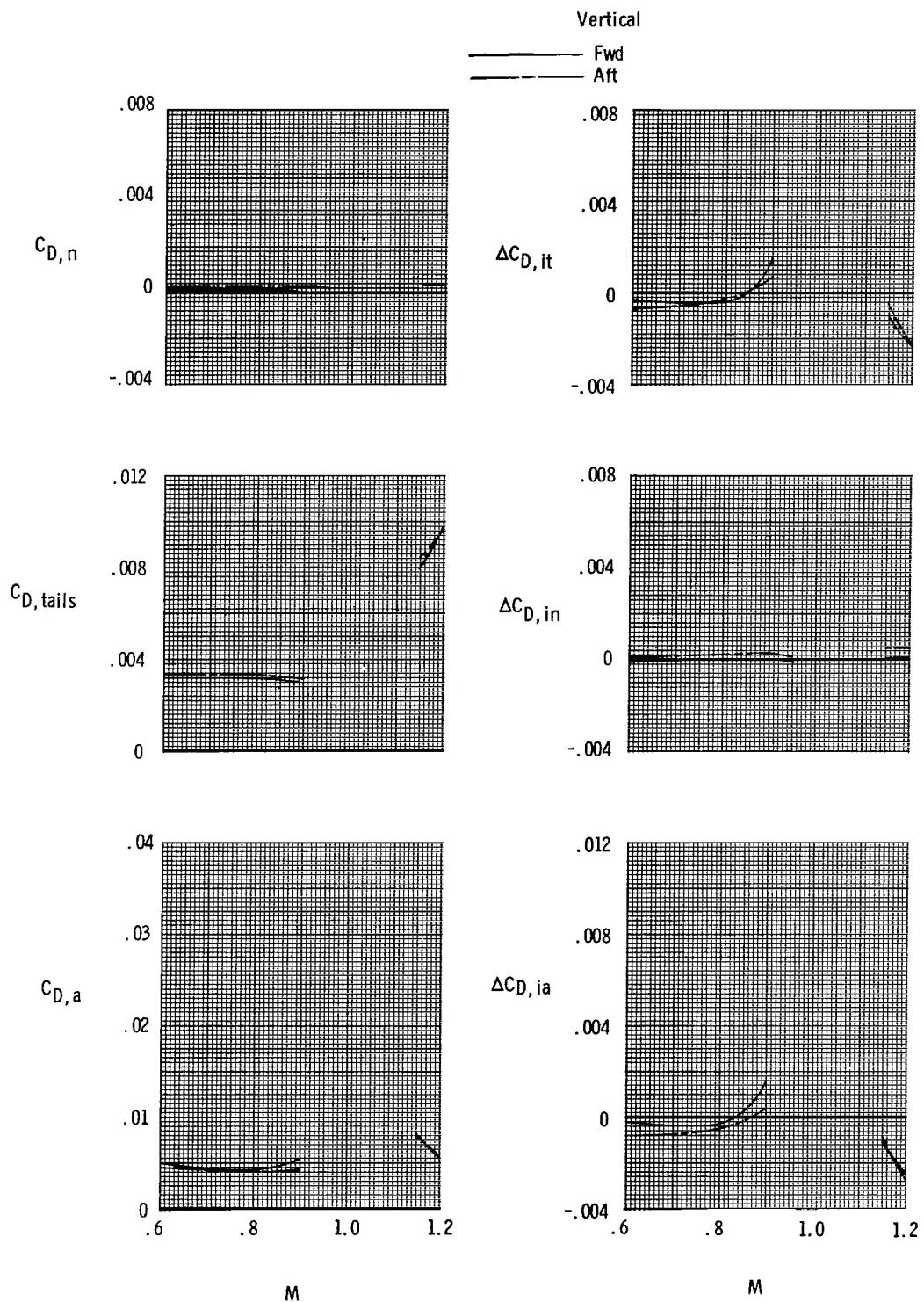
(b) Aft-end drag-coefficient components and tail interference drag-coefficient increments for  $\alpha_{nom} = 0.1^\circ$ .

Figure 42.- Concluded.



(a) Total aft-end lift and drag coefficient.

Figure 43.- Effects of twin vertical tail location on variation of afterbody characteristics with Mach number for scheduled jet total-pressure ratios with A/B nozzles, booms off, and horizontal tails aft.



(b) Aft-end drag-coefficient components and tail interference drag-coefficient increments for  $\alpha_{nom} = 0.1^\circ$ .

Figure 43.- Concluded.

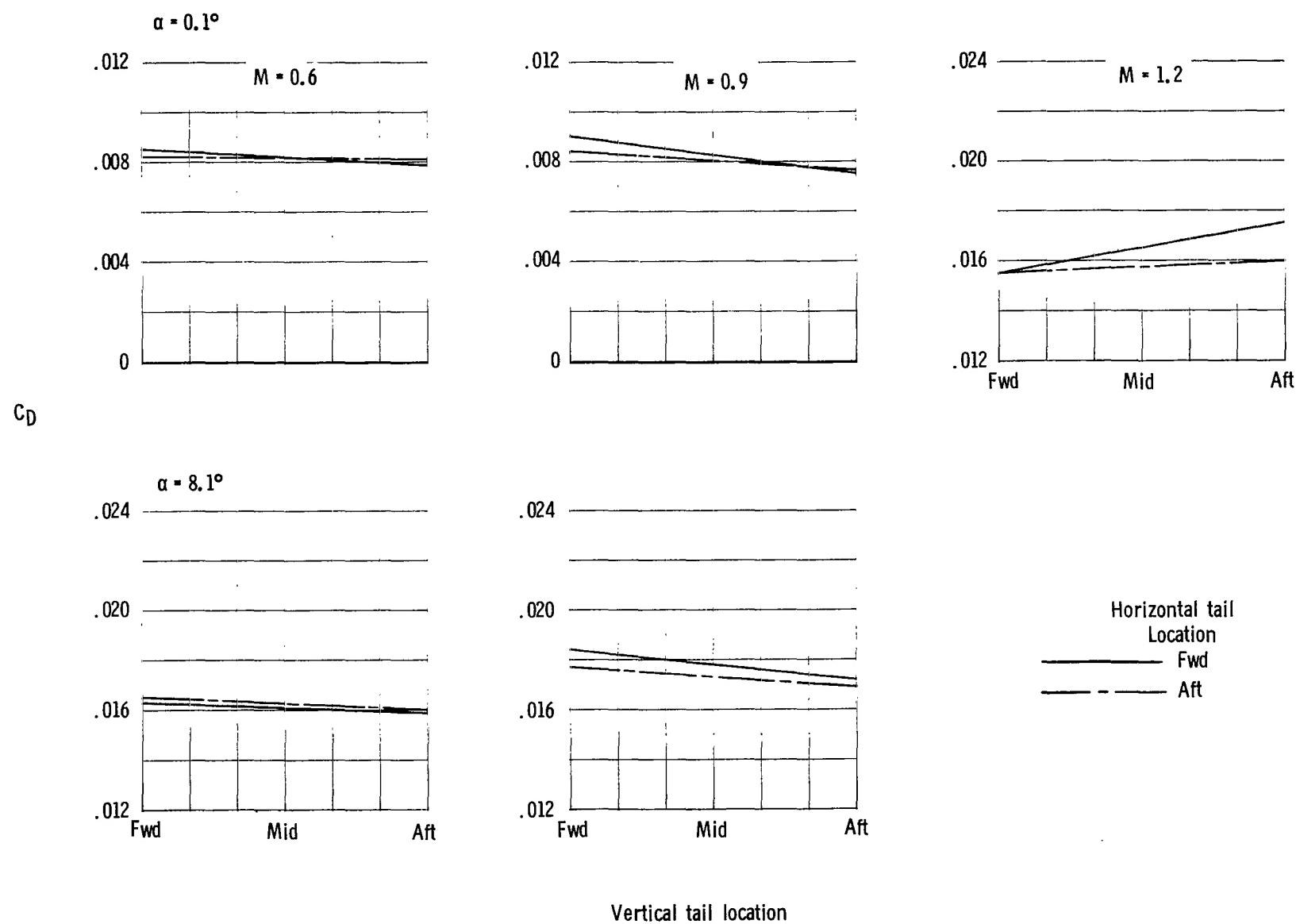
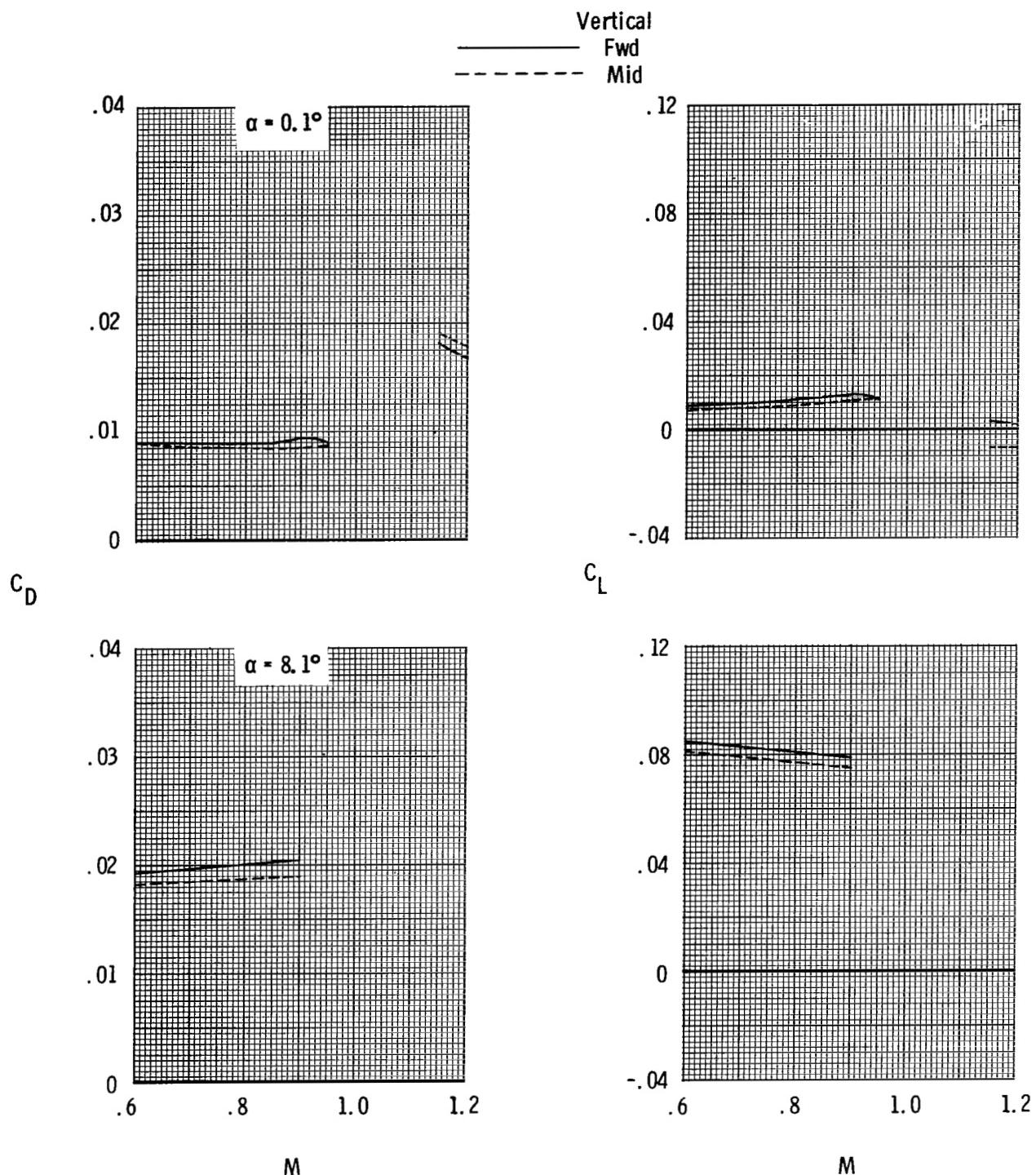
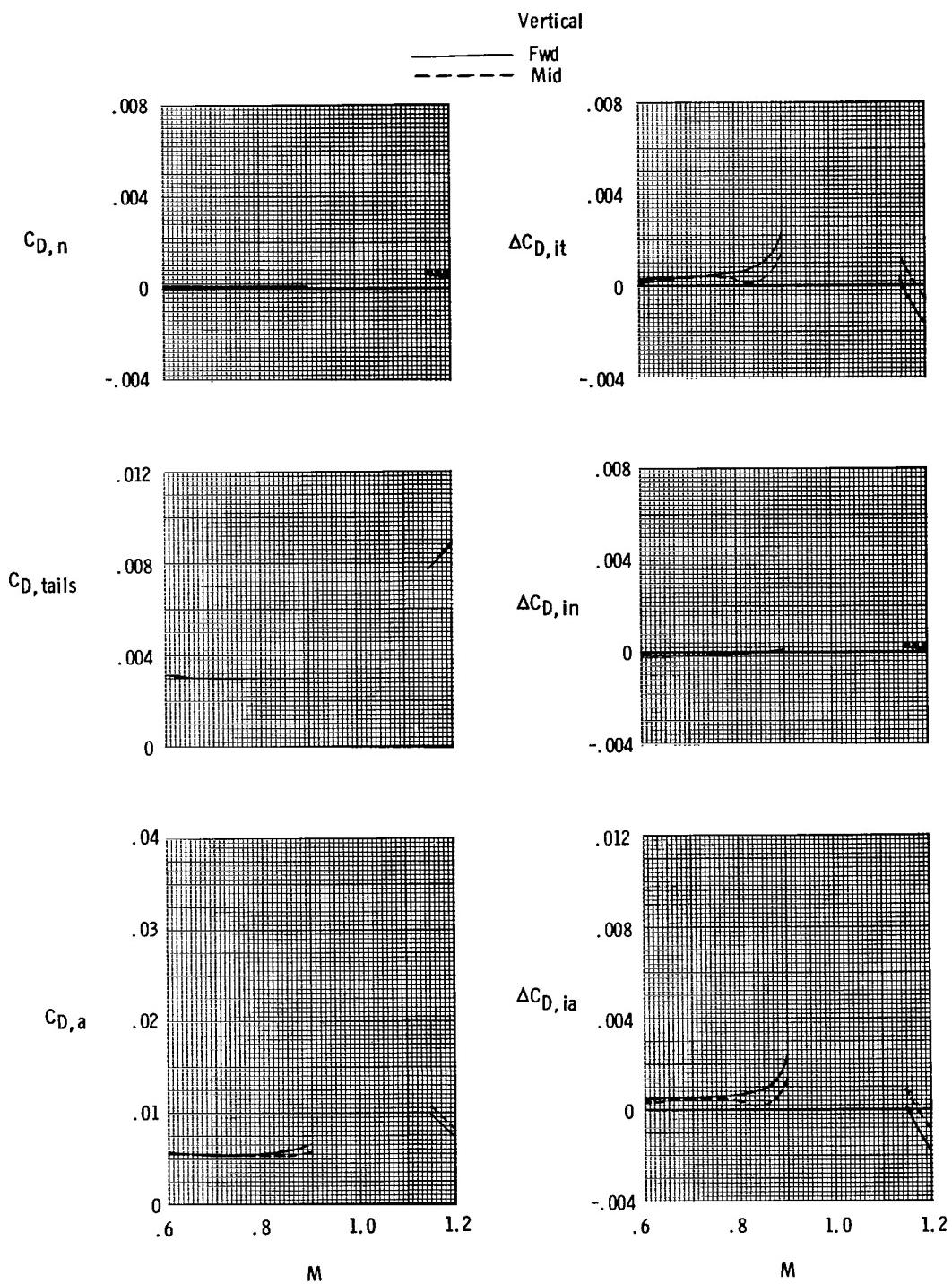


Figure 44.- Summary of effects of twin vertical tail location on total aft-end drag characteristics at scheduled jet total-pressure ratios with A/B nozzles and booms off.



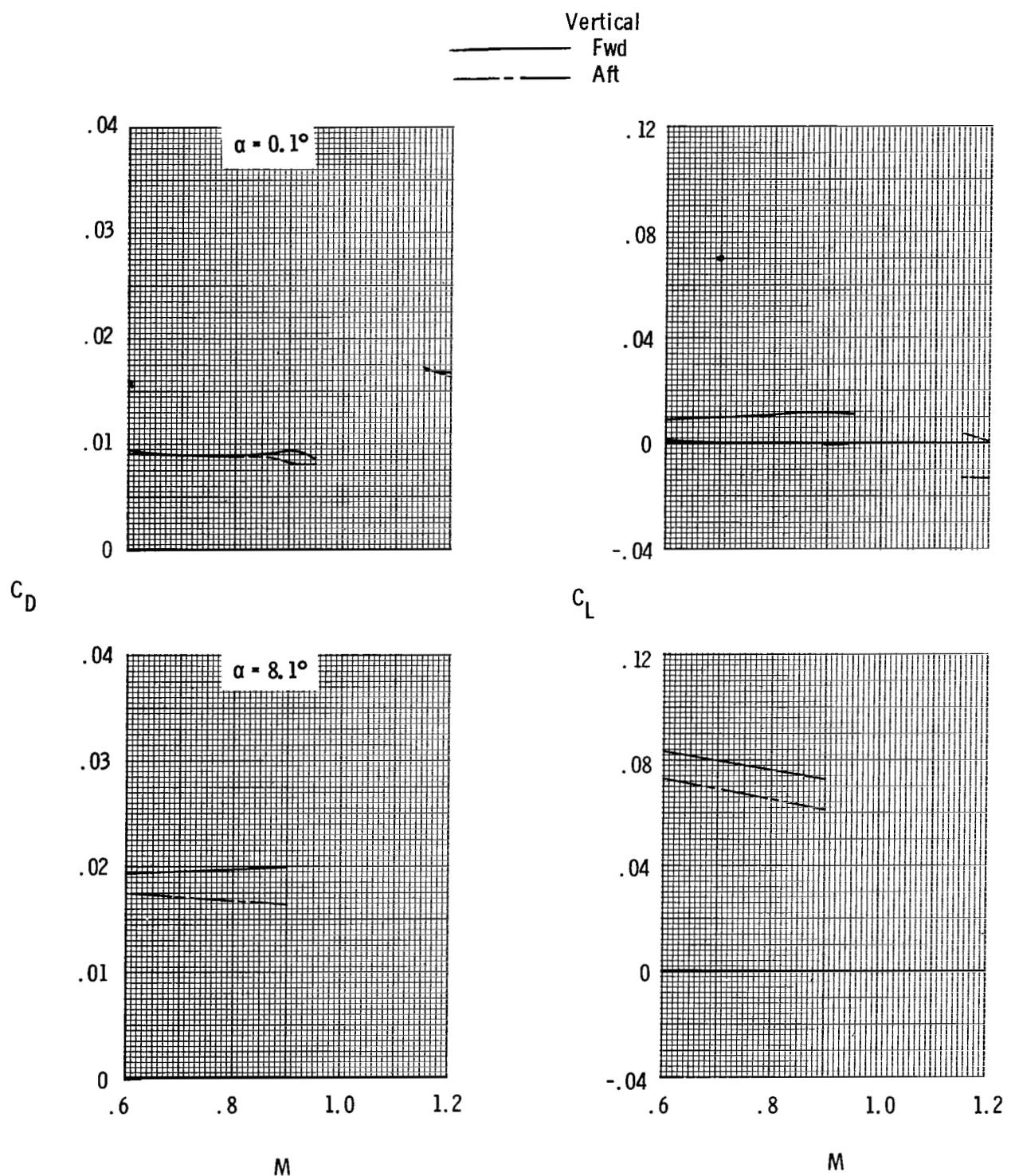
(a) Total aft-end lift and drag coefficient.

Figure 45.- Effects of twin vertical tail location on variation of afterbody characteristics with Mach number for scheduled jet total-pressure ratios with A/B nozzles, booms on, and horizontal tails forward.



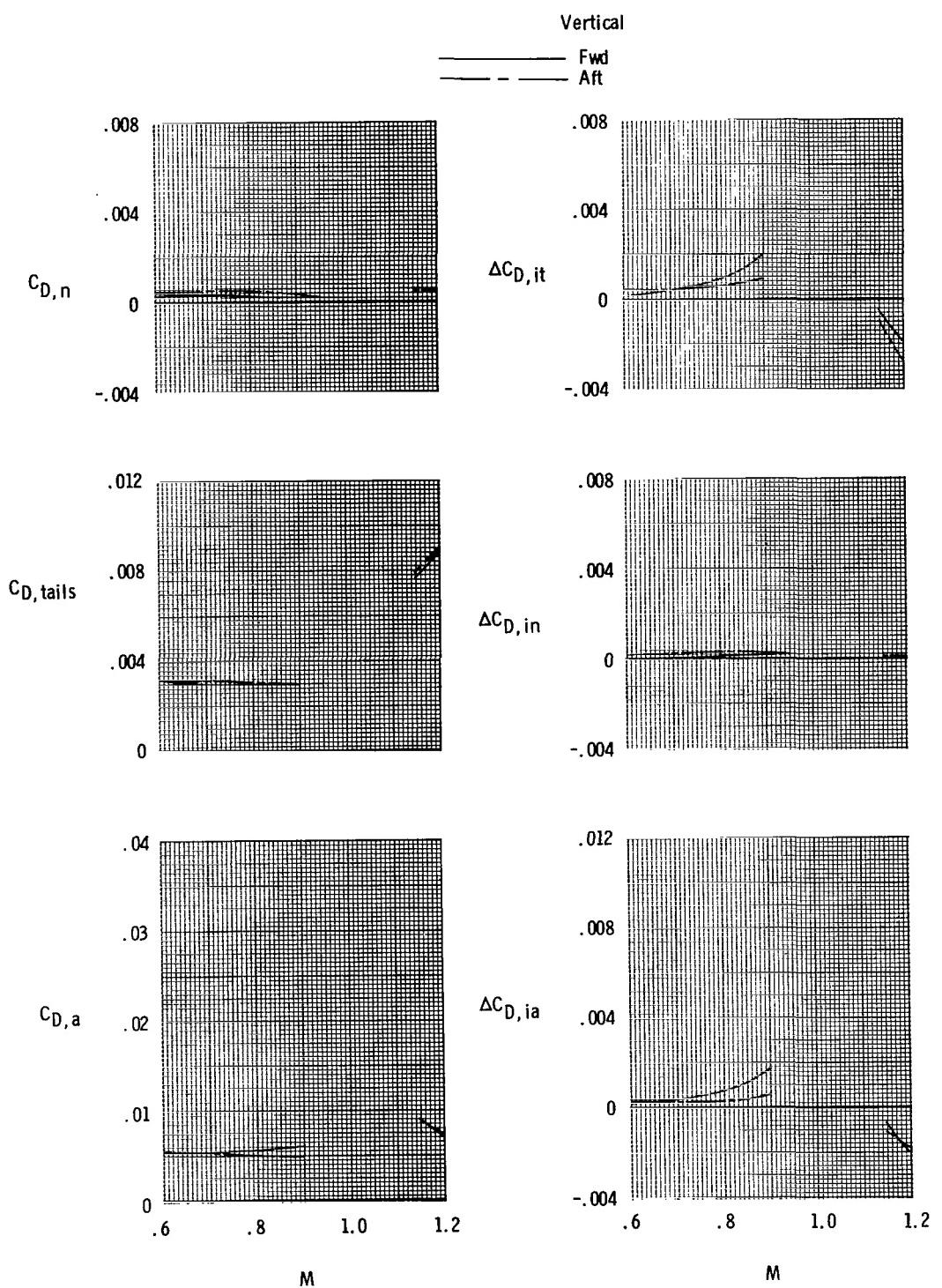
(b) Aft-end drag-coefficient components and tail interference drag-coefficient increments for  $\alpha_{nom} = 0.1^\circ$ .

Figure 45.- Concluded.



(a) Total aft-end lift and drag coefficients.

Figure 46.- Effects of twin vertical tail location on variation of afterbody characteristics with Mach number for scheduled jet total-pressure ratios with A/B nozzles, booms on, and horizontal tails aft.



(b) Aft-end drag-coefficient components and tail interference drag-coefficient increments for  $\alpha_{nom} = 0.1^\circ$ .

Figure 46.- Concluded.

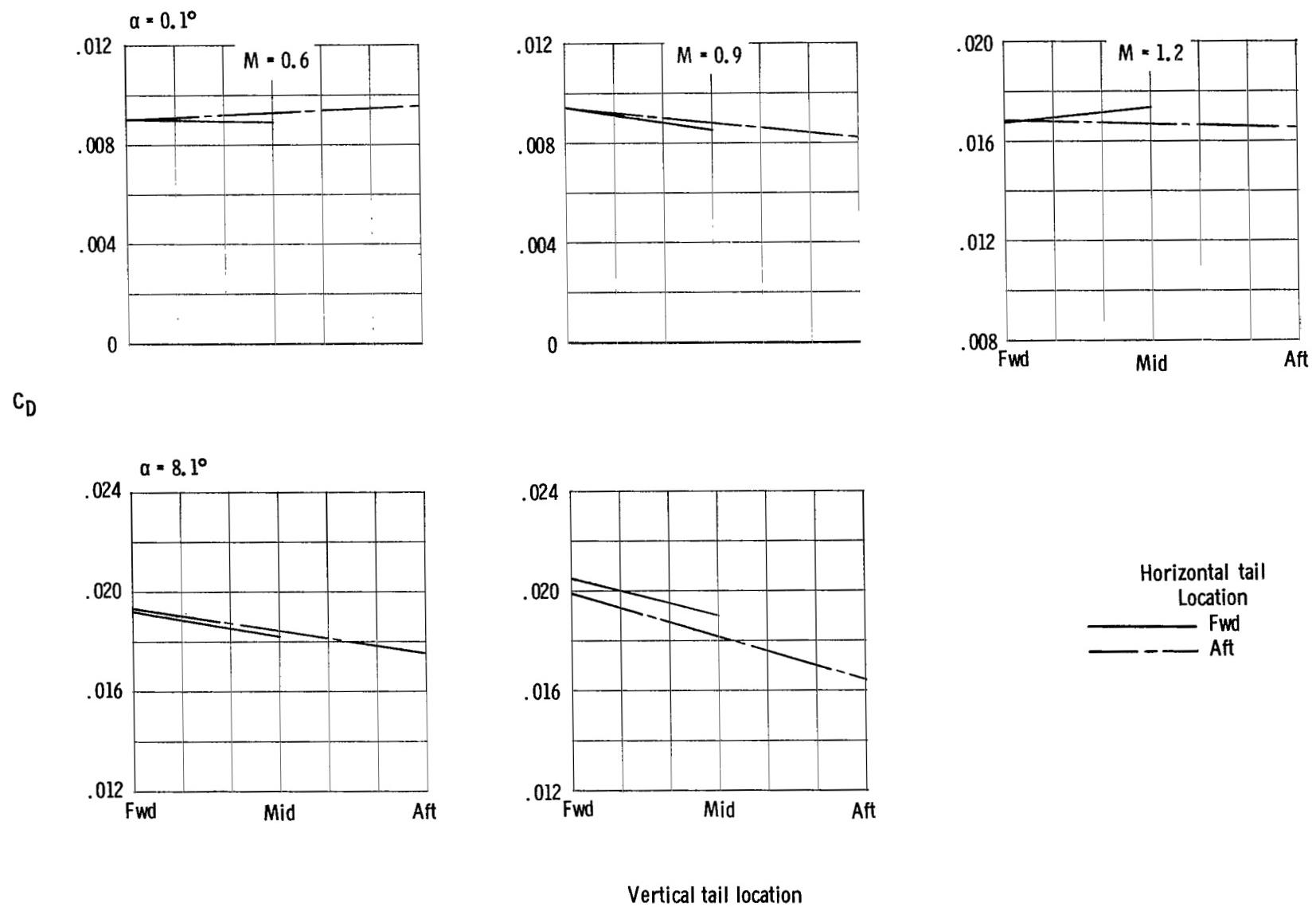
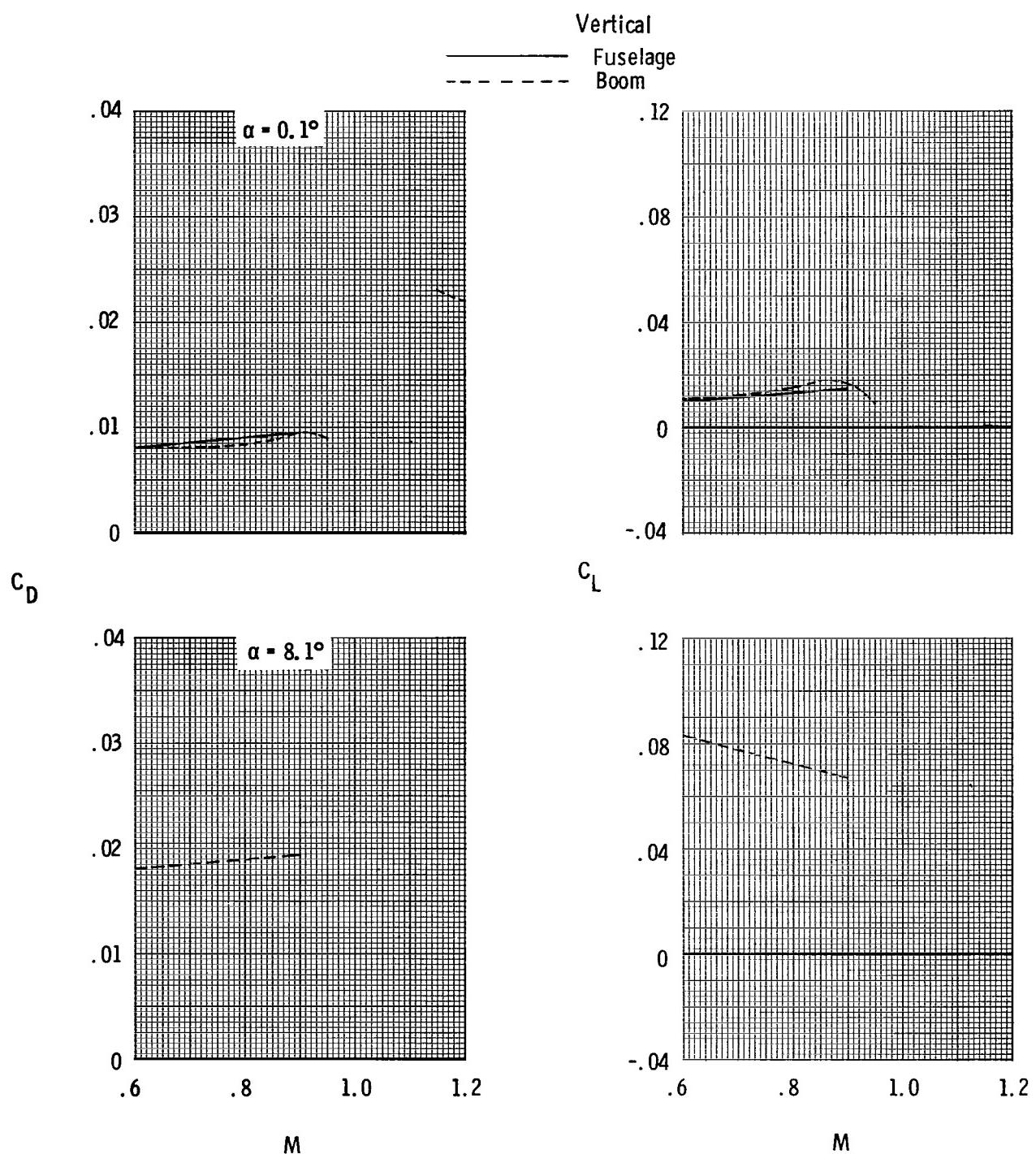
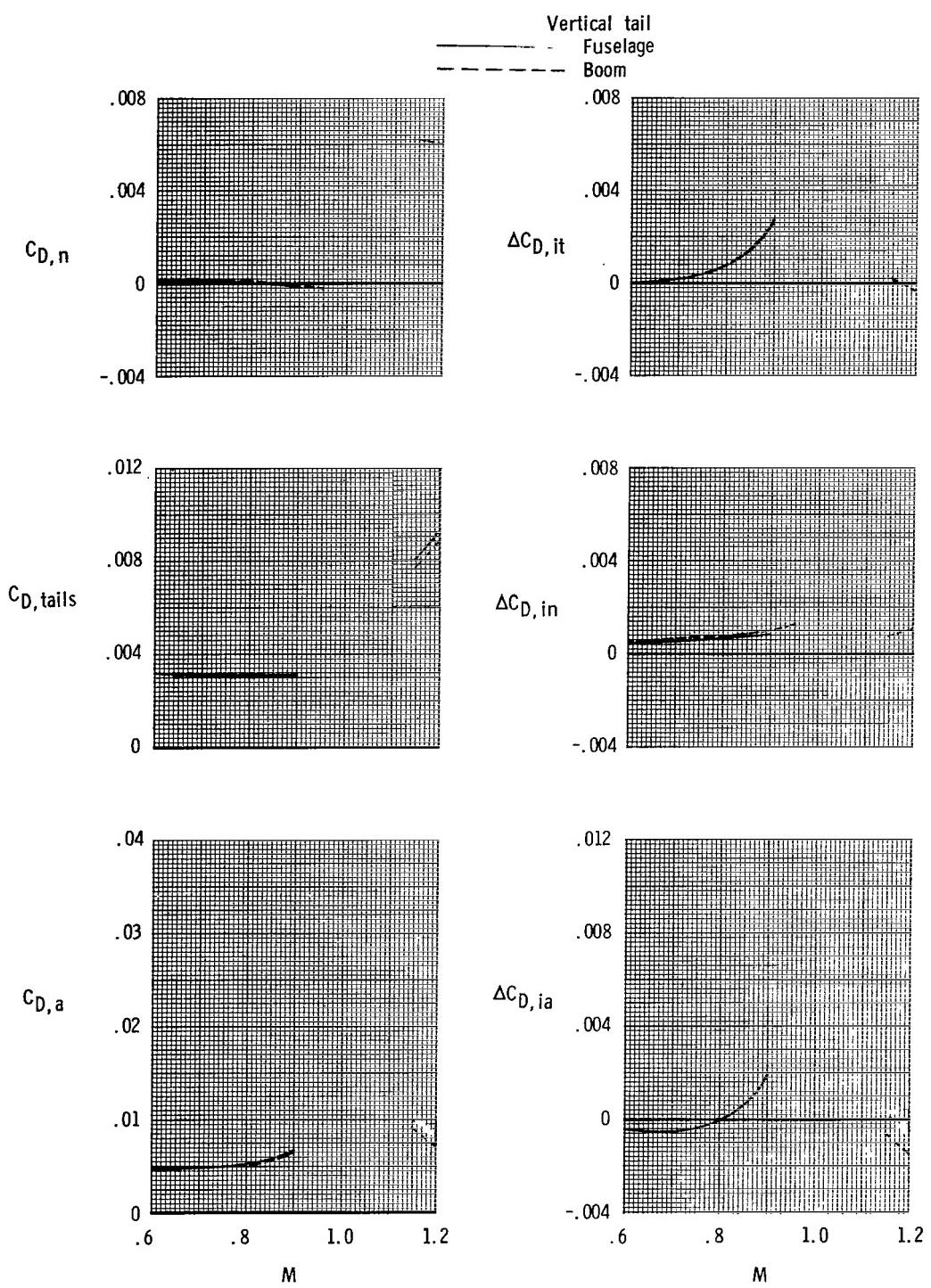


Figure 47.- Summary of effects of twin vertical tail location on total aft-end drag characteristics at scheduled jet total-pressure ratios with A/B nozzles and booms on.



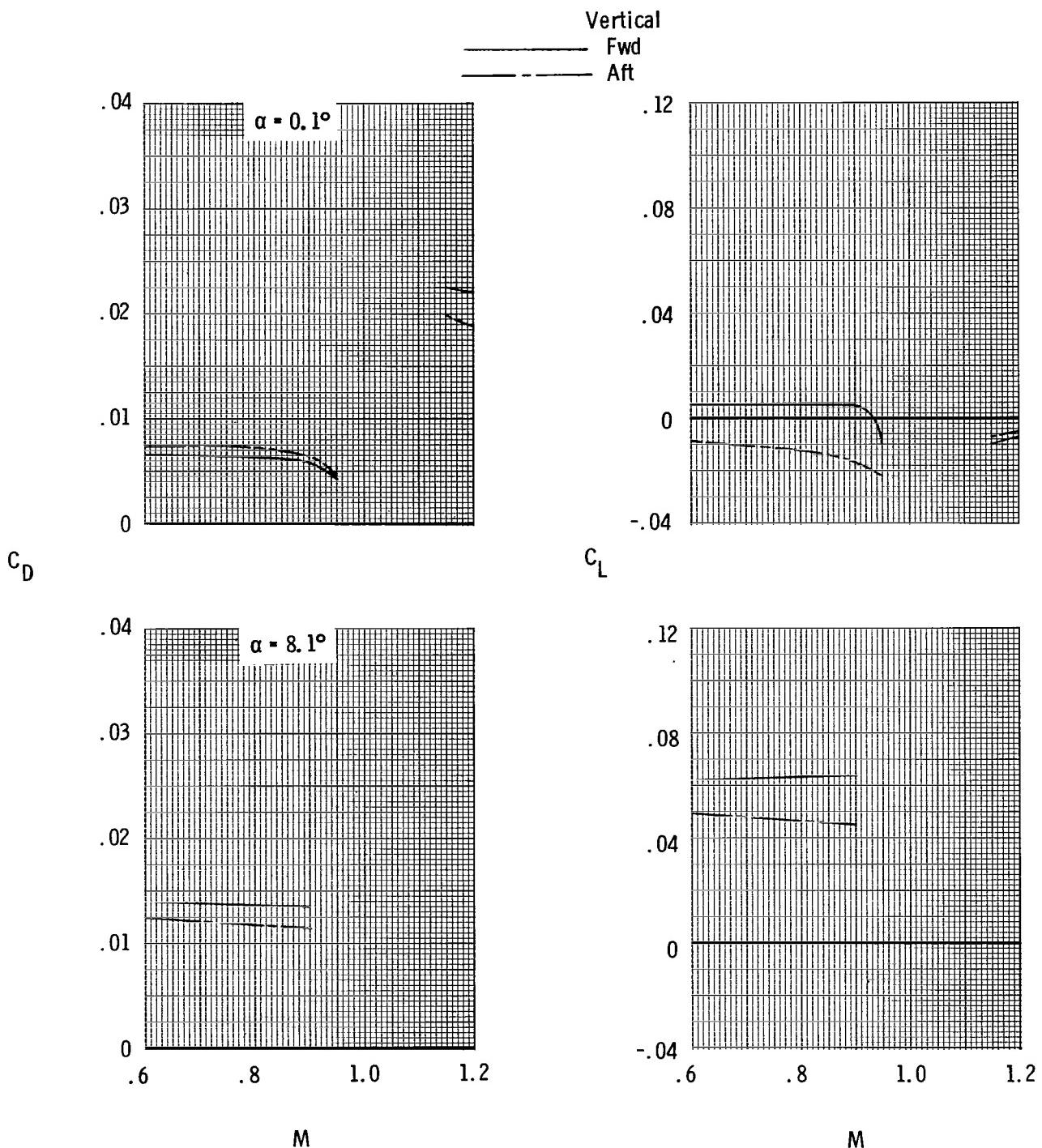
(a) Total aft-end lift and drag coefficient.

**Figure 48.-** Effects of twin vertical tail lateral location on variation of afterbody characteristics with Mach number for scheduled jet total-pressure ratios with dry power nozzles, booms on, and horizontal tails aft. Vertical tails at FS 136.68.



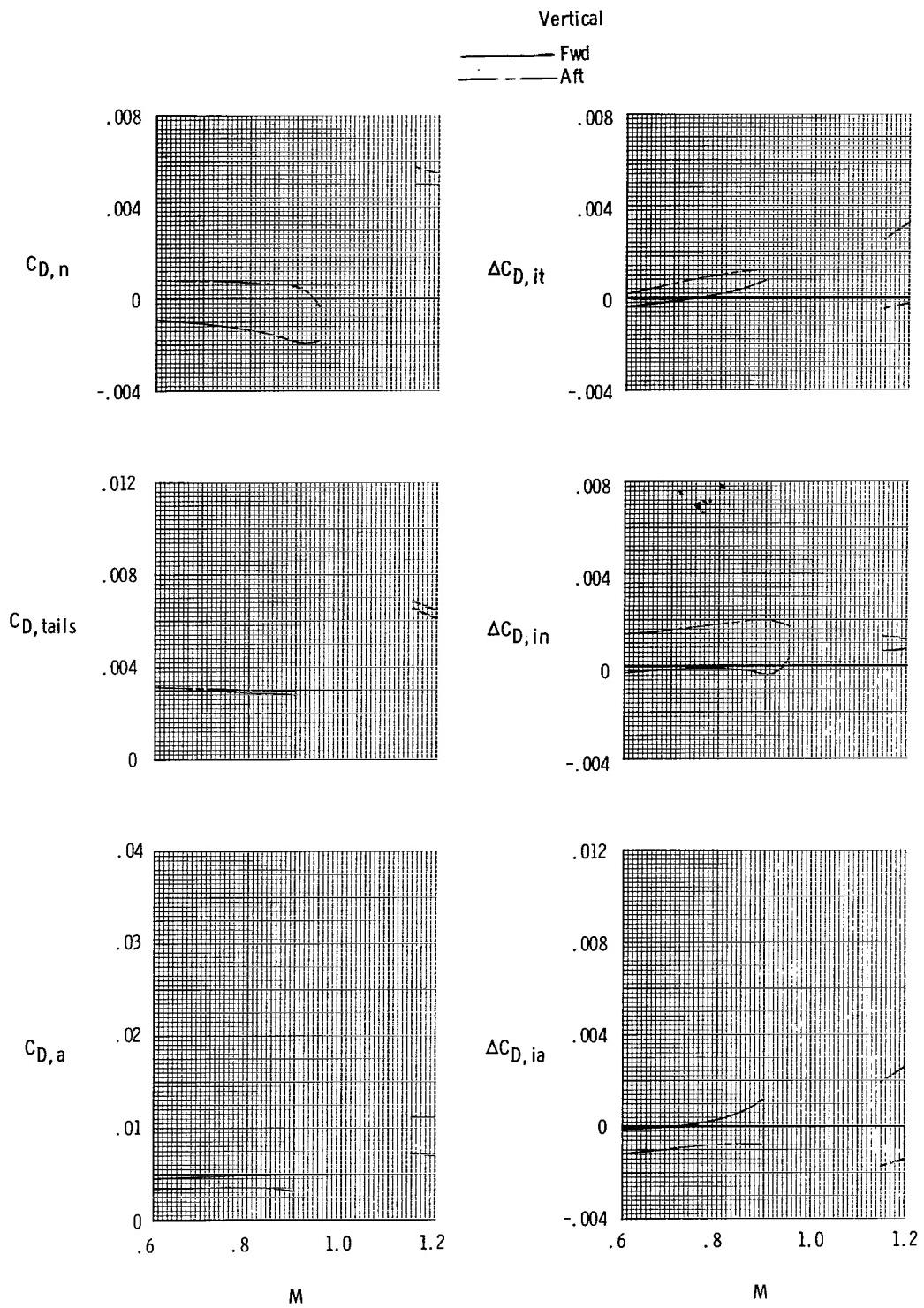
(b) Aft-end drag-coefficient components and tail interference drag-coefficient increments for  $\alpha_{nom} = 0.1^\circ$ .

Figure 48.- Concluded.



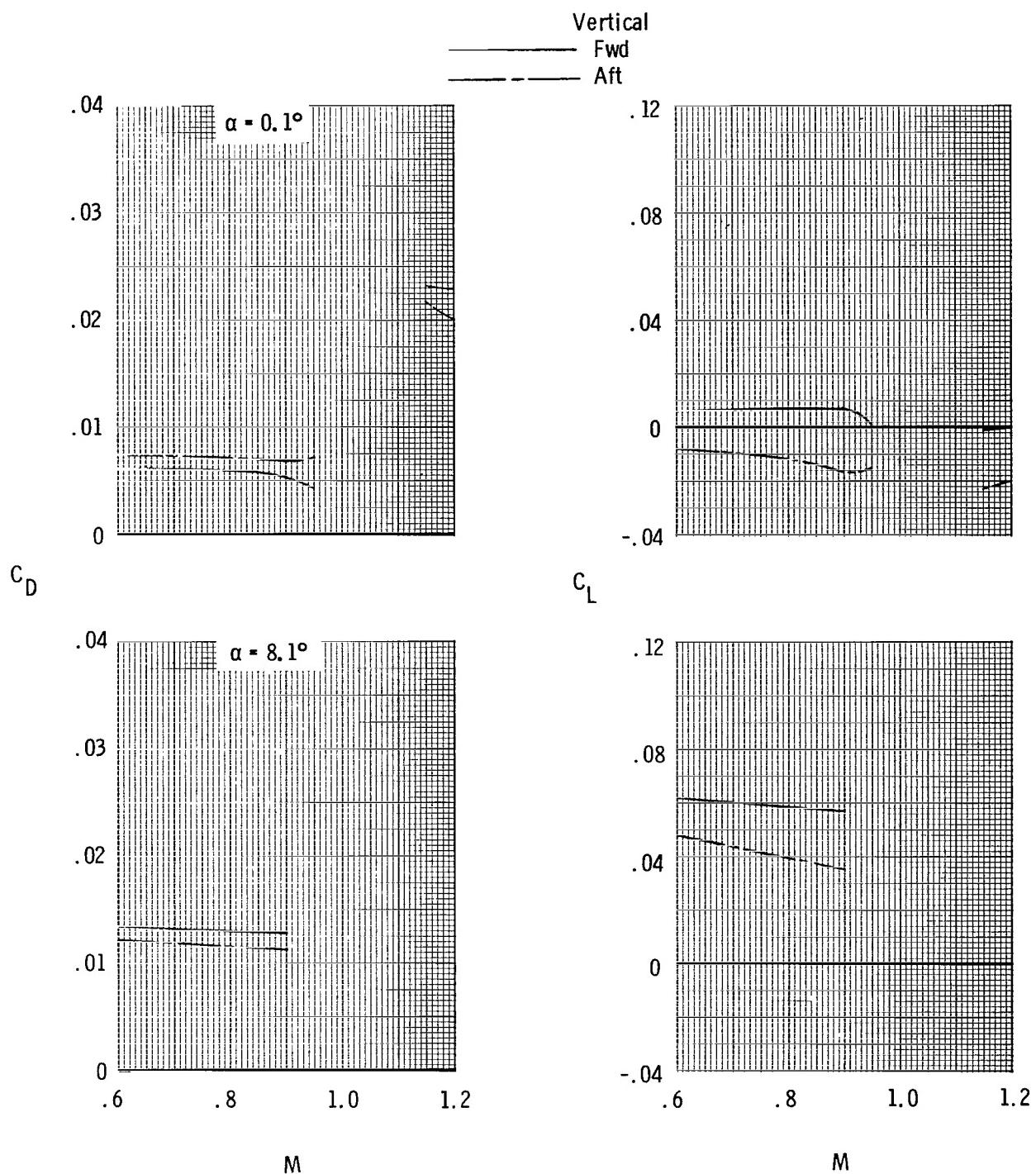
(a) Total aft-end lift and drag coefficient.

Figure 49.-- Effects of single vertical tail location on variation of afterbody characteristics with Mach number for scheduled jet total-pressure ratios with dry power nozzles, booms off, and horizontal tails forward.



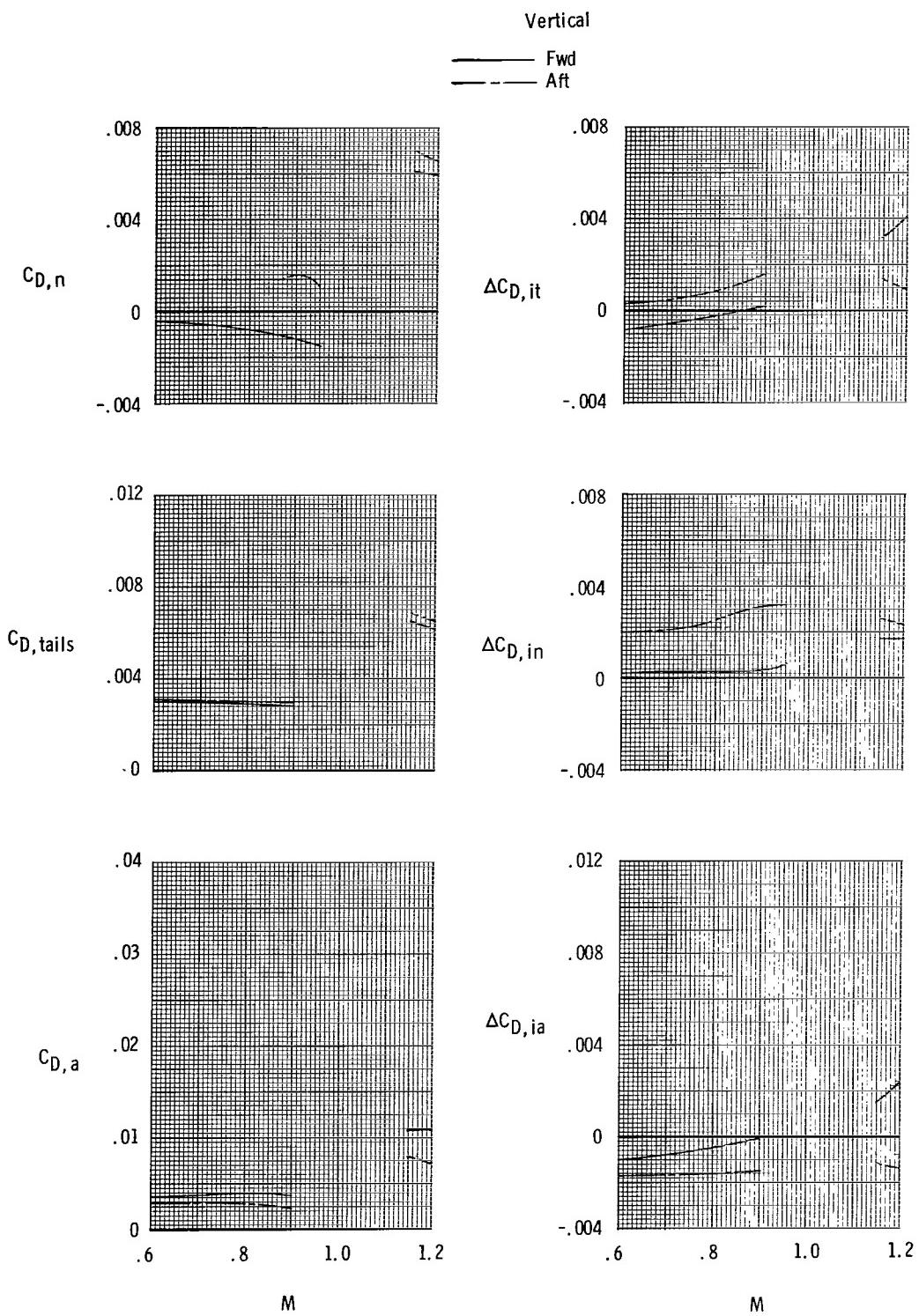
(b) Aft-end drag-coefficient components and tail interference drag-coefficient increments for  $\alpha_{nom} = 0.1^\circ$ .

Figure 49.- Concluded.



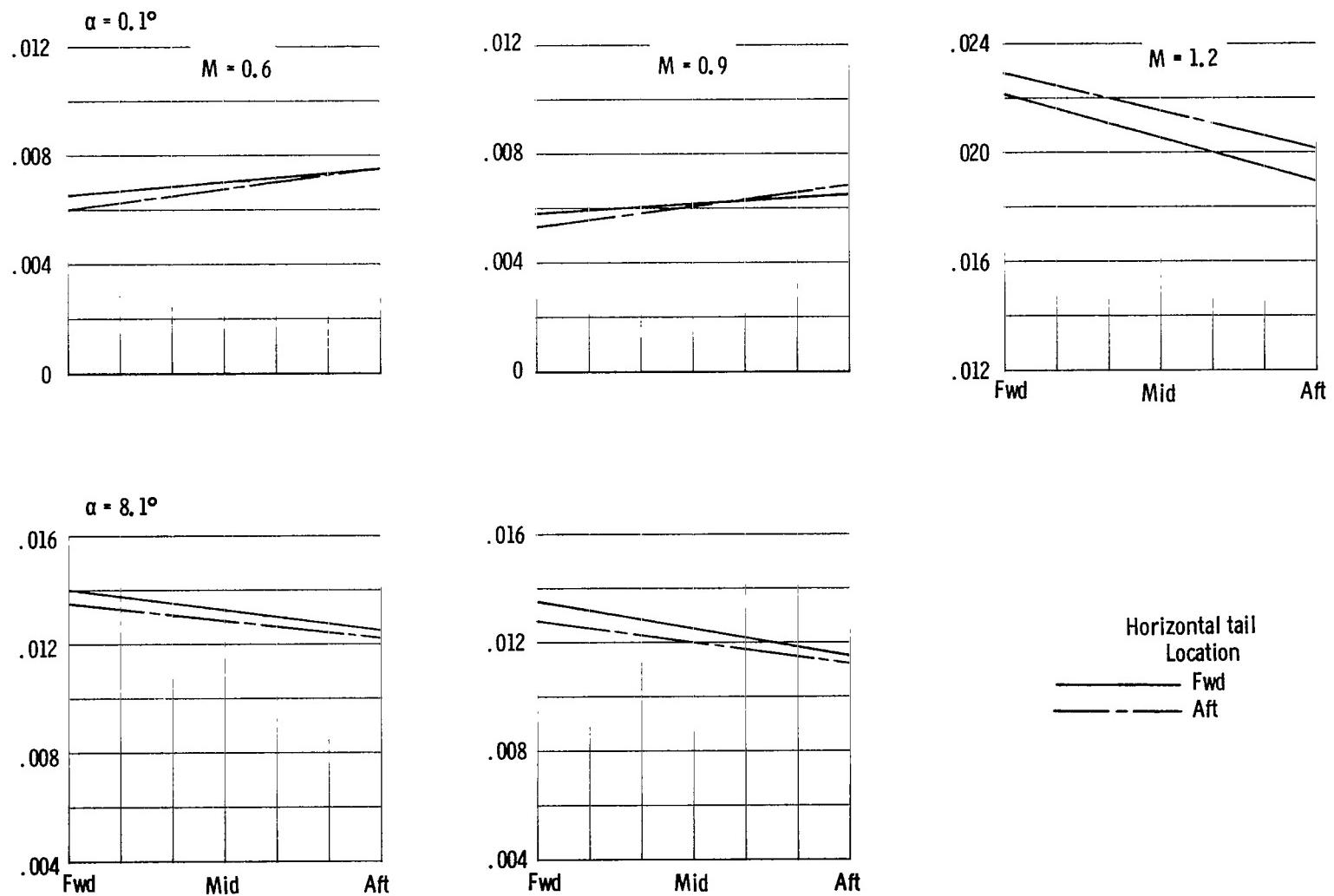
(a) Total aft-end lift and drag coefficient.

Figure 50.- Effects of single vertical tail location on variation of afterbody characteristics with Mach number for scheduled jet total-pressure ratios with dry power nozzles, booms off, and horizontal tails aft.



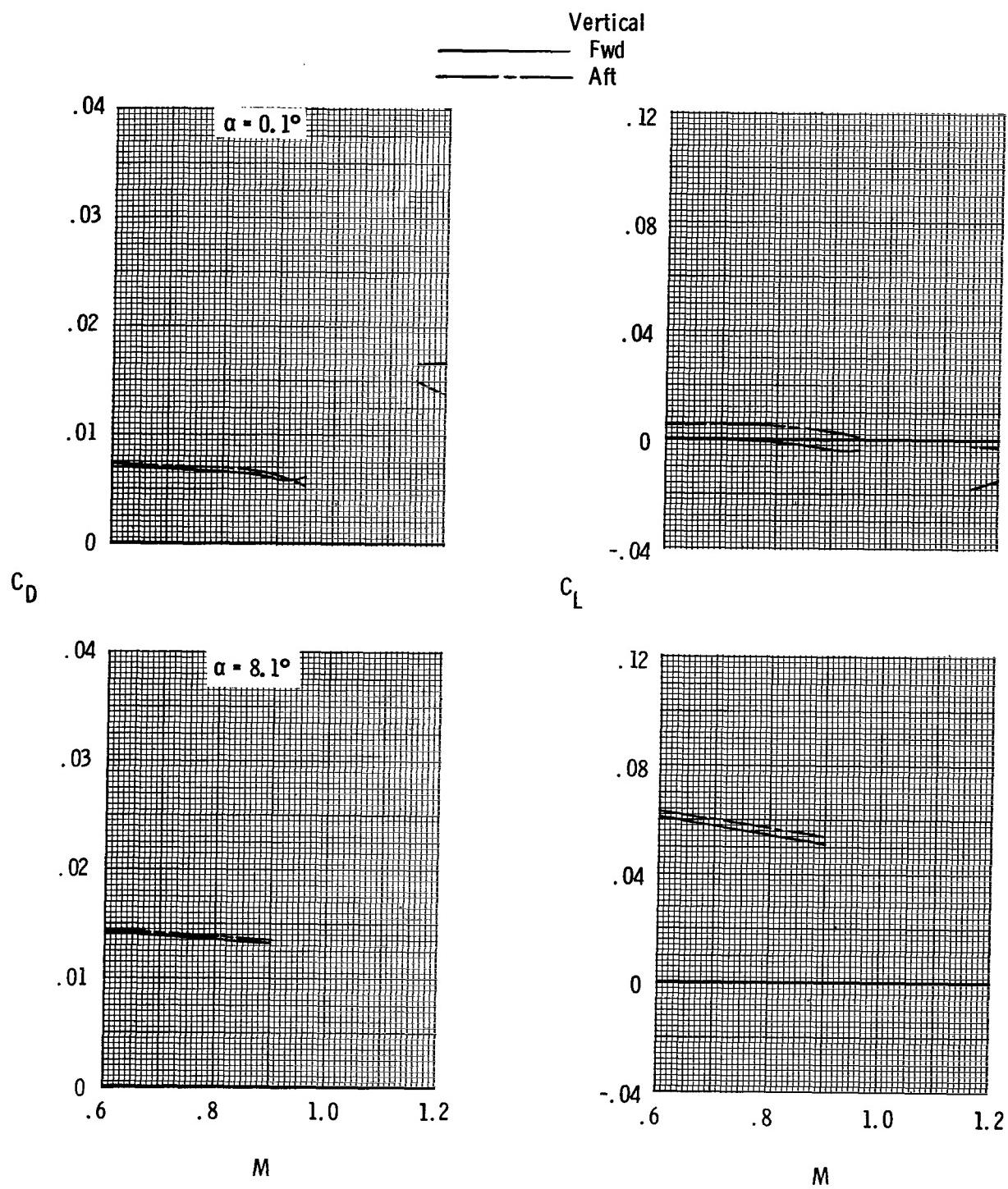
(b) Aft-end drag-coefficient components and tail interference drag-coefficient increments for  $\alpha_{nom} = 0.1^\circ$ .

Figure 50.- Concluded.



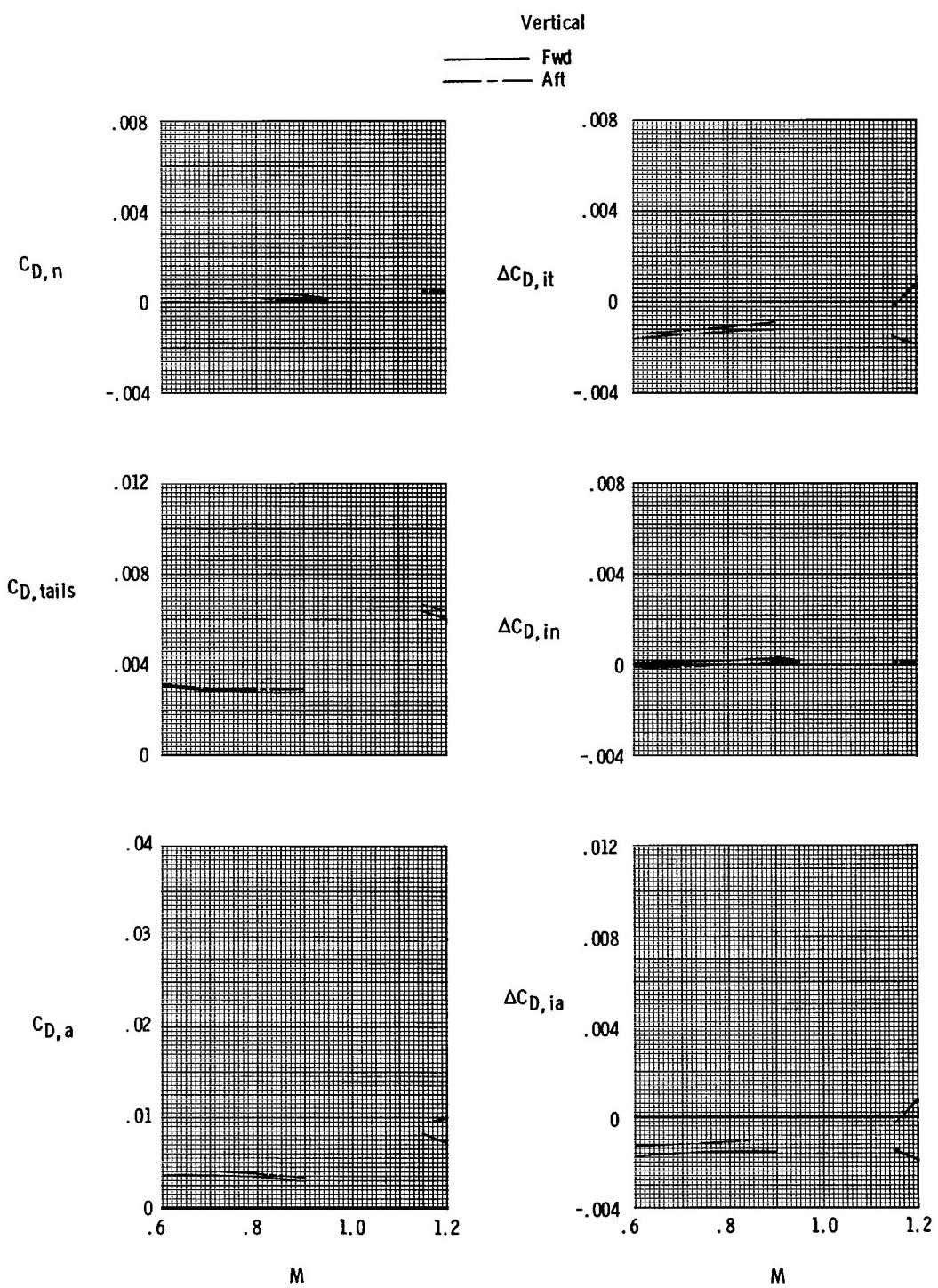
Single vertical tail location

Figure 51.- Summary of effects of single vertical tail location on total aft-end drag characteristics at scheduled jet total-pressure ratios with dry power nozzles and booms off.



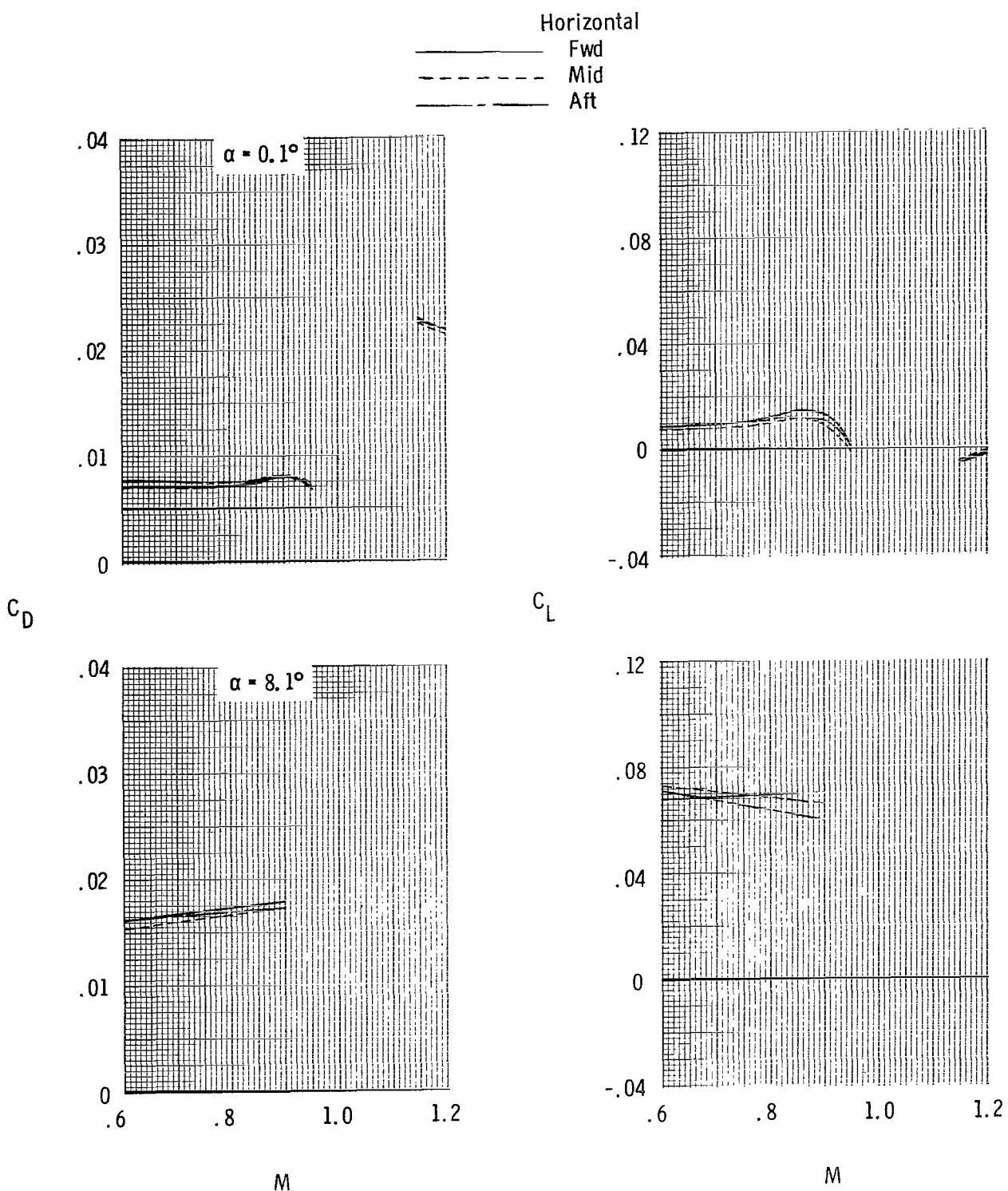
(a) Total aft-end lift and drag coefficient.

Figure 52.- Effects of single vertical tail location on variation of afterbody characteristics with Mach number for scheduled jet total-pressure ratios with A/B nozzles, booms off, and horizontal tails aft.



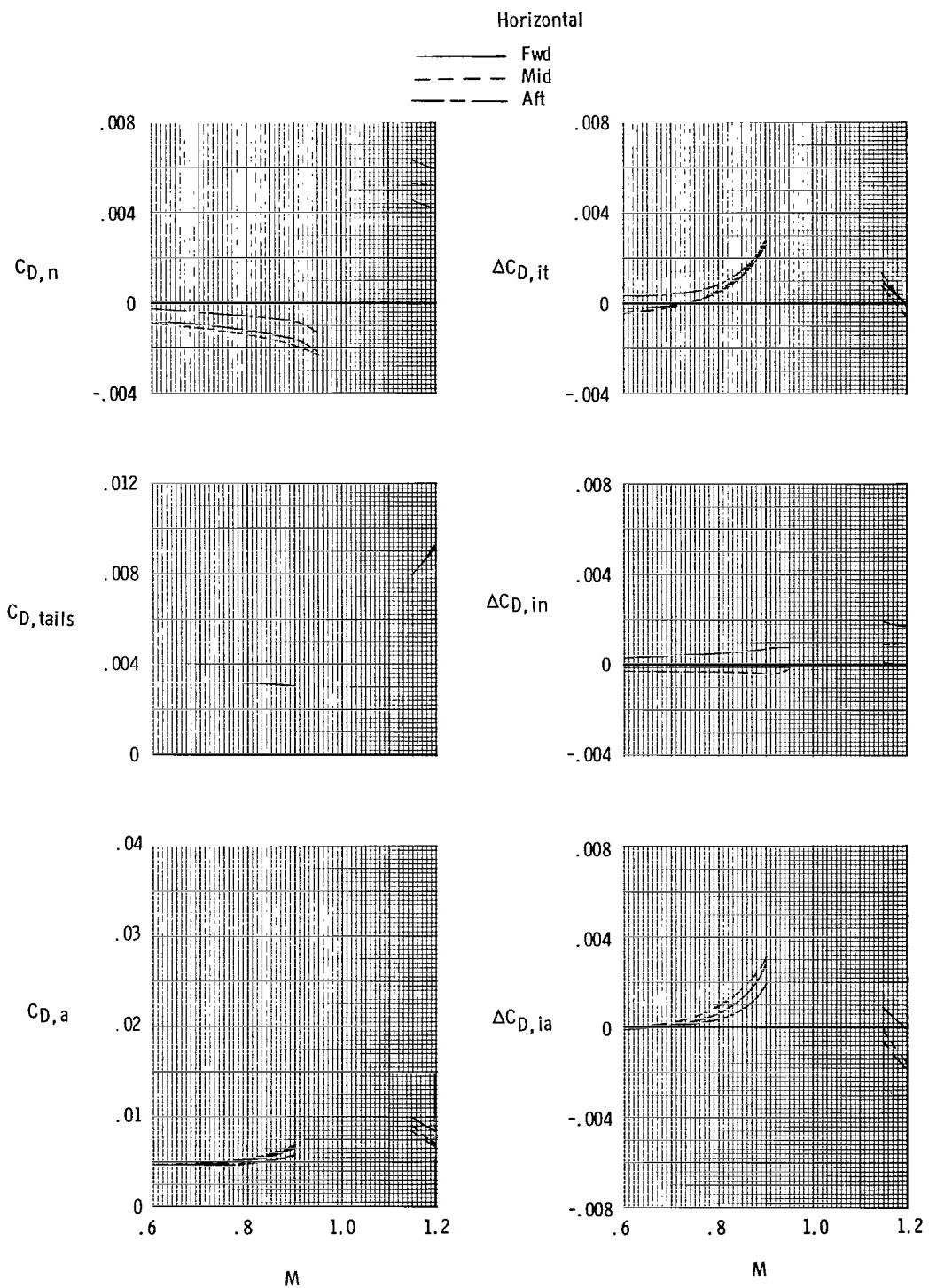
(b) Aft-end drag-coefficient components and tail interference drag-coefficient increments for  $\alpha_{nom} = 0.1^\circ$ .

Figure 52.- Concluded.



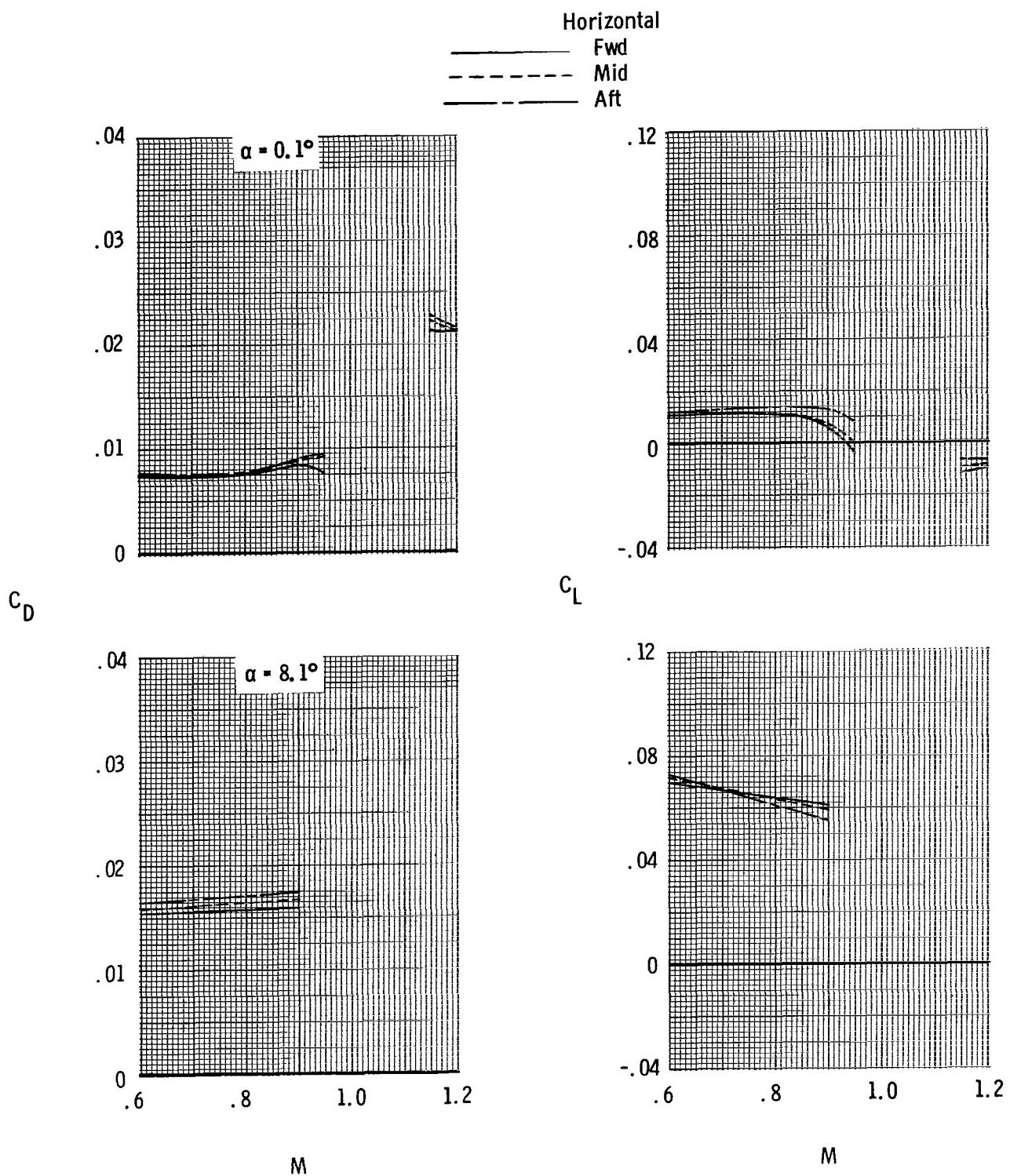
(a) Total aft-end lift and drag coefficient.

Figure 53.- Effects of horizontal tail location on variation of afterbody characteristics with Mach number for scheduled jet total-pressure ratios with dry power nozzles, booms off, and twin vertical tails forward.



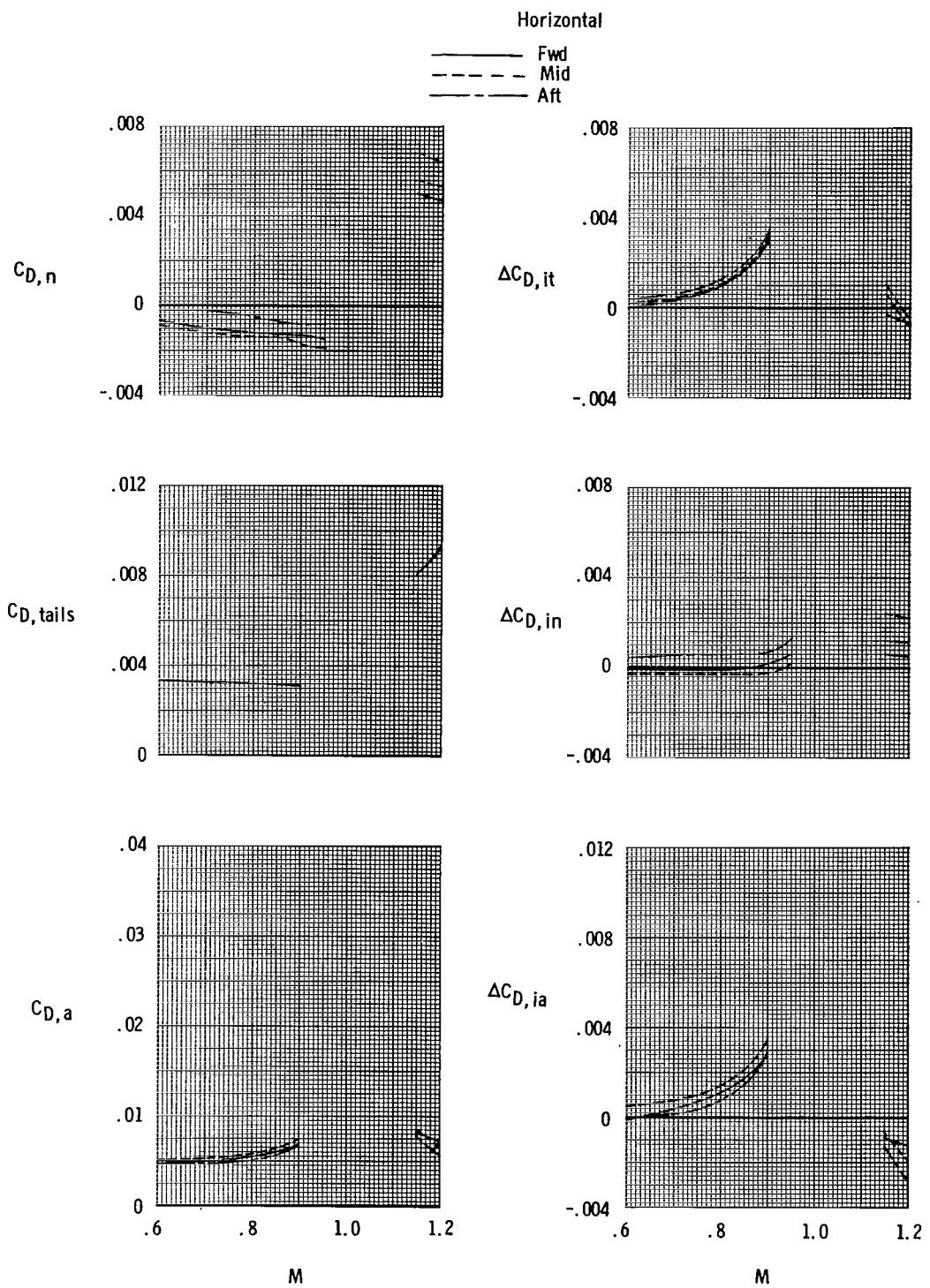
(b) Aft-end drag-coefficient components and tail interference drag-coefficient increments for  $\alpha_{nom} = 0.1^\circ$ .

Figure 53.- Concluded.



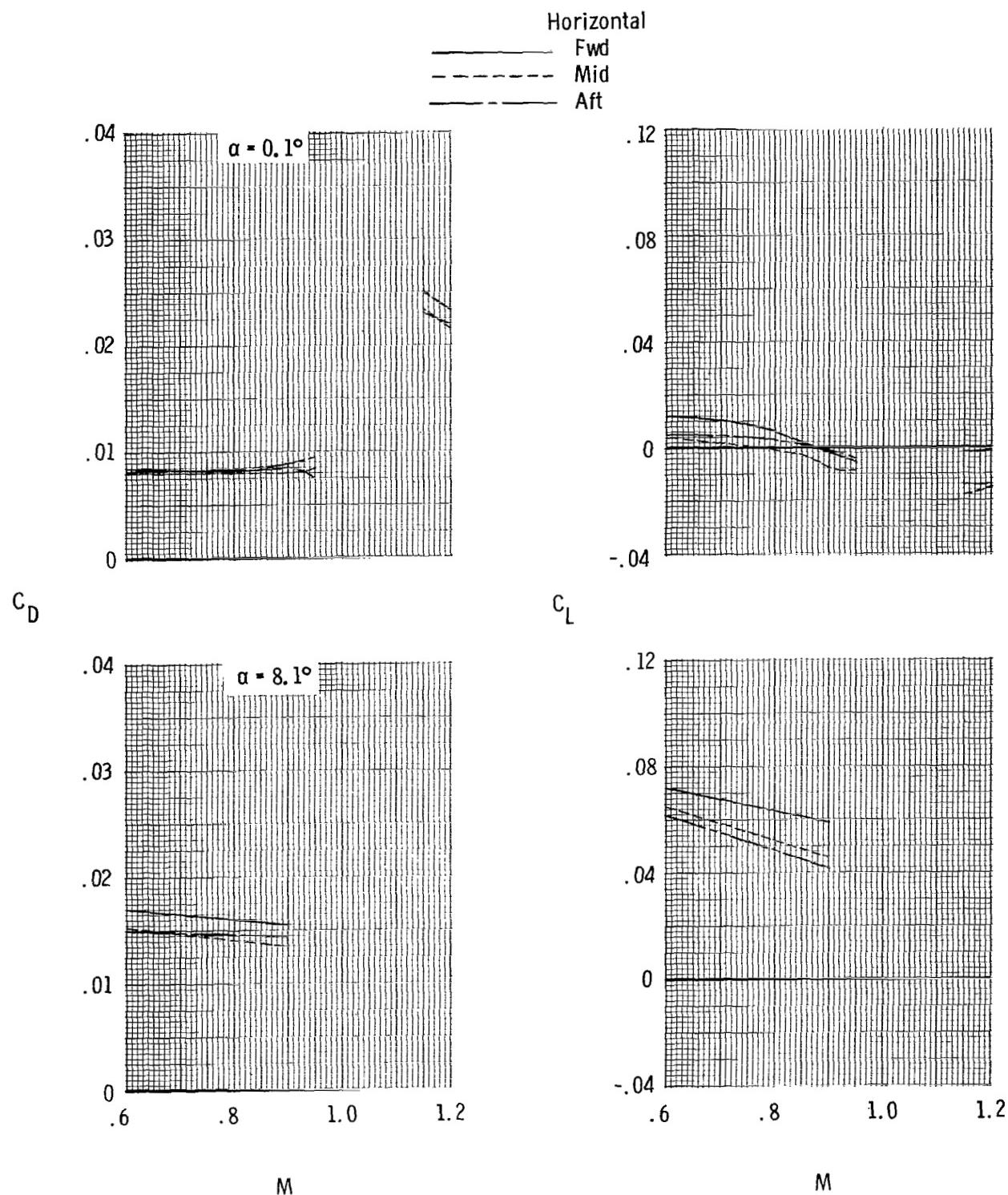
(a) Total aft-end lift and drag coefficient.

Figure 54.- Effects of horizontal tail location on variation of afterbody characteristics with Mach number for scheduled jet total-pressure ratios with dry power nozzles, booms off, and twin vertical tails mid.



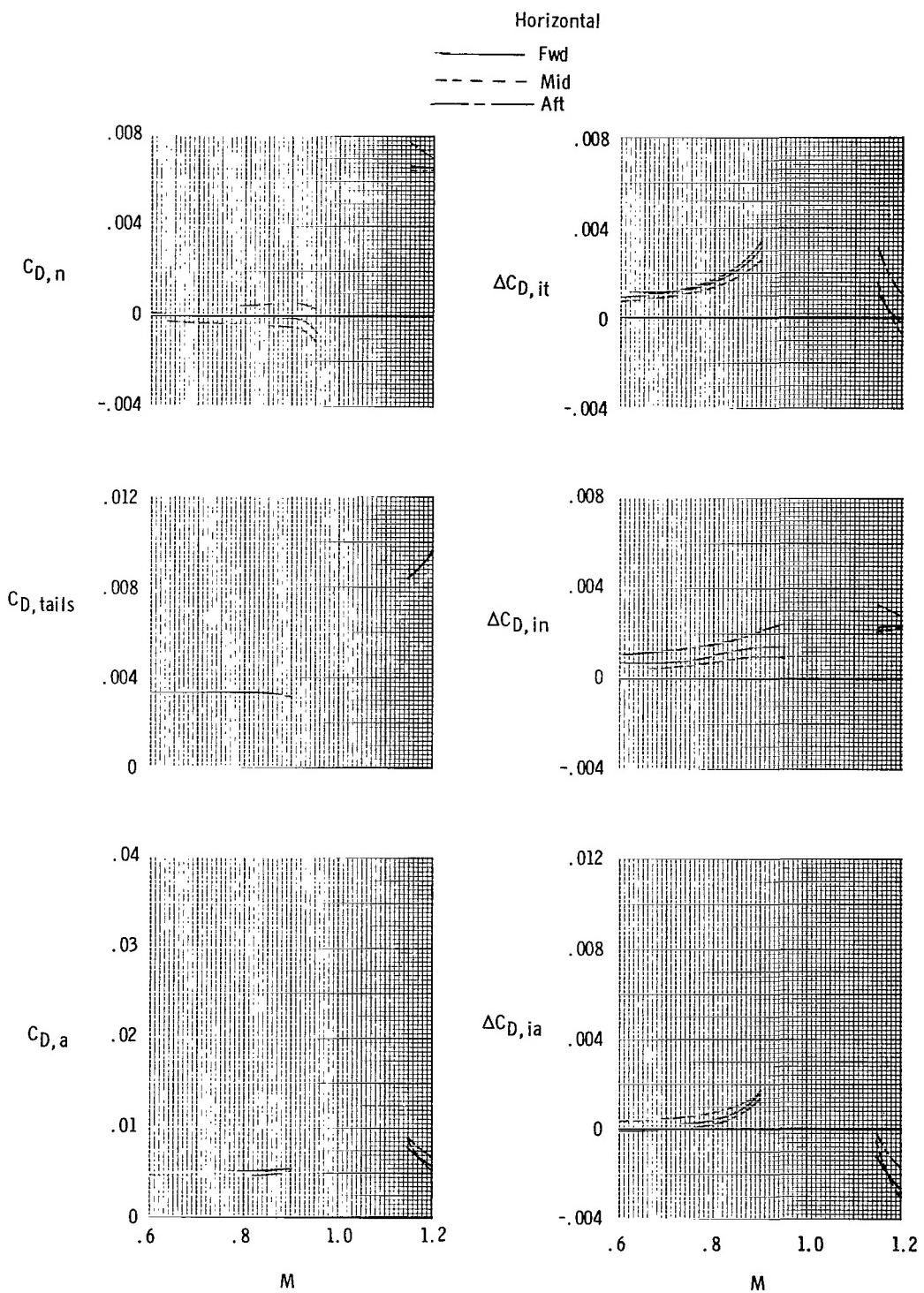
(b) Aft-end drag-coefficient components and tail interference drag-coefficient increments for  $\alpha_{nom} = 0.1^\circ$ .

Figure 54.- Concluded.



(a) Total aft-end lift and drag coefficient.

Figure 55.- Effects of horizontal tail location on variation of afterbody characteristics with Mach number for scheduled jet total-pressure ratios with dry power nozzles, booms off, and twin vertical tails aft.



(b) Aft-end drag-coefficient components and tail interference drag-coefficient increments for  $\alpha_{nom} = 0.1^\circ$ .

Figure 55.- Concluded.

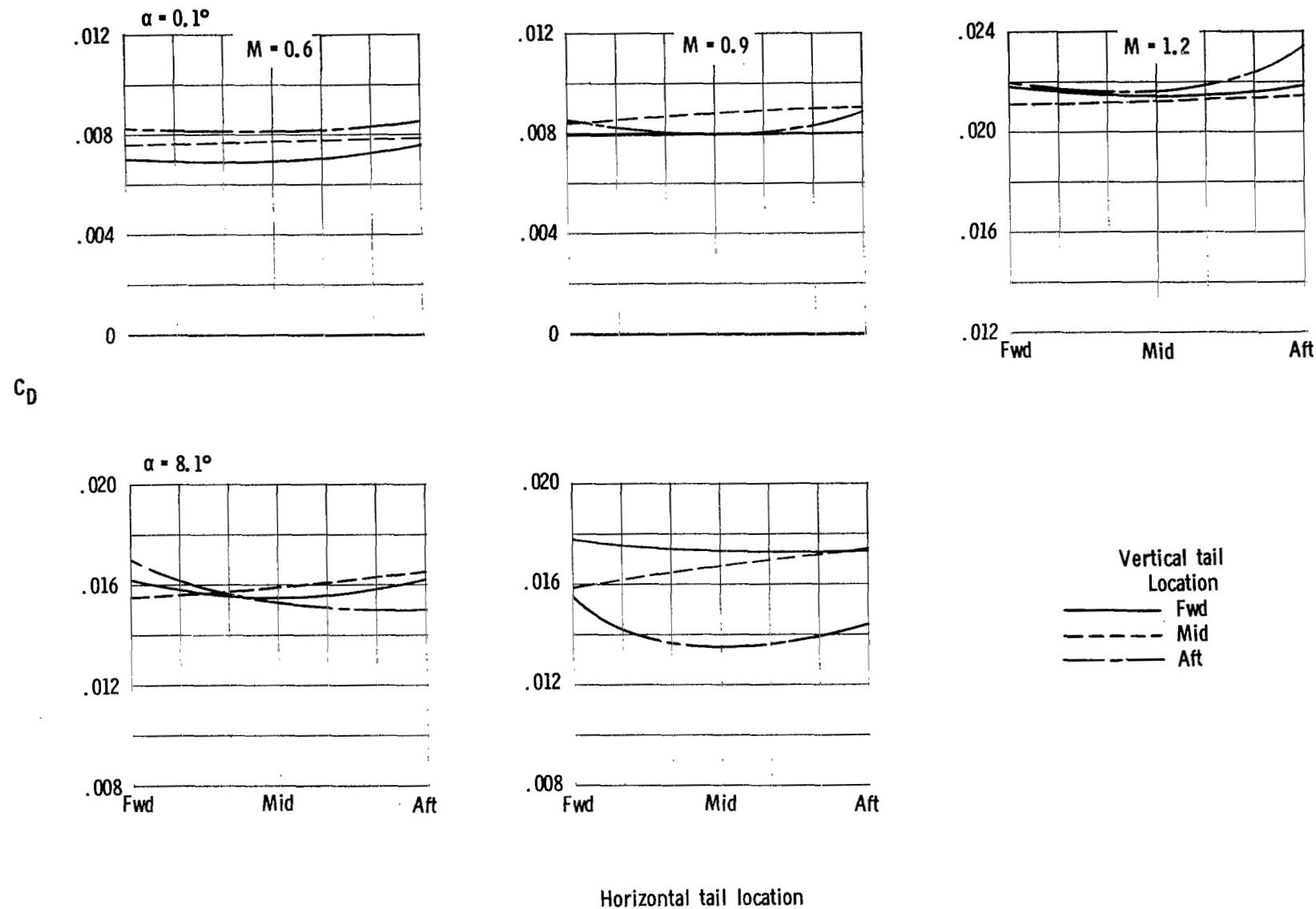
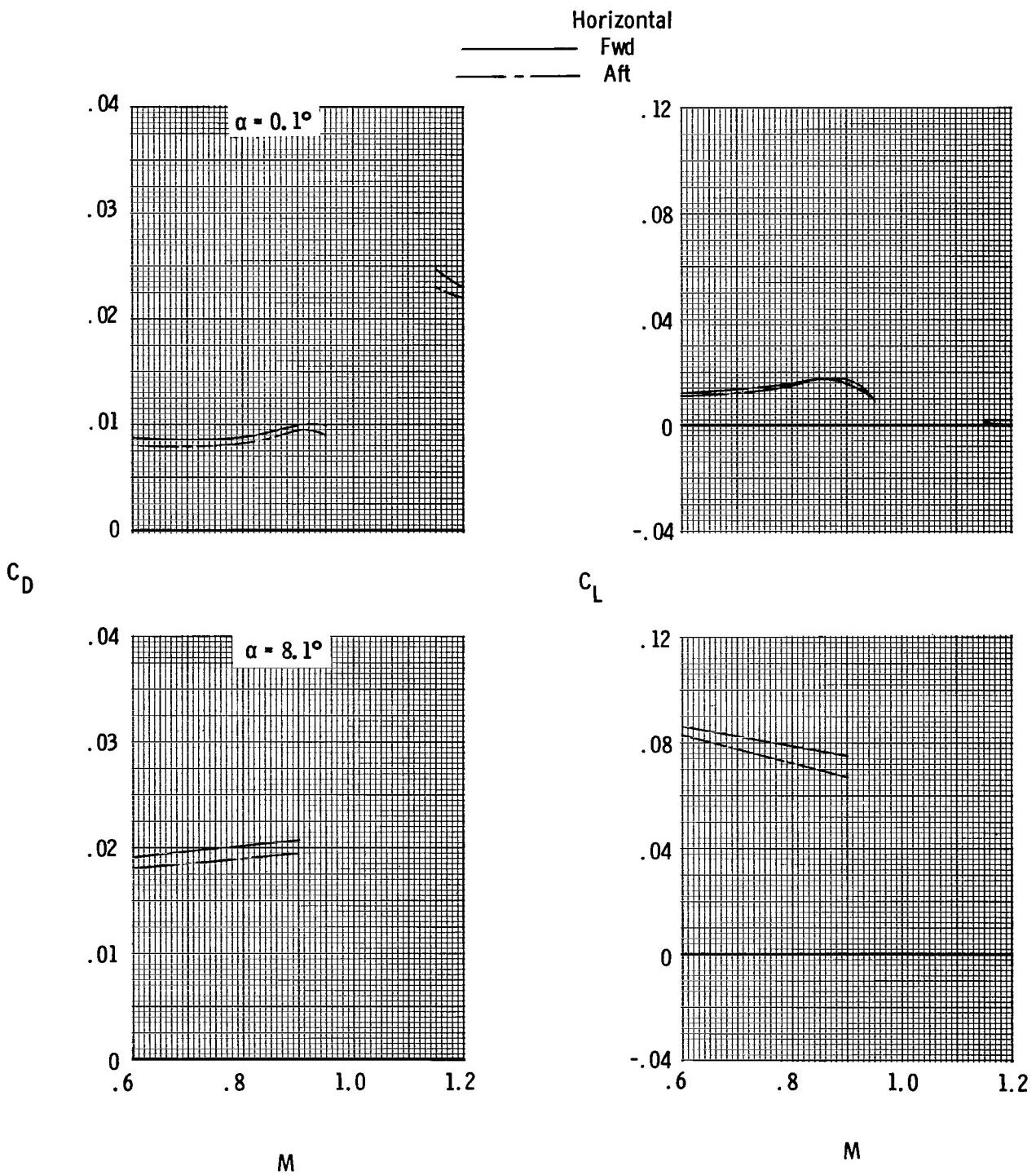
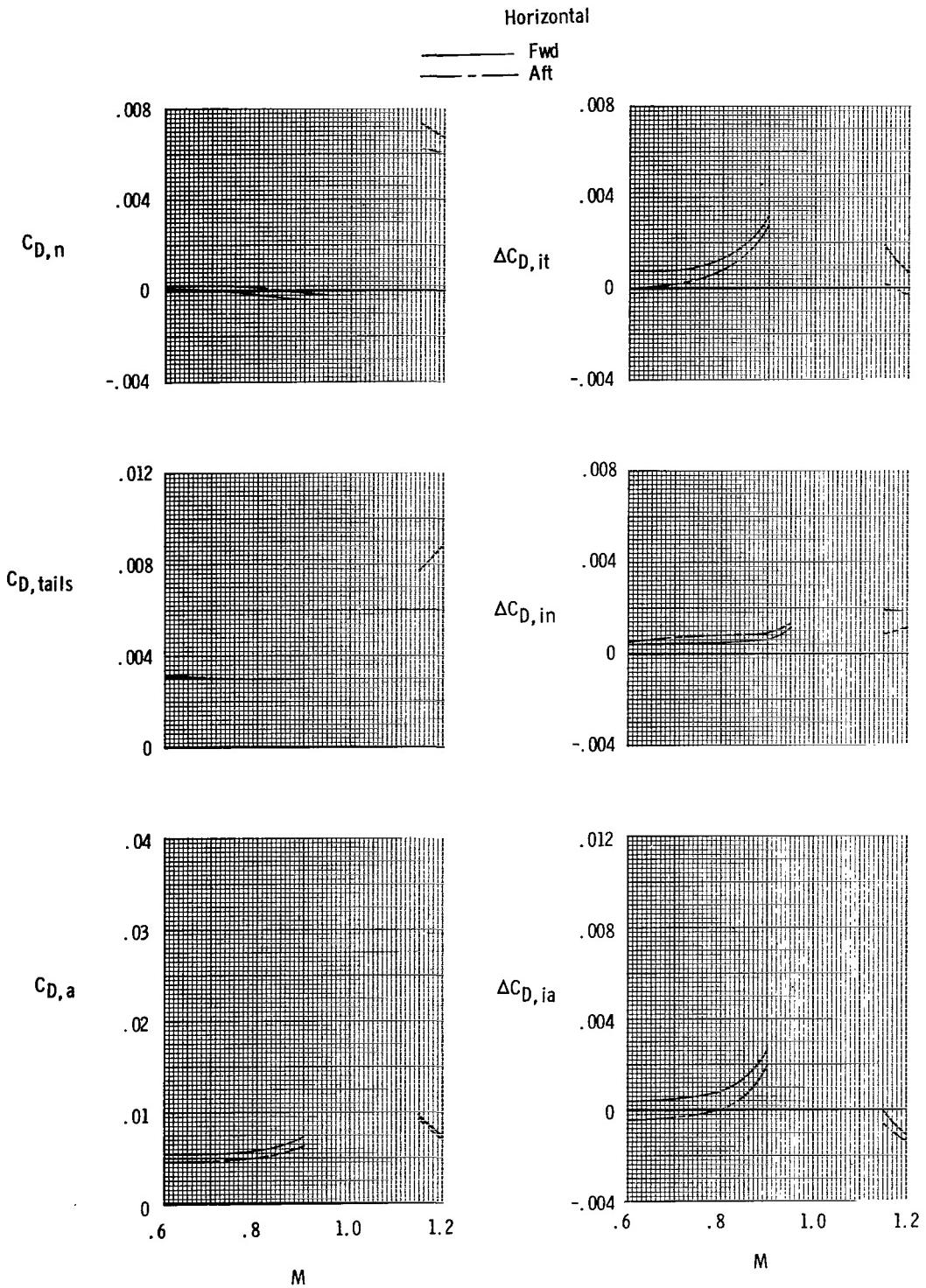


Figure 56.- Summary of effects of horizontal tail location on total aft-end drag characteristics at scheduled jet total-pressure ratios with dry power nozzles, booms off, and twin vertical tails.



(a) Total aft-end lift and drag coefficient.

Figure 57.- Effects of horizontal tail location on variation of afterbody characteristics with Mach number for scheduled jet total-pressure ratios with dry power nozzles, booms on, and twin vertical tails forward.



(b) Aft-end drag-coefficient components and tail interference drag-coefficient increments for  $\alpha_{nom} = 0.1^\circ$ .

Figure 57.- Concluded.

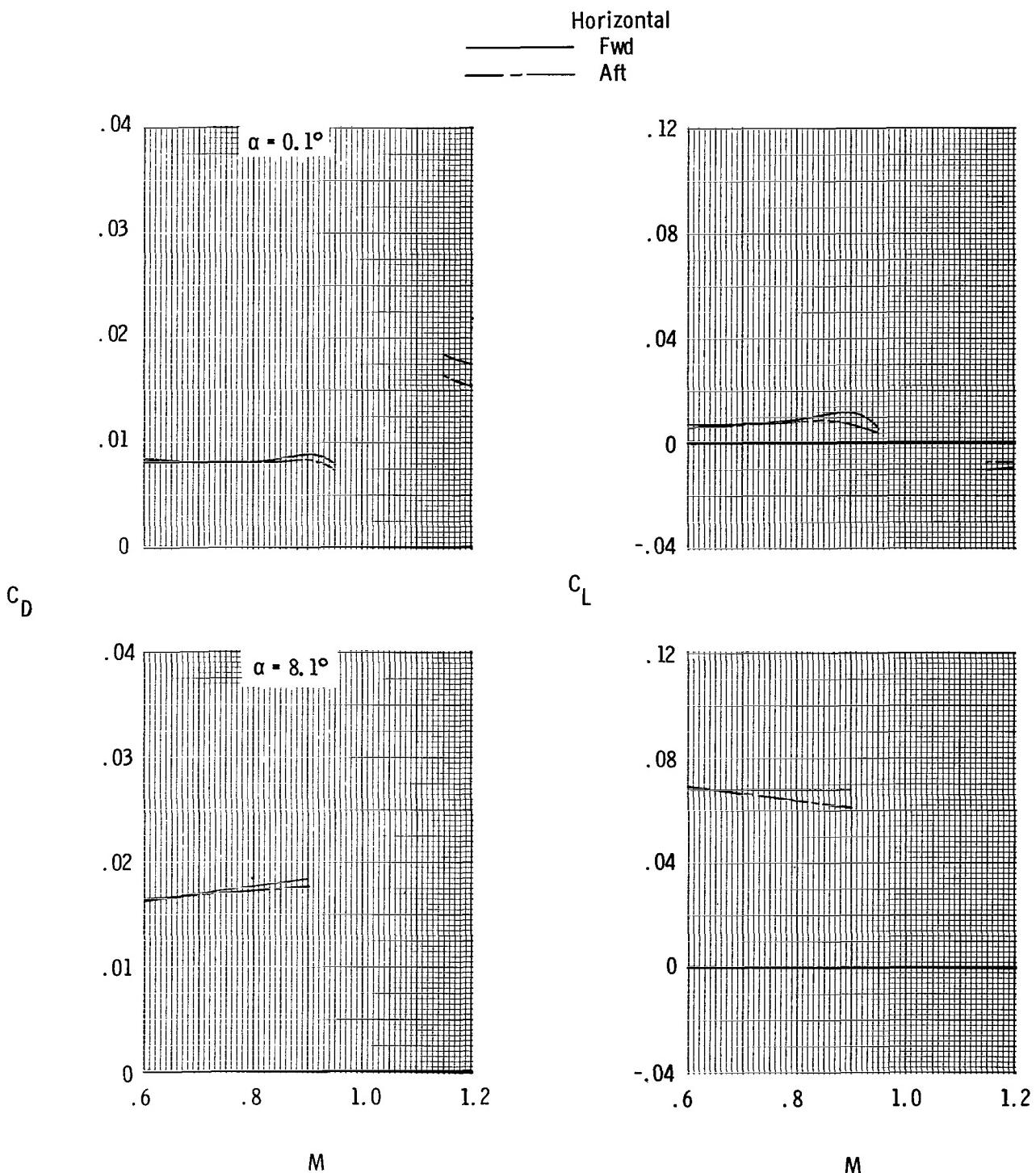


Figure 58.- Effects of horizontal tail location on variation of total aft-end drag and lift coefficient with Mach number for scheduled jet total-pressure ratios with A/B nozzles, booms off, and twin vertical tails forward.

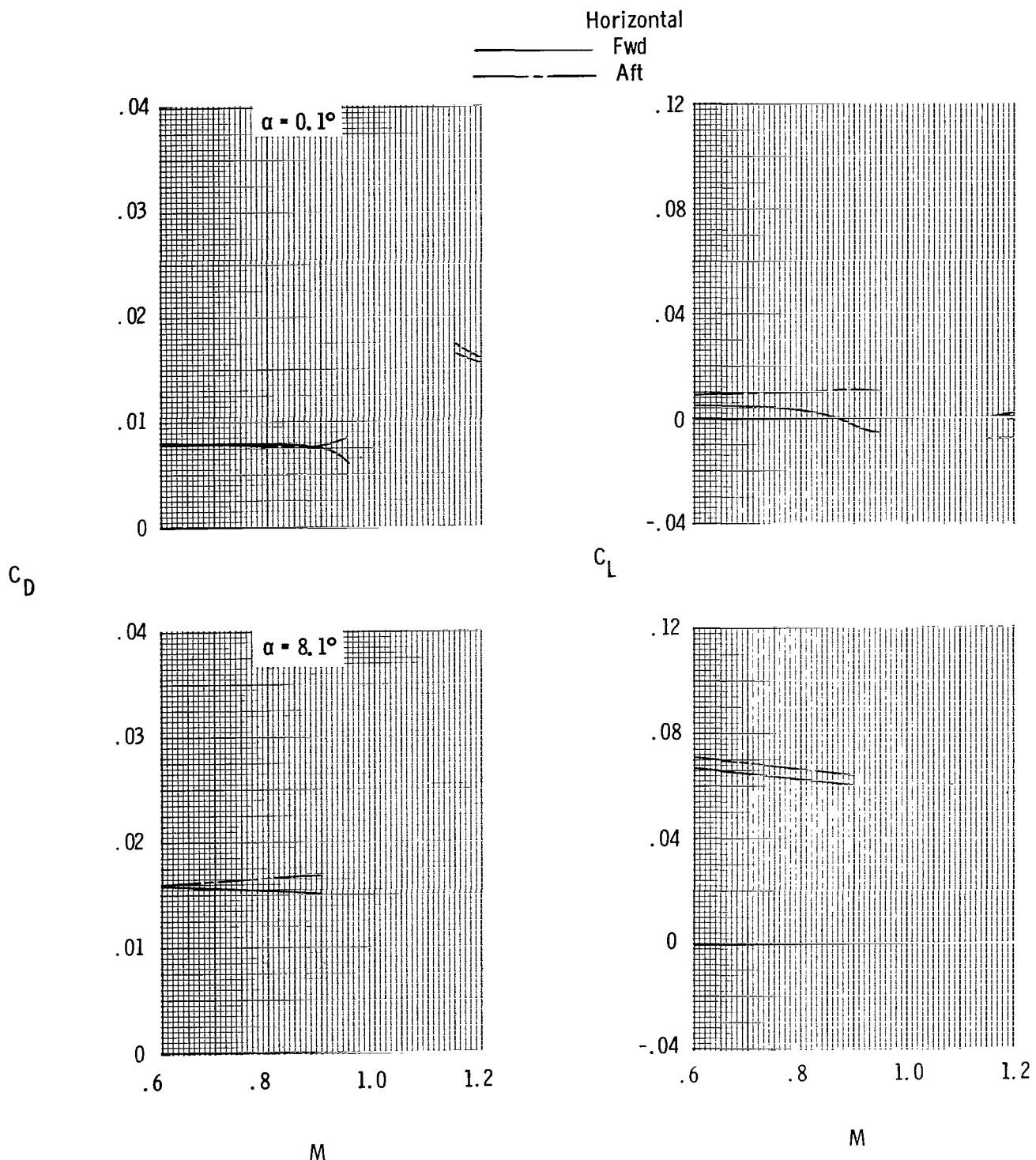


Figure 59.- Effects of horizontal tail location on variation of total aft-end drag and lift coefficient with Mach number for scheduled jet total-pressure ratios with A/B nozzles, booms off, and twin vertical tails aft.

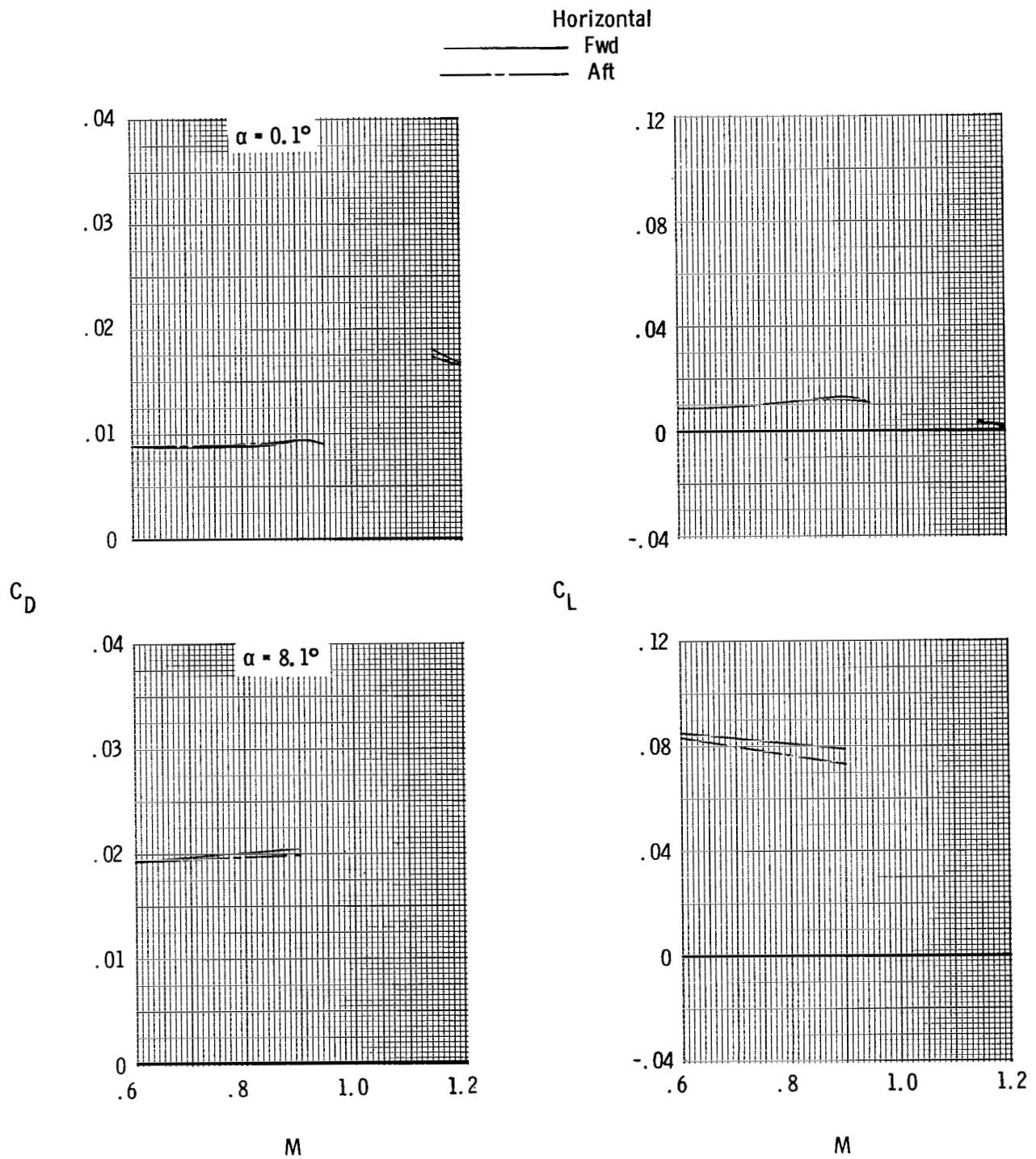


Figure 60.- Effects of horizontal tail location on variation of total aft-end drag and lift coefficient with Mach number for scheduled jet total-pressure ratios with A/B nozzles, booms on, and twin vertical tails forward.

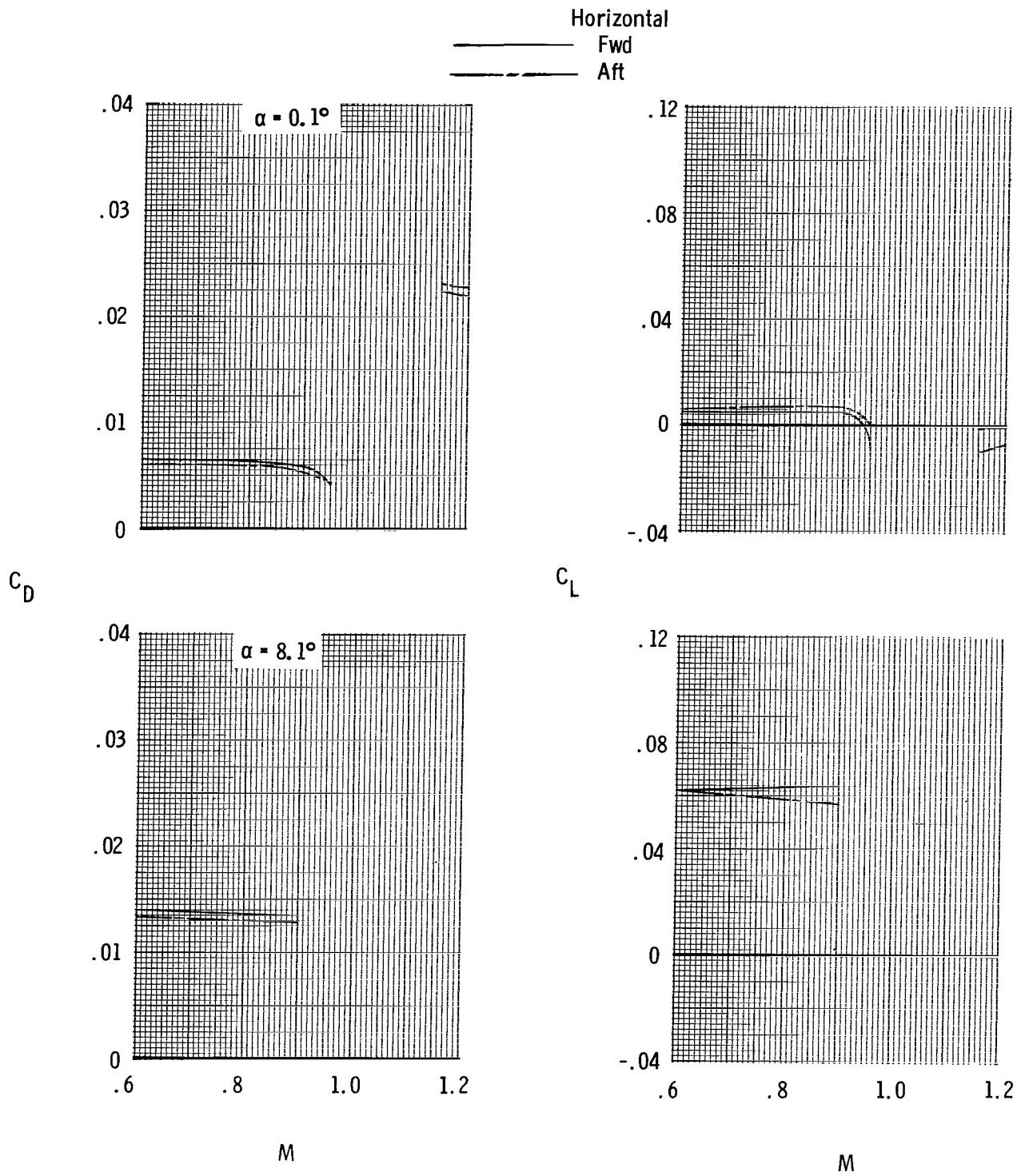


Figure 61.— Effects of horizontal tail location on variation of total aft-end drag and lift coefficient with Mach number for scheduled jet total-pressure ratios with dry power nozzles, booms off, and single vertical tail forward.

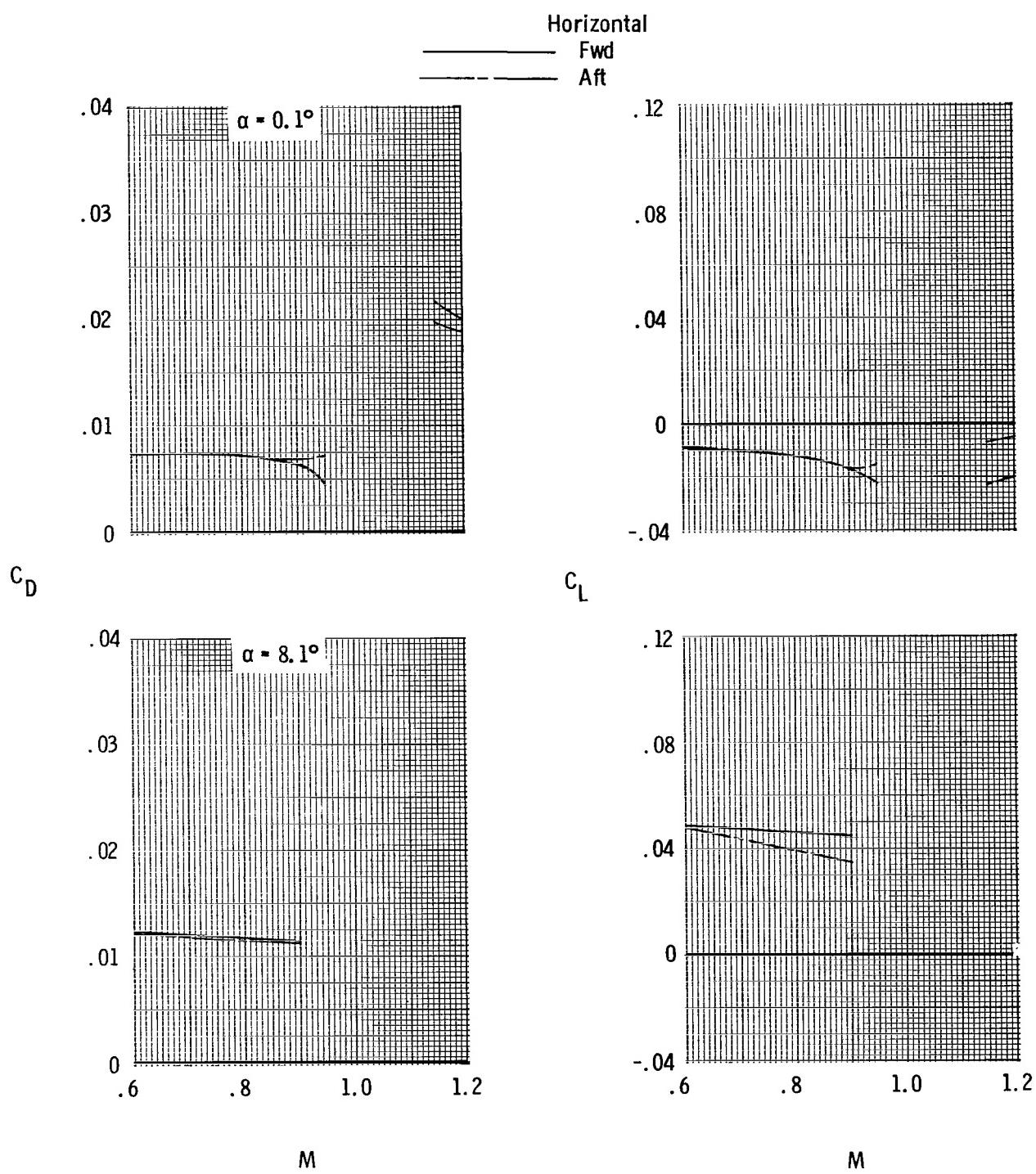


Figure 62.- Effects of horizontal tail location on variation of total aft-end drag and lift coefficient with Mach number for scheduled jet total-pressure ratios with dry power nozzles, booms off, and single vertical tail aft.

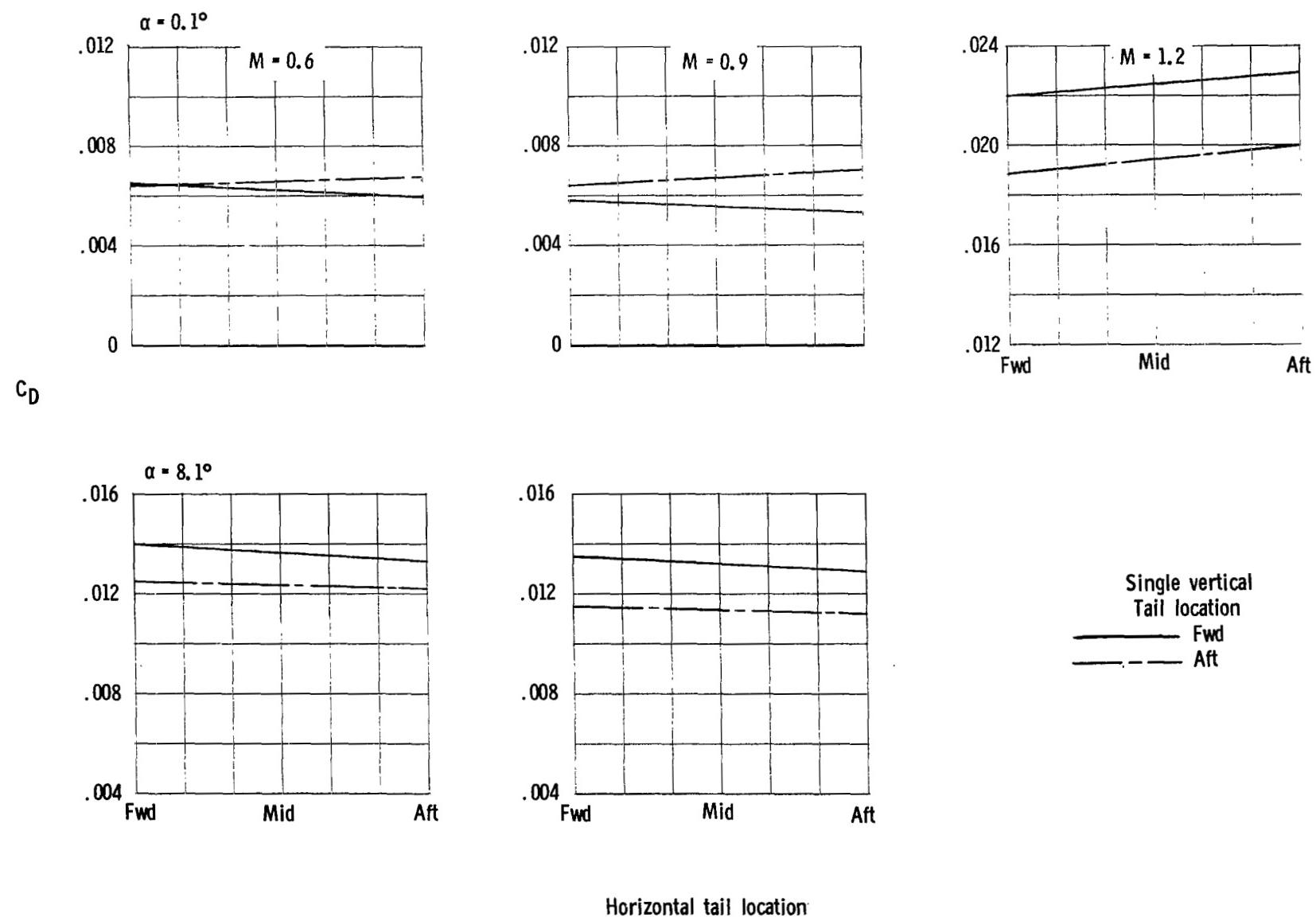
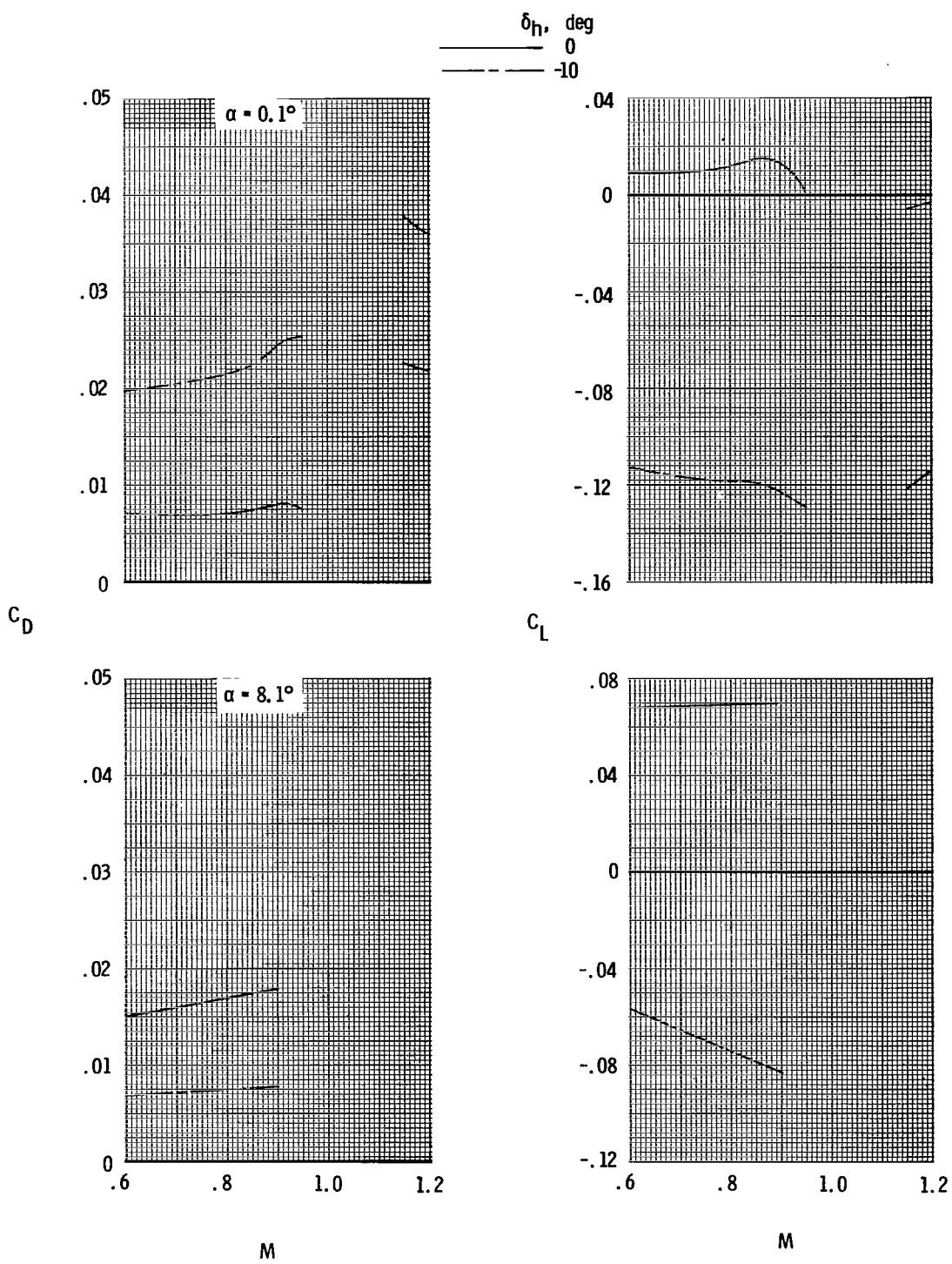
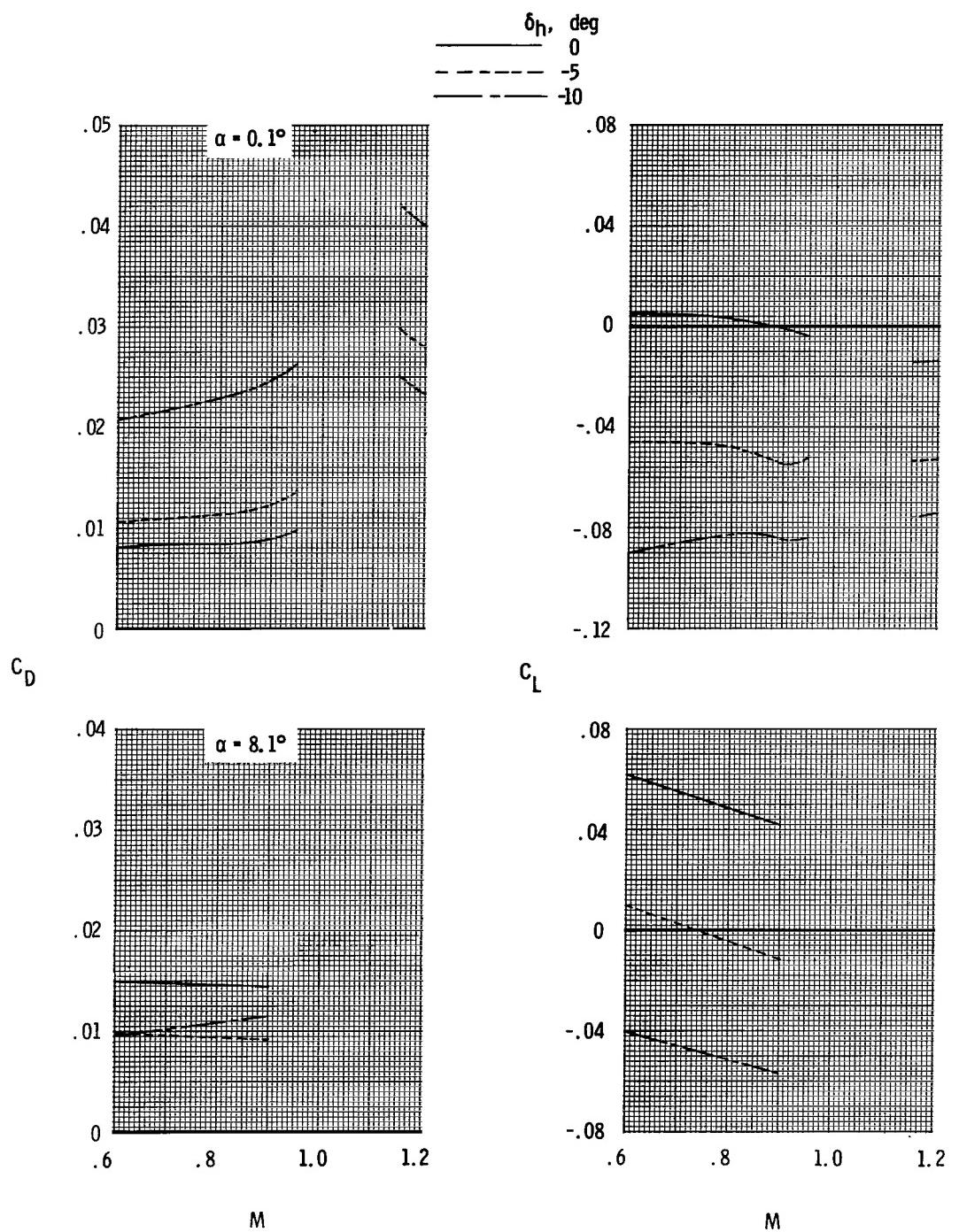


Figure 63.- Summary of effects of horizontal tail location on total aft-end drag characteristics at scheduled jet total-pressure ratios with dry power nozzles, booms off, and single vertical tail.



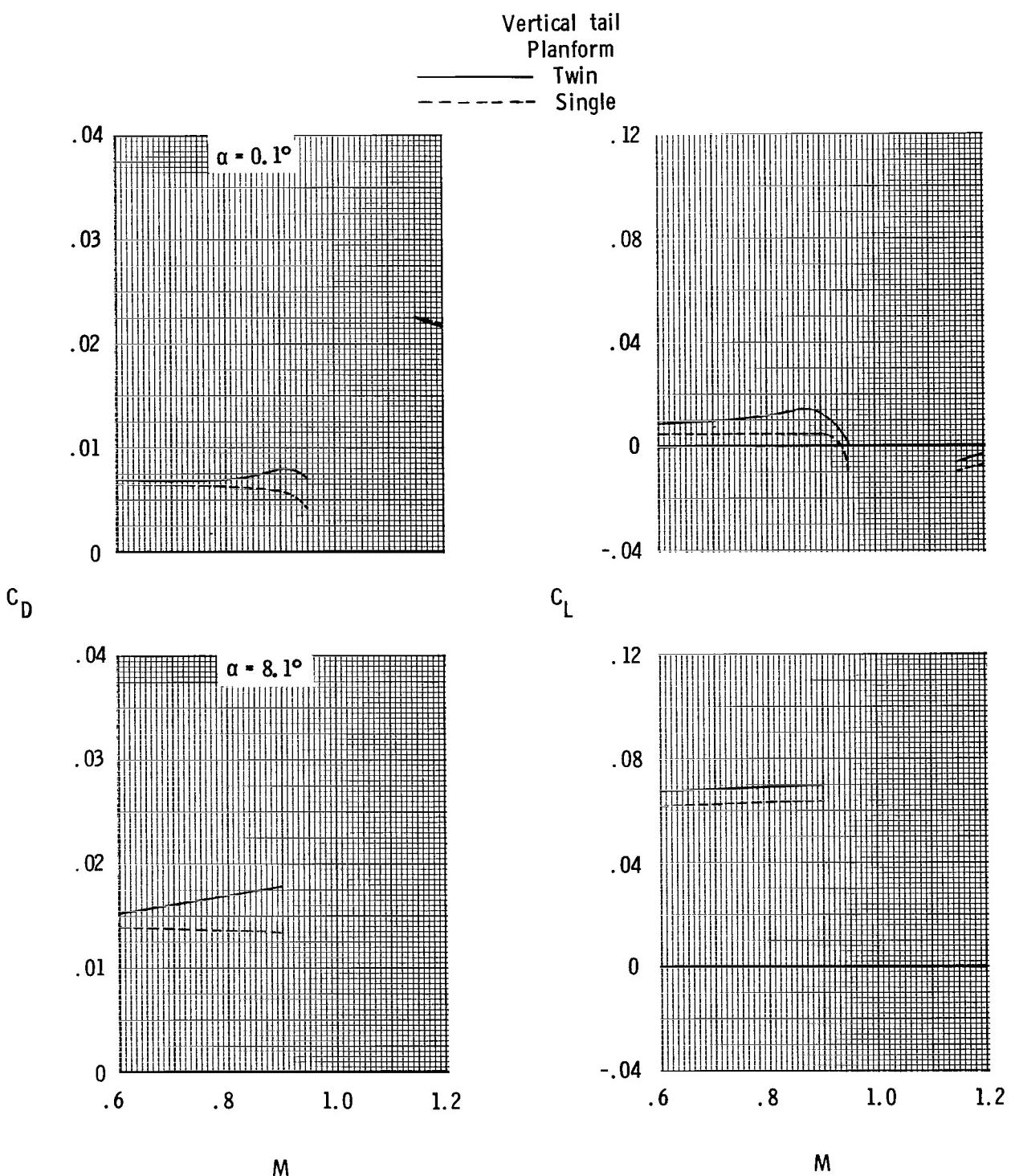
(a) Horizontal tails forward; vertical tails forward.

**Figure 64.-** Effects of horizontal tail incidence on variation of total aft-end drag and lift coefficient with Mach number for scheduled jet total-pressure ratios with dry power nozzles, booms off, and twin vertical tails.



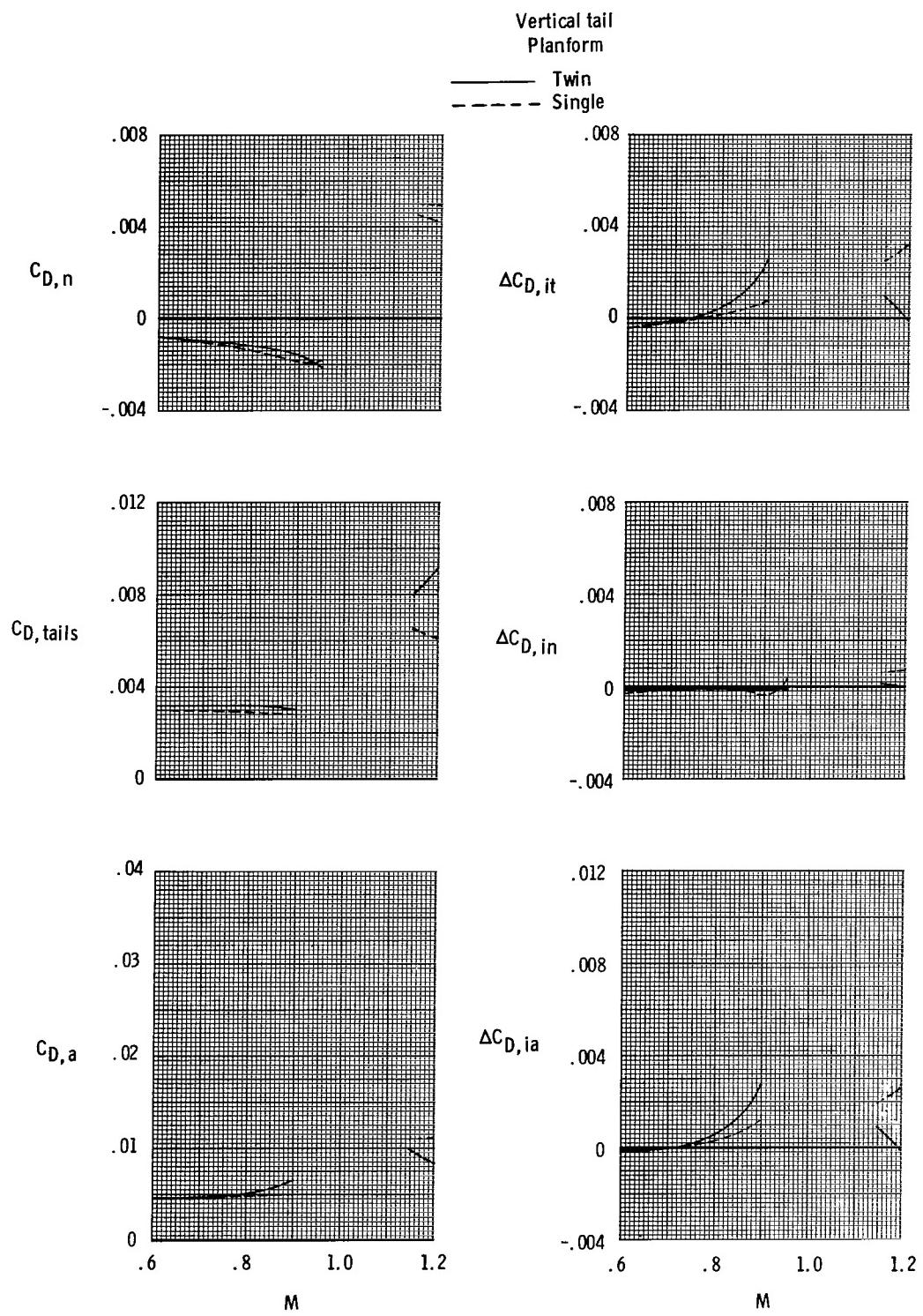
(b) Horizontal tails aft; vertical tails aft.

Figure 64.- Concluded.



(a) Total aft-end lift and drag coefficient.

Figure 65.- Effects of vertical tail planform on variation of afterbody characteristics with Mach number for scheduled jet total-pressure ratios with dry power nozzles, booms off, horizontal tails forward, and vertical tails forward.



(b) Aft-end drag-coefficient components and tail interference drag-coefficient increments for  $\alpha_{nom} = 0.1^\circ$ .

Figure 65.- Concluded.

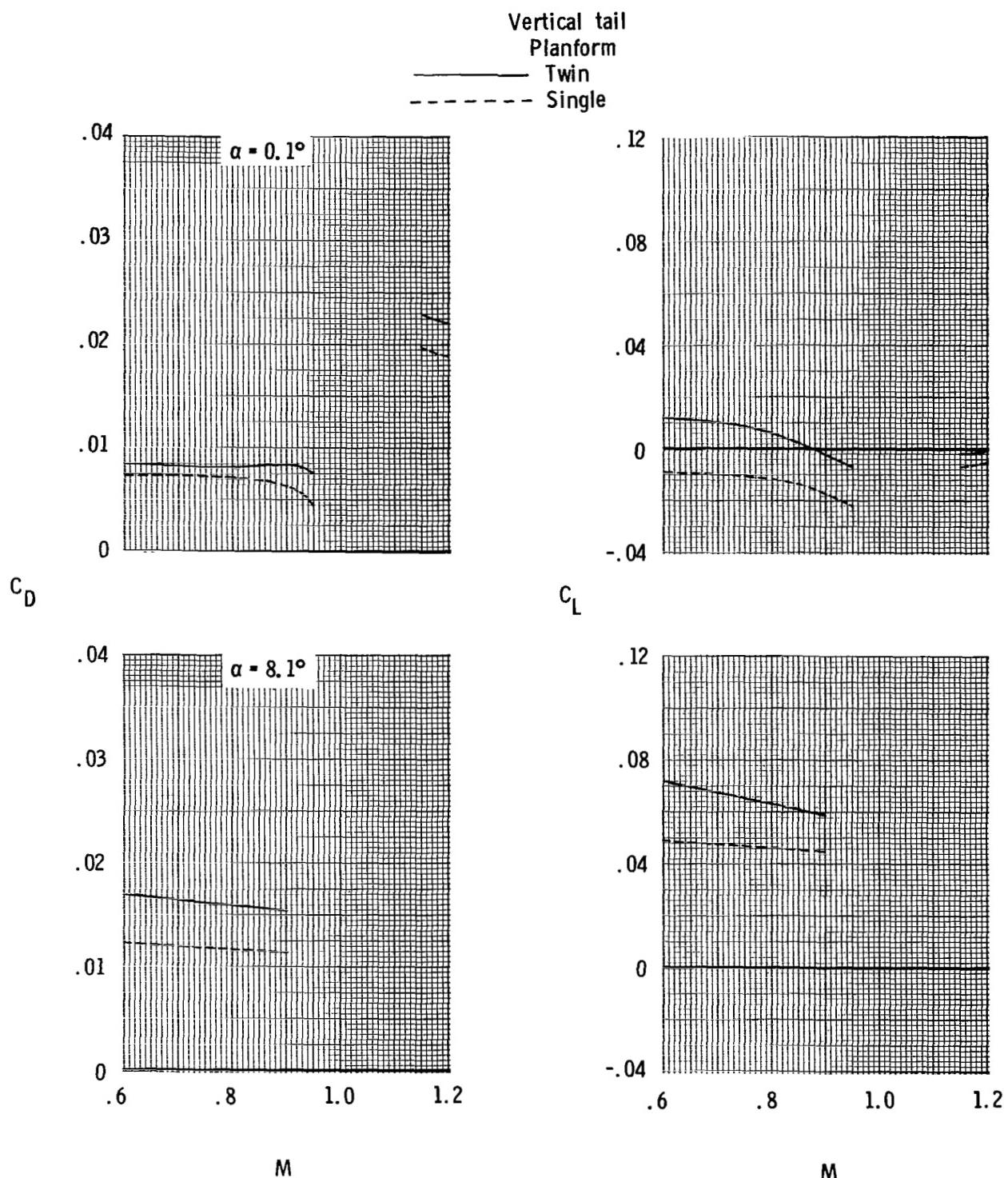


Figure 66.- Effects of vertical tail planform on variation of total aft-end drag and lift coefficient with Mach number for scheduled jet total-pressure ratios with dry power nozzles, booms off, horizontal tails forward, and vertical tails aft.

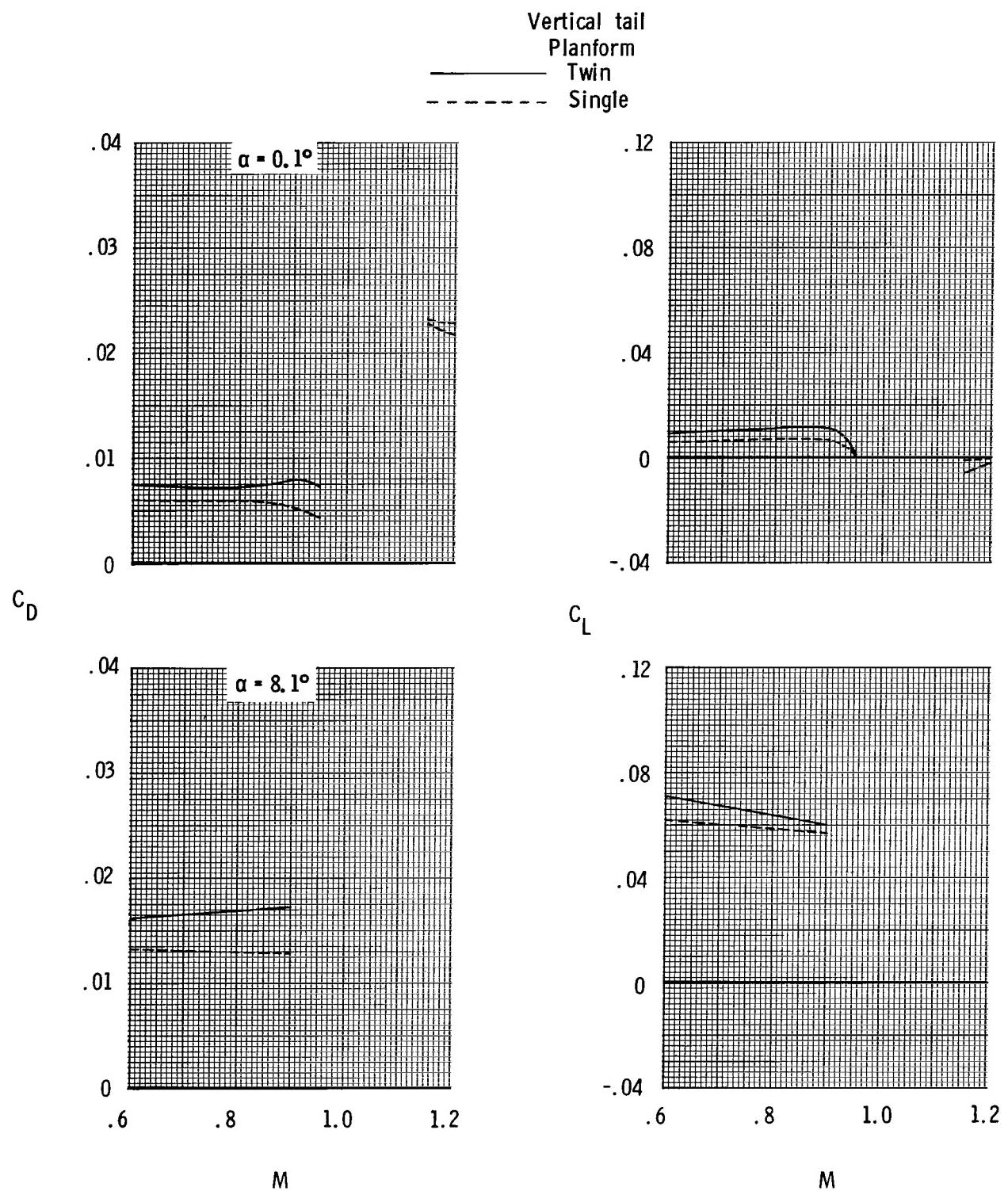
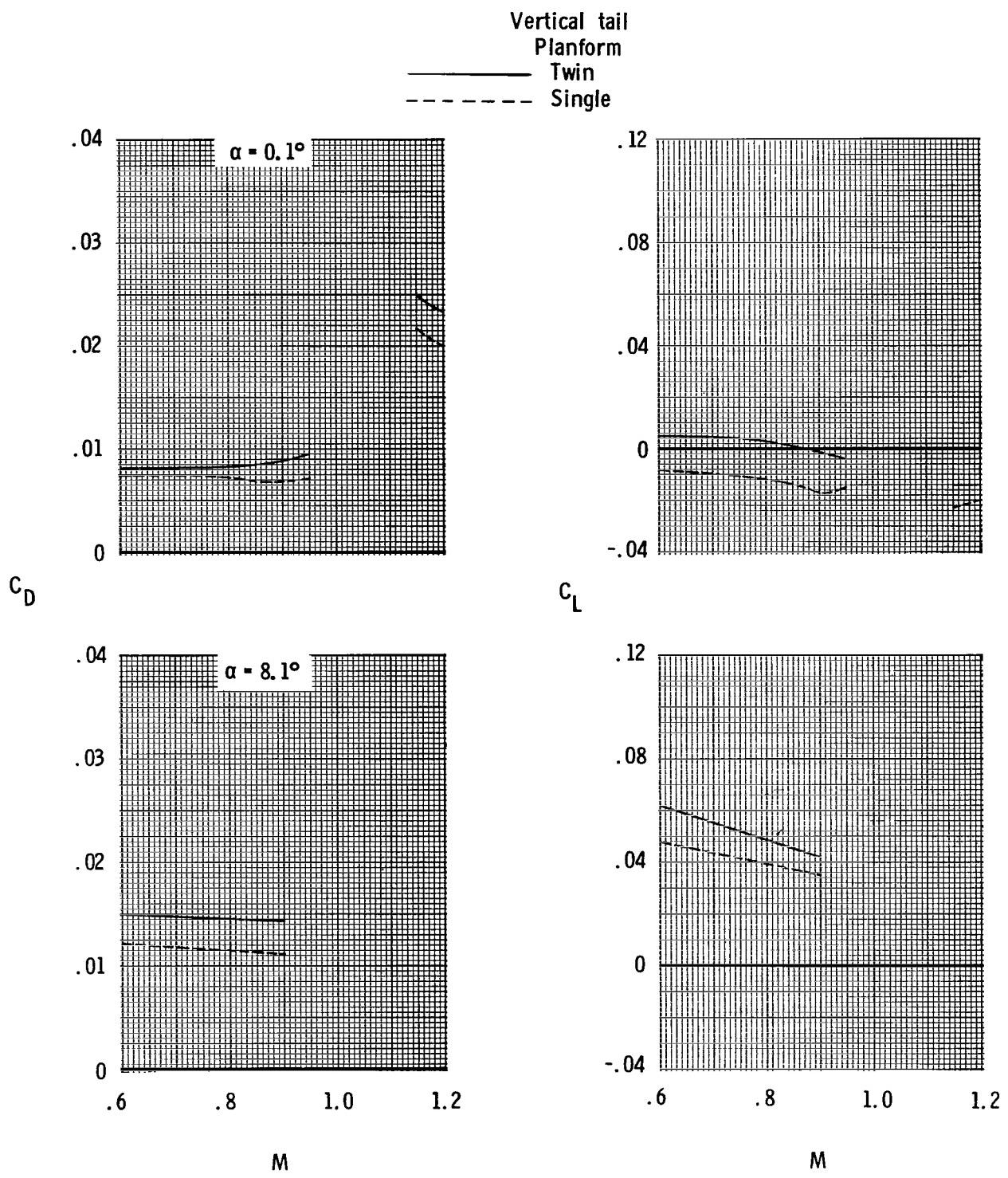
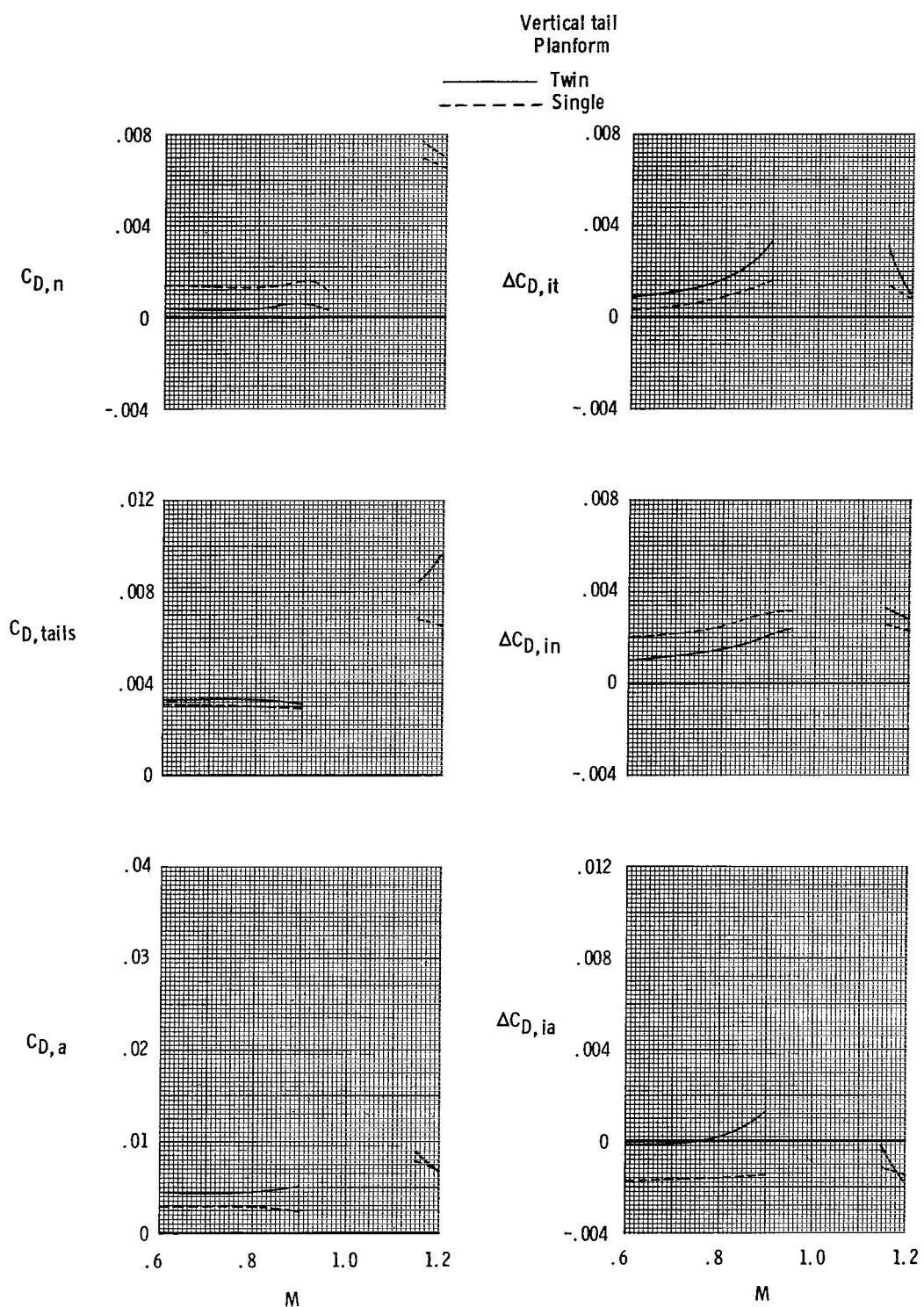


Figure 67.- Effects of vertical tail planform on variation of total aft-end drag and lift coefficient with Mach number for scheduled jet total-pressure ratios with dry power nozzles, booms off, horizontal tails aft, and vertical tails forward.



(a) Total aft-end lift and drag coefficient.

Figure 68.- Effects of vertical tail planform on variation of afterbody characteristics with Mach number for scheduled jet total-pressure ratios with dry power nozzles, booms off, horizontal tails aft, and vertical tails aft.



(b) Aft-end drag-coefficient components and tail interference drag-coefficient increments for  $\alpha_{nom} = 0.1^\circ$ .

Figure 68.- Concluded.

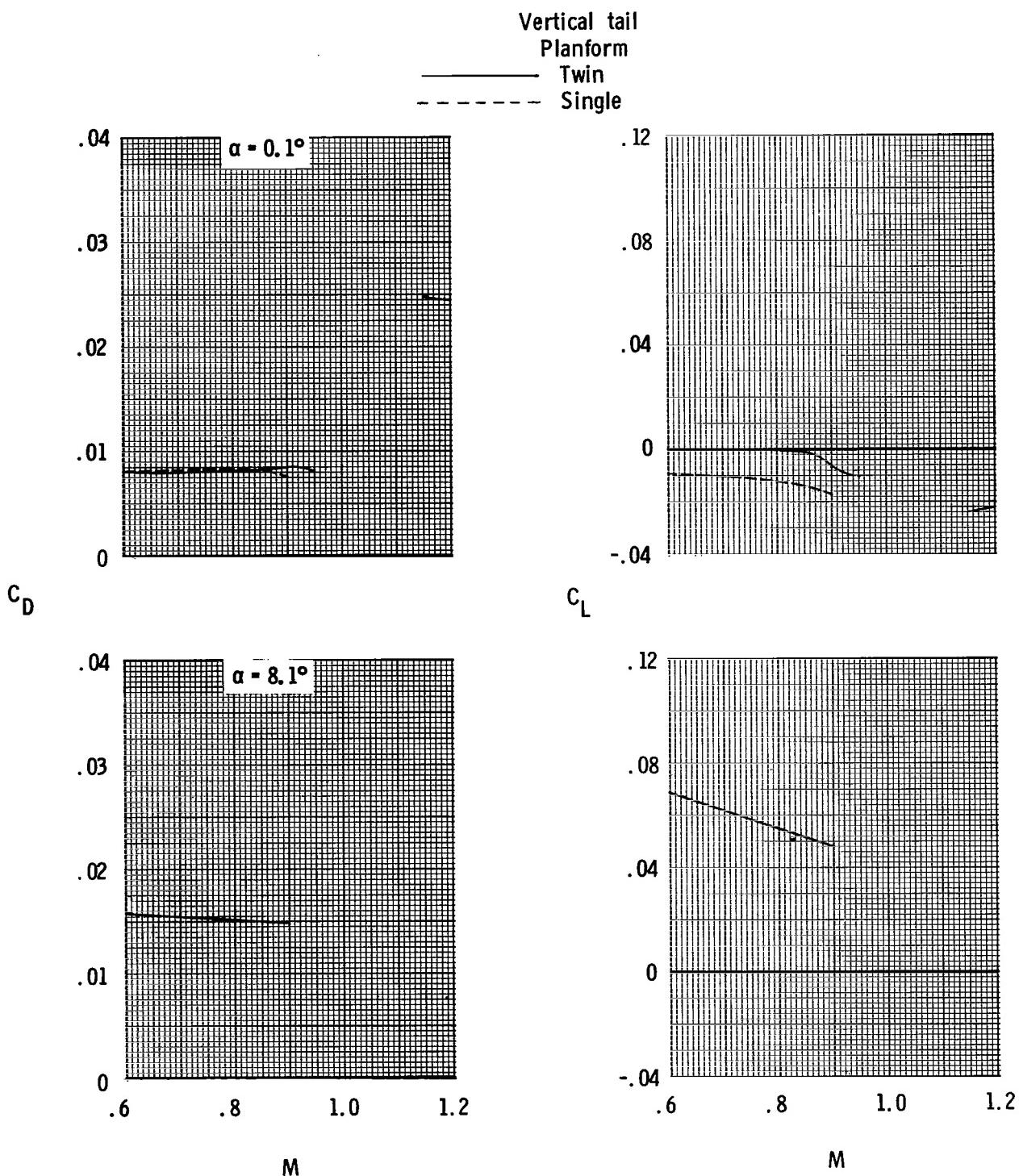


Figure 69.- Effects of vertical tail planform on variation of total aft-end drag and lift coefficient with Mach number for scheduled jet total-pressure ratios with dry power nozzles, booms on, horizontal tails aft, and vertical tails aft.

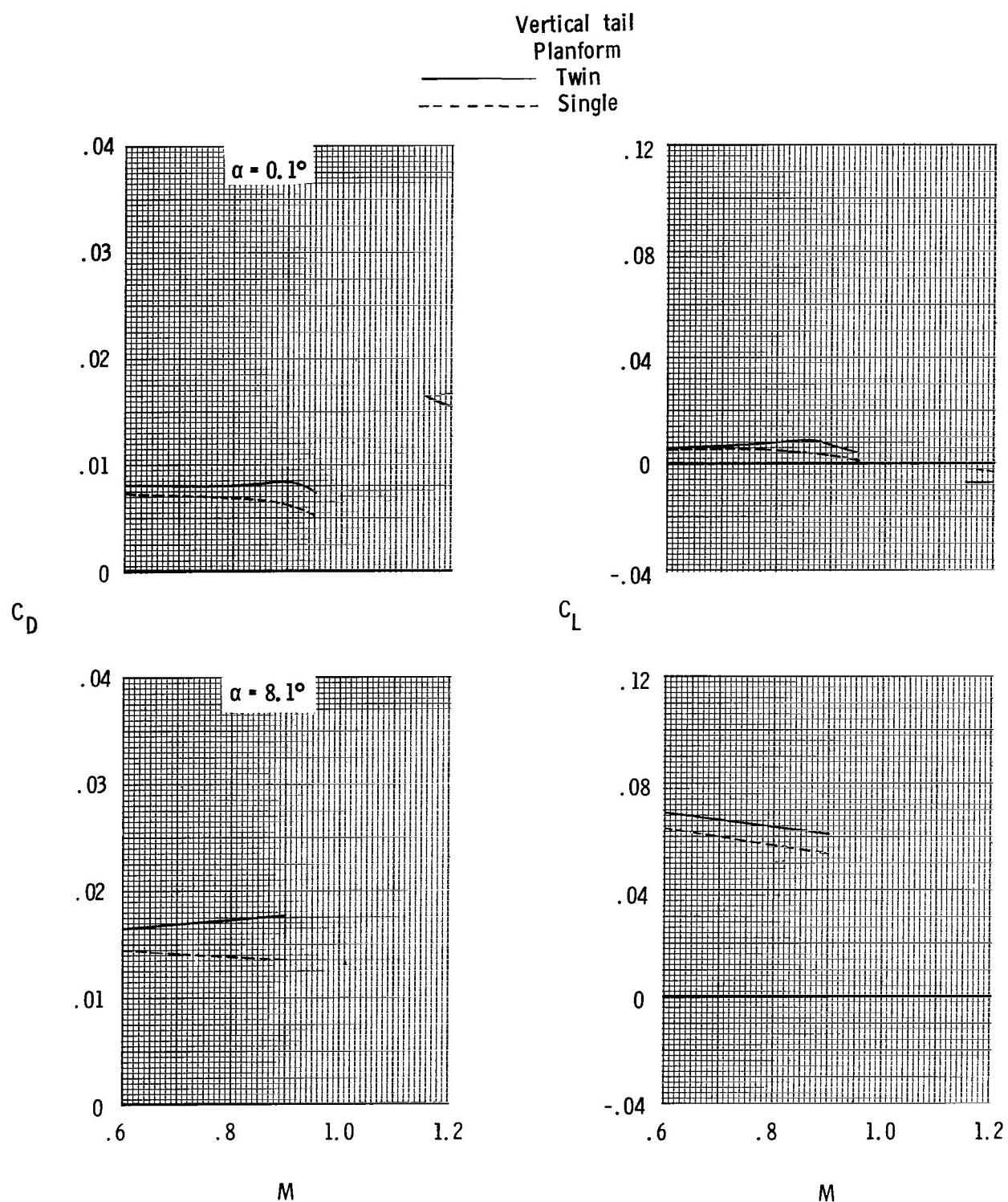


Figure 70.- Effects of vertical tail planform on variation of total aft-end drag and lift coefficient with Mach number for scheduled jet total-pressure ratios with A/B nozzles, booms off, horizontal tails aft, and vertical tails forward.

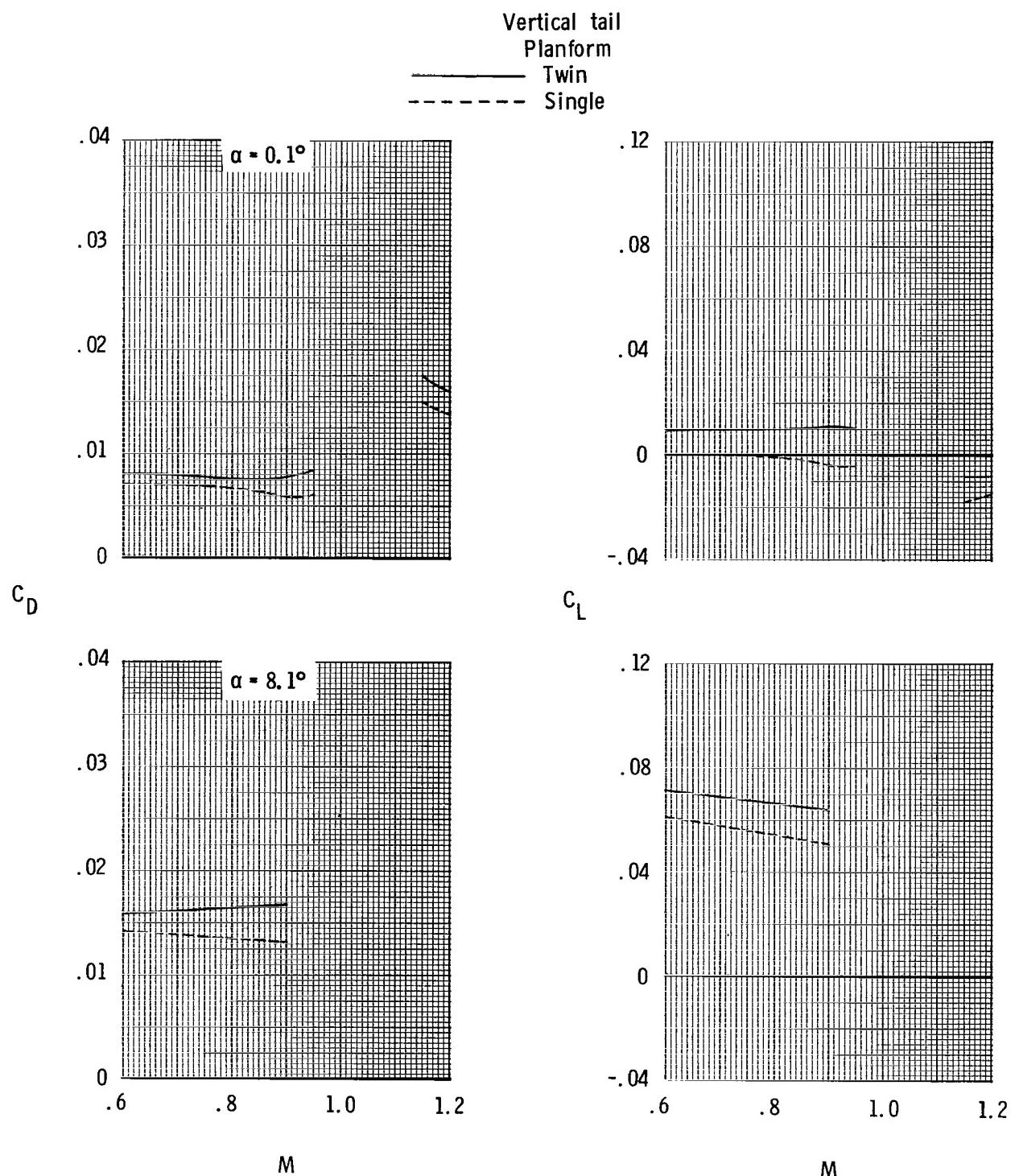
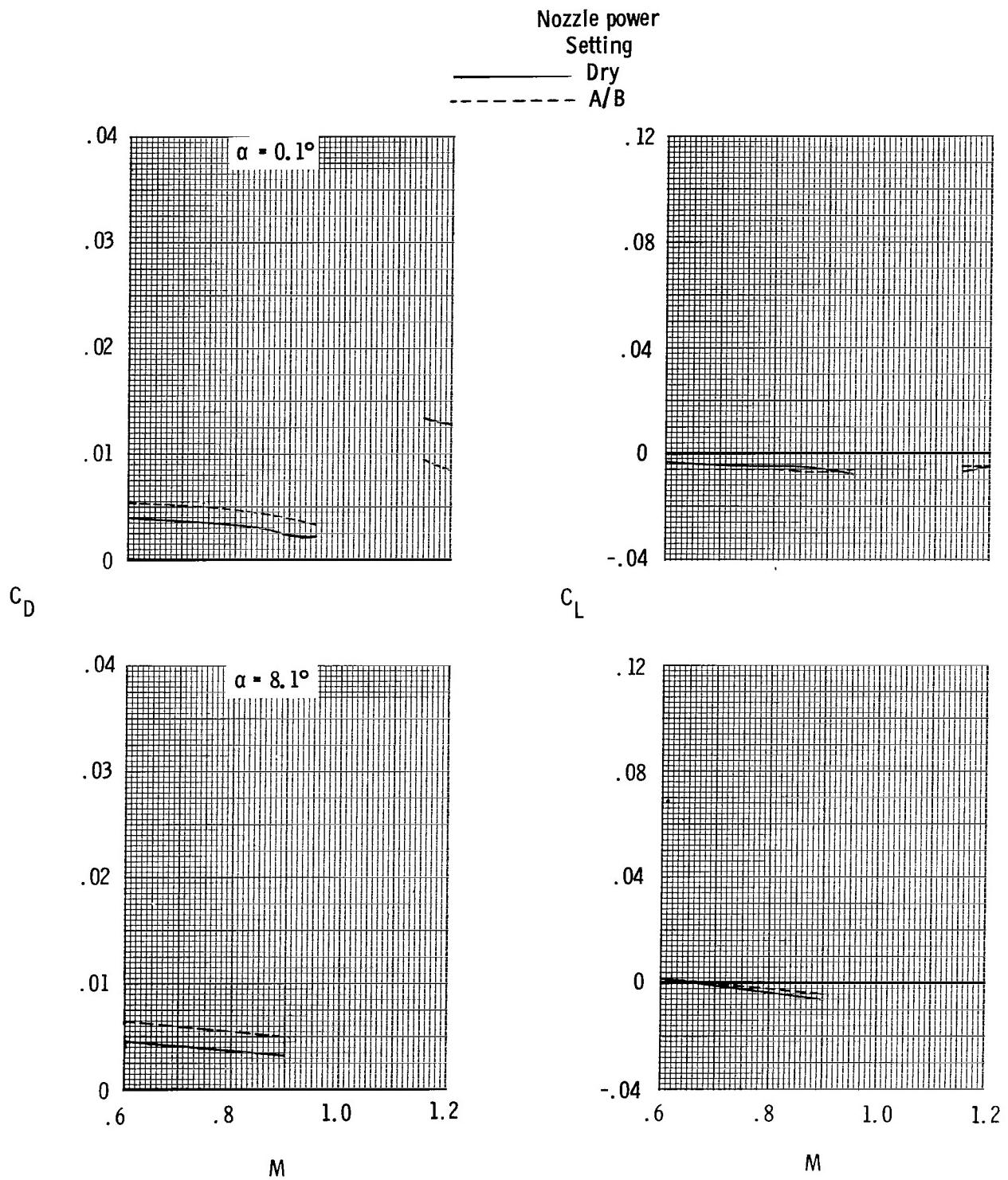
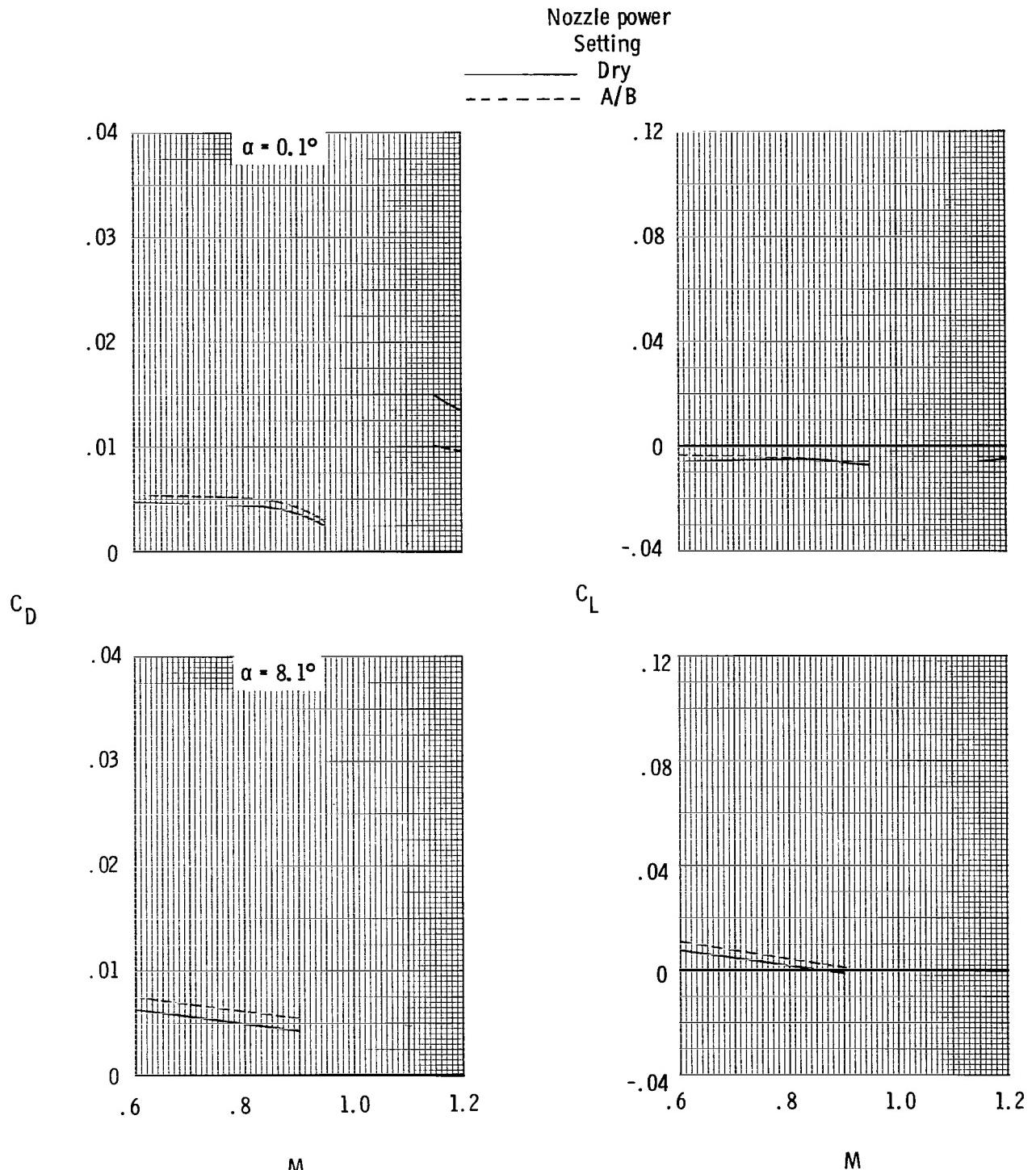


Figure 71.- Effects of vertical tail planform on variation of total aft-end drag and lift coefficient with Mach number for scheduled jet total-pressure ratios with A/B nozzles, booms off, horizontal tails aft, and vertical tails aft.



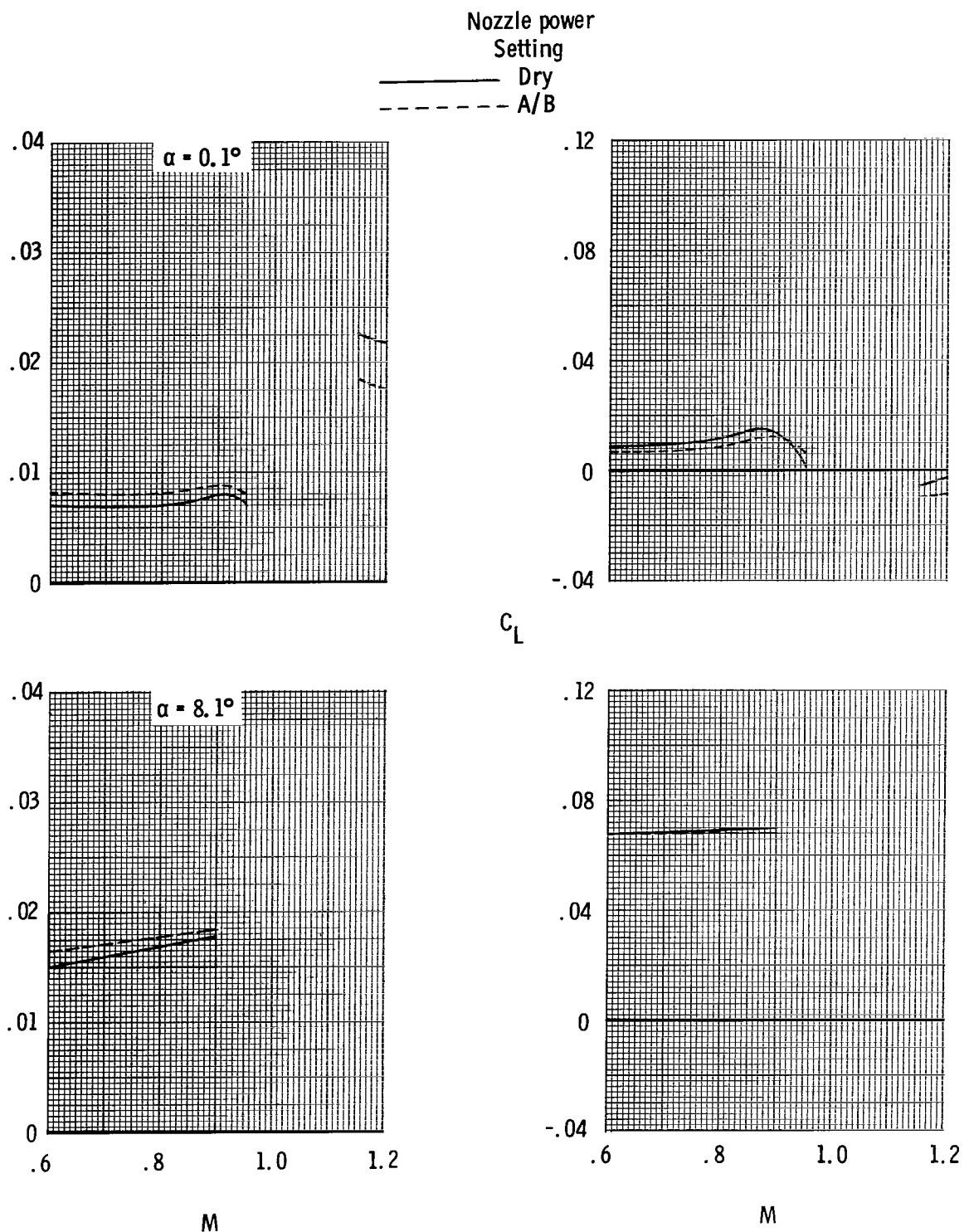
(a) Booms off; tails off.

Figure 72.- Effects of nozzle power setting on variation of total aft-end drag and lift coefficient with Mach number for scheduled jet total-pressure ratios.



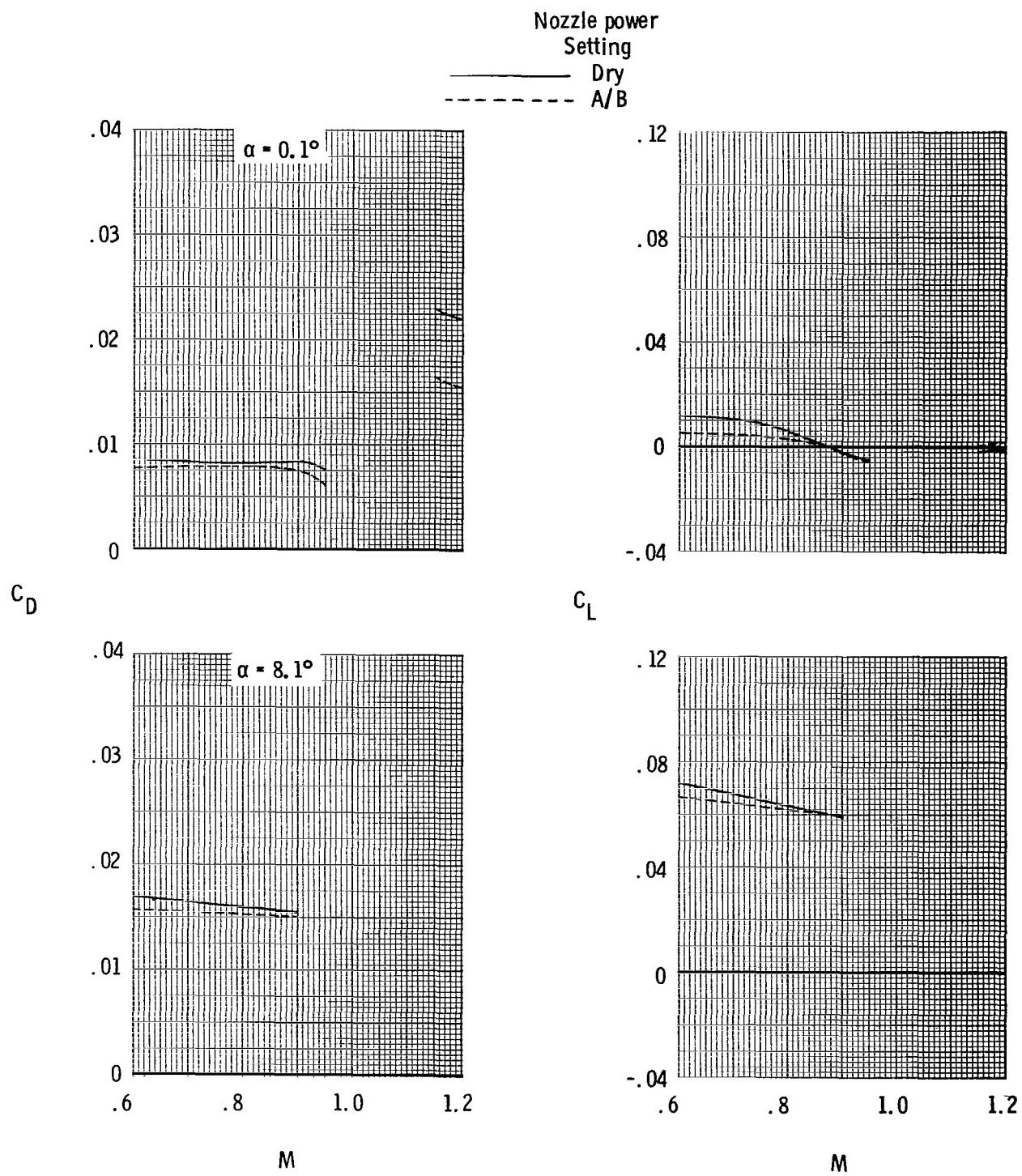
(b) Booms on; tails off.

Figure 72.- Continued.



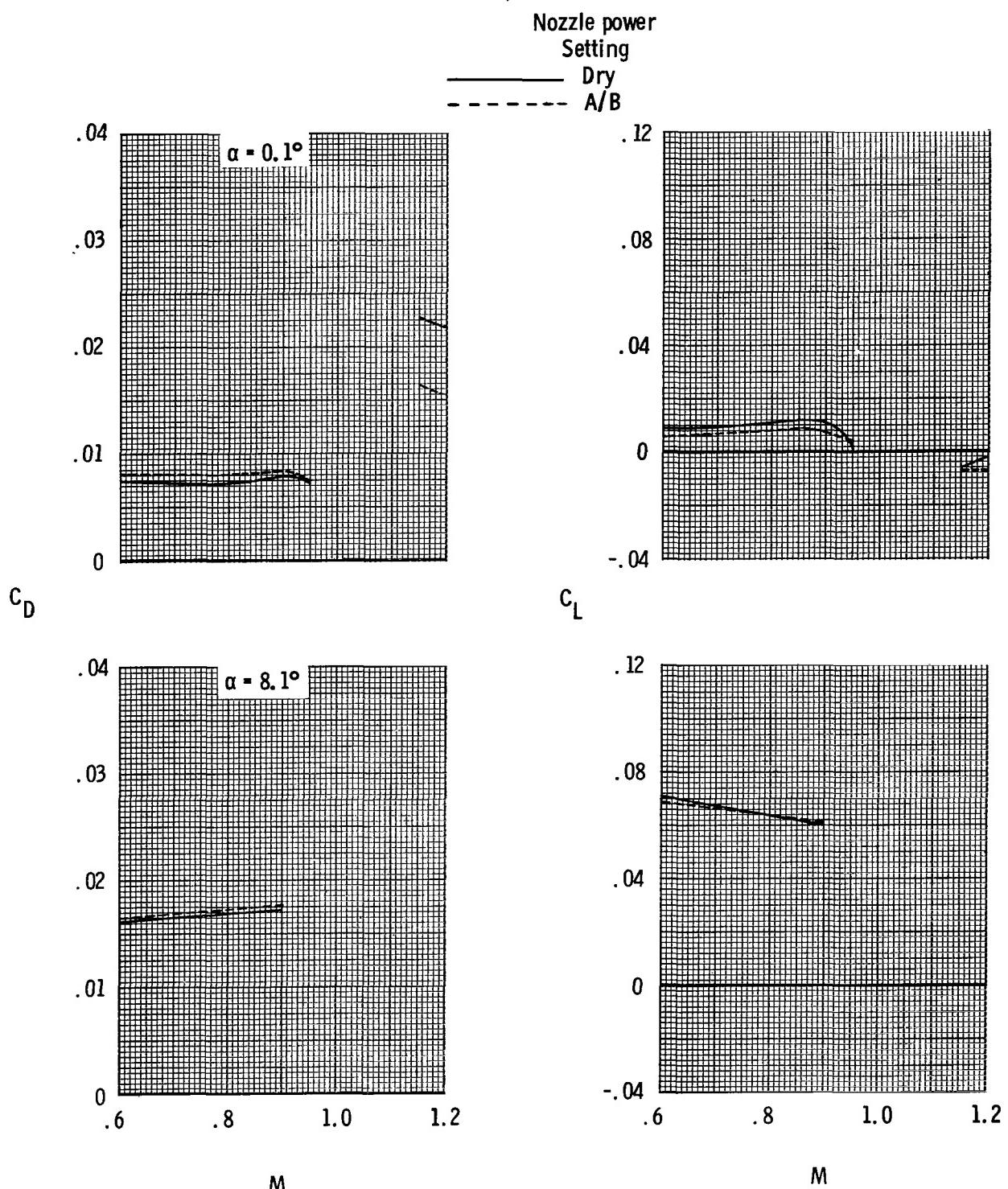
(c) Booms off; horizontal tails forward; twin vertical tails forward.

Figure 72.- Continued.



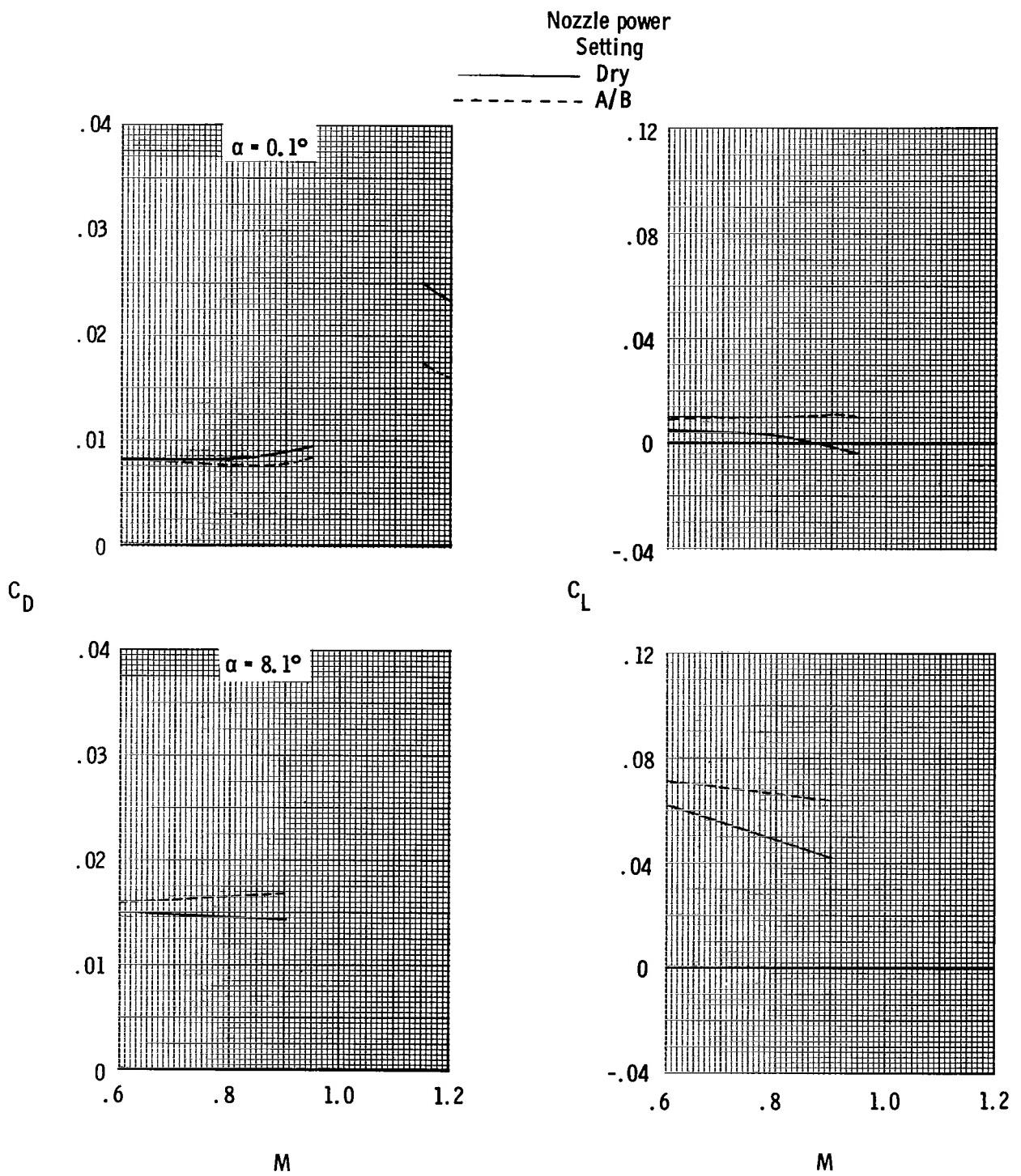
(d) Booms off; horizontal tails forward; twin vertical tails aft.

Figure 72.- Continued.



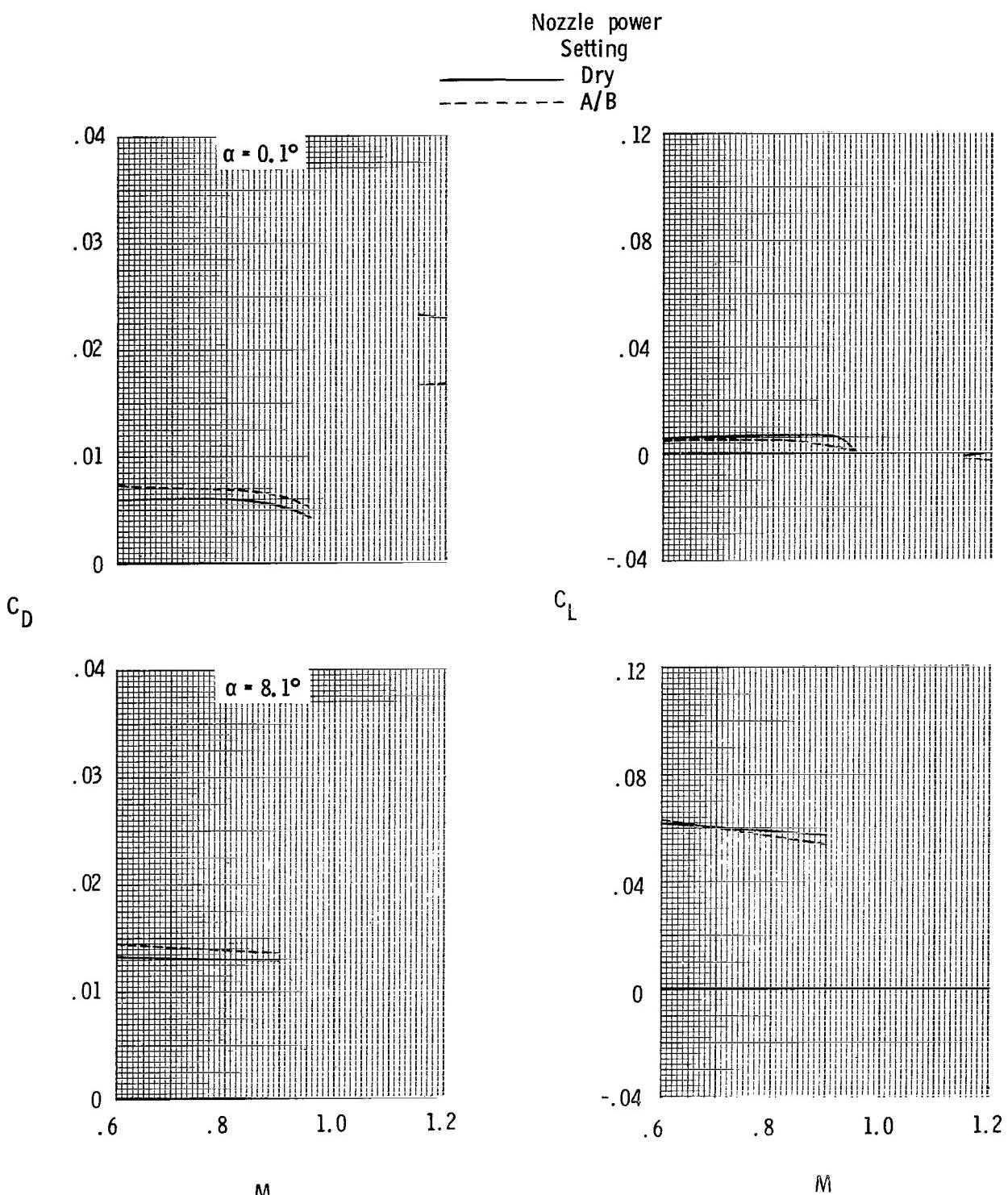
(e) Booms off; horizontal tails aft; twin vertical tails forward.

Figure 72.- Continued.



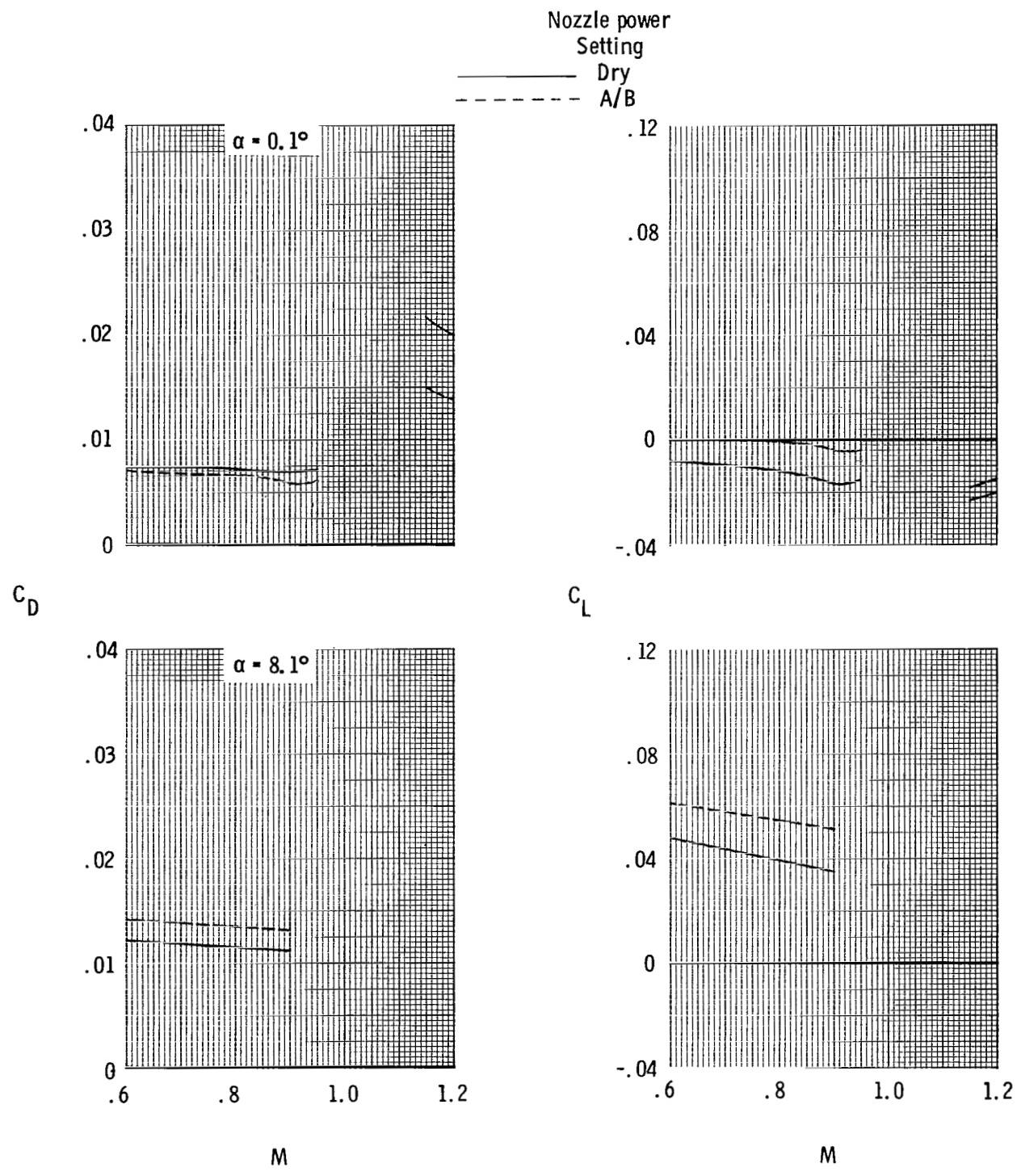
(f) Booms off; horizontal tails aft; twin vertical tails aft.

Figure 72.- Continued.



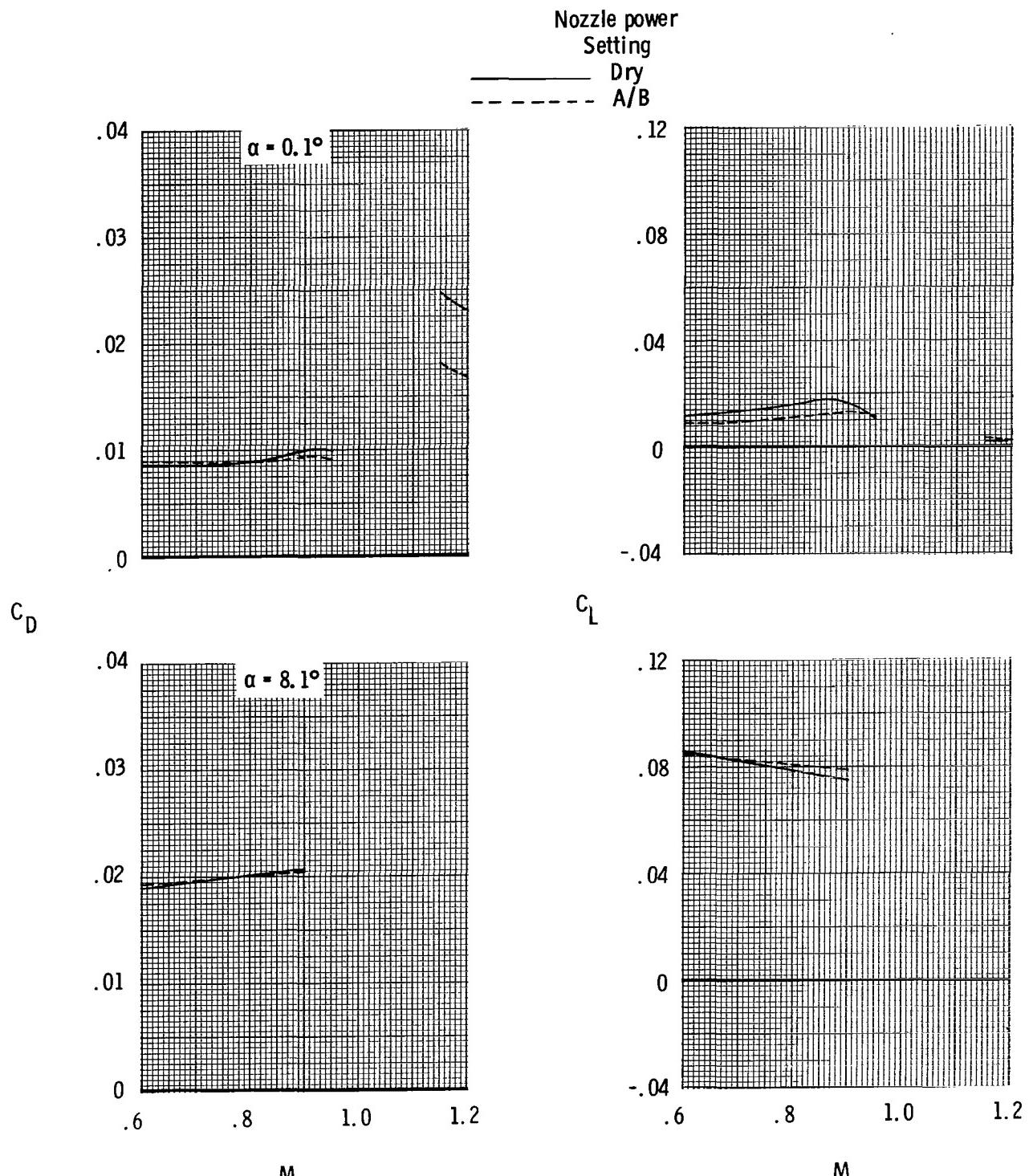
(g) Booms off; horizontal tails aft; single vertical tail forward.

Figure 72.- Continued.



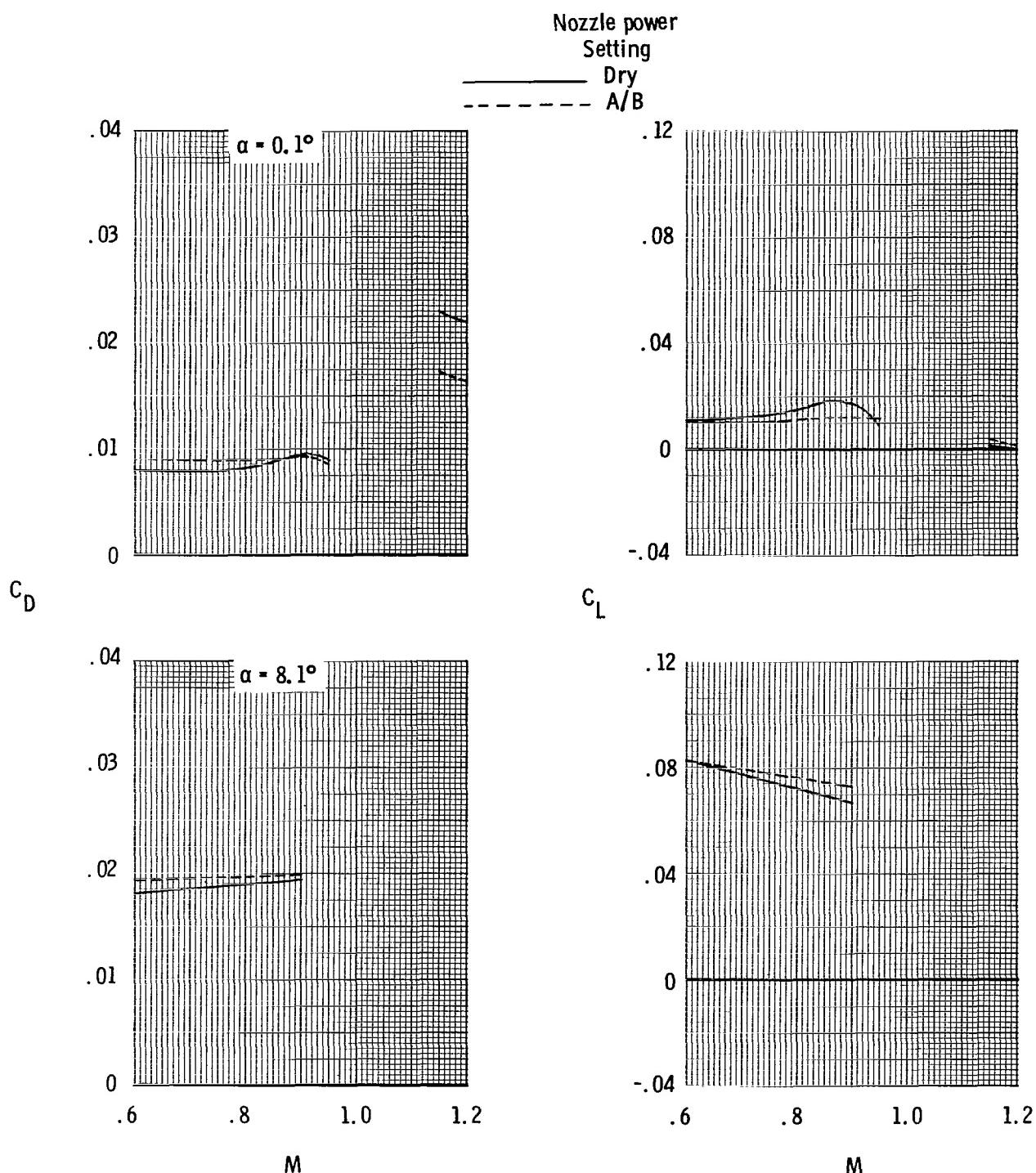
(h) Booms off; horizontal tails aft; single vertical tail aft.

Figure 72.- Continued.



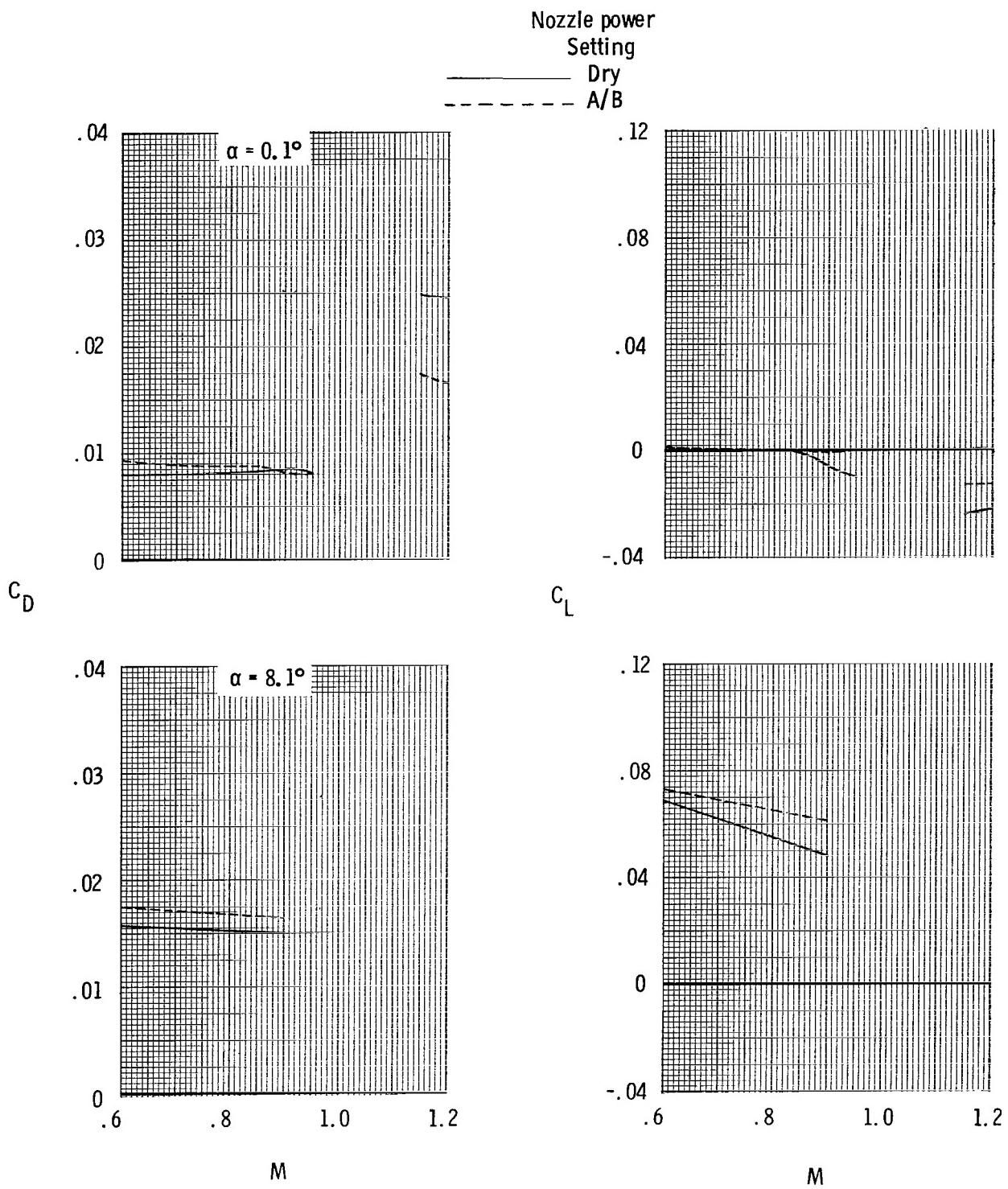
(i) Booms on; horizontal tails forward; twin vertical tails forward.

Figure 72.- Continued.



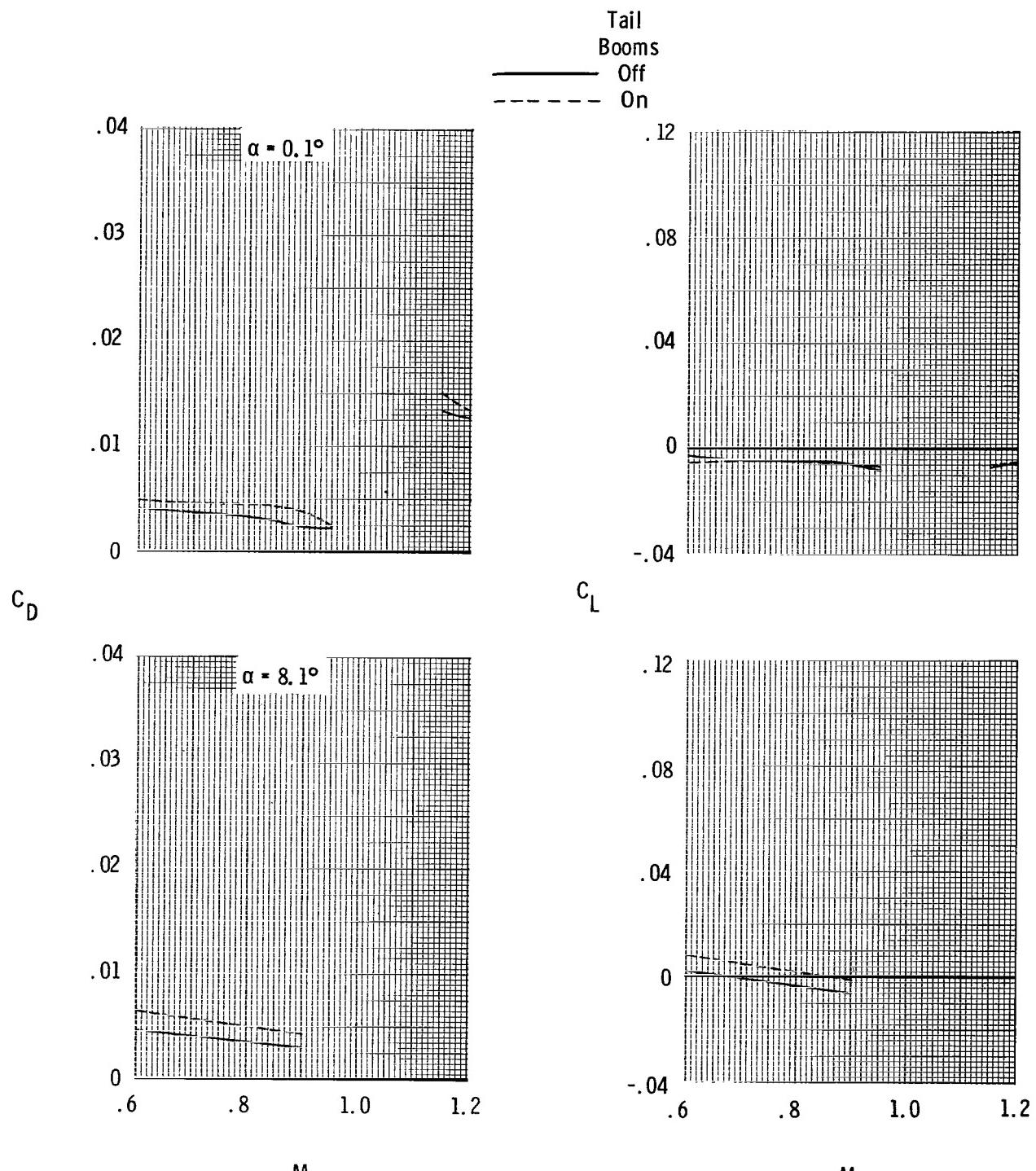
(j) Booms on; horizontal tails aft; twin vertical tails forward.

Figure 72.- Continued.



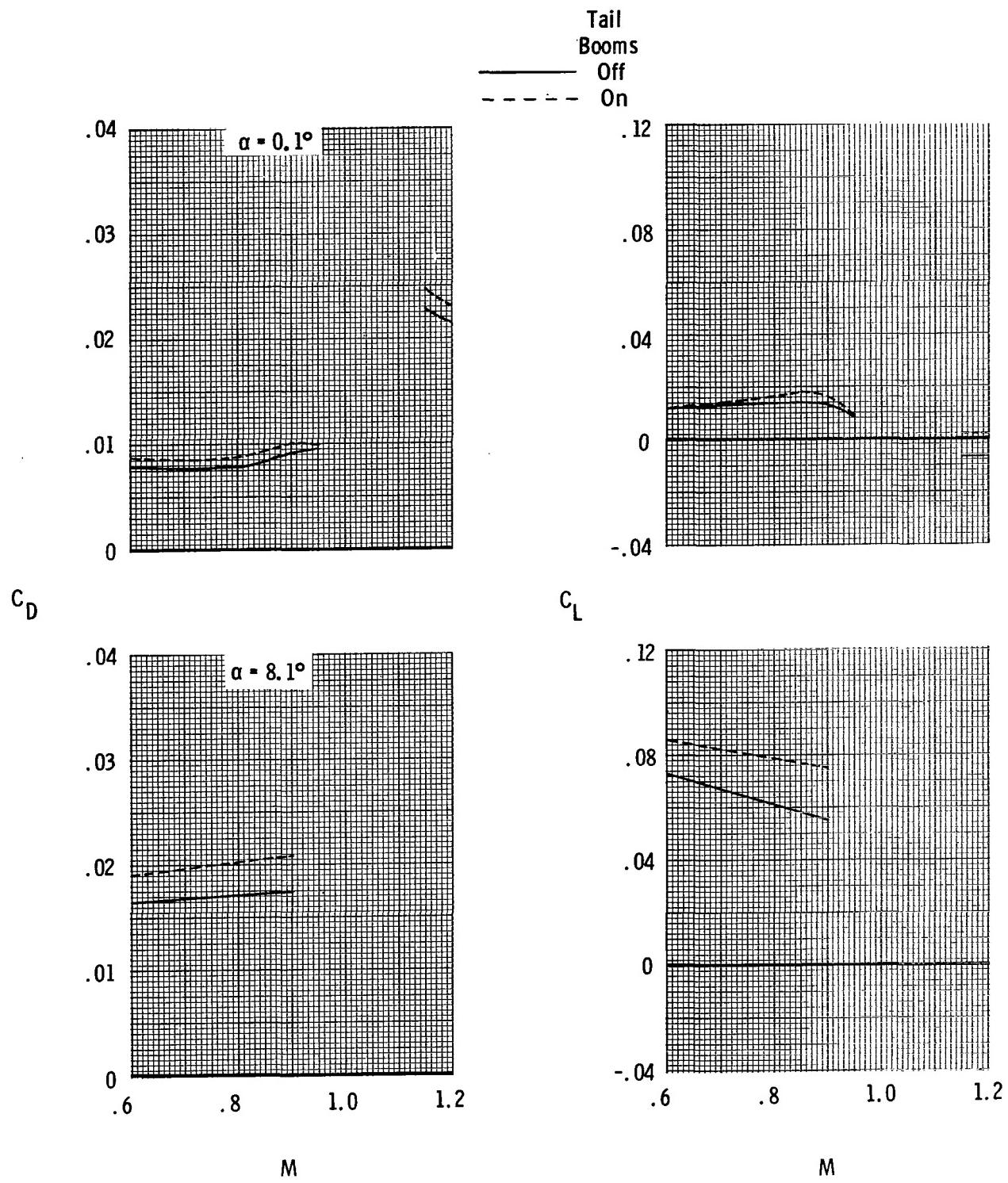
(k) Booms on; horizontal tails aft; twin vertical tails aft.

Figure 72.- Concluded.



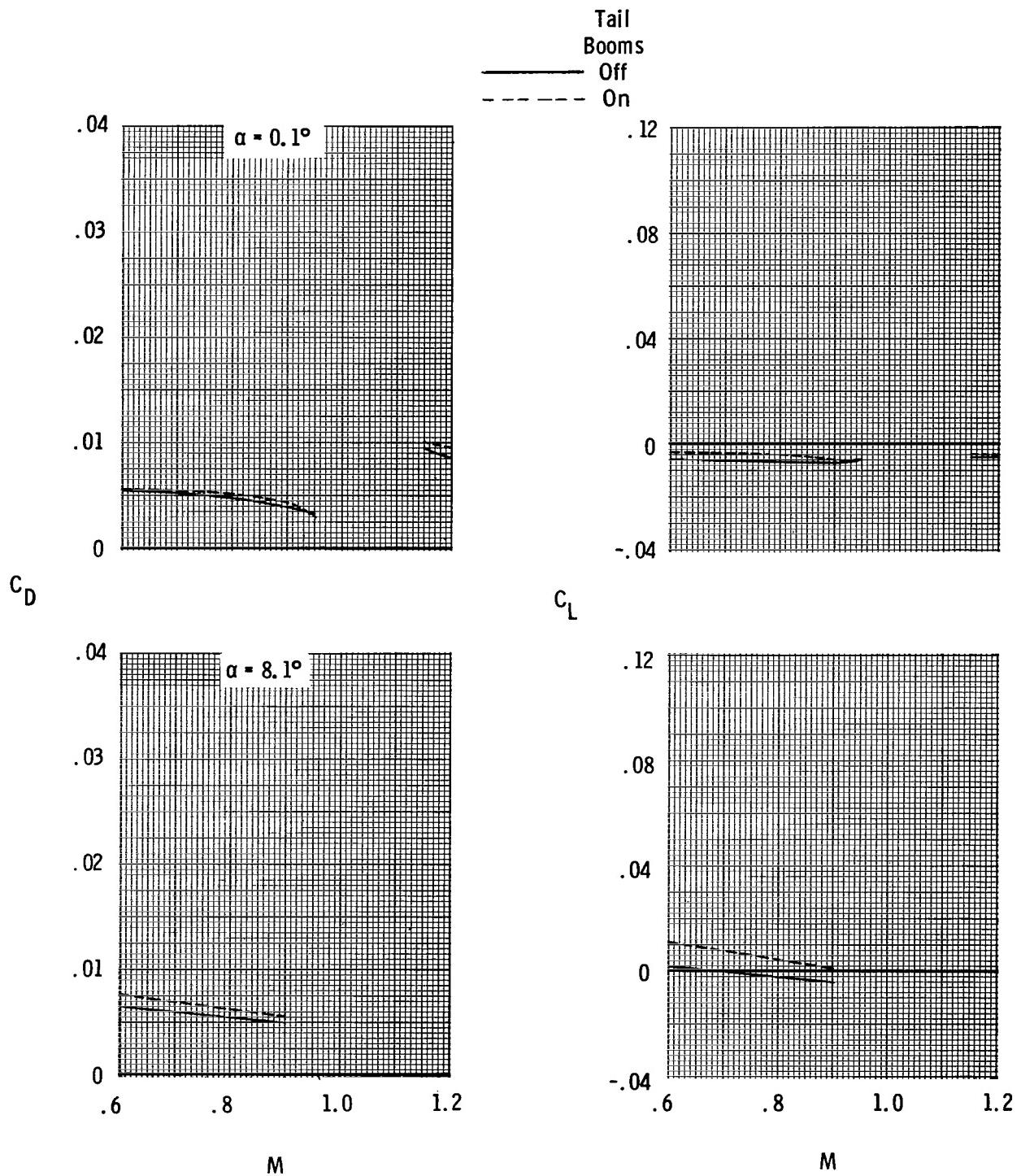
(a) Dry power nozzles; tails off.

Figure 73.- Effects of tail booms on variation of total aft-end drag and lift coefficient with Mach number for scheduled jet total-pressure ratios.



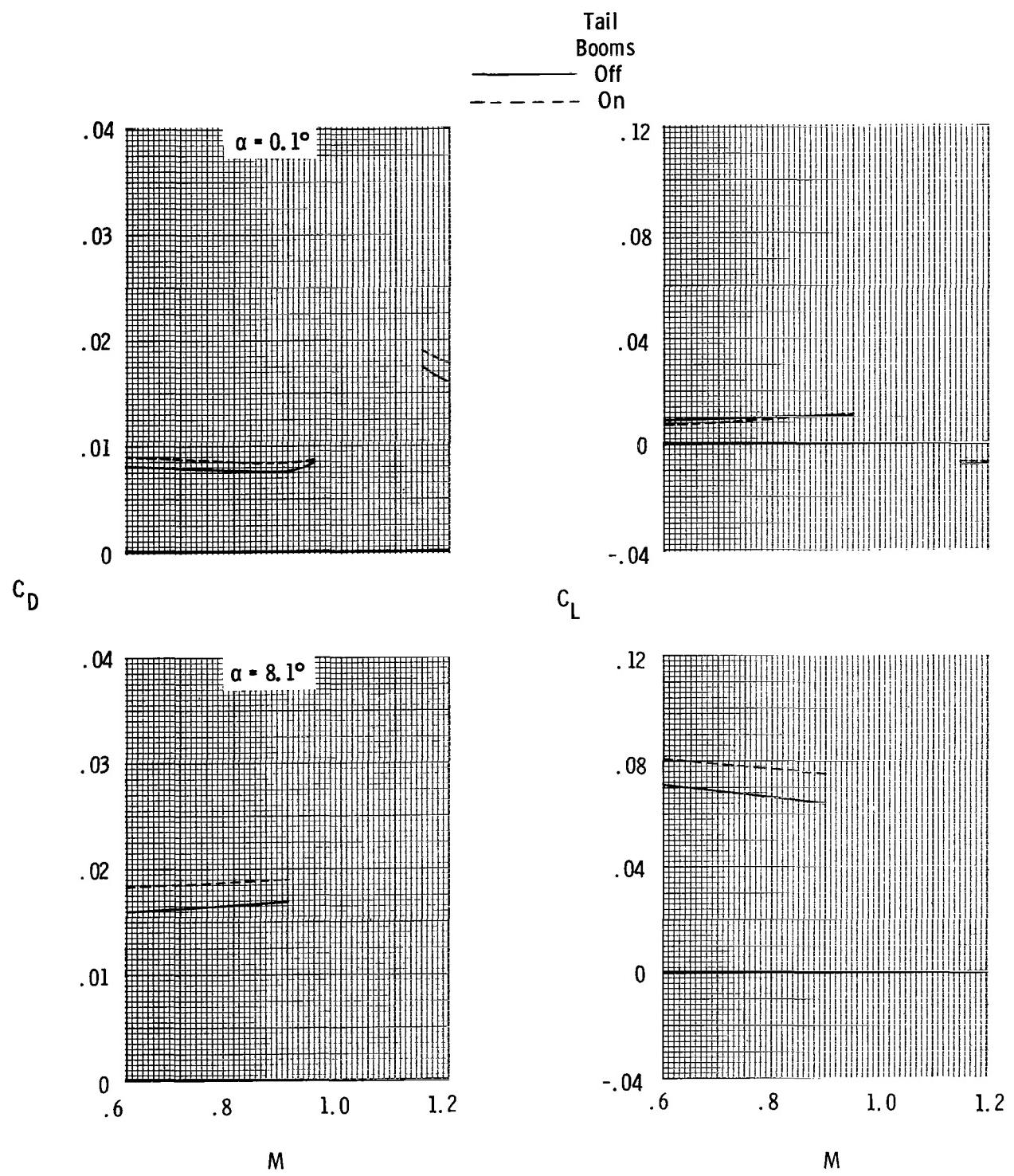
(b) Dry power nozzles; horizontal tails at FS 145.57; twin vertical tails at FS 136.68.

Figure 73.- Continued.



(c) A/B nozzles; tails off.

Figure 73.- Continued.



(d) A/B nozzles; horizontal tails at FS 145.57; twin vertical tails at FS 145.57.

Figure 73.- Concluded.

1. Report No. NASA TP-2116	2. Government Accession No.	3. Recipient's Catalog No.	
4. Title and Subtitle EFFECT OF EMPENNAGE LOCATION ON TWIN-ENGINE AFTERBODY/ NOZZLE AERODYNAMIC CHARACTERISTICS AT MACH NUMBERS FROM 0.6 TO 1.2		5. Report Date May 1983	
7. Author(s) Laurence D. Leavitt	6. Performing Organization Code 505-43-23-01		
9. Performing Organization Name and Address  NASA Langley Research Center Hampton, VA 23665	8. Performing Organization Report No. L-15527		
12. Sponsoring Agency Name and Address  National Aeronautics and Space Administration Washington, DC 20546	10. Work Unit No.		
15. Supplementary Notes	11. Contract or Grant No.		
16. Abstract	13. Type of Report and Period Covered Technical Paper		
An investigation has been conducted in the Langley 16-Foot Transonic Tunnel to determine the effects of several empennage and afterbody parameters on the aft-end aerodynamic characteristics of a twin-engine fighter-type configuration. Model variables were as follows: horizontal tail axial location and incidence, vertical tail axial location and configuration (twin- versus single-tail arrangements), tail booms, and nozzle power setting. Tests were conducted over a Mach number range from 0.6 to 1.2 and over an angle-of-attack range from -2° to 10°. Jet total-pressure ratio was varied from jet off to approximately 10.0.			
17. Key Words (Suggested by Author(s))  Tail interference Empennage location Twin engine Afterbody drag	18. Distribution Statement Unclassified - Unlimited		
Subject Category 02			
19. Security Classif. (of this report) Unclassified	20. Security Classif. (of this page) Unclassified	21. No. of Pages 222	22. Price A10

National Aeronautics and  
Space Administration

Washington, D.C.  
20546

Official Business

Penalty for Private Use, \$300

SPECIAL FOURTH CLASS MAIL  
BOOK

Postage and Fees Paid  
National Aeronautics and  
Space Administration  
NASA-451



4 11U,A, 830330 S00903DS  
DEPT OF THE AIR FORCE  
AF WEAPONS LABORATORY  
ATTN: TECHNICAL LIBRARY (SUL)  
KIRTLAND AFB NM 87117

**NASA**

POSTMASTER: If Undeliverable (Section 158  
Postal Manual) Do Not Return